Realistic Geometry-Based Stochastic Channel Models for Advanced Wireless MIMO Systems

by

Yi Yuan

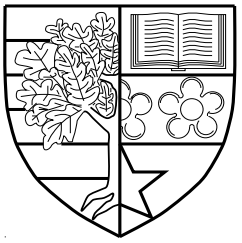

Submitted for the degree of Doctor of Philosophy
at
Heriot-Watt University and The University of Edinburgh
School of Engineering and Physical Sciences

May 2014

Abstract

The employment of multiple antennas at both the Transmitter (Tx) and Receiver (Rx) enables the so-called Multiple-Input Multiple-Output (MIMO) technologies to greatly improve the link reliability and increase the overall system capacity. MIMO has been recommended to be employed in various advanced wireless communication systems, e.g., the Fourth Generation (4G) wireless systems and beyond. For the successful design, performance test, and simulation of MIMO wireless communication systems, a thorough understanding of the underlying MIMO channels and corresponding models are indispensable. The approach of geometry-based stochastic modelling has widely been used due to its advantages, such as convenience for theoretical analysis and mathematical tractability.

In addition, wireless Vehicle-to-Vehicle (V2V) communications play an important role in mobile relay-based cellular networks, vehicular ad hoc networks, and intelligent transportation systems. In V2V communication systems, both the Tx and Rx are in motion and equipped with low elevation antennas. This is different from conventional Fixed-to-Mobile (F2M) cellular systems, where only one terminal moves. This PhD project is therefore devoted to the modelling and simulation of wireless MIMO channels for both V2V and F2M communication systems.

In this thesis, we first propose a novel narrowband Three Dimensional (3D) theoretical Regular-Shape Geometry Based Stochastic Model (RS-GBSM) and the corresponding Sum-of-Sinusoids (SoS) simulation model for non-isotropic MIMO V2V Ricean fading channels. The proposed RS-GBSM has the ability to study the impact of the Vehicular Traffic Density (VTD) on channel statistics and jointly considers the azimuth and elevation angles by using the von Mises-Fisher (VMF) distribution. Moreover, a novel parameter computation method is proposed for jointly calculating the azimuth and elevation angles in the SoS channel simulator. Based on the proposed 3D theoretical RS-GBSM and its SoS simulation model, statistical properties are derived and thoroughly investigated. The impact of the elevation angle in the 3D model on key statistical properties is investigated by comparing with those of the corresponding Two Dimensional (2D) model. It is demonstrated that the 3D model is more practical to characterise real V2V channels, in particular for pico-cell scenarios.

Secondly, actual V2V channel measurements have shown that the modelling assumption of Wide Sense Stationary (WSS) is valid only for very short time intervals. This

fact inspires the requirement of non-WSS V2V channel models. Therefore, we propose a novel 3D theoretical wideband MIMO non-WSS V2V RS-GBSM and corresponding SoS simulation model. Due to the dynamic movement of both the Tx and Rx, the Angle of Departure (AoD) and Angle of Arrival (AoA) are time-variant, which makes our model non-stationary. The proposed RS-GBSMs are sufficiently generic and adaptable to mimic various V2V scenarios. Furthermore, important local channel statistical properties are derived and thoroughly investigated. The impact of non-stationarity on these channel statistical properties is investigated by comparing with those of the corresponding WSS model. The proposed non-WSS RS-GBSMs are validated by measurements in terms of the channel stationary time.

Thirdly, realistic MIMO channel models with a proper trade-off between accuracy and complexity are indispensable for the practical application. By comparing the accuracy and complexity of two latest F2M standardised channel models (i.e., LTE-A and IMT-A channel models), we employ some channel statistical properties as the accuracy metrics and the number of Real Operations (ROs) as the complexity metric. It is shown that the LTE-A MIMO channel model is simple but has significant flaws in terms of the accuracy. The IMT-A channel model is complicated but has better accuracy. Therefore, we focus on investigating various complexity reduction methods to simplify the IMT-A channel model. The results have shown that the proposed methods do not degrade much the accuracy of the IMT-A channel model, whereas they can significantly reduce the complexity in terms of the number of ROs and channel coefficients computing time.

Finally, to investigate the non-stationarity of the IMT-A MIMO channel model, we further propose a non-WSS channel model with time-varying AoDs and AoAs. The proposed time-varying functions can be applied to various scenarios according to moving features of Moving Clusters (MCs) and a Mobile Station (MS). Moreover, the impacts of time-varying AoDs and AoAs on local statistical properties are investigated thoroughly. Simulation results prove that statistical properties are varied with time due to the non-stationarity of the proposed channel model.

In summary, the proposed reference models and channel simulators are useful for the design, testing, and performance evaluation of advanced wireless V2V and F2M MIMO communication systems.

To my family and colleagues

Acknowledgments

Without the support of my supervisors, colleagues, friends and family, this dissertation could not have been completed. I would like to take this opportunity to express my deepest gratitude to them.

First of all, my greatest appreciations to my primary supervisor Prof. Cheng-Xiang Wang for his excellent guidance and paternal encouragement. Besides his academic supervision, he was so considerate about my personal life as well. In addition, my heartfelt thanks must go to my second supervisor, Dr. David I. Laurenson, from the University of Edinburgh, for his valuable comments and discussions. I feel very lucky to have them as my supervisors. I owe both of you a big thank you.

Secondly, I am extremely delighted to have the privilege of knowing my colleagues of past and present in the Advanced Wireless Technologies (AWiTec) Group, namely, Xuemin Hong, Xiang Cheng, Zengmao Chen, Omar Salih, Margaret Anyaegbu, Pat Chambers, Ammar Ghazal, Yu Fu, Fourat Haider, Shangbin Wu, and Ahmed Al-Kinani. I really enjoy the time we spent together on discussions, conversations, seminars, lunches, dinners, coffees, parties, and so on. I thank all of you for sharing wonderful moments and hope our friendship will last forever.

Thirdly, the financial support from the Huawei Technologies Co. Ltd. is gratefully acknowledged for the project "Realistic MIMO Channel Models for 3GPP LTE and IMT-Advanced".

Last but not least, my special gratitude goes to my parents, Hongxin Yuan & Suzhen Zhou, and my wife, Jing Huang, for their unconditional love and infinite support. Dear our families, we feel regret that we have been living such long time away from you and our home town. We miss you so much...

Yi Yuan
Edinburgh, March 2014.

Declaration of Authorship

I, Yi Yuan, declare that this thesis titled, 'Realistic Geometry-Based Stochastic Channel Models for Advanced Wireless MIMO Systems' and the work presented in it are my own. I confirm that:

- This work was done wholly while in candidature for a research degree at Heriot-Watt University and The University of Edinburgh.
- Where I have consulted the published work of others, this is always clearly attributed.
- Where I have quoted from the work of others, the source is always given. With the exception of such quotations, this thesis is entirely my own work.
- I have acknowledged all main sources of help.
- Where the thesis is based on work done by myself jointly with others, I have made clear exactly what was done by others and what I have contributed myself.

Signed: _____

Date: _____

Contents

List of Figures

List of Tables

Abbreviations

2D	Two Dimensional
3D	Three Dimensional
3G	Third Generation
3GPP	Third Generation Partnership Project
4G	Fourth Generation
5G	Fifth Generation
AAoA	Azimuth AoA
AAoD	Azimuth AoD
ACF	Autocorrelation Function
AFD	Average Fade Duration
AoA	Angle of Arrival
AoD	Angle of Departure
AS	Angular Spread
ASA	AS of Arrival
ASD	AS of Departure
BER	Bit Error Rate
BS	Base Station
CBSM	Correlation Based Stochastic Model
CCDF	Complementary CDF

CCF	Cross-correlation Function
CDF	Cumulative Distribution Function
CDL	Clustered Delay Line
CF	Correlation Function
CIR	Channel Impulse Response
COST	European Cooperative in Science and Technology
DoA	Direction of Arrival
DoD	Direction of Departure
DS	Delay Spread
DSRC	Dedicated Short Range Communications
EAoA	Elevation AoA
EAoD	Elevation AoD
EMEDS	Extended Method of Exact Doppler Spread
eNB	eNode B
EPA	Extended Pedestrian A
ETU	Extended Typical Urban
EVA	Extended Vehicular A
F2M	Fixed-to-Mobile
FCF	Frequency Correlation Function
GBDM	Geometry Based Deterministic Model
GBSM	Geometry Based Stochastic Model
HST	High Speed Train
I-to-O	Indoor-to-Outdoor
i.i.d.	Independent and Identically Distributed
IMT-A	International Mobile Telecommunications Advanced

InH	Indoor Hotspot
IS-GBSM	Irregular-Shape Geometry Based Stochastic Model
IST	Information Society Technologies
ITS	Intelligent Transportation Systems
ITU	International Telecommunication Union
KBSM	Kronecker Based Stochastic Model
LAN	Local Area Network
LCR	Level Crossing Rate
LoS	Line-of-Sight
LPNM	Lp-Norm Method
LSF	Local Scattering Function
LSP	Large Scale Parameter
LTE	Long Term Evolution
LTE-A	LTE-Advanced
M2M	Mobile-to-Mobile
MC	Moving Cluster
MEV	Method of Equal Volume
MIMO	Multiple-Input Multiple-Output
MMEA	Modified Method of Equal Area
MPC	Multi-Path Component
MS	Mobile Station
NGSM	Non-Geometrical Stochastic Model
NLoS	Non-Line-of-Sight
O-to-I	Outdoor-to-Indoor
PAS	Power Azimuth Spectrum

PDF	Probability Density Function
PDP	Power Delay Profile
PSD	Power Spectral Density
RCM	Random Cluster Model
RMa	Rural Macro
RMS	Root Mean Square
RO	Real Operation
RS-GBSM	Regular-Shape Geometry Based Stochastic Model
RV	Random Variable
Rx	Receiver
SCM	Spatial Channel Model
SCME	SCM-Extension
SF	Shadow Fading
SI	Stationary Interval
SISO	Single-Input Single-Output
SMa	Suburban Macro
SNR	Signal-to-Noise Ratio
SoS	Sum-of-Sinusoids
SRL	Stationarity Region Length
SSP	Small Scale Parameter
ST	Space-Time
TDL	Tapped Delay Line
TTI	Transmission Time Interval
Tx	Transmitter
UE	User Equipment
UMa	Urban Macro
UMi	Urban Micro

V2V	Vehicle-to-Vehicle
VMF	von Mises-Fisher
VTD	Vehicular Traffic Density
WAVE	Wireless Access in Vehicular Environments
WIM	WINNER Channel Model
WIM+	WIM-Phase +
WIM1	WIM-Phase I
WIM2	WIM-Phase II
WINNER	Wireless World Initiative New Radio
WSS	Wide Sense Stationary
WSSUS	Wide Sense Stationary Uncorrelated Scattering

Symbols

$(\cdot)^T$	transpose of a matrix/vector
$(\cdot)^H$	Hermitian transpose of a matrix/vector
$(\cdot)^*$	complex conjugate
$\dot{(\cdot)}$	first derivative
$\hat{(\cdot)}$	corresponding parameters of stochastic simulation models
$\lvert\cdot\rvert$	absolute value (amplitude) of a complex vector
$\mathbf{arg}\{\cdot\}$	argument (phase) of a complex vector
$\mathbf{erf}(\cdot)$	error function
$\mathbf{gcd}\{\cdot\}$	greatest common divisor of a sequence
$\mathbf{max}\{\cdot\}$	maximum value of a vector
$\mathbf{min}\{\cdot\}$	minimum value of a vector
$\mathrm{Re}\{\cdot\}$	real part of of a complex
$\mathrm{Im}\{\cdot\}$	imaginary part of a complex
$\mathbf{H}\{\cdot\}$	Hilbert transform
$\mathbf{E}[\cdot]$	statistical expectation
$\mathbf{F}\{\cdot\}$	Fourier transform
$\mathrm{I}_0(\cdot)$	zeroth-order modified Bessel function of the first kind
$\mathrm{J}_0(\cdot)$	zeroth-order Bessel function of first kind
$\mathrm{J}_1(\cdot)$	first-order Bessel function of first kind
$\mathbf{Q}\{\cdot,\cdot\}$	Marcum Q-function
$\bigotimes$	Kronecker product of matrices

$\cup$	union of sets
$\sum$	summation
$\prod$	multiple product
α	azimuth angle of the VMF PDF
α_0	mean azimuth angle of the scatterers located on a sphere
α_{T0}	mean AAoD of the scatterers located on a sphere around the Tx
α_{R0}	mean AAoA of the scatterers located on a sphere around the Rx
α_m	ray offset angles of the mth sub-path
α_R^{LoS}	AAoA of the LoS paths
$\alpha_T^{(n_i)}$	AAoD of the waves that impinge on the effective scatterers $s^{(n_i)}$
$\alpha_R^{(n_i)}$	AAoA of the waves travelling from the effective scatterers $s^{(n_i)}$
$\alpha_T^{(n_{l,i})}$	AAoD of the waves that impinge on the effective scatterers $s^{(n_{l,i})}$
$\alpha_R^{(n_{l,i})}$	AAoA of the waves travelling from the effective scatterers $s^{(n_{l,i})}$
β	elevation angle of the VMF PDF
β_0	mean elevation angle of the scatterers located on a sphere
β_{T0}	mean EAoD of the scatterers located on a sphere around the Tx
β_{R0}	mean EAoA of the scatterers located on a sphere around the Rx
β_R^{LoS}	EAoA of the LoS paths
$\beta_T^{(n_i)}$	EAoD of the waves that impinge on the effective scatterers $s^{(n_i)}$
$\beta_R^{(n_i)}$	EAoA of the waves travelling from the effective scatterers $s^{(n_i)}$
$\beta_T^{(n_{l,i})}$	EAoD of the waves that impinge on the effective scatterers $s^{(n_{l,i})}$
$\beta_R^{(n_{l,i})}$	EAoA of the waves travelling from the effective scatterers $s^{(n_{l,i})}$
γ_T	moving direction of the Tx in the x-y plane
γ_R	moving direction of the Rx in the x-y plane
Γ	polarisation correlation matrix
δ_T	antenna elements spacing at the Tx
δ_R	antenna elements spacing at the Rx
$\delta_{P,k}$	movement of the MC and MS
$\delta_{MC,k}$	movement of the MC
$\delta_{MS,k}$	movement of the MS

Δf	frequency spacing
Δd_s	antenna elements spacing at the BS
Δd_u	antenna elements spacing at the MS
$\Delta_{P,k}$	movement of the Tx and Rx
$\Delta_{T,k}$	movement of the Tx
$\Delta_{R,k}$	movement of the Rx
$\Delta\varphi_{n,m}$	AoA offset
ε	RMS error
ε_{pq}	distances between T_p and T_q
ε_{pn_i}	distances between T_p and $s^{(n_i)}$
$\varepsilon_{n_1n_2}$	distances between $s^{(n_1)}$ and $s^{(n_2)}$
ε_{n_iq}	distances between $s^{(n_i)}$ and T_q
$\varepsilon_{pn_{l,i}}$	distances between T_p and $s^{(n_{l,i})}$
$\varepsilon_{n_{l,1}n_{l,2}}$	distances between $s^{(n_{l,1})}$ and $s^{(n_{l,2})}$
$\varepsilon_{n_{l,i}q}$	distances between $s^{(n_{l,i})}$ and T_q
$\zeta(t)$	amplitude process of $h_{pq}(t)$
η_{SB_i}	power-related parameter of ith single-bounced ray
η_{DB}	power-related parameter of the double-bounced ray
$\eta_{SB_{1,i}}$	power-related parameter of ith single-bounced ray in first tap
$\eta_{DB_{1,i}}$	power-related parameter of ith double-bounced ray in first tap
$\eta_{SB_{l,i}}$	power-related parameter of ith single-bounced ray in lth tap
$\eta_{DB_{l,i}}$	power-related parameter of ith double-bounced ray in lth tap
$\vartheta(t)$	phase process of $h_{pq}(t)$
θ_T	orientation of the Tx antenna array in the x-y plane
θ_R	orientation of the Rx antenna array in the x-y plane
θ_c	moving direction of the MC at BS
θ_v	relative moving direction of MS relative to MC
θ_{MC}	moving direction of the MC at MS
θ_{MS}	moving direction of the MS
λ	carrier wavelength
λ_G	generation rate of new clusters

λ_R	recombination rate of existing clusters
ξ	distances between T_p and O_R
$\xi_T^{n_3}$	distances between O_T and $s^{(n_3)}$
$\xi_R^{n_3}$	distances between O_R and $s^{(n_3)}$
ξ_{n_1}	distances between $s^{(n_1)}$ and O_R
ξ_{n_2}	distances between O_T and $s^{(n_2)}$
$\rho_{h_{pq}h_{p'q'}}(\tau)$	ST CF between $h_{pq}(t)$ and $h_{p'q'}(t)$
$\rho_{h_{l,pq}h_{l,p'q'}}(t,\tau)$	local ST CF between $h_{l,pq}(t)$ and $h_{l,p'q'}(t)$
$\rho_{H_{pq}H_{p'q'}}(t,\Delta f')$	local FCF
$\rho_{s_2u_2}^{s_1u_1}(\Delta d_s,\Delta d_u,\tau')$	ST CF between $h_{s_1u_1}(t)$ and $h_{s_2u_2}(t)$
σ_0^2	mean power of $h_{pq}(t)$
τ	time separation
τ'	time delay
τ_l	lth tap delay
τ_n	nth tap delay
$\tau_n(t)$	time-varying delay of the nth cluster
τ_{pq}	travel time of the wave through the link $T_p \to T_q$
τ_{pq,n_i}	travel time of the wave through the link $T_p \to S_{n_i} \to T_q$
τ_{pq,n_1,n_2}	travel time of the wave through the link $T_p \to S_{n_1} \to S_{n_2} \to T_q$
τ_{l,pq,n_i}	travel time of the wave through the link $T_p \to S_{l,n_i} \to T_q$
τ_{l,pq,n_1,n_l}	travel time of the wave through the link $T_p \to S_{n_1} \to S_{n_l} \to T_q$
τ_{l,pq,n_l,n_2}	travel time of the wave through the link $T_p \to S_{n_l} \to S_{n_2} \to T_q$
$\upsilon_{n,m}$	Doppler frequency of the MS related to $\varphi_{n,m}$
Υ	period
ϕ_n	mean AoD of nth cluster
$\phi_{n,m}$	AoD of nth cluster with mth offset
$\phi_{n,m}(t)$	time-varying AoD of nth effective scatterers
φ_n	mean AoA of nth cluster
$\varphi_{n,m}$	AoA of nth cluster with mth offset
$\varphi_{n,m}(t)$	time-varying AoA of nth effective scatterers
φ_T	elevation of the Tx antenna array relative to the x-y plane

φ_R	elevation of the Rx antenna array relative to the x-y plane
ψ_n	random phase of nth tap
ψ_{n_i}	random phase of the narrowband ith single-bounced rays
$\psi_{n1,n2}$	random phase of the narrowband double-bounced rays
$\psi_{n_{1,i}}$	random phase of the single-bounced rays in the first tap
$\psi_{n_{1,1},n_{1,2}}$	random phase of the double-bounced rays in the first tap
$\psi_{n_{l,i}}$	random phase of the single-bounced rays in the lth tap
$\psi_{n_{l,1},n_{l,2}}$	random phase of the double-bounced rays in the lth tap
$\Phi_{n,m}$	random phase
$\widehat{\Psi}_T(\Delta f)$	normalised FCF
Ω_{pq}	total power of the $T_p \rightarrow R_q$ link
χ_p	total power of all taps
a	semi-major axis of the narrowband elliptic-cylinder model
a_l	semi-major axis of the lth elliptic-cylinder model
$a(t_0)$	distance between MC Z and MS
b	semi-minor axis of the narrowband elliptic-cylinder model
b_l	semi-minor axis of the lth elliptic-cylinder model
$b(t_0)$	distance between BS and MS
B_c	coherence bandwidth
c	speed of light
$c(t_0)$	distance between BS and MC A
C	scaling factor defined by IMT-A
c_l	gain of the lth tap
D	Tx-Rx distance
f	half distance between two focal points of the elliptic-cylinder
f_l	half distance between two focal points of lth elliptic-cylinder
f_c	carrier frequency
f_D	Doppler frequency
f_{Tmax}	maximum Doppler frequency due to the motion of the Tx
f_{Rmax}	maximum Doppler frequency due to the motion of the Rx

$f(\alpha, \beta)$	VMF PDF
$h_{u,s}(t, \tau)$	fading envelope between the sth and uth antenna elements
$h_{pq}(t)$	fading envelope between the pth and qth antenna elements
$h_{p'q'}(t)$	fading envelope between the p'th and q'th antenna elements
$h_{pq}^{LoS}(t)$	fading envelope of the LoS component
$h_{pq}^{SB_i}(t)$	fading envelope of the ith single-bounced rays
$h_{pq}^{DB}(t)$	fading envelope of the double-bounced rays
$h_{pq}^{In}(t)$	in-phase component of $h_{pq}(t)$
$h_{pq}^{Qu}(t)$	quadrature component of $h_{pq}(t)$
$h_{pq}(t, \tau')$	wideband CIR between the pth and qth antenna elements
$h_{1,pq}(t)$	fading envelope of the first tap
$h_{1,pq}(t)$	fading envelope of the lth tap
$h_{1,pq}^{SB_i}(t)$	fading envelope of the single-bounced rays in the first tap
$h_{l,pq}^{SB_i}(t)$	fading envelope of the single-bounced rays in the lth tap
$h_{1,pq}^{DB}(t)$	fading envelope of the double-bounced rays in the first tap
$h_{l,pq}^{DB}(t)$	fading envelope of the double-bounced rays in the lth tap
$h_{u,s,n}(t)$	fading envelope between the sth and uth antenna elements in the nth tap
$H_{pq}(t, f')$	time-variant transfer function of $h_{pq}(t, \tau')$
$H_{p'q'}(t, f')$	time-variant transfer function of $h_{p'q'}(t, \tau')$
$\mathbf{H}(t)$	MIMO channel matrix
k	a parameter of VMF PDF that controls the angle spread
$k^{(1)}$	a parameter of VMF PDF at the Tx sphere
$k^{(2)}$	a parameter of VMF PDF at the Rx sphere
$k^{(3)}$	a parameter of VMF PDF at the elliptic-cylinder
$k^{(l,1)}$	a parameter of VMF PDF at the Tx sphere in lth tap
$k^{(l,2)}$	a parameter of VMF PDF at the Rx sphere in lth tap
$k^{(l,3)}$	a parameter of VMF PDF at the lth elliptic-cylinder
K	Ricean factor
L	total number of taps (or virtual confocal elliptic-cylinders)
$L(t)$	time-varying total number of taps

L_{new_k}	total number of new taps at time t_k
$L(r)$	envelope LCR
m	mth effective scatterers
M	number of independent sub-paths (irresolvable rays)
M_T	Tx antenna array
M_R	Rx antenna array
n	nth effective scatterers
N	number of independent effective scatterers
N_1	number of effective scatterers around the Tx lying on a sphere
N_2	number of effective scatterers around the Rx lying on a sphere
N_3	number of effective scatterers lying on the an elliptic-cylinder
N_l	number of effective scatterers lying on the lth elliptic-cylinder
$N_R(r_E)$	envelope LCR
$p_R(z)$	amplitude PDF of $R(t)$
$p_\zeta(z)$	amplitude PDF of $\zeta(t)$
$p_\vartheta(\theta)$	phase PDF of $\vartheta(t)$
P_c	a percentage of MPCs that contains moving scatterers
$P_n(t)$	normalised time-varying power of the nth cluster
$P'_n(t)$	time-varying power of the nth cluster
$P_{remain}(\Delta_{P,k})$	probability of remaining MPCs
$P_R(r_E)$	CDF of the amplitude process $R(t)$
r	signal envelope crosses level used for V2V models
r_E	signal envelope crosses level used for F2M models
$R(t)$	amplitude process of $h_{u,s,n}(t)$
R_T	radius of a sphere around the Tx in the two-sphere model
R_R	radius of a sphere around the Rx in the two-sphere model
$\widehat{R}_\tau(\tau)$	normalised PDP
$\mathbf{R}_{BS}$	spatial correlation matrix of BS antennas
$\mathbf{R}_{MS}$	spatial correlation matrix of MS antennas
$\mathbf{R}_{spat}$	spatial correlation matrix with the antenna polarisation
$\mathbf{R}_{MIMO}$	MIMO spatial correlation matrix of the KBSM

$s^{(n_1)}$	n_1th effective scatterer located on a sphere around the Tx
$s^{(n_2)}$	n_2th effective scatterer located on a sphere around the Rx
$s^{(n_3)}$	n_3th effective scatterer located on an elliptic-cylinder
$s^{(n_1,1)}$	$n_{1,1}$th effective scatterer located on a sphere around the Tx
$s^{(n_1,2)}$	$n_{1,2}$th effective scatterer located on a sphere around the Rx
$s^{(n_l,3)}$	$n_{l,3}$th effective scatterer located on the lth elliptic-cylinder
$S_{H_{pq}H_{p'q'}}(t,\tau')$	local PDP
t	time
$T(r)$	envelope AFD
$T_R(r_E)$	envelope AFD
v	relative speed of MS relative to MC
v_T	Tx velocity
v_R	Rx velocity
$\bar{v}_T$	mean Tx velocity
$\vec{v}_{MC}$	MC velocity
$\vec{v}_{MS}$	MS velocity
$\vec{v}_{MS/MC}$	velocity of MS relative to MC
$\vec{x}_R(t)$	motion difference of the Rx

Chapter 1

Introduction

1.1 Background

After the success stories of the traditional cellular network systems, the trend in wireless communication technologies requires more reliable and efficient technologies on Mobile-to-Mobile (M2M) communications. A typical cellular network connects different Mobile Station (MS) to one another through a fixed Base Station (BS). Cellular communication systems are normally called as Fixed-to-Mobile (F2M) systems which is the origin of modern wireless communications [1], [2]. In recent years, M2M communications have been encountered in many new applications, such as wireless mobile ad hoc peer-to-peer networks [3]–[5], cooperative systems [6], [7], and intelligent transportation systems [8]. In a M2M communication system, both the Transmitter (Tx) and Receiver (Rx) are in motion often mounted with low elevation antennas. This is different from conventional F2M cellular radio systems, where only one terminal moves as shown in Fig. 1.1. Therefore, existing channel models for F2M communications cannot be used directly for the design of M2M communication systems. Besides the F2M channel modelling, M2M modelling has also become a hot research topic.

One of the most promising technologies in mobile radio communications is Multiple-Input Multiple-Output (MIMO), in which multiple antennas are deployed at both the Tx and Rx. Information theory has shown that the capacity of a wireless channel can

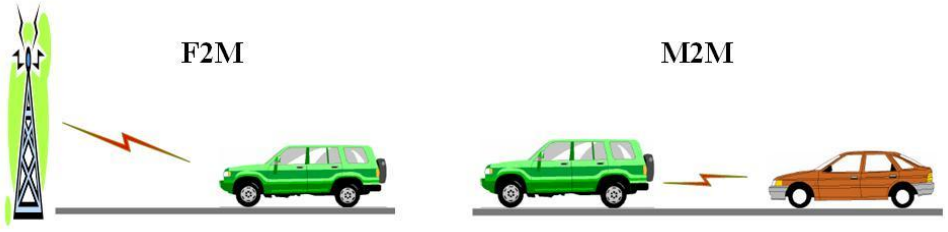

FIGURE 1.1: Difference between F2M and M2M communications.

be increased significantly if the spatial domain of multipath propagation is properly exploited by using MIMO technologies. Considering the demand for high-speed wireless services, MIMO technologies have widely been adopted for the Third Generation (3G), Fourth Generation (4G) and even Fifth Generation (5G) F2M cellular systems and also have been receiving more and more attention for M2M systems. Please note that M2M sometimes represents Machine-to-Machine in the literature. To clarify this confusion, we will mostly use Vehicle-to-Vehicle (V2V) to describe what we defined M2M, as the V2V is a general case of mobile-to-mobile systems.

From the conception of new wireless techniques to their performance evaluation and validation, a thoughtful understanding of the underlying propagation characteristics is essential. The knowledge of the real-world scenarios is necessary to identify the main influences of the environment on the transmitted signal. For the performance evaluation, conducting field trials are highly expensive and time consuming. Therefore, the system designers are endeavouring to find cost-effective solutions. One of the motivations is to reproduce the desired channel characteristics by computer simulations. Fig. 1.2 illustrates the principle of wireless MIMO channel modelling. It is absolutely crucial and indispensable that the channel simulation models accurately reflect the fading statistics of realistic physical channels. Whether to model fading channels for classical F2M systems or future V2V systems, there are many existing channel-modelling approaches, such as the Correlation Based Stochastic Model (CBSM) and Geometry Based Stochastic Model (GBSM). In [9] and [10], these two dominating approaches have been compared in terms of their statistical properties.

Many standardised channel models for F2M systems have been released in the past

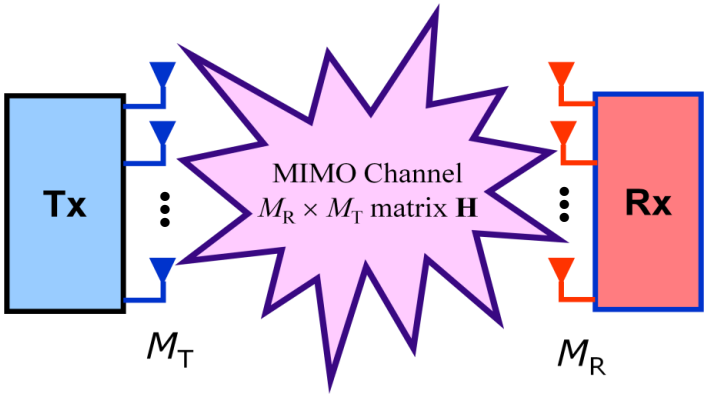

FIGURE 1.2: Wireless MIMO channel modelling.
(M_T and M_R are the antenna elements at the Tx and Rx, respectively.)

decade, such as European Cooperative in Science and Technology (COST) 259 [11]–[13], COST 273 [14], IEEE 802.11 TGn channel models [15], the Long Term Evolution (LTE) channel model [16]–[21] the LTE-Advanced (LTE-A) channel model [22]–[24], the Third Generation Partnership Project (3GPP) Spatial Channel Model (SCM) [25], [26], SCM-Extension (SCME) [27], the Information Society Technologies (IST) Wireless World Initiative New Radio (WINNER) series channel models, so called WINNER Channel Models (WIMs), (i.e., WIM-Phase I (WIM1) [28], WIM-Phase II (WIM2) [29], WIM-Phase + (WIM+) [30]), and International Telecommunication Union (ITU) International Mobile Telecommunications Advanced (IMT-A) channel model [31], [32].

Moreover, a vehicular communication system has been standardised, which is IEEE 802.11p [33], an approved amendment to the IEEE 802.11 standard adding Wireless Access in Vehicular Environments (WAVE). It defines enhancements to 802.11 required to support Intelligent Transportation Systems (ITS) applications. This includes data exchange between high-speed vehicles (i.e., V2V) and between roadside infrastructures and the vehicles (i.e., F2M) in the licensed ITS band of 5.9 GHz (5.85-5.925 GHz). The IEEE 802.11p is also considered for Dedicated Short Range Communications (DSRC) [34]. Consequently, standardised V2V channel models are expected to be developed in the near future.

In the following, we briefly summarise the evolution of wireless channel models. In

the literature, Regular-Shape Geometry Based Stochastic Models (RS-GBSMs) have been widely used to mimic wireless channels. The RS-GBSM assumes that the effective scatterers are located on a regular geometric shape, e.g. rings, ellipses, cylinders, spheres, etc. Akki and Haber were the first to propose a RS-GBSM for isotropic scattering Single-Input Single-Output (SISO) V2V Rayleigh fading channels in [35] and [36]. In [37], a two-ring RS-GBSM considering only double-bounced rays was presented for non-isotropic scattering MIMO V2V Rayleigh fading channels. In [38], Zajic and Stuber proposed a more general two-ring RS-GBSM that constructs the received complex fading envelope as a superposition of the Line-of-Sight (LoS), single-bounced, and double-bounced rays. In order to investigate the impact of Vehicular Traffic Density (VTD) on channel statistics, new RS-GBSMs for non-isotropic scattering MIMO V2V channels were proposed in [39]. In [40], the authors proposed a Three Dimensional (3D) two-cylinder RS-GBSM for non-isotropic scattering narrowband MIMO V2V channels. This narrowband 3D model was further extended into a wideband one in [41]. However, both the aforementioned narrowband and wideband 3D RS-GBSMs assumed the azimuth angle and elevation angle are completely independent and thus analyse them separately.

In the literature, there are many other research work related to both V2V and F2M channel models. In [7], this article compares a variety of models for wireless fading channels in cooperative communication systems, specifically, investigations on V2V fading channels in transparent relaying systems. In [42], three primary V2V simulation channel models found in the literature are reviewed. Also, two complete vehicular ad hoc networks simulation frameworks are presented. They emphasise the importance of realistic channel models in vehicular networking. In addition, there are a few preliminary 3D MIMO V2V channel models proposed, such as [43]–[45], etc. They all consider the von Mises-Fisher (VMF) distribution as the scattering distribution. However, to the best of my knowledge, only a few papers are relevant to 3D channel measurements [46].

In short, the development of wireless channel models are undergoing from SISO to MIMO, from isotropic to non-isotropic, from narrowband to wideband, from Two

Dimensional (2D) to 3D, and from Wide Sense Stationary (WSS) models to non-WSS models. The development of wireless channel modelling and simulations are becoming more and more comprehensive and effective. Moreover, it is foreseeable that more corresponding measurement campaign will be conducted to support the theoretical investigation of 3D non-WSS MIMO channel modelling.

1.2 Motivation

To investigate and analyse a real communication channel, accurate modelling of MIMO channels is an important prerequisite for MIMO system design, simulation, and deployment. Therefore, we need a practical channel simulation technique. Channel modelling, in short, is attempting to develop a model that describes a channel behaviour, response to input under different conditions, and determine the parameters that may mathematically represent the channel.

In channel modelling, accuracy and complexity are two key words. The accuracy measures the level of correctness of the model. For the complexity, it measures that how complicated the model is. Inaccurate or over-simplified channel models may lead to either over-optimistic or over-pessimistic performance evaluation results of the chosen algorithms and transmission schemes, which may cause wrong decisions on product development or standardisation. On the other hand, too complicated channel models may significantly increase simulation time and reduce the model usability. In order to achieve an acceptable balance, there must be a trade-off between both accuracy and complexity.

The geometry-based modelling approach has been widely used to simulate wireless channels due to its close agreement with the existing measured data and its mathematical tractability. Therefore, my PhD project is motivated by the geometry-based approach to achieve the characterisation, modelling, and simulation of MIMO channels for advanced wireless communication systems.

1.3 Contributions

The key contributions of the thesis are summarised as follows:

- Review the latest development of wireless channel measurements, modelling and simulations. Important existing achievements, including standardised channel models, are reviewed and classified.

Research on V2V channel models

- Propose a novel generic and adaptive 3D RS-GBSM for non-isotropic scattering narrowband MIMO V2V Ricean fading channels. The proposed model is sufficiently generic and adaptable to various V2V scenarios. Comprehensive statistical properties are derived and thoroughly investigated for the novel 3D theoretical RS-GBSM, i.e., amplitude and phase Probability Density Functions (PDFs), Space-Time (ST) Correlation Function (CF), Doppler Power Spectral Density (PSD), envelope Level Crossing Rate (LCR), and Average Fade Duration (AFD).

- Investigate the impacts of the VTD and elevation angle of the 3D theoretical RS-GBSM on these channel statistical properties by comparing with those of the corresponding 2D model. In addition, the corresponding Sum-of-Sinusoids (SoS) simulation model is proposed by considering a finite number of scatterers at the Tx and Rx.

- Propose a novel parameter computation method, namely the Method of Equal Volume (MEV), which is to calculate the azimuth and elevation angles of proposed SoS simulation model. It is the first method for 3D MIMO channel models jointly computing the azimuth and elevation angles.

- The statistical properties of our SoS simulation model are verified by comparing with those of the reference model and simulated results. The results show that the simulation model is an excellent approximation of the reference model

according to their statistical properties. More importantly, our model is the first 3D RS-GBSM that has the ability to study the impact of VTD on channel statistics.

- Propose a novel 3D wideband non-isotropic MIMO V2V RS-GBSM with time-varying parameters. Also, the model considers the impact of channel non-stationarity on channel statistics. Based on the 3D wideband theoretical RS-GBSM, important channel statistical properties are derived and thoroughly investigated, i.e., local ST CF, local Frequency Correlation Function (FCF), and local Power Delay Profile (PDP).

- Originate the corresponding 3D wideband SoS simulation model by the MEV. Moreover, the impacts of the non-stationarity and VTD on ST CF are investigated by comparing with those of the corresponding stationary model. The proposed non-WSS RS-GBSM has been validated by measurements according to stationary time.

Research on F2M channel models

- Derive and compare theoretical expressions of the statistical properties of the IMT-A and LTE-A channel models, such as the spatial Cross-correlation Function (CCF), temporal Autocorrelation Function (ACF), amplitude PDF, envelope LCR/AFD, PDP, and FCF. The theoretical derivation results are verified by corresponding simulation results. The inaccuracy problems of the LTE-A model are also discussed.

- Investigate the computational complexities of IMT-A and LTE-A channel models in terms of the required number of Real Operations (ROs) to generate channel coefficients. To simplify the IMT-A channel model, several complexity reduction methods are proposed, which are shown to be effective in achieving a better trade-off between the model accuracy and complexity.

- Establish a non-stationary IMT-A channel model that includes time-varying Angle of Departures (AoDs) and Angle of Arrivals (AoAs). These time-variant

parameters are derived as functions of time with some parameters which are not time-variant and can be adjusted.

- Based on the proposed non-stationary IMT-A channel model and time-varying functions, important local statistical properties, i.e., the local spatial CCF and local temporal ACF are derived and analysed. The impacts of time-varying parameters on these statistical properties are investigated thoroughly by MATLAB simulations.

1.4 Original Publications

The work presented in this thesis has led to the following publications:

Refereed Journals Papers

1. **Y. Yuan**, C.-X. Wang, X. Cheng, B. Ai, and D. I. Laurenson, "Novel 3D geometry-based stochastic models for non-isotropic MIMO vehicle-to-vehicle channels," *IEEE Trans. Wireless Commun.*, vol. 14, no. 1, Jan. 2014.

2. **Y. Yuan**, C.-X. Wang, Y. He, e.-H. M. Aggoune, and M. M. Alwakeel, "Novel 3D wideband non-stationary geometry-based stochastic models for non-isotropic MIMO vehicle-to-vehicle channels," *IEEE Trans. Wireless Commun.*, 2014, submitted for publication.

3. Q. Yao, **Y. Yuan**, A. Ghazal, Y. Fu, C.-X. Wang, X. Zhang, X. Lu, and Z. Zhong, "Statistical properties and complexity analysis of IMT-A and LTE-A MIMO channel models," *IEEE Trans. Commun.*, to be re-submitted.

4. **Y. Yuan**, A. Ghazal, Q. Yao, and C.-X. Wang, "Non-stationary IMT-A MIMO channel models with time-varying AoDs and AoAs," *IEEE Trans. Vehi. Technol.*, to be submitted.

5. **Y. Yuan**, C.-X. Wang, Hongrui Zhou, and Weiming Duan, "Non-stationary IMT-A MIMO channel models with time-varying parameters," *IEEE Trans. Commun.*, to be submitted.

6. Y. Fu, C.-X. Wang, **Y. Yuan**, R. Mesleh, e. H. M. Aggoune, M. M. Alwakeel, and H. Hass, "BER performance of spatial modulation systems under 2D and 3D vehicle-to-vehicle channel models," *IEEE Trans. Vehi. Technol.*, 2014, submitted for publication.

Refereed Conferences Papers

1. **Y. Yuan**, X. Cheng, C.-X. Wang, D. I. Laurenson, X. Ge, and F. Zhao, "Space time correlation properties of a three-dimensional two-sphere model for non-isotropic MIMO mobile-to-mobile channels," in *Proc. IEEE GLOBECOM'10*, Miami, USA, Dec. 2010. pp. 1–5.

2. X. Cheng, C.-X. Wang, **Y. Yuan**, D. I. Laurenson, and X. Ge, "A novel three-dimensional regular-shaped geometry-based stochastic model for MIMO mobile-to-mobile Ricean fading channels," invited paper, in *Proc. IEEE VTC'10-Fall*, Ottawa, Canada, Sep. 2010. pp. 1–5.

3. Q. Yao, **Y. Yuan**, A. Ghazal, C.-X. Wang, L. Luan, and X. Lu, "Comparison of the statistical properties of the LTE-A and IMT-A channel models," in *Proc. IEEE WCNC'12*, Paris, France, Apr. 2012. pp. 393–398.

1.5 Thesis Organisation

The remainder of this thesis is organised as follows:

Chapter 2 provides extensive literature review on wireless MIMO fading channel modelling, simulation and standardised MIMO channel models. Different modelling approaches (i.e., correlation-based and geometry-based) are introduced and compared.

In this thesis, we will concentrate on the later, i.e., geometry-based channel models, because of its satisfied accuracy and mathematical tractability.

Chapter 3 investigates a narrowband 3D two-sphere and an elliptic-cylinder model for non-isotropic MIMO V2V channel, including theoretical model and corresponding simulation model. Comprehensive statistical properties are derived and analysed, i.e., amplitude and phase PDF, ST CF, Doppler PSD, envelope LCR and AFD. Moreover, the novel parameter computation method, namely the MEV, has been proposed to jointly calculate the azimuth and elevation angles.

Chapter 4 extends the proposed 3D narrowband MIMO V2V channel models into the wideband case in terms of the Tapped Delay Line (TDL) structure [2]. The channel non-stationarity is considered when Tx and Rx are moving in the same direction. Important local statistical properties are derived and analysed, e.g., local ST CF, local FCF and PDP. Moreover, the Bit Error Rate (BER) performance of the proposed models is tested by using IEEE 802.11p system.

Chapter 5 presents the research content of the Huawei project entitled "Realistic MIMO channel models for 3GPP LTE and IMT-Advanced". The first part of this chapter compares the accuracy and complexity of the two latest standardised MIMO channel models (i.e., LTE-A and IMT-A channel models). The second part of this chapter focuses on investigating various complexity reduction methods to simplify the IMT-A channel models.

Chapter 6 introduces non-stationary IMT-A MIMO channel models with time-varying AoDs and AoAs. Further to Chapter 5, the channel non-stationarity of the IMT-A channel models are investigated by considering the dynamic movements of the Moving Clusters (MCs) and MS. Some important local channel statistical properties are derived and simulated.

Chapter 7 concludes the thesis by summarising our key research findings and gives some suggestions for future research topics in wireless channel measurements, modelling and simulations.

Chapter 2

Wireless MIMO Channel Modelling and Simulation

2.1 Introduction

The essential investigation of the multipath propagation is required for successful design of wireless communication systems. This highlights the importance of developing realistic models to simulate the wireless channels. In addition, it has been proved that MIMO technologies can efficiently exploit the spatial domain of propagation channels to design highly reliable and high-speed transmission in wireless communication systems with limited bandwidth.

Channel fading refers to the time variation of the received signal envelope through physical transmission medium. In general, fading can be categorised as large-scale fading and small-scale fading. Path loss and shadowing belong to large-scale fading since they are dominant when the MS moves over distances of several tens of wavelengths [47]. Large-scale fading is very important for the system design at the network level, such as the cellular coverage, handovers, and system throughput. On the other hand, small-scale fading appears due to the multipath propagation. Small-scale fading determines the link level performance, such as BER, envelope LCR and AFD, etc.

In this thesis, we focus on our interests in the investigation of small-scale fading for two different kinds of channels, namely, V2V channels and F2M channels. First of all, this chapter will give a brief overview of existing propagation models and introduces important approaches for the modelling and simulation of MIMO V2V and F2M channels.

2.2 Correlation-Based Stochastic Models

CBSMs assume that the channel coefficients are generated from zero-mean complex Independent and Identically Distributed (i.i.d.) Random Variables (RVs). Thus, the statistical behaviour of the channel can be fully characterised by the first and second statistical orders. Different from GBSMs, the CBSMs describe the MIMO characteristics by correlation matrices instead of the directional propagation parameters like AoD/AoA. The spatial correlation of the propagated wave is assumed to be independent at the two link ends, which means that the correlation properties at one end of the link connection are independent of the other end. The separable correlation properties approach is based on the assumption that the correlation between two adjacent antenna elements results in the close surrounding scatterers. Therefore, the correlation between two paths can be obtained by the product of the correlation between the antenna elements at their paths' end. A narrowband CBSM was proposed in [48] and then extended to wideband MIMO CBSM [49]. In both models, the correlation properties at the Tx and Rx have been characterised using separable correlation matrices. The spatial correlation matrix of the system can be calculated by the Kronecker product of these correlation matrices in what so called Kronecker Based Stochastic Model (KBSM) which is considered as a simplified CBSM.

Because of the "independent" assumption, the approach of CBSMs is able to represent the spatial correlation with a single realisation which makes them suitable for link level simulation. However, this assumption is criticised in the literature because it over simplifies the channel model, which has been reflected on the model performance and makes it inappropriate for system level simulations.

2.3 Geometry-Based Stochastic Models

GBSMs are derived from a predefined stochastic distribution of scatterers' locations by applying the fundamental laws of reflection, diffraction and scattering of electromagnetic waves. Based on the spatial locations of the scatters in the propagation environment, several models have been developed, such as [50]–[53]. Other examples of such GBSMs are one-ring models [54] where single bounce scatterers are located around the MS and distributed uniformly on ring shape, two rings models [55] that consider both the Tx and Rx are surrounded by a local scattering ring, and elliptical models where the scatterers are uniformly distributed on an ellipse where the BS and User Equipment (UE) are located at the focuses.

GBSMs can also be described by using selected parameters such as AoD, AoA. These parameters are chosen in a stochastic (random) way according to a certain distribution. On the other hand, GBSMs are very complex with the large number of random model parameters and therefore their computational complexity has been criticised in the literature especially for link level simulations. This remarkable randomness is the main reason of GBSMs' accuracy but with high complexity.

Overall, GBSMs have the following advantages [56]:

- They have immediate relations to physical reality.
- Many effects are implicitly reproduced.
- Their high accuracy and flexibility make them suitable for system level simulations.
- They are capable of utilising different kind of antenna radiation pattern in each element.
- All information is inherent to the distribution of the scatterers.
- Tx/Rx and scatterer movement as well as shadowing and the appearance/disappearance of propagation paths can be easily implemented.

GBSMs can be further classified as pure-GBSMs and semi-GBSMs. In another way, we also call them as RS-GBSMs and Irregular-Shape Geometry Based Stochastic Models (IS-GBSMs), respectively, depending on whether effective scatterers are placed on regular shapes, e.g., one-ring, two-ring, two-sphere, and ellipses, or irregular shapes.

2.3.1 Pure-GBSM

A pure-GBSM is derived from a predefined stochastic distribution of effective scatterers by applying the purely geometrical assumption. Such models can be easily adapted to different scenarios by changing the shape of the scattering region. In general, pure-GBSMs are widely used for theoretical analysis of channel statistics and theoretical performance evaluation of wireless communication systems. To preserve the mathematical tractability, pure-GBSMs assume that all the effective scatterers are located on regular shapes.

Akki and Haber [35] were the first to propose a 2D two-ring pure-GBSM with only double-bounced rays for narrowband isotropic scattering SISO V2V Rayleigh fading channels. In [38], the authors proposed a general 2D two-ring pure-GBSM with both single- and double-bounced rays for narrowband non-isotropic scattering MIMO V2V Ricean channels. The 2D narrowband two-ring pure-GBSM in [38] was further extended to a 3D wideband two-concentric-cylinder pure-GBSM in [41]. However, all the aforementioned pure-GBSM in [35], [38], [41] cannot study the impact of the VTD on V2V channel statistics.

To fill the above gaps, we have proposed novel 3D non-isotropic scattering MIMO V2V pure-GBSMs, which include both narrowband (Chapter 3) and wideband (Chapter 4) models with respect to the frequency-selectivity. The wideband pure-GBSM is based on the TDL structure and thus can investigate the per-tap channel statistics. Based on the typical V2V environment described in Fig. 4.1, it shows that the geometrical description of our wideband model that combines a two-sphere model and an elliptic-cylinder model consisting of LoS, single-, and double-bounced rays. By considering the impact of the VTD on channel statistics for every tap in the proposed models, we

distinguish between the moving cars around the Tx and Rx and the stationary roadside environments, which are described by a two-sphere model and multiple confocal elliptic-cylinder models, respectively. Detailed descriptions of the narrowband and wideband models will be given in Chapter 3 and Chapter 4, respectively. Therefore, the pure-GBSM approach will be used to develop the V2V channel models in this thesis.

2.3.2 Semi-GBSM

Unlike pure-GBSMs, semi-GBSMs intend to reproduce the physical reality and thus need to modify the location and properties of the effective scatterers of pure-GBSMs. Semi-GBSMs place the effective scatterers with specified properties at random locations with certain statistical distributions. The signal contributions of the effective scatterers are determined from a simplified ray-tracing method and the total signal is the summation of the Channel Impulse Response (CIR). In [57], to provide better agreement with the measurement results presented in [58], the CIR is further divided into four parts, i.e., the LoS component, discrete components from reflections of mobile scatterers (e.g., moving cars), discrete components from reflections of strong static scatterers (e.g., building and road signs located on the roadside), and diffuse components from reflections of weak static scatterers located on the roadside.

Therefore, semi-GBSMs are actually a relatively-simplified version of GBSMs while suitable for various wireless scenarios by properly adjusting the statistical distributions of the effective scatterers. With the ray-tracing approach, the semi-GBSM in [57] can easily handle the non-stationarity of V2V channels by prescribing the motion of the Tx, Rx, and moving scatterers. Note that only single-bounced rays were considered in this semi-GBSM due to the fairly low VTD of the measurements in [58]. For a high VTD environment, it is indispensable that double-bounced rays should be considered as well. In this thesis, the channel modelling approach of semi-GBSMs is especially applied to F2M communication systems. Chapter 5 and Chapter 6 will carry on this method to establish realistic channel models for IMT-A and capture the non-stationarity with time-varying parameters, respectively.

2.4 Standardised MIMO Channel Models

2.4.1 IEEE 802.11 TGn channel model

The IEEE 802.11 TGn channel models [15] are designed for indoor wireless Local Area Networks (LANs) for bandwidths of up to 100 MHz, at frequencies of 2 and 5 GHz. The channel models comprise a set of 6 profiles, labelled as A to F, which cover the scenarios of "A: flat fading", "B: residential", "C: residential/small office", "D: typical office", "E: large office", and "F: large space (indoors and outdoors)". Each channel model has a path loss model including shadowing, and a MIMO multipath fading model, which describes the multipath delay profile, the spatial properties, the Ricean K-factor, and the Doppler spectrum.

Each channel model has a certain number of taps (one for scenario A, and 9 to 18 for scenarios B–F). Each tap is characterised by a relative delay (with respect to the first path delay). Each model of scenarios further comprises a number of clusters, which correspond to overlapping subsets of the tap delays. Each cluster is assigned a set of spatial properties, i.e., a mean AoD, a AoA, and Angular Spreads (ASs) at the both Tx and Rx. These parameters assume the same values for all tap delays pertaining to a given cluster. These parameters determine the correlation matrices associated with each tap delay.

The IEEE 802.11 TGn channel models make the following assumptions: 1) The Power Azimuth Spectrum (PAS) and the PDP are separable, i.e., each tap is modelled independently. 2) The PAS and the Doppler spectrum for each tap are separable, i.e., the spatial correlation (correlation matrices) and temporal correlation (Doppler spectrum) for each tap are modelled independently. 3) Each tap is modelled using the Kronecker approach for Ricean channels. Hence, it is assumed that the Tx and Rx correlation matrices are separable for each tap.

The KBSM is a simplified CBSM. Due to the "separable" assumption, the spatial correlation matrix $\mathbf{R}_{MIMO}$ can be expressed as the Kronecker product of the spatial correlation matrices at the Tx $\mathbf{R}_{Tx}$ and the Rx $\mathbf{R}_{Rx}$, i.e., $\mathbf{R}_{MIMO} = \mathbf{R}_{Tx} \bigotimes \mathbf{R}_{Rx}$.

Such an assumption makes this modelling approach less flexible in terms of antenna radiation pattern. The spatial correlation function of the KBSM has been under investigation and the representing expressions have been derived for different PAS distribution, such as uniform, Gaussian and Laplacian PASs [59].

The KBSM further assumes that the spatial complex correlation coefficients observed at the Tx or Rx are independent of the antenna elements which means that the AoDs and AoAs are independently distributed. On the other hand, the KBSM enforces that all Direction of Departure (DoD) and Direction of Arrival (DoA) are linked to each other, thus the joint DoD/DoA spectrum will be the product of the average DoD and average DoA spectrum. This assumption is unrealistic as it is very likely that a single DoD is only linked to a single DoA.

Another shortcoming of the KBSM has been proved in [60] as the comparison of the channel modelling using KBSM and the measurement data shows that KBSMs always underestimate the mutual information (channel capacity). Moreover, this mismatch in the capacity between KBSM and the measurement increased apparently in correlated environments where KBSM fails to estimate the decreased mutual information with the increased correlation. Another comparison between KBSM and measurement data [61] has proved that besides the error in estimating the capacity, the Kronecker approach leads to high error in covariance matrix representation.

To combat such deficiencies resulting from the Kronecker product, a generalised stochastic MIMO channel model has been proposed in [62] that model the joint correlation properties using the average coupling between the eigenvalues of the Tx and Rx. Besides the IEEE 802.11 TGn channel models [15], because of the simplicity of the KBSM, it has become popular and adopted by other standardised channel models like the 3GPP LTE channel model [16]–[21].

2.4.2 3GPP LTE-A channel model

The 3GPP LTE [16] has been proposed by the 3GPP as the technology for 4G wireless communication systems. Thereafter, an evolution of the LTE [22] has been initiated

to meet all of the requirements of the IMT-A as defined by ITU [31], [32] in what so called LTE-A [22]–[24]. The LTE channel model uses the correlation based modelling approach [17]–[21]. Therefore, the spatial correlation is explicitly defined in the model, which is far different from GBSMs.

The LTE-A MIMO channel model [22] is formed by combining a power delay profile, a Doppler spectrum, and spatial correlation properties. The spatial correlation matrix is also assumed to be the Kronecker product of three correlation matrices $\mathbf{R}_{spat} = \mathbf{R}_{BS} \bigotimes \Gamma \bigotimes \mathbf{R}_{MS}$, where Γ is the polarisation correlation matrix, $\mathbf{R}_{BS}$ and $\mathbf{R}_{MS}$ are the spatial correlation at the BS antenna and MS antenna, respectively. Thus, the LTE channel model is able to provide the spatial correlation characteristics with single realisation.

The LTE channel model is based on correlation-based approach, which decouples the implementation of Doppler spectrum and the spatial correlation. So, the Doppler spectrum can be simulated without any limitations from the spatial correlation. The 3GPP LTE channel model defined three different correlation matrices in terms of the correlation level, namely, the high, medium and low MIMO correlation matrices. These matrices are based on antenna configurations, polarisations and patterns that defined in [63] and evaluated in [64].

The supported scenarios by the LTE channel model are introduced as a combination of channel model parameters, i.e., delay spread and Doppler frequency. Therefore, all defined propagation scenarios are Extended Pedestrian A (EPA) 5 Hz, Extended Vehicular A (EVA) 5 Hz, EVA 70 Hz, Extended Typical Urban (ETU) 70 Hz, ETU 300 Hz and High Speed Train (HST) 750 Hz.

In addition, the 3GPP LTE assumes that the PAS follows the Laplacian distribution and all paths have the same AoD, AoA and AS parameter in order to simplify the simulation. The later assumption is far away from reality since different paths will undergo different reflection and scattering that will cause different angular information for sure. However, such an assumption will reduce the complexity as all paths will have the same spatial correlation matrix [16], [19]–[22].

Since it is based on the KBSM, the 3GPP LTE channel model will suffer from the same deficiencies that the KBSM does, like the unrealistic assumption of the independence between the AoD and AoA especially for indoor scenarios. Moreover, the time-invariant spatial correlation matrix is assumed to be independent of Doppler PSD, this assumption is not justified and cannot be applied in some cases.

To combat the complexity problem of GBSMs, the LTE-A channel model makes the above assumptions that are not yet well-justified. These simplifications and assumptions made by the LTE-A MIMO channel model may potentially result in poor accuracy and consequently inaccurate system performance predictions. In [60], it is also proved that the mutual information predicted by the Kronecker model is always below the estimation from the measured channel. Companies, which adopt such an inaccurate MIMO channel model, could make wrong decisions on LTE-A product development.

2.4.3 3GPP spatial channel model

The SCM [25] was developed by 3GPP to be a common reference for evaluating different MIMO concepts in outdoor environments at a centre frequency of 2 GHz and a system bandwidth of 5 MHz. The SCM consists of two parts: a calibration model and a system simulation model.

- **Calibration model**

The calibration model is an over-simplified channel model whose purpose is to check the correctness of simulation implementations. In the course of standardisation work, it is often necessary to compare the implementations of the same algorithm by different companies.

Comparing the performance of the algorithm in the "calibration" channels allows to easily assess whether two implementations are equivalent. We stress that the calibration model is not intended for performance assessment of algorithms or systems.

The calibration model, as described in the 3GPP standard, can be implemented either as a physical model or as an analytical model. It is a spatial extension of the ITU channel models [31], [32], which describe the wideband characteristics of the channel as a TDL model. Taps with different delays are independently fading, and each tap is characterised by its own PAS (which is uniform or Laplacian distribution), AS, and mean direction, at both the BS and MS. The parameters (i.e., AS, mean direction, etc.) are fixed. Thus, the model represents stationary channel conditions. The Doppler spectrum is defined implicitly by introducing speed and direction of travel of the MS. The model also defines a number of antenna configurations.

- **Simulation model**

The SCM intended for performance evaluation is called the simulation model. The model is a physical model and distinguishes between three different environments: urban macro cell, suburban macro cell, and urban micro cell. The model structure and simulation methodology are identical for all these environments, but the parameters, such as AS, Delay Spread (DS), etc., are different.

The simulation model employs both geometrical and stochastic components. Let us first describe the simulation procedure for a single link between one BS and one MS. The geometrical component is that the MSs are placed randomly within a given cell, and the orientation of the antenna array, as well as the direction of movement within the cell, are also chosen at random. Each tap shows angular dispersion at the BS and MS; this dispersion is implemented by representing each tap by a number of sub-paths that all have the same delay, but different DoD and DoA. Physically, this means that each path consists of a cluster of 20 scatterers with slightly different directions but equal time of arrival. Specifically, the modelling of the angular dispersion works as follows: the mean DoD and DoA of the total arriving power (weighted average over all the taps) is determined by the location of MS and the orientation of the antenna array. The mean DoD (or DoA) of one tap is chosen at random from a Gaussian distribution that is centred on this total mean (the variance of this distribution is one of the model parameters). Adding up the different sub-paths (which all have

deterministic amplitudes, but different phases) results in Rayleigh or Rice fading. Temporal variations of the CIR are effected by movement of the MS, which in turn leads to different phase shifts of the sub-paths.

When using the SCM, the simulation of the system behaviour is carried out as a sequence of "drops", where a "drop" is defined as one simulation run over a certain (short) time period. That period is assumed to be short, so that it is justified to assume (as the model does) that large-scale channel parameters, such as AS, mean DoD or DoA, delay spread, and shadowing stay constant during a drop. For each drop, these large-scale channel parameters are drawn according to distribution functions. The MS positions are varied randomly at the beginning of each drop.

In some cases, we wish to simulate the channels between multiple BS cells/sectors and multiple MSs linked to these BSs. The cell layout and BS locations are fixed for a certain number of successive drops, but (as in the single-cell case) the MS positions are still varied at random at the beginning of each drop. Antenna radiation patterns, antenna geometries, and orientations can be chosen arbitrarily, that means the model is antenna independent. When all the parameters and antenna effects are defined, analytical formulations can be extracted from the physical model. Note that each drop results in a different correlation matrix for the analytical model.

2.4.4 3GPP spatial channel model-extension

The SCME model is an extension to the SCM model, thus it is also a GBSM. This extension was performed to improve the SCM and remain the backwards compatibility with the SCM.

The first improvement aims to the bandwidth. To increase the bandwidth from 5 MHz to 20 MHz that the SCME supports the backwards compatibility with the SCM. The SCM model is limited to 2 GHz band only. To extend this frequency range to 5 GHz, a new path loss model proposed in SCME for 5 GHz with an offset of 8 dB to the 2 GHz one. Moreover, the SCME extended the support of LoS components to other scenarios while it is limited to the urban micro scenario in SCM. On the other hand, since the

SCME forced to keep compatibility with the SCM, the achieved improvements are limited. Accordingly, the major shortcomings of the SCME are highlighted as follows. The SCME does not extend new scenarios comparing with the SCM. Thus, the lack of supporting rural or indoor scenarios still exist in the SCME. The elevation angles are still not considered. Similarly to the SCM, the SCME does not support the cross-correlation between the Large Scale Parameters (LSPs).

Because of the aforementioned deficiencies, a new standardised MIMO channel model with better performance has been developed by IST WINNER project.

2.4.5 IST WINNER series channel models

The WINNER series channel models are developed by IST to support the challenging requirements of 4G systems. The WINNER series MIMO channel models include WIM1 [28], WIM2 [29], WIM+ [30].

The WIM1 channel model is a ray tracing double directional channel model developed based on channel measurement performed at 2 and 5 GHz [28]. It is suitable for MIMO channel modelling with arbitrary feature to fit to the different statistical properties extracted from the measurements of different propagation scenarios. Unlike the previous standardised GBSMs, SCM and SCME, WIM1 channel model is capable of 3D channel modelling by considering the elevation angle of AoD and AoA. It also supports the cross-correlation between the LSPs that has been discovered in the measurements. The number of supported scenarios are extended by specifying indoor and rural ones. However, the set of scenarios is still considered as very limited.

The WIM2 further increases the number of scenarios to 13 [29]. The defined scenarios are with the support of LoS and Non-Line-of-Sight (NLoS) components except the Indoor-to-Outdoor (I-to-O) and Outdoor-to-Indoor (O-to-I) scenarios. Moreover, it is possible to change the different attributes of the antenna or the geometry, such as MIMO configuration or beam formation. The WIM2 channel model can cover most of the typical cases for different simulation levels, e.g., cluster level, link level, or system level. Another important improvement is the extension of the frequency

range to support 2–6 GHz bands. In addition to the generic model the WIM2 channel model proposed a Clustered Delay Line (CDL) structure for calibration use. The CDL models propose non-complex channel model with fixed and tabulated parameters, thus the simulation results can be verified.

The novel features of the WIM+ models are the elevation modelling using the same modelling approach as in the WIM2 models, extension of the model down to 450 MHz [30]. WIM+ can be used as comparison of different algorithms, technologies and products. The models can be applied to any wireless system operating in 450 MHz - 6 GHz frequency range with up to 100 MHz bandwidth. The model supports MIMO technologies, polarisation, multi-user, multi-cell, and multi-hop networks and 3D modelling.

2.4.6 ITU IMT-A channel model

IMT-A channel model [31], [32] has been developed and proposed by the ITU as a GBSM to achieve requirements of 4G wireless communication systems, like increasing the peak data rates (the target is 100 Mbps for high mobility and 1 Gbps for low mobility [65]), supporting high quality multimedia applications and achieving significant enhancement in performance and quality of service.

The IMT-A channel model consists of a primary module and an extension module. The primary module originates from the WIM2 [29], whereas the extension module has been added to enable the tests of wireless systems operating in the scenarios beyond those specified by the IMT-A system requirements. The primary module covers the parameter tables and channel model definition for the evaluations. The extension module is a tool that allows us to select modified parameters to generate LSPs of the simulated scenarios.

Based on the WIM2, the ITU IMT-A channel models proposed two types of channel models, namely a generic model and a CDL model. The generic model is a double directional GBSM that describes the geometric distribution of the scatterers considering the AoDs to the first scatterers involved from the BS side and the AoAs from the last bounce scatterers, and enables the separation of propagation parameters and

antennas. This model is mainly for system level simulation purposes. The CDL model is a spatial extension of the TDL model for calibration use only. The reduced variability of CDL has been achieved through fixing all of the parameters except for the phases of the rays.

The IMT-A MIMO channel model can support bandwidth up to 100 MHz within a frequency range of 2–6 GHz for evaluation phase. It covers a limited set of propagation scenarios for evaluation: Indoor Hotspot (InH), Urban Micro (UMi), Urban Macro (UMa), Suburban Macro (SMa), and Rural Macro (RMa), with the support of LoS and NLoS cases for each scenario, besides supporting O-to-I case for UMi scenario. Although the defined propagation scenarios are limited but they span all over the range of the possible cases, unlike the 3GPP SCM that defined limited set of scenarios without supporting Indoor environments and LoS/O-to-I components.

The extension module is an optional feature that helps the UMa, RMa and SMa to be extended to cover cases beyond IMT-A by providing additional level of parameter variability. This module is based on the time-spatial propagation model that is a geometric channel model calculates the LSPs by considering several key parameters (e.g. city structure) and targets bandwidth up to 100 MHz, the full details of this extension can be found in [31], [32]. The IMT-A channel model supports bandwidth up to 40 MHz within a frequency range (2-6 GHz) for evaluation phase. However, it has been stated clearly that extension to support higher bandwidth (up to 100 MHz) is necessary for future development.

Similar to WIM2, the IMT-A channel model parameters for individual snapshots are determined stochastically based on statistical distributions extracted from channel measurements. The LSPs are assumed to follow a log-normal distribution that has been found to fit accurately the measurement results in [66], while the PAS follows a wrapped Gaussian distribution (Gaussian distribution with tails wrapped over $\pm 180°$) in all the defined scenarios except the InH where the AoD and AoA distribution is assumed to follow the Laplacian distribution.

Another important feature the IMT-A channel model is the simulation of the relays that consider as promised technology for throughput enhancement and coverage extension. The links from the BSs to relay stations can be modelled with conventional links, while the links from the relay stations to UEs can be modelled similar to the links between the BSs and UEs.

2.5 Summary

It has been proved in many literatures that implementing MIMO technologies is promising for achieving the high demands of 4G and 5G communication systems, especially the high date rate requirement. MIMO channel models can be classified into several classes. A widely known classification categorises MIMO channel models into CBSMs and GBSMs. Each channel modelling approach has its advantages and disadvantages. GBSMs use selected parameters of the channel like AoD and AoA, delays and powers to characterise MIMO channel model where the parameters of the individual paths are defined by their probability distribution.

Despite of their high accuracy, GBSMs are very complex with large number of random parameters and therefore they are computationally inefficient especially for link-level simulations. Thus, some standardised channel models like LTE and TGn adopted CBSMs because of their relative simplicity and fewer model parameters. In CBSMs, the exact spatial correlation characteristics can be achieved without requiring many realisations. Also, the decoupling of the Doppler spectrum and the spatial correlation in the CBSMs enables the Doppler spectrum to be accurately simulated without limitations. This is not the case in GBSMs.

Many standardised channel models are reviewed in this chapter. The 3GPP developed the LTE channel model as a candidate channel model for 4G wireless mobile communication systems. The 3GPP LTE channel model is based on correlation-based structure to avoid the complexity concerns of the GBSMs. However, CBSMs have been questioned about their unjustified simplification assumptions in MIMO channel

modelling by neglecting significant variations of individual links, which may overestimate or underestimate the system performance and leads to wrong decisions on system design. Hence, we need to develop new realistic MIMO channel models for both V2V and F2M communication systems with satisfied trade-off between accuracy and complexity. The following chapters will introduce our research achievements in detail.

Chapter 3

Modelling and Simulation of Narrowband 3D MIMO V2V Channels

3.1 Introduction

In recent years, V2V communications [33] have been encountered in many new applications, such as wireless mobile ad hoc peer-to-peer networks [3], [4] cooperative systems [6], [7], and intelligent transportation systems. In V2V communication systems, both the Tx and Rx are in motion and equipped with low elevation antennas. This is different from conventional F2M cellular radio systems, where only one terminal moves. Moreover, MIMO technologies, where multiple antennas are deployed at both the Tx and Rx [56], have widely been adopted in advanced F2M cellular systems and have also been receiving more and more attention in V2V systems [67].

In order to evaluate the performance of a V2V communication system, accurate channel models are indispensable. Existing channel models for F2M communications systems cannot be used directly for the design of V2V systems. V2V channel models available in the literature [8], [35]–[45], [57], [68]–[72] can be classified as Geometry Based Deterministic Models (GBDMs) [68] and stochastic models, which can further be categorised as Non-Geometrical Stochastic Models (NGSMs) [8] and GBSMs [35]–[45], [57], [69]–[72]. Furthermore, GBSMs can be classified as RS-GBSMs [35]–[41],

[43]–[45], [70], [71] and IS-GBSMs [42], [57], [72], [73], depending on whether effective scatterers are located on regular shapes, e.g., one-ring, two-ring, ellipses, or irregular shapes.

RS-GBSMs [35]–[41], [43]–[45], [70], [71] have widely been used to mimic V2V channels due to their convenience for theoretical analysis of channel statistics. To preserve the mathematical tractability, RS-GBSMs assume that all the effective scatterers are located on regular shapes. Akki and Haber were the first to propose a 2D RS-GBSM [35] and investigate corresponding statistical properties for narrowband isotropic scattering SISO V2V Rayleigh channels [36]. In [37], a 2D two-ring RS-GBSM considering only double-bounced rays was presented for non-isotropic scattering MIMO V2V Rayleigh fading channels. In [38], the authors proposed a 2D two-ring RS-GBSM with both single- and double-bounced rays for narrowband non-isotropic scattering MIMO V2V Ricean channels. In [39], the authors proposed an adaptive RS-GBSM consisting of two rings and one ellipse also with both single- and double-bounced rays for narrowband non-isotropic MIMO V2V Ricean channels. As 2D models assume that waves travel only in the horizontal plan, they neglect signal variations in the vertical plane and are valid only when the Tx and Rx are sufficiently separated. In reality, waves do travel in three dimensions. Meanwhile, [74] is a simplified model and focuses on ST correlation properties compared to [70]. Therefore, a 3D two-cylinder RS-GBSM was developed for narrowband non-isotropic scattering MIMO V2V channels in [40]. It was further extended to a wideband one in [41]. Other 3D V2V channel models include a 3D two-sphere RS-GBSM for narrowband non-isotropic SISO V2V channels [45] and a 3D two-concentric-quasi-sphere RS-GBSM for wideband non-isotropic MIMO V2V channels [44].

The aforementioned 3D RS-GBSMs [40], [41], [44], [45] all assumed that the azimuth angle and elevation angle are completely independent and thus analysed them separately. Moreover, although the measurement campaigns in [8] demonstrated that the VTD significantly affects the V2V channel statistical properties, the impact of the VTD on channel statistics was not considered in the existing 3D RS-GBSMs.

To fill the above research gaps, the first part of this chapter proposes a novel theoretical 3D RS-GBSM, which is the combination of LoS components, a two-sphere model, and an elliptic-cylinder model [70], for non-isotropic MIMO V2V channels. The proposed 3D RS-GBSM is sufficiently generic and adaptive to model various V2V channels in different scenarios. It is the first 3D RS-GBSM that has the ability to study the impact of the VTD on channel statistics, and jointly considers the azimuth and elevation angles by applying the VMF distribution as the scatterer distribution. As the 3D theoretical RS-GBSM assumes infinite number of effective scatterers, which results in the infinite complexity, it cannot be implemented in practice. However, a theoretical model can be used as a starting point to design a realizable simulation model that considers limited number of scatterers and has a reasonable complexity. Hence, the second part of this chapter concentrates on developing a corresponding 3D MIMO V2V SoS based simulation model with a novel parameter computation method. Note that the proposed models have already considered the effect of diffuse scattering [57] by using double-bounced rays. Also, the impact of vehicles as obstacles on the LoS obstruction, as studied in measurements [73] and [75], can be captured in our models by adjusting relevant model parameters, e.g., the Ricean factor.

Overall, the major contributions and novelties of this chapter are summarised as follows:

1. Based on the novel 3D theoretical RS-GBSM, comprehensive statistical properties are derived and thoroughly investigated, i.e., amplitude and phase PDFs, ST CF, Doppler PSD, envelope LCR, and AFD. Meanwhile, some inaccurate expressions in [70] are corrected.

2. The impacts of the VTD and elevation angle on aforementioned channel statistical properties are investigated by comparing with those of the corresponding 2D model.

3. The corresponding SoS simulation model is proposed by considering a finite number of scatterers at the Tx and Rx.

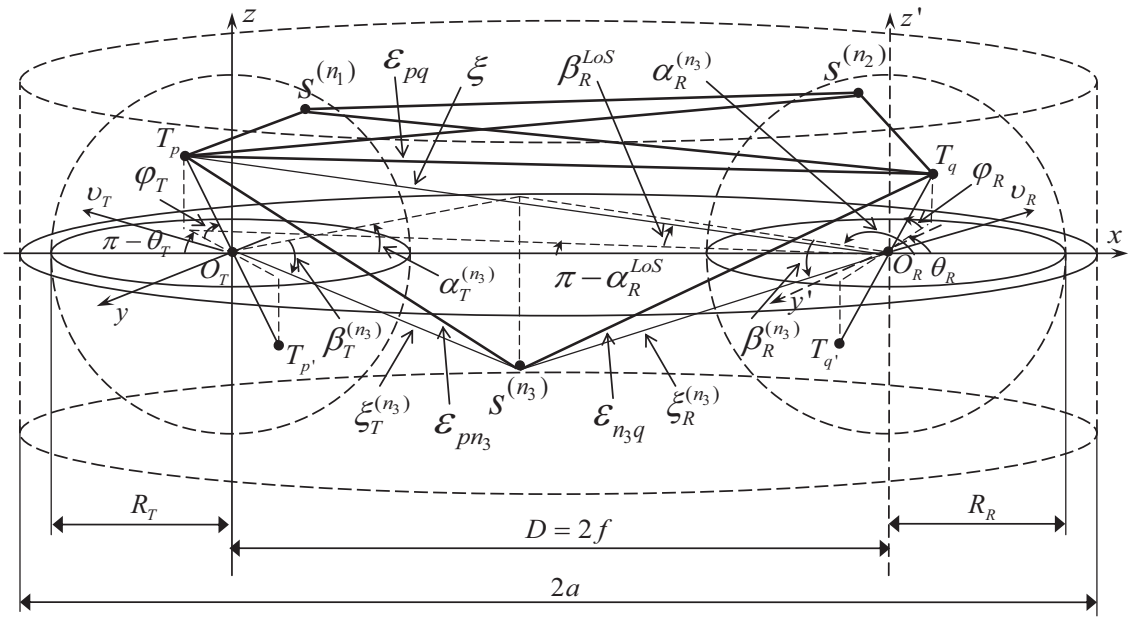

FIGURE 3.1: The proposed 3D MIMO V2V RS-GBSM combining a two-sphere model and an elliptic-cylinder model (only showing the detailed geometry of LoS components and single-bounced rays in the elliptic-cylinder model).

4. A novel parameter computation method, namely the MEV, is proposed to calculate the azimuth and elevation angles of proposed SoS simulation model. It is the first method for 3D MIMO channel models jointly computing the azimuth and elevation angles.

5. The statistical properties of our SoS simulation model are verified by comparing with those of the reference model and simulated results. The results show that the simulation model is an excellent approximation of the reference model according to their statistical properties.

The remainder of this chapter is structured as follows. Section 3.2 introduces a novel 3D theoretical RS-GBSM for non-isotropic narrowband MIMO V2V Ricean channels. In Section 3.3, the corresponding 3D simulation model is developed with parameters calculated by the MEV. Simulation results and analysis are unveiled in Section 3.4. Finally, we draw conclusions in Section 3.5.

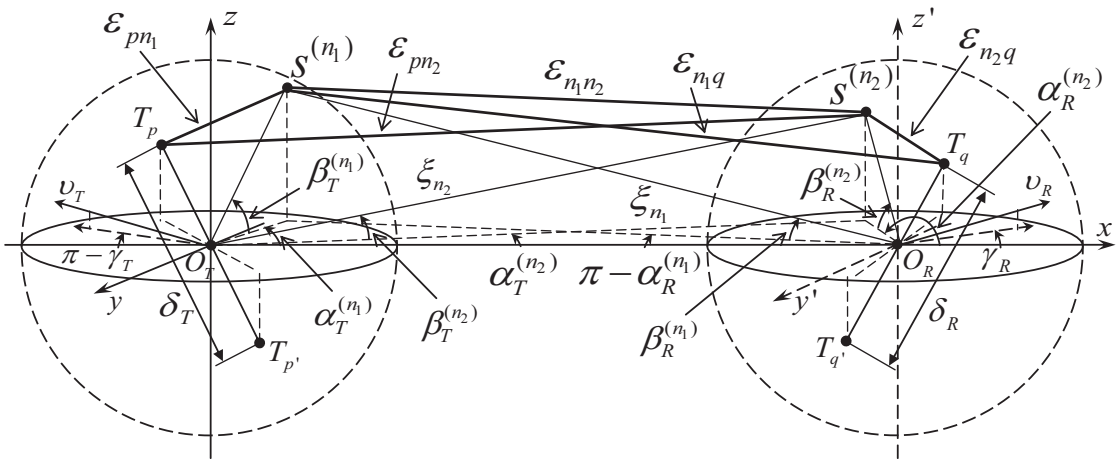

FIGURE 3.2: The detailed geometry of the single- and double-bounced rays in the two-sphere model of the proposed 3D RS-GBSM.

3.2 Theoretical Model for Narrowband 3D MIMO V2V Channels

3.2.1 Description of the 3D MIMO V2V theoretical model

Let us consider a narrowband MIMO V2V communication system with M_T transmit and M_R receive omnidirectional antenna elements. The radio propagation environment is characterised by 3D effective scattering with LoS and NLoS components between the Tx and Rx. Different from physical scatterers, an effective scatterer may include several physical scatterers which are unresolvable in delay and angle domains. Fig. 3.1 and Fig. 3.2 illustrate the proposed 3D RS-GBSM, which is the combination of LoS components, a single- and double-bounced two-sphere model, and a single-bounced elliptic-cylinder model. To consider the impact of the VTD on channel statistics, we need to distinguish between the moving vehicles around the Tx and Rx and the stationary roadside environments (e.g., buildings, trees, parked cars, etc.). Therefore, we use a two-sphere model to mimic the moving vehicles and an elliptic-cylinder model to depict the stationary roadside environments. It is worth mentioning that in order to significantly reduce the complexity of the 3D theoretical RS-GBSM, only the double-bounced rays via scatterers on the two-sphere model are considered

TABLE 3.1: Definition of parameters in Fig. 3.1 and Fig. 3.2.

D	distance between the centres of the Tx and Rx spheres
R_T, R_R	radius of the Tx and Rx spheres, respectively
a, f	semi-major axis and half spacing between two foci of the elliptic-cylinder, respectively
δ_T, δ_R	antenna element spacing at the Tx and Rx, respectively
θ_T, θ_R	orientation of the Tx and Rx antenna array in the x-y plane, respectively
φ_T, φ_R	elevation of the Tx and Rx antenna array relative to the x-y plane, respectively
υ_T, υ_R	velocities of the Tx and Rx, respectively.
γ_T, γ_R	moving directions of the Tx and Rx in the x-y plane, respectively
$\alpha_T^{(n_i)}$ $(i = 1, 2, 3)$	Azimuth AoD (AAoD) of the waves that impinge on the effective scatterers $s^{(n_i)}$
$\alpha_R^{(n_i)}$ $(i = 1, 2, 3)$	Azimuth AoA (AAoA) of the waves travelling from the effective scatterers $s^{(n_i)}$
$\beta_T^{(n_i)}$ $(i = 1, 2, 3)$	Elevation AoD (EAoD) of the waves that impinge on the effective scatterers $s^{(n_i)}$
$\beta_R^{(n_i)}$ $(i = 1, 2, 3)$	Elevation AoA (EAoA) of the waves travelling from the effective scatterers $s^{(n_i)}$
α_R^{LoS}, β_R^{LoS}	AAoA and EAoA of the LoS paths, respectively
ε_{pq}, ε_{pn_i}, $\varepsilon_{n_1n_2}$, ε_{n_iq}, ξ, $\xi_{T(R)}^{n_3}$, ξ_{n_1}, ξ_{n_2} $(i = 1, 2, 3)$	distances $d(T_p, T_q)$, $d(T_p, s^{(n_i)})$, $d(s^{(n_1)}, s^{(n_2)})$, $d(s^{(n_i)}, T_q)$, $d(T_p, O_R)$, $d(O_T(O_R), s^{(n_3)})$, $d(s^{(n_1)}, O_R)$, $d(O_T, s^{(n_2)})$, respectively

because other double-bounced rays (via one scatterer on a sphere and the other one on the elliptic-cylinder) show similar channel statistics [39]. For readability purposes, Fig. 3.1 only shows the geometry of LoS components, and the single-bounced elliptic-cylinder model. The detailed geometry of the single- and double-bounced two-sphere model is given in Fig. 3.2. Note that in both Fig. 3.1 and Fig. 3.2, we adopted uniform linear antenna arrays with $M_T = M_R = 2$ as an example. The proposed RS-GBSM can be extended with arbitrary number of antenna elements. By modeling effective scatterers, we assume that the two-sphere model defines two spheres of effective scatterers, one around the Tx and the other around the Rx. Suppose there are N_1 effective scatterers around the Tx lying on a sphere of radius R_T and the n_1th $(n_1 = 1, ..., N_1)$ effective scatterer is denoted by $s^{(n_1)}$. Similarly, assume there are N_2 effective scatterers around the Rx lying on a sphere of radius R_R and the n_2th $(n_2 = 1, ..., N_2)$ effective scatterer is denoted by $s^{(n_2)}$. For the elliptic-cylinder model, N_3 effective scatterers lie on an elliptic-cylinder with the Tx and Rx located at the foci and the n_3th $(n_3 = 1, ..., N_3)$ effective scatterer is denoted by $s^{(n_3)}$. The

parameters in Fig. 3.1 and Fig. 3.2 are defined in Table 3.1. Note that the reasonable assumptions $D \gg \max\{R_T, R_R\}$ and $\min\{R_T, R_R, a-f\} \gg \max\{\delta_T, \delta_R\}$ are applied in this theoretical model [39].

The 3D MIMO V2V channel is described by an $M_T \times M_R$ matrix of complex fading envelopes, i.e., $\mathbf{H}(t) = [h_{pq}(t)]_{M_T \times M_R}$. The subscripts p and q denote the MIMO antenna elements. Therefore, the received complex fading envelope between the pth ($p = 1, ..., M_T$) Tx and the qth ($q = 1, ..., M_R$) Rx at the carrier frequency f_c is a superposition of the LoS, single- and double-bounced components, and can be expressed as

$$h_{pq}(t) = h_{pq}^{LoS}(t) + \sum_{i=1}^{I} h_{pq}^{SB_i}(t) + h_{pq}^{DB}(t) \tag{3.1}$$

where

$$h_{pq}^{LoS}(t) = \sqrt{\frac{K}{K+1}} e^{-j2\pi f_c \tau_{pq}} \times e^{j2\pi f_{T_{max}} t \cos\left(\alpha_T^{LoS} - \gamma_T\right) \cos\beta_T^{LoS}} \times e^{j2\pi f_{R_{max}} t \cos\left(\alpha_R^{LoS} - \gamma_R\right) \cos\beta_R^{LoS}} \tag{3.2a}$$

$$h_{pq}^{SB_i}(t) = \sqrt{\frac{\eta_{SB_i}}{K+1}} \lim_{N_i \to \infty} \sum_{n_i=1}^{N_i} \frac{1}{\sqrt{N_i}} e^{j\left(\psi_{n_i} - 2\pi f_c \tau_{pq,n_i}\right)} \times e^{j2\pi f_{T_{max}} t \cos\left(\alpha_T^{(n_i)} - \gamma_T\right) \cos\beta_T^{(n_i)}} \times e^{j2\pi f_{R_{max}} t \cos\left(\alpha_R^{(n_i)} - \gamma_R\right) \cos\beta_R^{(n_i)}} \tag{3.2b}$$

$$h_{pq}^{DB}(t) = \sqrt{\frac{\eta_{DB}}{K+1}} \times \lim_{N_1, N_2 \to \infty} \sum_{n_1, n_2 = 1}^{N_1, N_2} \frac{1}{\sqrt{N_1 N_2}} e^{j\left(\psi_{n_1,n_2} - 2\pi f_c \tau_{pq,n_1,n_2}\right)} \times e^{j2\pi f_{T_{max}} t \cos\left(\alpha_T^{(n_1)} - \gamma_T\right) \cos\beta_T^{(n_1)}} \times e^{j2\pi f_{R_{max}} t \cos\left(\alpha_R^{(n_2)} - \gamma_R\right) \cos\beta_R^{(n_2)}} \tag{3.2c}$$

with $\alpha_T^{LoS} \approx \beta_T^{LoS} \approx \beta_R^{LoS} \approx 0$, $\alpha_R^{LoS} \approx \pi$, $\tau_{pq} = \varepsilon_{pq}/c$, $\tau_{pq,n_i} = (\varepsilon_{pn_i} + \varepsilon_{n_i q})/c$, and $\tau_{pq,n_1,n_2} = (\varepsilon_{pn_1} + \varepsilon_{n_1 n_2} + \varepsilon_{n_2 q})/c$. Here, c is the speed of light, K designates the Ricean factor, and $I = 3$ which means there are three subcomponents for single-bounced rays, i.e., SB_1 from the Tx sphere, SB_2 from the Rx sphere, and SB_3 from the elliptic-cylinder. Power-related parameters η_{SB_i} and η_{DB} specify the amount of powers that

the single- and double-bounced rays contribute to the total scattered power $1/(K+1)$. Note that these power-related parameters satisfy $\sum_{i=1}^{I} \eta_{SB_i} + \eta_{DB} = 1$. The phases ψ_{n_i} and ψ_{n_1,n_2} are i.i.d. random variables with uniform distributions over $[-\pi, \pi)$, $f_{T_{max}}$ and $f_{R_{max}}$ are the maximum Doppler frequencies with respect to the Tx and Rx, respectively. Note that we have corrected inaccurate expressions (2a) and (2c) in [70], corresponding to (3.2a) and (3.2c) in this chapter, respectively.

Based on the law of cosines in appropriate triangles and small angle approximations (i.e., $\sin x \approx x$ and $\cos x \approx 1$ for small x), we have

$$\varepsilon_{pq} \approx \xi - \frac{\delta_R}{2\xi}\left[\frac{\delta_T}{2}\sin\varphi_T \sin\varphi_R - Q\cos\varphi_R\cos\theta_R\right] \tag{3.3a}$$

$$\varepsilon_{pn_1} \approx R_T - \frac{\delta_T}{2}\left[\sin\beta_T^{(n_1)}\sin\varphi_T + \cos\beta_T^{(n_1)}\cos\varphi_T\cos(\theta_T - \alpha_T^{(n_1)})\right] \tag{3.3b}$$

$$\varepsilon_{n_1q} \approx \xi_{n_1} - \frac{\delta_R}{2\xi_{n_1}}\left[R_T\sin\beta_T^{(n_1)}\sin\varphi_R - Q_{n_1}\cos\varphi_R\cos(\alpha_R^{(n_1)} - \theta_R)\right] \tag{3.3c}$$

$$\varepsilon_{pn_2} \approx \xi_{n_2} - \frac{\delta_T}{2\xi_{n_2}}\left[R_R\sin\beta_R^{(n_2)}\sin\varphi_T + Q_{n_2}\cos\varphi_T\cos(\alpha_T^{(n_2)} - \theta_T)\right] \tag{3.3d}$$

$$\varepsilon_{n_2q} \approx R_R - \frac{\delta_R}{2}\left[\sin\beta_R^{(n_2)}\sin\varphi_R + \cos\beta_R^{(n_2)}\cos\varphi_R\cos(\theta_R - \alpha_R^{(n_2)})\right] \tag{3.3e}$$

$$\begin{aligned}\varepsilon_{n_1n_2} \approx \Bigg\{&\left[D - R_T\cos\alpha_T^{(n_1)} - R_R\cos(\alpha_R^{(n_1)} - \alpha_R^{(n_2)})\right]^2 \\ &+ \left[R_T\cos\beta_T^{(n_1)} - R_R\cos\beta_R^{(n_2)}\right]^2\Bigg\}^{1/2}\end{aligned} \tag{3.3f}$$

$$\varepsilon_{pn_3} \approx \xi_T^{(n_3)} - \frac{\delta_T}{2\xi_T^{(n_3)}}\left[\xi_R^{(n_3)}\sin\beta_R^{(n_3)}\sin\varphi_T + Q_{n_3}\cos\varphi_T\cos(\alpha_T^{(n_3)} - \theta_T)\right] \tag{3.3g}$$

$$\varepsilon_{n_3 q} \approx \xi_R^{(n_3)} - \delta_R \left[\sin\beta_R^{(n_3)} \sin\varphi_R + \cos\beta_R^{(n_3)} \cos\varphi_R \cos(\alpha_R^{(n_3)} - \theta_R)\right] \tag{3.3h}$$

where $\xi \approx Q \approx D - \frac{\delta_T}{2}\cos\varphi_T \cos\theta_T$, $\xi_{n_1} = \sqrt{Q_{n_1}^2 + R_T^2 \sin^2\beta_T^{(n_1)}}$, $Q_{n_1} \approx D - R_T \cos\beta_T^{(n_1)} \times \cos\alpha_T^{(n_1)}$, $\xi_{n_2} = \sqrt{Q_{n_2}^2 + R_R^2 \sin^2\beta_R^{(n_2)}}$, $Q_{n_2} \approx D + R_R \cos\beta_R^{(n_2)} \cos\alpha_R^{(n_2)}$, $\xi_R^{(n_3)} = \frac{2a - Q_{n_3}}{\cos\beta_R^{(n_3)}}$, $\xi_T^{(n_3)} = \sqrt{Q_{n_3}^2 + (\xi_R^{(n_3)})^2 \sin^2\beta_R^{(n_3)}}$, and $Q_{n_3} = \frac{a^2 + f^2 + 2af\cos\alpha_R^{(n_3)}}{a + f\cos\alpha_R^{(n_3)}}$.

Note that the azimuth/elevation angle of departure (AAoD/EAoD), (i.e., $\alpha_T^{(n_i)}$, $\beta_T^{(n_i)}$), and azimuth/elevation angle of arrival (AAoA/EAoA), (i.e., $\alpha_R^{(n_i)}$, $\beta_R^{(n_i)}$), are independent for double-bounced rays, while are correlated for single-bounced rays. According to geometric algorithms, for the single-bounced rays resulting from the two-sphere model, we can derive the relationship between the AoDs and AoAs as $\alpha_R^{(n_1)} \approx \pi - \frac{R_T}{D}\sin\alpha_T^{(n_1)}$, $\beta_R^{(n_1)} \approx \arccos\left(\frac{D - R_T\cos\beta_T^{(1)}\cos\alpha_T^{(1)}}{\xi_{n_1}}\right)$, and $\alpha_T^{(n_2)} \approx \frac{R_R}{D}\sin\alpha_R^{(n_2)}$, $\beta_T^{(n_2)} \approx \arccos\left(\frac{D + R_R\cos\beta_R^{(2)}\cos\alpha_R^{(2)}}{\xi_{n_2}}\right)$. For the single-bounced rays resulting from elliptic-cylinder model, the angular relationship $\alpha_T^{(n_3)} = \arcsin\left(\frac{b^2\sin\alpha_R^{(n_3)}}{a^2 + f^2 + 2af\cos\alpha_R^{(n_3)}}\right)$ and $\beta_T^{(n_3)} = \arccos\left[\frac{a^2 + f^2 + 2af\cos\alpha_R^{(n_3)}}{\left(a + f\cos\alpha_R^{(n_3)}\right)\xi_T^{(n_3)}}\right]$ hold with $b = \sqrt{a^2 - f^2}$ denoting the semi-minor axis of the elliptic-cylinder. The undefined $\beta_R^{(n_1)}$, $\beta_T^{(n_2)}$, and $\beta_T^{(n_3)}$ in Line 12 of the left column on Page 3 in [70] have been given here.

For the theoretical RS-GBSM, as the number of scatterers tends to infinity, the discrete AAoD $\alpha_T^{(n_i)}$, EAoD $\beta_T^{(n_i)}$, AAoA $\alpha_R^{(n_i)}$, and EAoA $\beta_R^{(n_i)}$ can be replaced by continuous random variables $\alpha_T^{(i)}$, $\beta_T^{(i)}$, $\alpha_R^{(i)}$, and $\beta_R^{(i)}$, respectively. In [46], the assumption of 3D scattering has been validated. To jointly consider the impact of the azimuth and elevation angles on channel statistics, we use the VMF PDF to characterise the distribution of effective scatterers, which is defined as [76]

$$f(\alpha, \beta) = \frac{k\cos\beta}{4\pi\sinh k} \times e^{k[\cos\beta_0\cos\beta\cos(\alpha - \alpha_0) + \sin\beta_0\sin\beta]} \tag{3.4}$$

where $\alpha, \beta \in [-\pi, \pi)$, $\alpha_0 \in [-\pi, \pi)$ and $\beta_0 \in [-\pi, \pi)$ account for the mean values of the azimuth angle α and elevation angle β, respectively, and k ($k \geq 0$) is a real-valued parameter that controls the concentration of the distribution relative to the mean direction identified by α_0 and β_0.

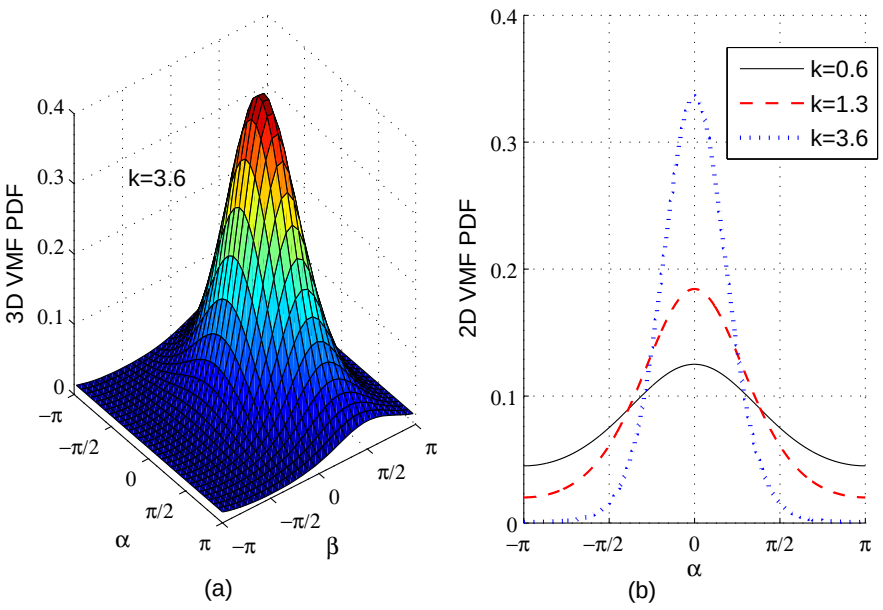

FIGURE 3.3: (a) The 3D VMF PDF ($\alpha_0 = 0°$, $\beta_0 = 31.6°$, $k = 3.6$) and (b) 2D VMF PDF ($\alpha_0 = 0°$, $\beta_0 = 31.6°$, $\beta = 0°$, $k = 0.6, 1.3, 3.6$).

To demonstrate the VMF distribution, we set the mean angles $\alpha_0 = 0°$ and $\beta_0 = 31.6°$ as an example, and plot the corresponding PDF in both 3D and 2D figures in Fig. 3.3 (a) and Fig. 3.3 (b), respectively. Fig. 3.3 (a) shows the 3D VMF PDF with $k = 3.6$. For the purpose of comparison, in Fig. 3.3 (b), we plot the 2D VMF PDF only for azimuth angle α with $\beta = 0°$ and different $k = 0.6, 1.3, 3.6$. Fig. 3.3 (b) tells that the larger the value of k, the VMF PDF is more concentrated towards the mean direction. For $k \to 0$ the distribution is isotropic, while for $k \to \infty$ the distribution becomes extremely non-isotropic. For the high VTD scenario with many moving vehicles around the Tx and Rx, k is small and the scatterer distribution approaches isotropic. Note that when the elevation angle $\beta = \beta_0 = 0°$, the VMF PDF reduces to von Mises PDF, which has widely been applied as a scatterer distribution in 2D propagation environments [77]. In this chapter, for the angles of interest, i.e., the AAoD $\alpha_T^{(1)}$ and EAoD $\beta_T^{(1)}$ for the Tx sphere, the AAoA $\alpha_R^{(2)}$ and EAoA $\beta_R^{(2)}$ for the Rx sphere, and the AAoA $\alpha_R^{(3)}$ and EAoA $\beta_R^{(3)}$ for the elliptic-cylinder, the parameters (α_0, β_0, and k) of the VMF PDF in (3.4) can be replaced by ($\alpha_{T0}^{(1)}$, $\beta_{T0}^{(1)}$, and $k^{(1)}$), ($\alpha_{R0}^{(2)}$, $\beta_{R0}^{(2)}$, and $k^{(2)}$), and ($\alpha_{R0}^{(3)}$, $\beta_{R0}^{(3)}$, and $k^{(3)}$), respectively.

It is important to emphasise that the proposed model is adaptable to a wide variety of V2V propagation environments by adjusting important parameters, which

are the Ricean factor K, energy-related parameters η_{SB_i} and η_{DB}, and environment parameters $k^{(i)}$. In general, for a low VTD, the value of K is large since the LoS component can bear a significant amount of power. Moreover, the received scattered power is mainly from waves reflected by the stationary roadside environments described by the scatterers located on the elliptic-cylinder. The moving vehicles represented by the scatterers located on the two spheres are sparse and thus more likely to be single-bounced, rather than double-bounced. This indicates that $\eta_{SB_3} > \max\{\eta_{SB_1}, \eta_{SB_2}\} > \eta_{DB}$. For a high VTD, the value of K is smaller than that in the low VTD scenario. In addition, due to dense moving vehicles, the double-bounced rays of the two-sphere model bear more energy than single-bounced rays of the two-sphere and elliptic-cylinder models, i.e., $\eta_{DB} > \max\{\eta_{SB_1}, \eta_{SB_2}, \eta_{SB_3}\}$. Therefore, the consideration of the VTD can be well characterised by utilising a combined two-sphere model and elliptic-cylinder model with the LoS component.

3.2.2 Statistical properties of the 3D MIMO V2V theoretical model

For the proposed 3D MIMO V2V theoretical RS-GBSM, statistical properties will be derived in this section, i.e., amplitude and phase PDFs, ST CF, Doppler PSD, envelope LCR, and AFD.

3.2.2.1 Amplitude and phase PDFs

Based on the proposed 3D theoretical RS-GBSM, the amplitude and phase processes can be expressed as $\zeta(t) = |h_{pq}(t)|$ and $\vartheta(t) = \arg\{h_{pq}(t)\}$, respectively. According to the same procedure in [78], the amplitude PDF of the 3D V2V reference model can be derived as

$$p_\zeta(z) = \frac{z}{\sigma_0^2} e^{-\frac{z^2+K_0^2}{2\sigma_0^2}} I_0\left(\frac{zK_0}{\sigma_0^2}\right) \tag{3.5}$$

where z presents the amplitude variable, $K_0 = \sqrt{\frac{K}{K+1}}$ and $I_0(\cdot)$ is the zeroth-order modified Bessel function of the first kind.

In addition, the phase PDF of the reference model can be derived as

$$p_\vartheta(\theta) = \frac{e^{-\frac{K_0^2}{2\sigma_0^2}}}{2\pi}\left\{1 + \frac{K_0}{\sigma_0}\sqrt{\frac{\pi}{2}}\cos\left(\theta - \theta_K\right) e^{\frac{K_0^2\cos^2(\theta-\theta_K)}{2\sigma_0^2}} \times \left[1 + \operatorname{erf}\left(\frac{K_0\cos(\theta-\theta_K)}{\sigma_0\sqrt{2}}\right)\right]\right\} \tag{3.6}$$

where $\theta_K = \arg\left\{h_{pq}^{LoS}(t)\right\}$. Due to the over-complicated procedure, detailed derivations are omitted here.

3.2.2.2 Space-time correlation function

Under the WSS condition, the normalised ST CF between any two complex fading envelopes $h_{pq}(t)$ and $h_{p'q'}(t)$ is defined as [70]

$$\rho_{h_{pq}h_{p'q'}}(\tau) = \frac{\mathbf{E}\left[h_{pq}(t)h_{p'q'}^*(t-\tau)\right]}{\sqrt{\mathbf{E}\left[|h_{pq}(t)|^2\right]\mathbf{E}\left[|h_{p'q'}(t)|^2\right]}} = \mathbf{E}\left[h_{pq}(t)\,h_{p'q'}^*(t-\tau)\right](K+1) \tag{3.7}$$

where $(\cdot)^*$ denotes the complex conjugate operation and $\mathbf{E}[\cdot]$ designates the statistical expectation operator. Substituting (3.1) into (3.7) and applying the corresponding VMF distribution, we can obtain the ST CF of the LoS, single-, and double-bounced components as follows:

(a) In the case of the LoS component,

$$\rho_{h_{pq}^{LoS}h_{p'q'}^{LoS}}(\tau) = Ke^{\frac{j2\pi}{\lambda}A^{LoS} + j2\pi\tau(f_{T_{max}}\cos\gamma_T - f_{R_{max}}\cos\gamma_R)} \tag{3.8}$$

where $A^{LoS} = 2D\cos\varphi_R\cos\theta_R$.

(b) In terms of the single-bounced components SB_i $(i = 1, 2, 3)$ resulting from the Tx sphere, Rx sphere, and elliptic-cylinder, respectively,

$$\rho_{h_{pq}^{SB_i} h_{p'q'}^{SB_i}}(\tau) = \eta_{SB_i} \int_{-\pi}^{\pi} \int_{-\pi}^{\pi} \Big[e^{-\frac{j2\pi}{\lambda} A^{(i)}} \times e^{j2\pi\tau\left(f_{T_{max}} B^{(i)} + f_{R_{max}} C^{(i)}\right)} f(\alpha_{T/R}^{(i)}, \beta_{T/R}^{(i)}) \Big] d(\alpha_{T/R}^{(i)}, \beta_{T/R}^{(i)}) \tag{3.9}$$

with $A^{(1)} = \delta_T \big[\sin\beta_T^{(1)} \sin\varphi_T + \cos\beta_T^{(1)} \cos\varphi_T \cos\left(\theta_T - \alpha_T^{(1)}\right) \big] + \frac{\delta_R}{\xi_{n_1}} \big[R_T \sin\beta_T^{(1)} \sin\varphi_R - Q_{n_1} \cos\varphi_R \cos\left(\theta_R - \alpha_R^{(1)}\right) \big]$, $B^{(i)} = \cos\left(\alpha_T^{(i)} - \gamma_T\right) \cos\left(\beta_T^{(i)}\right)$, $C^{(i)} = \cos\left(\alpha_R^{(i)} - \gamma_R\right) \times \cos\left(\beta_R^{(i)}\right)$, $A^{(2)} = \delta_R \big[\sin\beta_R^{(2)} \sin\varphi_R + \cos\beta_R^{(2)} \cos\varphi_R \cos\left(\theta_R - \alpha_R^{(2)}\right) \big] + \frac{\delta_T}{\xi_{n_2}} \big[R_R \sin\beta_R^{(2)} \times \sin\varphi_T + Q_{n_2} \cos\varphi_T \times \cos\left(\theta_T - \alpha_T^{(2)}\right) \big]$, $A^{(3)} = \frac{\delta_T}{\xi_T^{(n_3)}} \big[\xi_R^{(n_3)} \sin\beta_R^{(3)} \sin\varphi_T + Q_{n_3} \cos\varphi_T \times \cos\left(\theta_T - \alpha_T^{(3)}\right) \big] + \delta_R \big[\sin\beta_R^{(3)} \sin\varphi_R + \cos\beta_R^{(3)} \times \cos\varphi_R \cos\left(\theta_R - \alpha_R^{(3)}\right) \big]$, where the expressions of $\alpha_R^{(i)}$, $\beta_R^{(i)}$, Q_{n_i}, ξ_{n_1}, ξ_{n_2}, and $\xi_{T(R)}^{n_3}$ are given in Section 3.2. Note that the subscripts T and R are applied to $i = 1$ and $i = 2, 3$, respectively.

(c) In terms of the double-bounced component resulting from the Tx and Rx spheres,

$$\begin{aligned} \rho_{h_{pq}^{DB} h_{p'q'}^{DB}}(\tau) &= \rho_{pp'}^{T}(\tau) \rho_{qq'}^{R}(\tau) \\ &= \eta_{DB} \int_{-\pi}^{\pi} \int_{-\pi}^{\pi} \int_{-\pi}^{\pi} \int_{-\pi}^{\pi} \Big[e^{-\frac{j2\pi}{\lambda} A^{DB}} \cdot e^{j2\pi\tau\left(f_{T_{max}} B^{DB} + f_{R_{max}} C^{DB}\right)} \\ &\quad \times f(\alpha_T^{(1)}, \beta_T^{(1)}) \cdot f(\alpha_R^{(2)}, \beta_R^{(2)}) \Big] d(\alpha_T^{(1)}, \beta_T^{(1)}) d(\alpha_R^{(2)}, \beta_R^{(2)}) \end{aligned} \tag{3.10}$$

where $A^{DB} = \delta_T \big[\sin\beta_T^{(1)} \sin\varphi_T + \cos\beta_T^{(1)} \cos\varphi_T \cos\left(\theta_T - \alpha_T^{(1)}\right) \big] + \delta_R \big[\sin\beta_R^{(2)} \sin\varphi_R + \cos\beta_R^{(2)} \cos\varphi_R \cos\left(\theta_R - \alpha_R^{(2)}\right) \big]$, $B^{DB} = \cos\left(\alpha_T^{(1)} - \gamma_T\right) \cos\beta_T^{(1)}$, and $C^{DB} = \cos\left(\alpha_R^{(2)} - \gamma_R\right) \cos\beta_R^{(2)}$.

The normalised theoretical ST CF can be expressed as the summation of (3.8) – (3.10), i.e.,

$$\rho_{h_{pq} h_{p'q'}}(\tau) = \rho_{h_{pq}^{LoS} h_{p'q'}^{LoS}}(\tau) + \sum_{i=1}^{I} \rho_{h_{pq}^{SB_i} h_{p'q'}^{SB_i}}(\tau) + \rho_{h_{pq}^{DB} h_{p'q'}^{DB}}(\tau) . \tag{3.11}$$

3.2.2.3 Doppler PSD

Applying the Fourier transform to the ST CF, we can obtain the corresponding Doppler PSD as $S_{h_{pq}h_{p'q'}}(f_D) = \mathbf{F}\left\{\rho_{h_{pq}h_{p'q'}}(\tau)\right\} = \int_{-\infty}^{\infty} \rho_{h_{pq}h_{p'q'}}(\tau)e^{-j2\pi f_D \tau}d\tau$, where f_D is the Doppler frequency. Substituting (3.11) into the above equation, the Doppler PSD can be expressed as

$$\begin{aligned} S_{h_{pq}h_{p'q'}}(f_D) = \mathbf{F}\left\{\rho_{h_{pq}^{LoS}h_{p'q'}^{LoS}}(\tau)\right\} + \sum_{i=1}^{I} \mathbf{F}\left\{\rho_{h_{pq}^{SB_i}h_{p'q'}^{SB_i}}(\tau)\right\} \\ + \mathbf{F}\left\{\rho_{pp'}^{T}(\tau)\right\} \odot \mathbf{F}\left\{\rho_{qq'}^{R}(\tau)\right\} \end{aligned} \tag{3.12}$$

where $\odot$ denotes the convolution and $\mathbf{F}\{\cdot\}$ indicates the Fourier transform.

3.2.2.4 Envelope LCR and AFD

To assess system characteristics such as handoff, fading rate and velocities of the Tx and Rx, accurate characterisation of the second-order statistic (i.e., envelope LCR and AFD) is indispensable. In this subsection, based on the developed reference model in (3.1) and (3.2), we will derive the LCR and AFD for a non-isotropic scattering environment. The LCR at a specified level r, $L(r)$, is defined as the rate at which the signal envelope crosses level r in the positive/negative going direction. Using the traditional PDF-based method [79], we derive the expression of the LCR for V2V channels as

$$\begin{aligned} L(r) = \frac{2r\sqrt{K+1}}{\pi^{3/2}}\sqrt{\frac{b_2}{b_0} - \frac{b_1^2}{b_0^2}} \times e^{-K-(K+1)r^2} \\ \times \int_0^{\pi/2} \cosh\left(2\sqrt{K(K+1)}\cdot r\cos\theta\right) \times \left[e^{-(\chi\sin\theta)^2} + \sqrt{\pi}\chi\sin\theta\cdot\mathrm{erf}(\chi\sin\theta)\right] d\theta \end{aligned} \tag{3.13}$$

where $\cosh(\cdot)$ is the hyperbolic cosine function, $\mathrm{erf}(\cdot)$ is the error function, and $\chi = \sqrt{\frac{Kb_1^2}{(b_0b_2 - b_1^2)}}$. Finally, parameters b_0, b_1, and b_2 are defined as

$$b_0 \triangleq E\left[h_{pq}^{In}(t)^2\right] = E\left[h_{pq}^{Qu}(t)^2\right] \tag{3.14}$$

$$b_1 \triangleq E\left[h_{pq}^{In}(t)\dot{h}_{pq}^{Qu}(t)\right] = E\left[h_{pq}^{Qu}(t)\dot{h}_{pq}^{In}(t)\right] \tag{3.15}$$

$$b_2 \triangleq E\left[\dot{h}_{pq}^{In}(t)^2\right] = E\left[\dot{h}_{pq}^{Qu}(t)^2\right] \tag{3.16}$$

where $h_{pq}^{In}(t)$ and $h_{pq}^{Qu}(t)$ denote the in-phase and quadrature components of the complex fading envelope $h_{pq}(t)$, and $\dot{h}_{pq}^{In}(t)$ and $\dot{h}_{pq}^{Qu}(t)$ denote the first derivative of $h_{pq}^{In}(t)$ and $h_{pq}^{Qu}(t)$, respectively. By substituting (3.1) into (3.14), the parameter b_0 becomes

$$b_0 = \sum_{i=1}^{I} b_0^{SB_i} + b_0^{DB} = \frac{1}{2(K+1)} \tag{3.17}$$

where

$$b_0^{SB_i} = \frac{\eta_{SB_i}}{2(K+1)} \int_{-\pi}^{\pi}\int_{-\pi}^{\pi} f(\alpha_T^{(i)}, \beta_T^{(i)}) d(\alpha_T^{(i)}, \beta_T^{(i)}) = \frac{\eta_{SB_i}}{2(K+1)} \tag{3.18a}$$

$$\begin{aligned} b_0^{DB} = \frac{\eta_{DB}}{2(K+1)} &\int_{-\pi}^{\pi}\int_{-\pi}^{\pi} f(\alpha_T^{(1)}, \beta_T^{(1)}) d(\alpha_T^{(1)}, \beta_T^{(1)}) \\ &\times \int_{-\pi}^{\pi}\int_{-\pi}^{\pi} f(\alpha_R^{(2)}, \beta_R^{(2)}) d(\alpha_R^{(2)}, \beta_R^{(2)}) = \frac{\eta_{DB}}{2(K+1)}. \end{aligned} \tag{3.18b}$$

Similarly, by substituting (3.1) into (3.15) and (3.16), the parameters b_1 and b_2 become

$$b_m = \sum_{i=1}^{I} b_m^{SB_i} + b_m^{DB}, \tag{3.19}$$

where $m \in \{1, 2\}$ and

$$\begin{aligned} b_m^{SB_i} = \frac{\eta_{SB_i}}{2(K+1)}(2\pi)^m &\int_{-\pi}^{\pi}\int_{-\pi}^{\pi} f(\alpha_R^{(i)}, \beta_R^{(i)}) \times \left[f_{T_{max}} \cos\left(\alpha_T^{(i)} - \gamma_T\right) \cos\beta_T^{(i)}\right]^m \\ &\times \left[f_{R_{max}} \cos\left(\alpha_R^{(i)} - \gamma_R\right) \cos\beta_R^{(i)}\right]^m d(\alpha_R^{(i)}, \beta_R^{(i)}) \end{aligned} \tag{3.20a}$$

$$\begin{aligned} b_m^{DB} = \frac{\eta_{DB}}{2(K+1)}(2\pi)^m &\int_{-\pi}^{\pi}\int_{-\pi}^{\pi} f(\alpha_T^{(1)}, \beta_T^{(1)}) \\ &\times \left[f_{T_{max}} \cos\left(\alpha_T^{(1)} - \gamma_T\right) \cos\beta_T^{(1)}\right]^m d(\alpha_T^{(1)}, \beta_T^{(1)}) \end{aligned}$$

$$\times \int_{-\pi}^{\pi}\int_{-\pi}^{\pi} f(\alpha_R^{(2)},\beta_R^{(2)}) \times \left[f_{R_{max}}\cos\left(\alpha_R^{(2)}-\gamma_R\right)\cos\beta_R^{(2)}\right]^m d(\alpha_R^{(2)},\beta_R^{(2)}). \quad (3.20b)$$

The AFD, $T(r)$, is defined as the average time over which the signal envelope, $|h_{pq}(t)|$, remains below a certain level r. In the proposed 3D RS-GBSM, the AFD can be written as [2]

$$T(r) = \frac{1-\mathbf{Q}\left(\sqrt{2K},\sqrt{2(K+1)r^2}\right)}{L(r)} \quad (3.21)$$

where $\mathbf{Q}(\,\cdot\,,\,\cdot\,)$ is the Marcum Q function.

3.3 The 3D SoS Simulation Model for MIMO V2V Channels

Based on the proposed 3D theoretical RS-GBSM described in Section 3.2, the corresponding SoS simulation model can be further developed by using finite number of scatterers or sinusoids N_1, N_2, and N_3. According to (3.1) – (3.2c), the SoS simulation model for the link $T_p \to T_q$ can be expressed as

$$\hat{h}_{pq}(t) = \hat{h}_{pq}^{LoS}(t) + \sum_{i=1}^{I}\hat{h}_{pq}^{SB_i}(t) + \hat{h}_{pq}^{DB}(t) \quad (3.22)$$

where

$$\hat{h}_{pq}^{LoS}(t) = \sqrt{\frac{K}{K+1}}e^{-j2\pi f_c\tau_{pq}} \times e^{j2\pi f_{T_{max}}t\cos\left(\alpha_T^{LoS}-\gamma_T\right)\cos\beta_T^{LoS}} \times e^{j2\pi f_{R_{max}}t\cos\left(\alpha_R^{LoS}-\gamma_R\right)\cos\beta_R^{LoS}} \quad (3.23a)$$

$$\hat{h}_{pq}^{SB_i}(t) = \sqrt{\frac{\eta_{SB_i}}{K+1}}\sum_{n_i=1}^{N_i}\frac{1}{\sqrt{N_i}}e^{j\left(\psi_{n_i}-2\pi f_c\tau_{pq,n_i}\right)} \times e^{j2\pi f_{T_{max}}t\cos\left(\alpha_T^{(n_i)}-\gamma_T\right)\cos\beta_T^{(n_i)}} \times e^{j2\pi f_{R_{max}}t\cos\left(\alpha_R^{(n_i)}-\gamma_R\right)\cos\beta_R^{(n_i)}} \quad (3.23b)$$

$$\hat{h}_{pq}^{DB}(t) = \sqrt{\frac{\eta_{DB}}{K+1}} \sum_{n_1,n_2=1}^{N_1,N_2} \frac{1}{\sqrt{N_1 N_2}} e^{j\left(\psi_{n_1,n_2} - 2\pi f_c \tau_{pq,n_1,n_2}\right)} \times e^{j2\pi f_{Tmax} t \cos\left(\alpha_T^{(n_1)} - \gamma_T\right) \cos\beta_T^{(n_1)}} \times e^{j2\pi f_{Rmax} t \cos\left(\alpha_R^{(n_2)} - \gamma_R\right) \cos\beta_R^{(n_2)}}. \tag{3.23c}$$

It is clear that the unknown simulation model parameters to be determined are only the discrete AoDs and AoAs, while the remaining parameters are identical to those of the theoretical model. Our task is thus to determine the discrete AAoDs ($\alpha_T^{(n_1)}$, $\alpha_T^{(n_2)}$, $\alpha_T^{(n_3)}$), EAoDs ($\beta_T^{(n_1)}$, $\beta_T^{(n_2)}$, $\beta_T^{(n_3)}$), AAoAs ($\alpha_R^{(n_1)}$, $\alpha_R^{(n_2)}$, $\alpha_R^{(n_3)}$), and EAoAs ($\beta_R^{(n_1)}$, $\beta_R^{(n_2)}$, $\beta_R^{(n_3)}$) for the simulation model. Furthermore, there are actually correlations between AoDs and AoAs for the single-bounce case. Therefore, we only need to determine the discrete sets of $\left\{\alpha_T^{(n_1)}, \beta_T^{(n_1)}\right\}_{n_1=1}^{N_1}$, $\left\{\alpha_R^{(n_2)}, \beta_R^{(n_2)}\right\}_{n_2=1}^{N_2}$, and $\left\{\alpha_R^{(n_3)}, \beta_R^{(n_3)}\right\}_{n_3=1}^{N_3}$. In [47], different parameter computation methods have been introduced. In general, there are three widely adopted methods, i.e., Extended Method of Exact Doppler Spread (EMEDS), Modified Method of Equal Area (MMEA), and Lp-Norm Method (LPNM). The EMEDS is especially recommended for isotropic scattering. However, all the above methods are only valid for 2D horizontal models. To jointly calculate the azimuth and elevation angles, we propose a novel parameter computation method that can be applied to our 3D channel models. The method is named as MEV, which is developed from MMEA [80].

3.3.1 MEV for parameterization of the proposed SoS simulation model

As we mentioned before, the VMF distribution is adopted in order to jointly consider the impact of the azimuth and elevation angles on channel statistics. Furthermore, the Cumulative Distribution Function (CDF) of α and β, i.e., the double integral of the 3D VMF PDF, denotes the volume of Fig. 3.3 (a). The idea of MEV is designed to select the set of $\left\{\alpha^{(n_i)}, \beta^{(n_i)}\right\}_{n_i=1}^{N_i}$ in such a manner that the volume of the VMF PDF $f(\alpha, \beta)$ in different ranges of $\left\{\alpha^{(n_i-1)}, \beta^{(n_i-1)}\right\} \leqslant \{\alpha, \beta\} < \left\{\alpha^{(n_i)}, \beta^{(n_i)}\right\}$ are equal to each other with the initial condition $\int_{-\pi}^{\alpha^{(1)}} \int_{-\pi}^{\beta^{(1)}} f(\alpha, \beta) d\alpha d\beta = \frac{1-1/4}{N_i}$. The

application of the MEV to the 3D V2V channel model requires the joint computation of the discrete model parameters, i.e., $\left\{\alpha_T^{(n_1)}, \beta_T^{(n_1)}\right\}_{n_1=1}^{N_1}$, $\left\{\alpha_R^{(n_2)}, \beta_R^{(n_2)}\right\}_{n_2=1}^{N_2}$, and $\left\{\alpha_R^{(n_3)}, \beta_R^{(n_3)}\right\}_{n_3=1}^{N_3}$. In the following, we will derive the MEV that has the ability to meet the two accuracy-efficiency design criteria [80] for 3D scattering MIMO V2V channels with the joint VMF distribution. Using the design of the AAoDs $\left\{\alpha_T^{(n_1)}\right\}_{n_1=1}^{N_1}$ and EAoDs $\left\{\beta_T^{(n_1)}\right\}_{n_1=1}^{N_1}$ as an example, the MEV includes the following three steps:

Step 1: Define a pair of random variables, i.e., $\acute{\alpha_T}^{(n_1)} \in \left[\alpha_{T0}^{(1)} - \pi, \alpha_{T0}^{(1)} + \pi\right)$ and $\acute{\beta_T}^{(n_1)} \in \left[\beta_{T0}^{(1)} - \pi, \beta_{T0}^{(1)} + \pi\right)$. They follow the VMF distribution having the same $\alpha_{T0}^{(1)}$, $\beta_{T0}^{(1)}$, and k_1.

Step 2: Temporarily design the proper set of $\left\{\acute{\alpha_T}^{(n_1)}\right\}_{n_1=1}^{N_1}$ and $\left\{\acute{\beta_T}^{(n_1)}\right\}_{n_1=1}^{N_1}$, as $\acute{\alpha_T}^{(n_1)}, \acute{\beta_T}^{(n_1)} := F_{\alpha/\beta}^{-1}\left(\frac{n_1 - 1/4}{N_1}\right)$, where $F_{\alpha/\beta}^{-1}(\cdot)$ denotes the inverse function of the VMF CDF derived from VMF PDF for $\acute{\alpha_T}^{(n_1)}$ and $\acute{\beta_T}^{(n_1)}$.

Step 3: Obtain the desired set of $\left\{\alpha_T^{(n_1)}\right\}_{n_1=1}^{N_1}$ and $\left\{\beta_T^{(n_1)}\right\}_{n_1=1}^{N_1}$ by mapping $\left\{\acute{\alpha_T}^{(n_1)}\right\}_{n_1=1}^{N_1}$ and $\left\{\acute{\beta_T}^{(n_1)}\right\}_{n_1=1}^{N_1}$ into the range of $[-\pi, \pi)$, respectively.

Consequently, the jointly calculated AAoDs and EAoDs, $\left\{\alpha_T^{(n_1)}, \beta_T^{(n_1)}\right\}_{n_1=1}^{N_1}$ are obtained. Similarly, AAoAs $\left\{\alpha_R^{(n_2)}\right\}_{n_2=1}^{N_2}$ and $\left\{\alpha_R^{(n_3)}\right\}_{n_3=1}^{N_3}$ and EAoAs $\left\{\beta_R^{(n_2)}\right\}_{n_2=1}^{N_2}$ and $\left\{\beta_R^{(n_3)}\right\}_{n_3=1}^{N_3}$ can be obtained by following the same procedure.

3.3.2 Statistical properties of the proposed SoS simulation model

Based on our 3D MIMO V2V theoretical RS-GBSM and its statistical properties, it is achievable to derive the corresponding statistical properties for the SoS simulation model. As the detailed derivations have been explained in Section 3.2, those of the corresponding simulation model with similar derivations are only briefly explained. Applying the discrete model parameters to (3.5), (3.6), (3.11), (3.12), (3.13), and

(3.21), we have the corresponding statistical properties for the SoS simulation model as follows:

3.3.2.1 Amplitude and phase PDFs

The amplitude and phase processes of the SoS simulation model can be expressed as $\hat{\zeta}(t) = \left|\hat{h}_{pq}(t)\right|$ and $\hat{\vartheta}(t) = \arg\left\{\hat{h}_{pq}(t)\right\}$, respectively. Still using the similar procedure in [78], the amplitude PDF of the SoS simulation model can be derived as

$$p_{\hat{\zeta}}(z) = 4\pi^2 z \int_0^\infty \left[\prod_{n_1=1}^{N_1} J_0\left(2\pi \left|G_{SB_1}\right| x\right) \times \prod_{n_2=1}^{N_2} J_0\left(2\pi \left|G_{SB_2}\right| x\right) \times \prod_{n_3=1}^{N_3} J_0\left(2\pi \left|G_{SB_3}\right| x\right) \times \prod_{n_1,n_2=1}^{N_1,N_2} J_0\left(2\pi \left|G_{DB}\right| x\right)\right] J_0\left(2\pi z x\right) J_0\left(2\pi K_0 x\right) x dx \tag{3.24}$$

where $G_{SB_i} = \sqrt{\frac{\eta_{SB_i}}{N_i(K+1)}}$ $(i = 1, 2, 3)$, and $G_{DB} = \sqrt{\frac{\eta_{DB}}{N_1 N_2 (K+1)}}$.

In addition, the phase PDF of the SoS simulation model can be derived as

$$p_{\hat{\vartheta}}(\theta) = 2\pi \int_0^\infty \int_0^\infty \left[\prod_{n_1=1}^{N_1} J_0\left(2\pi \left|G_{SB_1}\right| x\right) \times \prod_{n_2=1}^{N_2} J_0\left(2\pi \left|G_{SB_2}\right| x\right) \times \prod_{n_3=1}^{N_3} J_0\left(2\pi \left|G_{SB_3}\right| x\right) \times \prod_{n_1,n_2=1}^{N_1,N_2} J_0\left(2\pi \left|G_{DB}\right| x\right)\right] \times J_0\left(2\pi x \sqrt{z^2 + K_0^2 - 2zK_0 \cos\left(\theta - \theta_K\right)}\right) x z dx dz. \tag{3.25}$$

3.3.2.2 Space-time correlation function

As we should represent the spatial components, here we rewrite the ST CF as

$$\hat{\rho}_{h_{pq}h_{p'q'}}\left(\delta_T, \delta_R, \tau\right) = \hat{\rho}_{h_{pq}^{LoS} h_{p'q'}^{LoS}}\left(\delta_T, \delta_R, \tau\right) + \sum_{i=1}^{I} \hat{\rho}_{h_{pq}^{SB_i} h_{p'q'}^{SB_i}}\left(\delta_T, \delta_R, \tau\right) + \hat{\rho}_{h_{pq}^{DB} h_{p'q'}^{DB}}\left(\delta_T, \delta_R, \tau\right). \tag{3.26}$$

(a) In the case of the LoS component,

$$\hat{\rho}_{h_{pq}^{LoS}h_{p'q'}^{LoS}}(\delta_T,\delta_R,\tau)=Ke^{\frac{j2\pi}{\lambda}A^{LoS}}\times e^{j2\pi\tau(f_{T_{max}}\cos\gamma_T-f_{R_{max}}\cos\gamma_R)}. \tag{3.27}$$

Please note that the LoS ST CF of the SoS simulation model is identical to that of the 3D theoretical RS-GBSM.

(b) In terms of the single-bounced components SB_i $(i=1,2,3)$ resulting from the Tx sphere, Rx sphere, and elliptic-cylinder, respectively,

$$\hat{\rho}_{h_{pq}^{SB_i}h_{p'q'}^{SB_i}}(\delta_T,\delta_R,\tau)=\frac{\eta_{SB_i}}{N_i}\sum_{n_i=1}^{N_i}e^{\frac{j2\pi}{\lambda}A^{(i)}}\times e^{j2\pi\tau\left(f_{T_{max}}B^{(i)}+f_{R_{max}}C^{(i)}\right)}. \tag{3.28}$$

(c) In terms of the double-bounced component resulting from the Tx and Rx spheres,

$$\begin{aligned}\hat{\rho}_{h_{pq}^{DB}h_{p'q'}^{DB}}(\delta_T,\delta_R,\tau)&=\hat{\rho}_{pp'}^{T}(\delta_T,\tau)\hat{\rho}_{qq'}^{R}(\delta_R,\tau)=\eta_{DB}\times\frac{1}{N_1}\sum_{n_1}^{N_1}e^{\frac{j2\pi}{\lambda}A^{DB_T}}\times e^{j2\pi\tau f_{T_{max}}B^{DB}}\\&\times\frac{1}{N_2}\sum_{n_2}^{N_2}e^{\frac{j2\pi}{\lambda}A^{DB_R}}\times e^{j2\pi\tau f_{R_{max}}C^{DB}}\end{aligned} \tag{3.29}$$

where $A^{DB_T}=\delta_T\left[\sin\beta_T^{(1)}\sin\varphi_T+\cos\beta_T^{(1)}\cos\varphi_T\cos\left(\theta_T-\alpha_T^{(1)}\right)\right]$, $A^{DB_R}=\delta_R\left[\sin\beta_R^{(2)}\times\sin\varphi_R+\cos\beta_R^{(2)}\cos\varphi_R\cos\left(\theta_R-\alpha_R^{(2)}\right)\right]$, and A^{LoS}, $A^{(i)}$, $B^{(i)}$, $C^{(i)}$, B^{DB}, and C^{DB} have been given in Section 3.2.

3.3.2.3 Doppler PSD

The Doppler PSD of the SoS simulation model can be expressed as

$$\hat{S}_{h_{pq}h_{p'q'}}(f_D)=\mathbf{F}\left\{\hat{\rho}_{h_{pq}^{LoS}h_{p'q'}^{LoS}}(\tau)\right\}+\sum_{i=1}^{I}\mathbf{F}\left\{\hat{\rho}_{h_{pq}^{SB_i}h_{p'q'}^{SB_i}}(\tau)\right\}+\mathbf{F}\left\{\hat{\rho}_{pp'}^{T}(\tau)\right\}\odot\mathbf{F}\left\{\hat{\rho}_{qq'}^{R}(\tau)\right\}. \tag{3.30}$$

TABLE 3.2: Key parameters of different VTD scenarios.

	K	η_{SB_1}	η_{SB_2}	η_{SB_3}	η_{DB}	$k^{(1)}$	$k^{(2)}$	$k^{(3)}$
Low VTD	3.786	0.335	0.203	0.411	0.051	9.6	3.6	11.5
High VTD	0.156	0.126	0.126	0.063	0.685	0.6	1.3	11.5

3.3.2.4 Envelope LCR and AFD

Similarly, according to (3.13), the envelope LCR of the SoS simulation model, $\hat{L}(r)$, can be derived as

$$\hat{L}(r) = \frac{2r\sqrt{K+1}}{\pi^{3/2}}\sqrt{\frac{\hat{b}_2}{\hat{b}_0} - \frac{\hat{b}_1^2}{\hat{b}_0^2}} \times e^{-K-(K+1)r^2} \times \int_0^{\pi/2} \cosh\left(2\sqrt{K(K+1)}\cdot r\cos\theta\right) \times \left[e^{-(\hat{\chi}\sin\theta)^2} + \sqrt{\pi}\hat{\chi}\sin\theta\cdot\mathrm{erf}(\hat{\chi}\sin\theta)\right] d\theta \tag{3.31}$$

with $\hat{\chi} = \sqrt{\frac{K\hat{b}_1^2}{\hat{b}_0\hat{b}_2 - \hat{b}_1^2}}$, $\hat{b}_0 = \frac{1}{2(K+1)}$, and $\hat{b}_m = \sum_{i=1}^{I}\hat{b}_m^{SB_i} + \hat{b}_m^{DB}$ $(m = 1, 2)$, where

$$\hat{b}_m^{SB_i} = \frac{\eta_{SB_i}}{2(K+1)}(2\pi)^m \times \frac{1}{N_i}\sum_{n_i=1}^{N_i}\left[f_{Tmax}\cos\left(\alpha_T^{(n_i)} - \gamma_T\right)\cos\beta_T^{(n_i)} \times f_{Rmax}\cos\left(\alpha_R^{(n_i)} - \gamma_R\right)\cos\beta_R^{(n_i)}\right]^m \tag{3.32a}$$

$$\hat{b}_m^{DB} = \frac{\eta_{DB}}{K+1}(2\pi)^m \times \frac{1}{N_1}\sum_{n_1=1}^{N_1}\left[f_{Tmax}\cos\left(\alpha_T^{(n_1)} - \gamma_T\right)\cos\beta_T^{(n_1)}\right]^m \times \frac{1}{N_2}\sum_{n_2=1}^{N_2}\left[f_{Rmax}\cos\left(\alpha_R^{(n_2)} - \gamma_R\right)\cos\beta_R^{(n_2)}\right]^m. \tag{3.32b}$$

Similarly, according to (3.21), the envelope AFD of the SoS simulation model, $\hat{T}(r)$, can be expressed as

$$\hat{T}(r) = \frac{1 - \mathbf{Q}\left(\sqrt{2K}, \sqrt{2(K+1)r^2}\right)}{\hat{L}(r)}. \tag{3.33}$$

3.4 Simulation Results and Analysis

In this section, we investigate both the 3D and 2D models in detail for each statistical property. Based on measured scenarios in [8], the following main parameters were chosen for our simulations: $f_c = 5.9$ GHz, $D = 300$ m, $f_{Tmax} = f_{Rmax} = 570$ Hz, $a = 180$ m, $R_T = R_R = 15$ m, $\gamma_T = \gamma_R = 0°$, $\varphi_T = \varphi_R = 45°$, $\theta_T = \theta_R = 45°$, $\alpha_{T0}^{(1)} = 21.7°$, $\beta_{T0}^{(1)} = 6.7°$, $\alpha_{R0}^{(2)} = 147.8°$, $\beta_{R0}^{(2)} = 17.2°$, $\alpha_{R0}^{(3)} = 171.6°$, and $\beta_{R0}^{(3)} = 31.6°$. Considering the constraints of the Ricean factor and power-related parameters in [70], we have $k^{(1)} = 9.6$, $k^{(2)} = 3.6$, $k^{(3)} = 11.5$, $K = 3.786$, $\eta_{SB_1} = 0.335$, $\eta_{SB_2} = 0.203$, $\eta_{SB_3} = 0.411$, and $\eta_{DB} = 0.051$ for low VTD scenario. For high VTD scenario, we have $k^{(1)} = 0.6$, $k^{(2)} = 1.3$, $k^{(3)} = 11.5$, $K = 0.156$, $\eta_{SB_1} = 0.126$, $\eta_{SB_2} = 0.126$, $\eta_{SB_3} = 0.063$, and $\eta_{DB} = 0.685$. Please note that $k^{(3)} = 11.5$ for both low VTD and high VTD scenarios are applied. Table 3.2 summarises key parameters adopted by low and high VTD scenarios. The environment-related parameters $k^{(1)}$, $k^{(2)}$, and $k^{(3)}$ are related to the distribution of scatterers (normally, the smaller values of $k^{(1)}$ and $k^{(2)}$ the more dense moving vehicles/scatterers, i.e., the higher VTD). In both high and low VTDs, $k^{(3)}$ is large as the scatterers reflected from static roadsides are normally concentrated. Also, Ricean factor K is small in higher VTD, as the LoS component does not have dominant power. The reason is that dense vehicles (i.e., more vehicles/obstacles between Tx and Rx) on the road result in less likelihood of strong LoS components. For the SoS simulation model, we must first choose adequate values for the number of discrete scatterers N_1, N_2, and N_3. Based on our own simulation experiences and suggested by [47], a reasonable values for N_i can be 40, which can be considered as a good trade-off between realisation complexity and accuracy. Certainly, if we simulate rigorous channels, e.g., very high VTD, the number of effective scatterers can be increased to improve the performance of the channel simulator. In addition, when $\beta_T^{(n1)} = \beta_R^{(n2)} = \beta_R^{(n3)} = 0°$, the proposed 3D model will be reduced to a 2D two-ring and elliptic model. The impact of elevation angle is evaluated in this section by comparing between the 3D and 2D models in terms of their statistical properties.

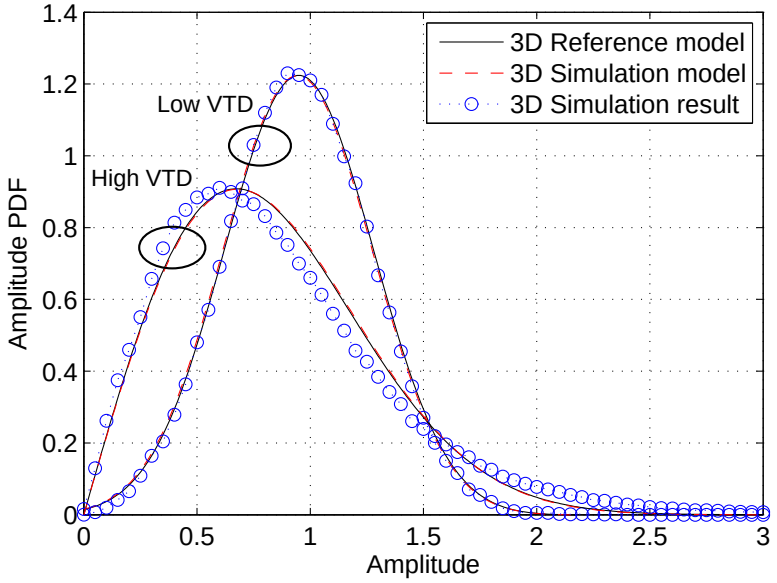

FIGURE 3.4: The amplitude PDFs for the 3D reference model, 3D simulation model, and 3D simulation result ($\delta_T = \delta_R = 0$, $\beta_{T0}^{(1)} = 6.7°$, $\beta_{R0}^{(2)} = 17.2°$, $\beta_{R0}^{(3)} = 31.6°$).

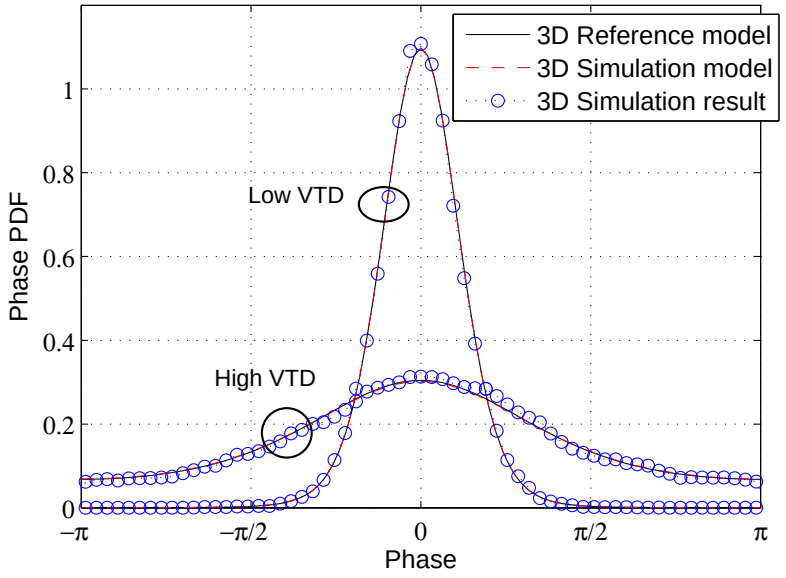

FIGURE 3.5: The phase PDFs for the 3D reference model, 3D simulation model, and 3D simulation result ($\delta_T = \delta_R = 0$, $\beta_{T0}^{(1)} = 6.7°$, $\beta_{R0}^{(2)} = 17.2°$, $\beta_{R0}^{(3)} = 31.6°$).

3.4.1 Amplitude and phase PDFs

Fig. 3.4 and Fig. 3.5 show the amplitude and phase PDFs, respectively, for the 3D reference model, 3D simulation model with $N_1 = N_2 = N_3 = 40$, and 3D simulation results for both low and high VTD scenarios. Note that the simulation results were obtained from the channel coefficients generated by the proposed channel simulator.

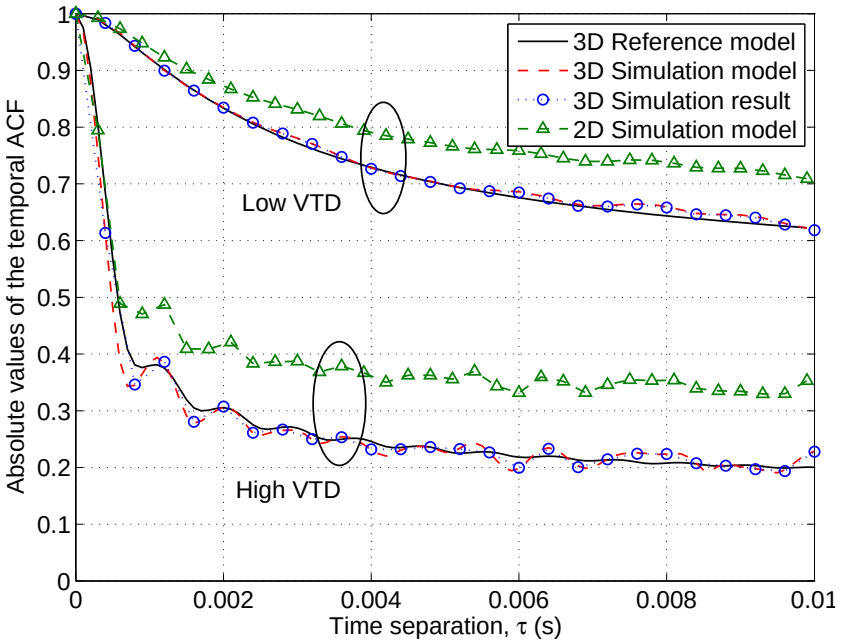

FIGURE 3.6: The absolute values of the temporal ACFs for the 3D reference model, 3D simulation model, 3D simulation result, and 2D simulation model ($\delta_T = \delta_R = 0$, 3D model: $\beta_{T0}^{(1)} = 6.7°$, $\beta_{R0}^{(2)} = 17.2°$, $\beta_{R0}^{(3)} = 31.6°$, 2D model: $\beta_T^{(n1)} = \beta_R^{(n2)} = \beta_R^{(n3)} = \beta_{T0}^{(1)} = \beta_{R0}^{(2)} = \beta_{R0}^{(3)} = 0°$).

It is clear that both amplitude and phase PDFs of the simulation model, i.e., (3.24) and (3.25), respectively, are completely determined by the number of scatterers N_i, the gains G_{SB_i} and G_{DB}, and LoS amplitude K_0, whereas other model parameters have no influence at all. In addition, Fig. 3.4 and Fig. 3.5 demonstrate that the choice of $N_1 = N_2 = N_3 = 40$ is sufficient to obtain an excellent agreement between the simulation model and reference model in both low and high VTD scenarios.

3.4.2 Temporal autocorrelation function

We investigate the temporal ACF, which can be derived from the ST CF (3.26) by setting $d_T = d_R = 0$. Therefore, the temporal ACF can be expressed as

$$\hat{\rho}_{h_{pq}h_{p'q'}}(\tau) = \hat{\rho}_{h_{pq}h_{p'q'}}(0, 0, \tau). \tag{3.34}$$

Fig. 3.6 presents the absolute values of the temporal ACFs for the 3D reference model, 3D simulation model with $N_1 = N_2 = N_3 = 40$, and 3D simulation result for both low

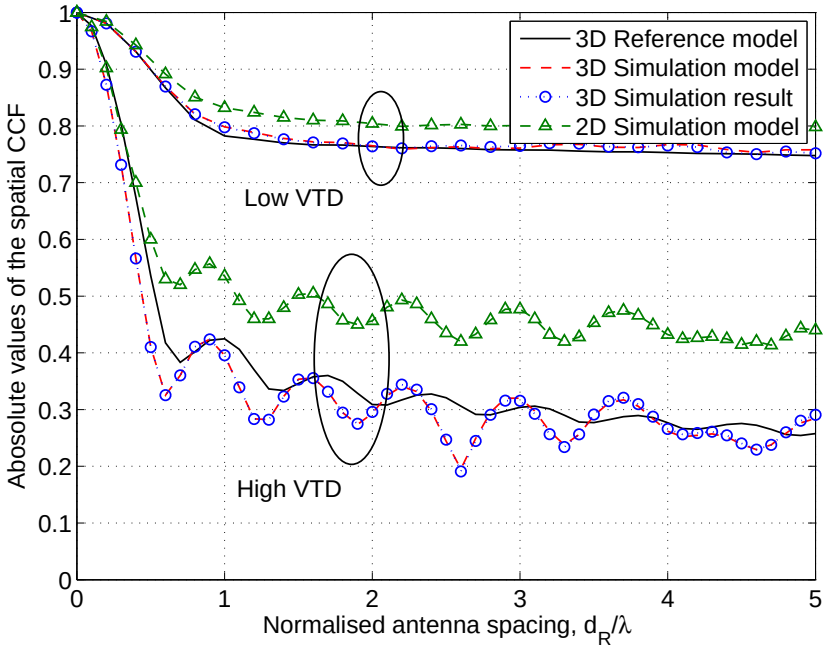

FIGURE 3.7: The absolute values of the spatial CCFs for the 3D reference model, 3D simulation model, 3D simulation result, and 2D simulation model ($\tau = 0$, 3D model: $\beta_{T0}^{(1)} = 6.7°$, $\beta_{R0}^{(2)} = 17.2°$, $\beta_{R0}^{(3)} = 31.6°$, 2D model: $\beta_{T}^{(n1)} = \beta_{R}^{(n2)} = \beta_{R}^{(n3)} = \beta_{T0}^{(1)} = \beta_{R0}^{(2)} = \beta_{R0}^{(3)} = 0°$).

VTD and high VTD scenarios. The temporal ACFs of the 2D simulation model by setting $\beta_{T}^{(n1)} = \beta_{R}^{(n2)} = \beta_{R}^{(n3)} = 0°$ are also plotted in Fig. 3.6. It is clear that no matter what the VTD is, the ACFs of the 2D model always show higher correlation than that of the 3D model. This means that the 2D model overestimates the temporal ACFs. From Fig. 3.6, we observe that both the 3D simulation model and 3D simulation result closely match the 3D reference model. Moreover, the VTD significantly affects the temporal ACF. In low VTD scenario, the temporal ACF is always higher than that in high VTD scenario.

3.4.3 Spatial cross-correlation function

The spatial CCF can be derived from the ST CF by setting $\tau = 0$. Therefore, the spatial CCF can be expressed as

$$\hat{\rho}_{h_{pq}h_{p'q'}}(\delta_T, \delta_R) = \hat{\rho}_{h_{pq}h_{p'q'}}(\delta_T, \delta_R, 0)\,. \tag{3.35}$$

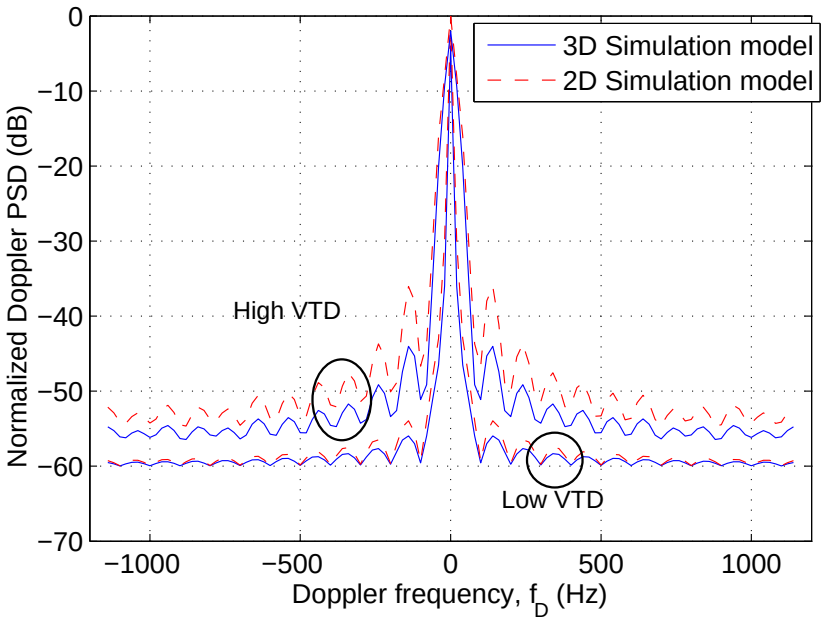

FIGURE 3.8: The normalized Doppler PSDs for the 3D and 2D simulation models ($\delta_T = \delta_R = 0$, 3D model: $\beta_{T0}^{(1)} = 6.7°$, $\beta_{R0}^{(2)} = 17.2°$, $\beta_{R0}^{(3)} = 31.6°$, 2D model: $\beta_T^{(n1)} = \beta_R^{(n2)} = \beta_R^{(n3)} = \beta_{T0}^{(1)} = \beta_{R0}^{(2)} = \beta_{R0}^{(3)} = 0°$).

In simulations, the basic parameters are the same as before except for $\delta_T = 0.5\lambda$. Fig. 3.7 presents the absolute values of the spatial CCFs for the 3D reference model, 3D simulation model, 3D simulation result, and 2D simulation model for the low VTD and high VTD scenarios. Both 3D and 2D simulation models have the number of effective scatterers $N_1 = N_2 = N_3 = 40$. Again, from Fig. 3.7, it is clear that higher VTD leads to lower spatial correlation properties. This is because the higher the VTD, the more spatial diversity the V2V channel has. Compared with the 3D models in Fig. 3.7, 2D simulation model overestimates the spatial correlations. In other words, the 2D model underestimates the spatial diversity gain. The reason is that the 2D model cannot capture the spatial diversity gain in the vertical plane. Moreover, in Fig. 3.6 and Fig. 3.7 we have shown that 3D simulation results match those of the 3D simulation model very well, indicating the correctness of our derivations. For clarity purposes, we only present 2D and 3D simulation models in the rest of the figures.

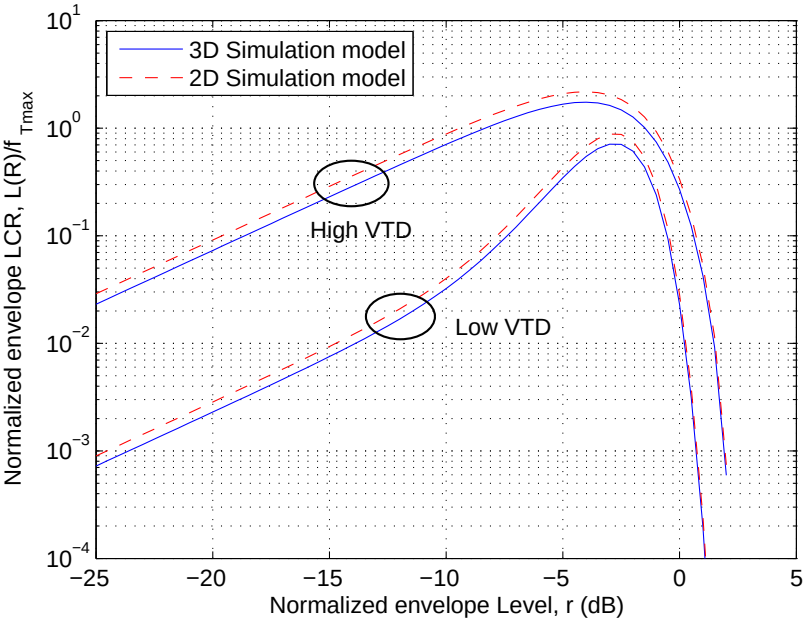

FIGURE 3.9: The normalized envelope LCRs for the 3D and 2D simulation models (3D model: $\beta_{T0}^{(1)} = \beta_{R0}^{(2)} = \beta_{R0}^{(3)} = 60°$, 2D model: $\beta_{T}^{(n1)} = \beta_{R}^{(n2)} = \beta_{R}^{(n3)} = \beta_{T0}^{(1)} = \beta_{R0}^{(2)} = \beta_{R0}^{(3)} = 0°$).

3.4.4 Doppler PSD

As the Doppler PSD is derived from the Fourier transform of corresponding temporal ACF, Fig. 3.8 shows the Doppler PSD of the proposed 3D model compared with 2D one at different VTDs. Comparing the Doppler PSDs with different VTDs in Fig. 3.8, it shows that the higher the VTD, the more evenly distributed the Doppler PSD is. The underlying physical reason is that in the high VTD scenario, the received power comes from all directions reflected by moving vehicles. However, in the low VTD scenario, the received power comes mainly from specific directions identified by main stationary roadside scatterers and LoS components. Fig. 3.8 also tells that compared with the 3D model, the 2D model underestimates the Doppler PSD in both low VTD and high VTD scenarios.

3.4.5 Envelope LCR and AFD

Fig. 3.9 and Fig. 3.10 depict the envelope LCRs and AFDs for different VTD scenarios (low and high), respectively. Again, the VTD significantly affects the envelope LCR

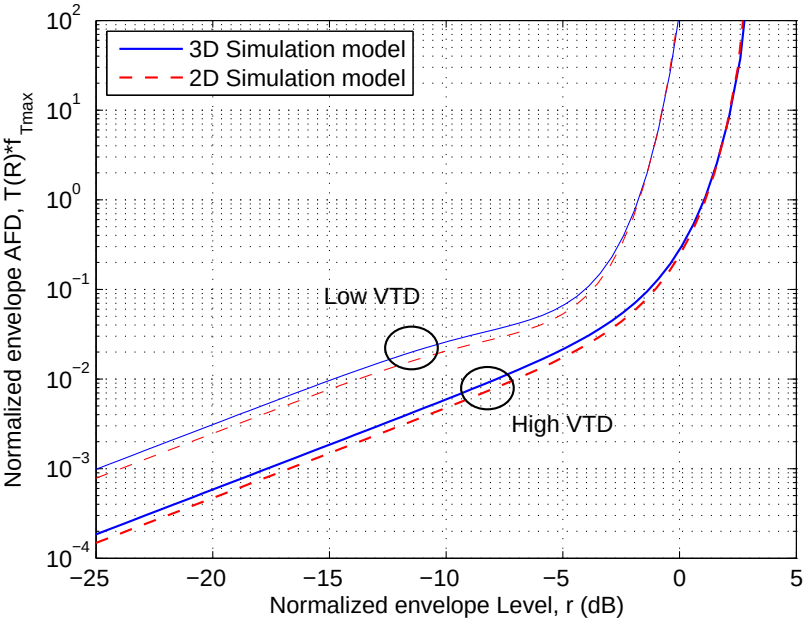

FIGURE 3.10: The normalized envelope AFDs for the 3D and 2D simulation models (3D model: $\beta_{T0}^{(1)} = \beta_{R0}^{(2)} = \beta_{R0}^{(3)} = 60°$, 2D model: $\beta_{T}^{(n1)} = \beta_{R}^{(n2)} = \beta_{R}^{(n3)} = \beta_{T0}^{(1)} = \beta_{R0}^{(2)} = \beta_{R0}^{(3)} = 0°$).

and AFD for V2V channels. Fig. 3.9 shows that the LCRs are smaller when the VTD is lower. Fig. 3.10 illustrates that the AFD tends to be larger with lower VTD. However, the elevation angles do not influence the LCR and AFD remarkably. If we used the same elevation parameters (i.e., $\beta_{T0}^{(1)} = 6.7°$, $\beta_{R0}^{(2)} = 17.2°$, and $\beta_{R0}^{(3)} = 31.6°$) as before, the LCR and AFD are barely discernible. The difference is noticeable when we increase the elevation parameters to $\beta_{T0}^{(1)} = \beta_{R0}^{(2)} = \beta_{R0}^{(3)} = 60°$ in Fig. 3.9 and Fig. 3.10. For the envelope LCR in Fig. 3.9, the 2D model shows higher LCR than the 3D model. For the envelope AFD, the 2D model exhibits smaller AFD than the 3D model. Overall, the elevation angle has minor impact on the envelope LCR and AFD.

3.5 Summary

In this chapter, we have proposed a novel 3D theoretical RS-GBSM and corresponding SoS simulation model for non-isotropic scattering MIMO V2V fading channels. The proposed models have the ability to investigate the impact of the VTD and elevation

angle on channel statistics. Furthermore, a novel parameter computation method, named as MEV, has been developed for jointly calculating the azimuth and elevation angles. Based on proposed models, comprehensive statistical properties have been derived and thoroughly investigated. The simulation results have validated the utility of the proposed model. The impact of the elevation angle on channel statistical properties has been investigated and analysed, i.e., the difference between the 3D and 2D models. By comparing these results, we can see that the VTD has a great impact on all channel statistical properties, whereas the elevation angle has significant impact only on ST CF and Doppler PSD. In addition, our simulations and analysis have clearly addressed that the low VTD condition always shows better channel performance than the high VTD case. Compared with the existing less complex 2D RS-GBSMs and 3D RS-GBSMs, the proposed 3D MIMO V2V RS-GBSMs are more practical to mimic a real V2V communication environment. Our research work can be considered as a theoretical guidance for establishing more purposeful V2V measurement campaigns in the future.

Chapter 4

Modelling and Simulation of Wideband 3D Non-WSS MIMO V2V Channels

4.1 Introduction

In Chapter 3 (i.e., [81]), we have proposed a novel 3D narrowband MIMO V2V RS-GBSM for non-isotropic scattering Ricean fading channels. However, most potential transmission schemes for V2V communications use relatively wide bandwidths (e.g., 10 MHz for the IEEE 802.11p standard [33]). The underlying V2V channels present frequency-selectivity since the signal bandwidth is larger than or in the order of the coherence bandwidth (normally 4–6 MHz [82]). Therefore, wideband V2V channel models are indispensable.

Most V2V channel models in the literature [35]–[45], [68]–[70] rely on the assumption of WSS. These WSS models assumed that channel statistics are unchanged with respect to time. However, measurement results for V2V channels in [58], [82]–[85] have shown that the WSS assumption is valid only for very short time intervals (in the order of millisecond). The growth of V2V channel measurements has forced researchers to re-evaluate the validity of the WSS conditions. This fact motivates us to develop non-stationary channel models. To the best of my knowledge, only few channel models [83]–[88] take into account the non-stationary behaviour of V2V channels. In [89],

the author first introduced the concept of the Local Scattering Function (LSF) to describe the channel non-stationarity. The generalised non-WSS narrowband MIMO V2V channel model has been characterised in [84]. The model has been further extended to wideband case in [85]. In [86] and [87], authors proposed 2D geometry-based non-WSS narrowband MIMO V2V channel models for straight road and T-junction scenarios, respectively. In [88], the impact of the channel non-stationarity on V2V channel capacity is addressed.

The 3D RS-GBSMs in [81] have been proved that the 3D scattering should be considered for realistic V2V channel modelling. In this chapter, we further propose 3D non-WSS wideband non-isotropic MIMO V2V channel models to fulfil the requirement of non-stationary models. The AoD and the AoA are supposed to be time-variant, which makes our channel model non-stationary. Besides that, V2V channel measurements in [82] have proved that the total number of taps also has the non-stationary feature. The death/birth process can be applied to describe the time-varying numbers of the taps.

The proposed theoretical non-WSS 3D RS-GBSM is the combination of LoS components, a two-sphere model, and multiple confocal elliptic-cylinder models with single- and double-bounced rays, for non-isotropic MIMO V2V channels, which is sufficiently generic and adaptable to model various non-stationary V2V channels for different scenarios. It is also the first 3D non-WSS RS-GBSM that has the ability to study the impact of the VTD on channel statistics, and jointly considers the azimuth and elevation angles by applying the VMF distribution as the scatterer distribution. The 3D theoretical RS-GBSM assumes infinite number of effective scatterers, which results in an infinite complexity and can not be implemented in practice. Hence, this chapter develops the corresponding 3D MIMO V2V SoS based simulation model with the novel parameter computation method proposed in [81].

Overall, the major contributions and novelties of this chapter are summarised as follows:

1. A novel non-WSS 3D wideband non-isotropic MIMO V2V RS-GBSM is proposed with time-varying parameters. The model considers the impact of moving and fixed scatterers on channel statistics.

2. Based on the novel 3D wideband theoretical RS-GBSM, important channel statistical properties are derived and thoroughly investigated, i.e., local ST CF, local FCF, and local PDP.

3. The corresponding SoS simulation model is developed by the novel parameter computation method, namely the MEV, which is able to jointly calculate the azimuth and elevation angles.

4. The impacts of the non-stationarity and VTD on ST CF are investigated by comparing with those of the corresponding stationary model.

5. The ST CF of our SoS simulation model are verified by comparing with that of the reference model and simulated results. The results show that the simulation model is an excellent approximation of the reference model.

6. The proposed non-WSS RS-GBSMs has been validated by measurements in [58] according to stationary time.

7. The proposed channel models are tested by the IEEE 802.11p system simulator in terms of the BER performance.

The rest of this chapter is organised as follows. In Section 4.2, the novel theoretical 3D non-WSS wideband MIMO V2V channel model is developed with the time-varying parameters. Section 4.3 presents the local statistical properties of the 3D V2V channel model. In Section 4.4, the corresponding 3D SoS simulation model is briefly introduced with the novel parameter computation method. Numerical simulation results and analysis are presented in Section 4.5. The proposed models are tested in IEEE 802.11p in Section 4.6. Finally, the conclusions are drawn in Section 4.7.

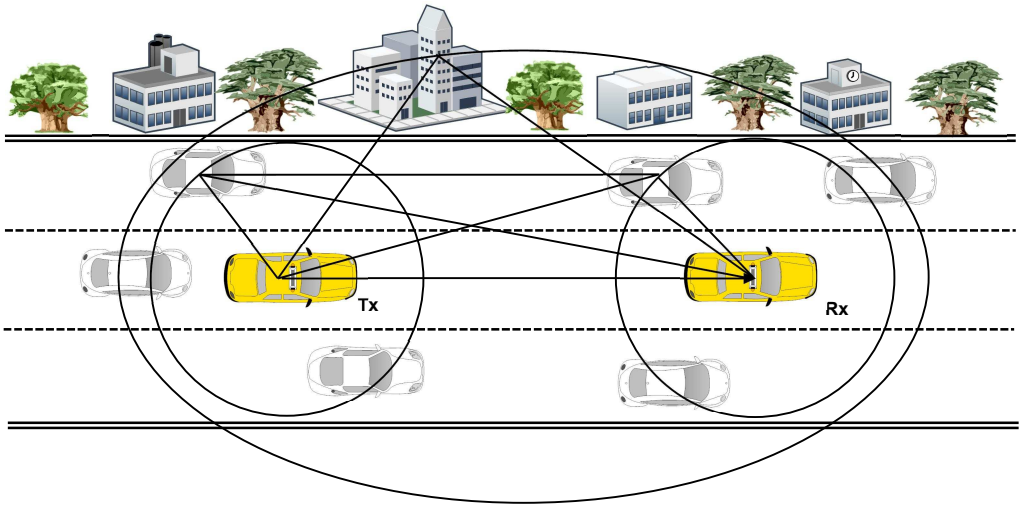

FIGURE 4.1: The typical V2V communication including moving and static scatterers with LoS, single- and double-bounced rays.

4.2 Novel 3D Wideband non-WSS MIMO V2V Theoretical Channel Models

Fig. 4.1 shows a typical V2V communication scenario with LoS, single- and double-bounced rays. The proposed generic wideband model employs a RS-GBSM approach to represent the multi-path propagation channel between a Tx and a Rx. Let us now consider a 3D wideband MIMO V2V communication system with M_T transmit and M_R receive omni-directional antenna elements. Both the Tx and Rx are equipped with low elevation antennas. The MIMO fading channel can be described by a matrix $\mathbf{H}(t) = [h_{pq}(t, \tau')]_{M_R \times M_T}$ of size $M_R \times M_T$. Fig. 4.2 and Fig. 4.3 illustrate the detailed 3D wideband V2V channel model between the Tx and Rx with LoS components, single- and double-bounced scattering. To consider the impact of the VTD on channel statistics, we need to distinguish between the moving vehicles around the Tx and Rx and the stationary roadside environments (e.g., buildings, trees, parked cars, etc.). Therefore, we use the two-sphere model to mimic the moving vehicles and the multiple confocal elliptic-cylinder models to depict the stationary roadside environments. For better readability purposes, Fig. 4.2 only shows the geometry of LoS components, and the single-bounced multiple confocal elliptic-cylinder models. The detailed geometry of the single- and double-bounced two-sphere model is given in Fig. 4.3. According

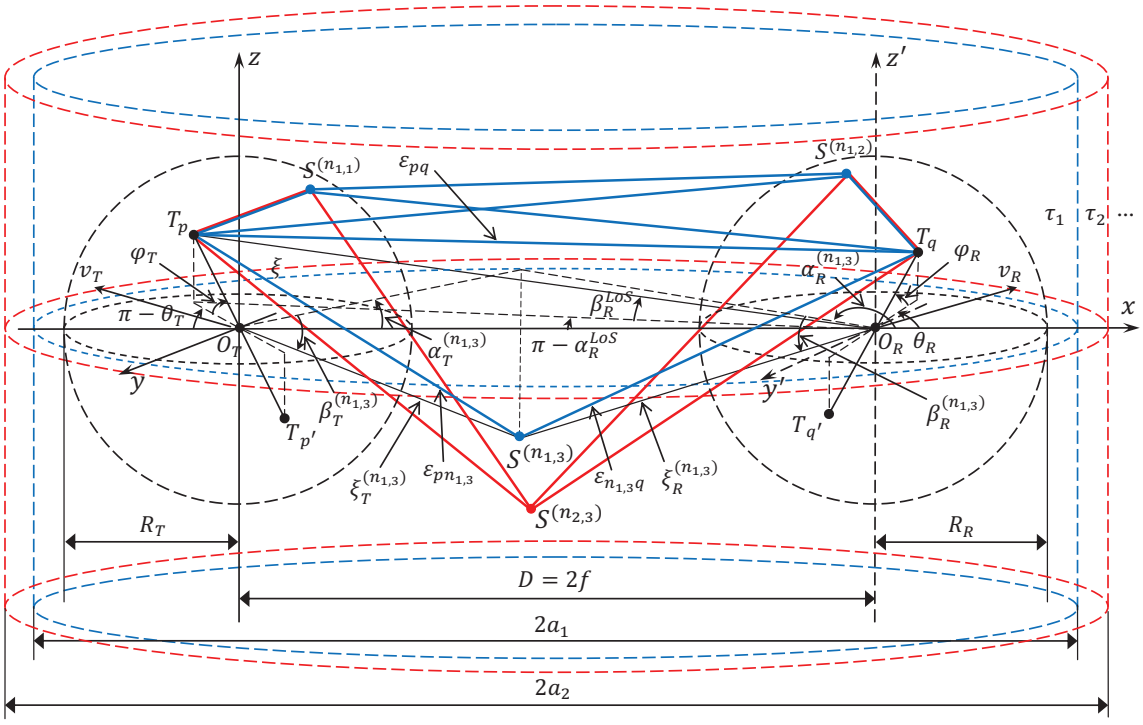

FIGURE 4.2: The proposed 3D RS-GBSM combining two-sphere model and multiple confocal elliptic-cylinder models with LoS, single- and double-bounced rays for a wideband MIMO V2V channel (Blue solid line: tap 1; Red solid line: tap 2) (only showing the detailed geometry of LoS components and single-bounced rays in the first tap elliptic-cylinder model).

to the TDL concept, the complex impulse response between the pth ($p = 1, ..., M_T$) antenna of Tx (i.e., T_p) and the qth ($q = 1, ..., M_R$) antenna of Rx (i.e., T_q) can be expressed as

$$h_{pq}(t, \tau') = \sum_{l=1}^{L(t)} c_l h_{l,pq}(t) \delta(\tau' - \tau_l') \tag{4.1}$$

where the subscript l is the tap number, $L(t)$ is the total number of taps, and c_l represents the gain of the lth tap. $h_{l,pq}(t)$ and τ_l' denote the complex time-variant tap coefficients and the discrete propagation delay of the lth tap, respectively. Hence, $h_{l,pq}(t)$ is a narrowband process.

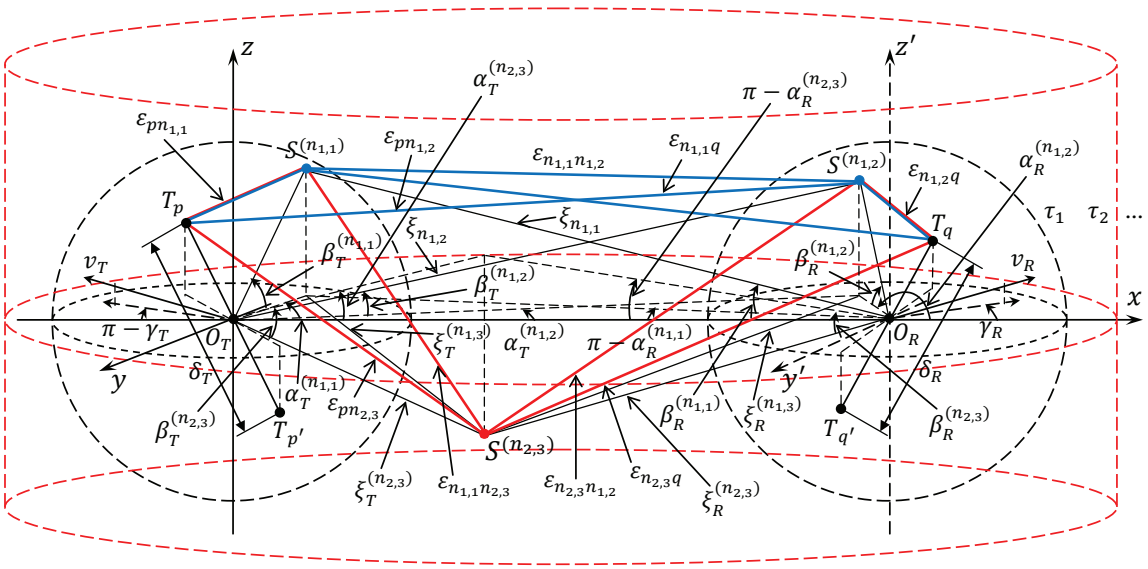

FIGURE 4.3: The detailed geometry of the single- and double-bounced rays in the two-sphere model and single-bounced rays in the second tap elliptic-cylinder model (Blue solid line: tap 1; Red solid line: tap 2).

4.2.1 First tap

In Fig. 4.2, we used uniform linear antenna arrays with $M_T = M_R = 2$ as an example. The two-sphere model defines two spheres of effective scatterers, one around the Tx and the other around the Rx. For the first tap, we suppose that there are $N_{1,1}$ effective scatterers around the Tx lying on a sphere of radius R_T and the $n_{1,1}$th ($n_{1,1} = 1, ..., N_{1,1}$) effective scatterer is denoted by $s^{(n_{1,1})}$. Similarly, assume there are $N_{1,2}$ effective scatterers around the Rx lying on a sphere of radius R_R and the $n_{1,2}$th ($n_{1,2} = 1, ..., N_{1,2}$) effective scatterer is denoted by $s^{(n_{1,2})}$.

The multiple confocal elliptic-cylinder models with the Tx and Rx located at the foci represents the TDL structure and have $N_{l,3}$ effective scatterers on the lth elliptic-cylinder (i.e., lth tap), where $l = 1, 2, ..., L(t)$ with $L(t)$ being the time-varying total number of elliptic-cylinders or taps. The semi-major axis of the lth elliptic-cylinder and the $n_{l,3}$th ($n_{l,3} = 1, ..., N_{l,3}$) effective scatterer are denoted by a_l and $s^{(n_{l,3})}$, respectively. The distance between the Tx and Rx is $D = 2f$ with f denoting the half length of the distance between the two focal points of ellipses. The antenna element spacings at the Tx and Rx are designated by δ_T and δ_R, respectively. The parameters

TABLE 4.1: Definition of parameters in Fig. 4.2 and Fig. 4.2.

D	distance between the centers of the Tx and Rx spheres
R_T, R_R	radius of the Tx and Rx spheres, respectively
a_l, f	semi-major axis and half spacing between two foci of the elliptic-cylinder, respectively
δ_T, δ_R	antenna element spacing at the Tx and Rx, respectively
θ_T, θ_R	orientation of the Tx and Rx antenna array in the x-y plane, respectively
φ_T, φ_R	elevation of the Tx and Rx antenna array relative to the x-y plane, respectively
υ_T, υ_R	velocities of the Tx and Rx, respectively
γ_T, γ_R	moving directions of the Tx and Rx in the x-y plane, respectively
$\alpha_T^{(n_{l,i})}$ $(i=1,2,3)$ $(l=1,2,...,L(t))$	AAoD of the waves that impinge on the effective scatterers $s^{(n_{l,i})}$
$\alpha_R^{(n_{l,i})}$ $(i=1,2,3)$ $(l=1,2,...,L(t))$	AAoA of the waves travelling from the effective scatterers $s^{(n_{l,i})}$
$\beta_T^{(n_{l,i})}$ $(i=1,2,3)$ $(l=1,2,...,L(t))$	EAoD of the waves that impinge on the effective scatterers $s^{(n_{l,i})}$
$\beta_R^{(n_{l,i})}$ $(i=1,2,3)$ $(l=1,2,...,L(t))$	EAoA of the waves travelling from the effective scatterers $s^{(n_{l,i})}$
α_R^{LoS}, β_R^{LoS}	AAoA and EAoA of the LoS paths, respectively
ε_{pq}, $\varepsilon_{pn_{l,i}}$, $\varepsilon_{n_{l,1}n_{l,2}}$, $\varepsilon_{n_{l,i}q}$, ξ, $\xi_{T(R)}^{n_{l,3}}$, $\xi_{n_{l,1}}$, $\xi_{n_{l,2}}$ $(i=1,2,3)$ $(l=1,2,...,L(t))$	distances $d(T_p,T_q)$, $d\left(T_p,s^{(n_{l,i})}\right)$, $d\left(s^{(n_{l,1})},s^{(n_{l,2})}\right)$, $d\left(s^{(n_{l,i})},T_q\right)$, $d(T_p,O_R)$, $d\left(O_T(O_R),s^{(n_{l,3})}\right)$, $d\left(s^{(n_{l,1})},O_R\right)$, $d\left(O_T,s^{(n_{l,2})}\right)$, respectively

in Fig. 4.2 and Fig. 4.3 are defined in Table 4.1. Note that the reasonable assumptions $D \gg \max\{R_T, R_R\}$ and $\min\{R_T, R_R, a-f\} \gg \max\{\delta_T, \delta_R\}$ are applied in this theoretical model [39].

From the above 3D RS-GBSM, the complex tap coefficient for the first tap of the $T_p \to T_q$ link is a superposition of the LoS, single- and double-bounced components, and can be expressed as

$$h_{1,pq}(t) = h_{1,pq}^{LoS}(t) + \sum_{i=1}^{I} h_{1,pq}^{SB_i}(t) + h_{1,pq}^{DB}(t) \tag{4.2}$$

with

$$h_{1,pq}^{LoS}(t) = \sqrt{\frac{K}{K+1}} e^{-j2\pi f_c \tau_{pq}} \times e^{j2\pi f_{T_{max}} t \cos\left(\alpha_T^{LoS}-\gamma_T\right)\cos\beta_T^{LoS}} \times e^{j2\pi f_{R_{max}} t \cos\left(\alpha_R^{LoS}-\gamma_R\right)\cos\beta_R^{LoS}} \tag{4.3a}$$

$$h_{1,pq}^{SB_i}(t) = \sqrt{\frac{\eta_{SB_{1,i}}}{K+1}} \lim_{N_{1,i}\to\infty} \sum_{n_{1,i}=1}^{N_{1,i}} \frac{1}{\sqrt{N_{1,i}}} e^{j\left(\psi_{n_{1,i}} - 2\pi f_c \tau_{pq,n_{1,i}}\right)} \times e^{j2\pi f_{T_{max}} t \cos\left(\alpha_T^{(n_{1,i})} - \gamma_T\right) \cos\beta_T^{(n_{1,i})}} \times e^{j2\pi f_{R_{max}} t \cos\left(\alpha_R^{(n_{1,i})} - \gamma_R\right) \cos\beta_R^{(n_{1,i})}} \tag{4.3b}$$

$$h_{1,pq}^{DB}(t) = \sqrt{\frac{\eta_{DB_{1,1}}}{K+1}} \lim_{N_{1,1},N_{1,2}\to\infty} \sum_{n_{1,1},n_{1,2}=1}^{N_{1,1},N_{1,2}} \frac{1}{\sqrt{N_{1,1}N_{1,2}}} e^{j\left(\psi_{n_{1,1},n_{1,2}} - 2\pi f_c \tau_{pq,n_{1,1},n_{1,2}}\right)} \times e^{j2\pi f_{T_{max}} t \cos\left(\alpha_T^{(n_{1,1})} - \gamma_T\right) \cos\beta_T^{(n_{1,1})}} \times e^{j2\pi f_{R_{max}} t \cos\left(\alpha_R^{(n_{1,2})} - \gamma_R\right) \cos\beta_R^{(n_{1,2})}} \tag{4.3c}$$

where $\tau_{pq} = \varepsilon_{pq}/c$, $\tau_{pq,n_{1,i}} = (\varepsilon_{pn_{1,i}} + \varepsilon_{n_{1,i}q})/c$, and $\tau_{pq,n_{1,1},n_{1,2}} = (\varepsilon_{pn_{1,1}} + \varepsilon_{n_{1,1}n_{1,2}} + \varepsilon_{n_{1,2}q})/c$ are travel times of the waves through the link $T_p \to T_q$, $T_p \to s^{(n_{1,i})} \to T_q$, and $T_p \to s^{(n_{1,1})} \to s^{(n_{1,2})} \to T_q$, respectively, as shown in Fig. 4.2 and Fig. 4.3. There are three single-bounced components in the first tap, i.e., I=3. The c and K designate the speed of light and the Ricean factor, respectively. Energy-related parameters $\eta_{SB_{1,i}}$ and $\eta_{DB_{1,1}}$ specify how much the single- and double-bounced rays contribute to the total scattered power of the first tap, respectively. Note that these energy-related parameters are normalised to satisfy $\sum_{i=1}^{I} \eta_{SB_{1,i}} + \eta_{DB_{1,1}} = 1$.

4.2.2 Other taps

The complex tap coefficient for other taps ($l > 1$) of the $T_p \to T_q$ link is a superposition of the single- and double-bounced components, and can be expressed as

$$h_{l,pq}(t) = h_{l,pq}^{SB_3}(t) + h_{l,pq}^{DB_1}(t) + h_{l,pq}^{DB_2}(t) \tag{4.4}$$

with

$$h_{l,pq}^{SB_3}(t) = \sqrt{\eta_{SB_{l,3}}} \lim_{N_{l,3}\to\infty} \sum_{n_{l,3}=1}^{N_{l,3}} \frac{1}{\sqrt{N_{l,3}}} e^{j\left(\psi_{n_{l,3}} - 2\pi f_c \tau_{pq,n_{l,3}}\right)} \times e^{j2\pi f_{T_{max}} t \cos\left(\alpha_T^{(n_{l,3})} - \gamma_T\right) \cos\beta_T^{(n_{l,3})}} \times e^{j2\pi f_{R_{max}} t \cos\left(\alpha_R^{(n_{l,3})} - \gamma_R\right) \cos\beta_R^{(n_{l,3})}} \tag{4.5a}$$

$$h_{l,pq}^{DB_1}(t) = \sqrt{\eta_{DB_{l,1}}} \lim_{N_{l,1},N_{l,3}\to\infty} \sum_{n_{l,1},n_{l,3}=1}^{N_{l,1},N_{l,3}} \frac{1}{\sqrt{N_{l,1}N_{l,3}}} e^{j\left(\psi_{n_{l,1},n_{l,3}} - 2\pi f_c \tau_{pq,n_{l,1},n_{l,3}}\right)} \times e^{j2\pi f_{T_{max}} t \cos\left(\alpha_T^{(n_{l,1})} - \gamma_T\right) \cos\beta_T^{(n_{l,1})}} \times e^{j2\pi f_{R_{max}} t \cos\left(\alpha_R^{(n_{l,3})} - \gamma_R\right) \cos\beta_R^{(n_{l,3})}} \tag{4.5b}$$

$$h_{l,pq}^{DB_2}(t) = \sqrt{\eta_{DB_{l,2}}} \lim_{N_{l,2},N_{l,3}\to\infty} \sum_{n_{l,2},n_{l,3}=1}^{N_{l,2},N_{l,3}} \frac{1}{\sqrt{N_{l,2}N_{l,3}}} e^{j\left(\psi_{n_{l,2},n_{l,3}} - 2\pi f_c \tau_{pq,n_{l,2},n_{l,3}}\right)} \times e^{j2\pi f_{T_{max}} t \cos\left(\alpha_T^{(n_{l,2})} - \gamma_T\right) \cos\beta_T^{(n_{l,2})}} \times e^{j2\pi f_{R_{max}} t \cos\left(\alpha_R^{(n_{l,3})} - \gamma_R\right) \cos\beta_R^{(n_{l,3})}} \tag{4.5c}$$

where $\tau_{pq,n_{l,3}} = (\varepsilon_{pn_{l,3}} + \varepsilon_{n_{l,3}q})/c$, $\tau_{pq,n_{1,1},n_{l,3}} = (\varepsilon_{pn_{1,1}} + \varepsilon_{n_{1,1}n_{l,3}} + \varepsilon_{n_{l,3}q})/c$, and $\tau_{pq,n_{l,3},n_{1,2}} = (\varepsilon_{pn_{l,3}} + \varepsilon_{n_{l,3}n_{1,2}} + \varepsilon_{n_{1,2}q})/c$ are travel times of the waves through the link $T_p \to s^{(n_{l,3})} \to T_q$, $T_p \to s^{(n_{1,1})} \to s^{(n_{l,3})} \to T_q$, and $T_p \to s^{(n_{l,3})} \to s^{(n_{1,2})} \to T_q$, respectively, as illustrated in Fig. 4.2 and Fig. 4.3. Again, energy-related parameters $\eta_{SB_{l,3}}$ and $\eta_{DB_{l,1(2)}}$ specify how much the single- and double-bounced rays contribute to the total scattered power of other taps, respectively. Note that these energy-related parameters also satisfy $\eta_{SB_{l,3}} + \eta_{DB_{l,1}} + \eta_{DB_{l,2}} = 1$. The phases $\psi_{n_{1,i}}$, $\psi_{n_{1,1},n_{1,2}}$, $\psi_{n_{l,3}}$, and $\psi_{n_{1,1(2)},n_{l,3}}$ are i.i.d. random variables with uniform distributions over $[-\pi, \pi)$, $f_{T_{max}}$ and $f_{R_{max}}$ are the maximum Doppler frequencies with respect to the Tx and Rx, respectively.

As introduced in [82], the VTD impact on statistical properties can not be neglected at all taps of a wideband V2V channel. To take the impact of the VTD into account, we must distinguish between the moving vehicles around the Tx (and Rx) and the stationary roadside environment. Therefore, we adopt the two-sphere model to mimic the moving vehicles and multiple confocal elliptic-cylinder models to depict the stationary roadside environment.

In summary, for the first tap, the single-bounced rays are generated from the scatterers located on either of the two spheres or the first elliptic-cylinder, while the double-bounced rays are produced from the scatterers located on both spheres. Note that only the first tap contains the LoS components, a two-sphere model with single- and double-bounced rays, and multiple confocal elliptic-cylinder models with single-bounced rays, as shown in Fig. 4.2 and Fig. 4.3. For a low VTD, the value of K

is large since the LoS component can bear a significant amount of power. Also, the received scattered power is mainly from waves reflected by the stationary roadside environment described by the scatterers located on the first elliptic-cylinder. The moving vehicles represented by the scatterers located on the two spheres are sparse and thus more likely to be single-bounced, rather than double-bounced. This indicates that $\eta_{SB_{1,3}} > \max\{\eta_{SB_{1,1}}, \eta_{SB_{1,2}}\} > \eta_{DB_{1,1}}$. For a high VTD, the value of K is smaller than the one in the low VTD scenario. Also, due to the dense moving vehicles, the double-bounced rays of the two-sphere model bear more energy than single-bounced rays of two-sphere and elliptic-cylinder models, i.e, $\eta_{DB_{1,1}} > \max\{\eta_{SB_{1,1}}, \eta_{SB_{1,2}}, \eta_{SB_{1,3}}\}$.

For other taps, we assume that the single-bounced rays are generated only from the scatterers located on the corresponding elliptic-cylinder, while the double-bounced rays are caused by the scatterers from the combined one sphere (either of the two spheres) and the corresponding elliptic-cylinder, as illustrated in Fig. 4.2. Note that according to the TDL structure, the double-bounced rays in the first tap must be smaller in distance than the single-bounced rays on the next elliptic-cylinder. This is valid only if the condition $\max\{R_T, R_R\} < \min\{a_l - a_{l-1}\}$ is fulfilled. For many current V2V channel measurement campaigns, e.g., in [8], [82], the resolution in delay is 100 ns. Then, the above condition can be modified as $\max\{R_T, R_R\} \leq 15$ m by calculating the equality $2(a_l - a_{l-1}) = c \cdot \tau'$ with $c = 3 \times 10^8$ m/s and $\tau' = 100$ ns. This indicates that the maximum acceptable width of the road is 30 m, which is sufficiently large to cover most roads in reality. In other words, the proposed wideband model with the specified TDL structure is valid for various scenarios. For a low VTD, the received scattered power is mainly from waves reflected by the stationary roadside environment described by the scatterers located on the elliptic-cylinder. This indicates that $\eta_{SB_{l,3}} > \max\{\eta_{DB_{l,1}}, \eta_{DB_{l,2}}\}$. For a high VTD, due to the large number of moving vehicles, the double-bounced rays from the combined one sphere and elliptic-cylinder models bear more energy than the single-bounced rays of the elliptic-cylinder model, i.e, $\min\{\eta_{DB_{l,1}}, \eta_{DB_{l,2}}\} > \eta_{SB_{l,3}}$.

From Fig. 4.2 and Fig. 4.3, based on the application of the law of cosines in triangles and the following assumptions $\min\{R_T, R_R, a - f\} \gg \max\{\delta_T, \delta_R\}$ and $D \gg$

$\max\{R_T, R_R\}$, and using the approximation $\sqrt{1+x} \approx 1 + x/2$ for small x. Also, based on the law of cosines in appropriate triangles and small angle approximations (i.e., $\sin x \approx x$ and $\cos x \approx 1$ for small x), we have

$$\varepsilon_{pq} \approx \xi - \frac{\delta_R}{2\xi}\left[\frac{\delta_T}{2}\sin\varphi_T \sin\varphi_R - Q\cos\varphi_R\cos\theta_R\right] \tag{4.6a}$$

$$\varepsilon_{pn_{1,1}} \approx R_T - \frac{\delta_T}{2}\left[\sin\beta_T^{(n_{1,1})}\sin\varphi_T + \cos\beta_T^{(n_{1,1})}\cos\varphi_T\cos(\theta_T - \alpha_T^{(n_{1,1})})\right] \tag{4.6b}$$

$$\varepsilon_{n_{1,1}q} \approx \xi_{n_{1,1}} - \frac{\delta_R}{2\xi_{n_{1,1}}}\left[R_T\sin\beta_T^{(n_{1,1})}\sin\varphi_R - Q_{n_{1,1}}\cos\varphi_R\cos(\alpha_R^{(n_{1,1})} - \theta_R)\right] \tag{4.6c}$$

$$\varepsilon_{pn_{1,2}} \approx \xi_{n_{1,2}} - \frac{\delta_T}{2\xi_{n_{1,2}}}\left[R_R\sin\beta_R^{(n_{1,2})}\sin\varphi_T + Q_{n_{1,2}}\cos\varphi_T\cos(\alpha_T^{(n_{1,2})} - \theta_T)\right] \tag{4.6d}$$

$$\varepsilon_{n_{1,2}q} \approx R_R - \frac{\delta_R}{2}\left[\sin\beta_R^{(n_{1,2})}\sin\varphi_R + \cos\beta_R^{(n_{1,2})}\cos\varphi_R\cos(\theta_R - \alpha_R^{(n_{1,2})})\right] \tag{4.6e}$$

$$\varepsilon_{n_{1,1}n_{1,2}} \approx \sqrt{\left[D - R_T\cos\alpha_T^{(n_{1,1})} - R_R\cos(\alpha_R^{(n_{1,1})} - \alpha_R^{(n_{1,2})})\right]^2 + \left[R_T\cos\beta_T^{(n_{1,1})} - R_R\cos\beta_R^{(n_{1,2})}\right]^2} \tag{4.6f}$$

$$\varepsilon_{pn_{1,3}} \approx \xi_T^{(n_{1,3})} - \frac{\delta_T}{2\xi_T^{(n_{1,3})}}\left[\xi_R^{(n_{1,3})}\sin\beta_R^{(n_{1,3})}\sin\varphi_T + Q_{n_{1,3}}\cos\varphi_T\cos(\alpha_T^{(n_{1,3})} - \theta_T)\right] \tag{4.6g}$$

$$\varepsilon_{n_{1,3}q} \approx \xi_R^{(n_{1,3})} - \delta_R\left[\sin\beta_R^{(n_{1,3})}\sin\varphi_R + \cos\beta_R^{(n_{1,3})}\cos\varphi_R\cos(\alpha_R^{(n_{1,3})} - \theta_R)\right] \tag{4.6h}$$

$$\varepsilon_{pn_{l,3}} \approx \xi_T^{(n_{l,3})} - \frac{\delta_T}{2\xi_T^{(n_{l,3})}}\left[\xi_R^{(n_{l,3})}\sin\beta_R^{(n_{l,3})}\sin\varphi_T + Q_{n_{l,3}}\cos\varphi_T\cos(\alpha_T^{(n_{l,3})} - \theta_T)\right] \tag{4.6i}$$

$$\varepsilon_{n_{l,3}q} \approx \xi_R^{(n_{l,3})} - \delta_R \left[\sin\beta_R^{(n_{l,3})} \sin\varphi_R + \cos\beta_R^{(n_{l,3})} \cos\varphi_R \cos(\alpha_R^{(n_{l,3})} - \theta_R)\right] \tag{4.6j}$$

where $\xi \approx Q \approx D - \frac{\delta_T}{2}\cos\varphi_T \cos\theta_T$, $\xi_{n_{1,1}} = \sqrt{Q_{n_{1,1}}^2 + R_T^2 \sin^2\beta_T^{(n_{1,1})}}$, $Q_{n_{1,1}} \approx D - R_T \times \cos\beta_T^{(n_{1,1})} \cos\alpha_T^{(n_{1,1})}$, $\xi_{n_{1,2}} = \sqrt{Q_{n_{1,2}}^2 + R_R^2 \sin^2\beta_R^{(n_{1,2})}}$, $Q_{n_{1,2}} \approx D + R_R \cos\beta_R^{(n_{1,2})} \cos\alpha_R^{(n_{1,2})}$, $\xi_R^{(n_{1,3})} = \frac{2a_1 - Q_{n_{1,3}}}{\cos\beta_R^{(n_{1,3})}}$, $\xi_T^{(n_{1,3})} = \sqrt{Q_{n_{1,3}}^2 + (\xi_R^{(n_{1,3})})^2 \sin^2\beta_R^{(n_{1,3})}}$, and $Q_{n_{1,3}} = \frac{a_1^2 + f^2 + 2a_1 f\cos\alpha_R^{(n_{1,3})}}{a_1 + f\cos\alpha_R^{(n_{1,3})}}$. $\alpha_T^{LoS} \approx \beta_T^{LoS} \approx \beta_R^{LoS} \approx 0$, $\alpha_R^{LoS} \approx \pi$, $\xi_T^{(n_{l,3})} = \frac{a_l^2 + f^2 + 2a_l f\cos\phi_R^{(n_{l,3})}}{a_l + f\cos\phi_R^{(n_{l,3})}}$, and $\xi_R^{(n_{l,3})} = \frac{b_l^2}{a_l + f\cos\phi_R^{(n_{l,3})}}$ with b_l denoting the semi-minor axis of the lth elliptic-cylinder. Note that the azimuth/elevation angle of departure (AAoD/EAoD), (i.e., $\alpha_T^{(n_{l,i})}$, $\beta_T^{(n_{l,i})}$), and azimuth/elevation angle of arrival (AAoA/EAoA), (i.e., $\alpha_R^{(n_{l,i})}$, $\beta_R^{(n_{l,i})}$), are independent for double-bounced rays, while are correlated for single-bounced rays. According to spacial solid geometrical algorithms, for the single-bounced rays resulting from the two-sphere model, we can derive the relationship between the AoDs and AoAs as $\alpha_R^{(n_{1,1})} \approx \pi - \frac{R_T}{D}\sin\alpha_T^{(n_{1,1})}$, $\beta_R^{(n_{1,1})} \approx \arccos\left(\frac{D - R_T\cos\beta_T^{(1,1)}\cos\alpha_T^{(1,1)}}{\xi_{n_{1,1}}}\right)$, and $\alpha_T^{(n_{1,2})} \approx \frac{R_R}{D}\sin\alpha_R^{(n_{1,2})}$, $\beta_T^{(n_{1,2})} \approx \arccos\left(\frac{D + R_R\cos\beta_R^{(1,2)}\cos\alpha_R^{(1,2)}}{\xi_{n_{1,2}}}\right)$. For the single-bounced rays resulting from elliptic-cylinder model, the angular relationship $\alpha_T^{(n_{l,3})} = \arcsin\left(\frac{b_l^2\sin\alpha_R^{(n_{l,3})}}{a_l^2 + f^2 + 2a_l f\cos\alpha_R^{(n_{l,3})}}\right)$ and $\beta_T^{(n_{l,3})} = \arccos\left[\frac{a_l^2 + f_l^2 + 2a_l f\cos\alpha_R^{(n_{l,3})}}{\left(a_l + f\cos\alpha_R^{(n_{l,3})}\right)\xi_T^{(n_{l,3})}}\right]$ hold with $b_l = \sqrt{a_l^2 - f^2}$ denoting the semi-minor axis of the lth elliptic-cylinder.

For the proposed theoretical 3D RS-GBSM, as the number of scatterers tends to infinity, the discrete AAoD $\alpha_T^{(n_{l,i})}$, EAoD $\beta_T^{(n_{l,i})}$, AAoA $\alpha_R^{(n_{l,i})}$, and EAoA $\beta_R^{(n_{l,i})}$ can be replaced by continuous random variables $\alpha_T^{(l,i)}$, $\beta_T^{(l,i)}$, $\alpha_R^{(l,i)}$, and $\beta_R^{(l,i)}$, respectively. To jointly consider the impact of the azimuth and elevation angles on channel statistics, again, we use the VMF PDF to characterise the distribution of effective scatterers, which has been defined in (3.4) Chapter 3.

In this chapter, for the angular descriptions, i.e., the AAoD $\alpha_T^{(1,1)}$ and EAoD $\beta_T^{(1,1)}$ for the Tx sphere, the AAoA $\alpha_R^{(1,2)}$ and EAoA $\beta_R^{(1,2)}$ for the Rx sphere, and the AAoA $\alpha_R^{(l,3)}$ and EAoA $\beta_R^{(l,3)}$ for multiple elliptic cylinders, the parameters (α_0, β_0, and k) of the VMF PDF in (3.4) can be replaced by ($\alpha_{T0}^{(l,1)}$, $\beta_{T0}^{(l,1)}$, and $k^{(l,1)}$), ($\alpha_{R0}^{(l,2)}$, $\beta_{R0}^{(l,2)}$, and $k^{(l,2)}$), and ($\alpha_{R0}^{(l,3)}$, $\beta_{R0}^{(l,3)}$, and $k^{(l,3)}$), respectively.

4.2.3 Non-stationary time-varying parameters

Based on the proposed 3D wideband V2V channel model, it is feasible to develop the corresponding non-WSS model by imposing the time-varying parameters.

4.2.3.1 The total number of taps

In [82], V2V channel measurements have proved that the total number of taps has the non-stationary tap persistence feature. A genetic appearance (birth) and disappearance (death) process for modelling the Multi-Path Components (MPCs) was proposed in [90]. Since in a time-variant (i.e., non-stationary) scenario, all multi-path components only exist over a certain time period. With ongoing time, MPCs appear and remain for a certain time span and then finally disappear. A suitable description for such a generation-recombination behaviour is given by discrete Markov processes. In V2V channel, the time variation of a wireless V2V channel is mainly caused by movements of the Tx and Rx. Therefore, the movement of scenarios is introduced and applied mathematically. The process of MPCs generation and recombination, i.e., time dependent channel fluctuations, is caused by the movement of Tx ($\Delta_{T,k}$) as well as the movement of Rx ($\Delta_{R,k}$) in the time span between t_{k-1} and t_k, i.e.,

$$\Delta_{P,k} = \Delta_{T,k} + \Delta_{R,k} \tag{4.7}$$

with

$$\Delta_{T,k} = \int_{t_{k-1}}^{t_k} P_c \cdot \bar{v}_T dt \tag{4.8}$$

and

$$\Delta_{R,k} = \int_{t_{k-1}}^{t_k} \left(|\vec{x}_R(t)|\right) dt \tag{4.9}$$

where P_c is a percentage of MPCs that contains moving scatterers with a mean velocity $\bar{v}_T$ and $\vec{x}_R(t)$ is the motion difference of the Rx. Because of the short time steps, a uniform motion in each time interval $|t_k - t_{k-1}|$ is assumed. This simplifies (4.8) and

(4.9) to

$$\Delta_{T,k} = (t_k - t_{k-1}) P_c \bar{v}_T \tag{4.10}$$

$$\Delta_{R,k} = \left| \vec{x}_R(t_k) - \vec{x}_R(t_{k-1}) \right|. \tag{4.11}$$

Therefore, $\Delta_{P,k}$ gives a measure for the correlation of CIRs at different time snapshots. A Markov birth-death description results in a time-varying number $L(t)$ of MPCs for CIR realisations. At any time instant t_k, one can distinguish between newly generated MPCs and MPCs that were already existing in the previous CIR at time instant t_{k-1}. The latter are known as inherited paths. The Markov process is described by a generation rate of new clusters (λ_G) and a recombination rate of existing ones (λ_R). The expectation of the total number, also defined as the initial number, of MPCs in a CIR realisation is given by

$$\mathbf{E}\left\{L(t)\right\} = L(t_0) = \frac{\lambda_G}{\lambda_R}. \tag{4.12}$$

Observing a time series of CIRs, each MPC remains from one CIR at t_{k-1} to a following one at t_k with the probability

$$P_{remain}(\Delta_{P,k}) = e^{-\lambda_R \cdot \Delta_{P,k}}. \tag{4.13}$$

Hence, a number of new MPCs is generated by the Markov process with expectation

$$\mathbf{E}\left\{L_{new_k}\right\} = \frac{\lambda_G}{\lambda_R}\left(1 - e^{-\lambda_R \cdot \Delta_{P,k}}\right). \tag{4.14}$$

The correlation between two evolving MPCs is quantified by the scenario movement $\Delta_{P,k}$. Mathematically, higher values of $\Delta_{P,k}$ result in a reduced correlation between the properties of an ancestor MPC at t_{k-1} and its successor at t_k. Therefore, the total

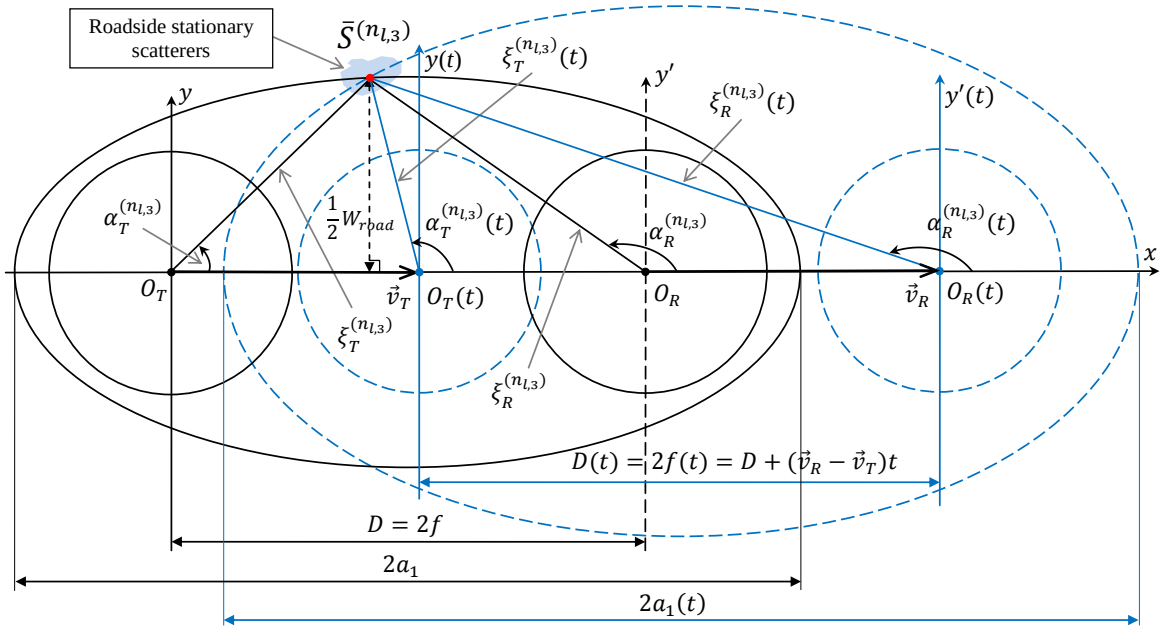

FIGURE 4.4: The non-stationary geometry of the single-bounced rays in the lth tap elliptic-cylinder model.

number of taps $L(t)$ in (4.1) is time-variant demonstrating the non-stationarity of the V2V channels.

4.2.3.2 Time-varying AoDs and AoAs

To derive time-varying AoDs and AoAs, we have to assume a V2V communication scenario. Fig. 4.4 presents the projection of a V2V communication with the Tx and Rx driving in the same direction along a straight road. In addition, the Rx always drives equally or faster than the Tx so that a car crash will never happen with time going. Please note that Fig. 4.4 only shows the time-varying AAoDs and AAoAs of the elliptic-cylinder model as the figure is the horizontal projection of the 3D model. Due to the over-complex issues, the corresponding 3D figure with MIMO antennas are omitted here for brevity. Based on the theory of relative motion and geometrical relationship in the model, the time-varying AoDs and AoAs can be derived in terms of the scenario in Fig. 4.4 as follows.

a) In the case of the LoS components, time-varying AAoD ($\alpha_T^{LoS}(t)$), EAoD ($\beta_T^{LoS}(t)$), AAoA ($\alpha_R^{LoS}(t)$), and EAoA ($\beta_R^{LoS}(t)$) can be expressed as

$$\alpha_T^{LoS}(t) \approx \beta_T^{LoS}(t) \approx \beta_R^{LoS}(t) = 0 \tag{4.15a}$$

$$\alpha_R^{LoS}(t) = \pi. \tag{4.15b}$$

b) In the case of the single-bounced components $SB_{1,i}(i = 1, 2)$ resulting from the Tx sphere and Rx sphere, respectively, time-varying AAoD ($\alpha_T^{(n_{1,i})}(t)$), EAoD ($\beta_T^{(n_{1,i})}(t)$), AAoA ($\alpha_R^{(n_{1,i})}(t)$), and EAoA ($\beta_R^{(n_{1,i})}(t)$) can be expressed as

$$\alpha_T^{(n_{1,i})}(t) \approx \alpha_T^{(n_{1,i})} \tag{4.16a}$$

$$\beta_T^{(n_{1,i})}(t) \approx \beta_T^{(n_{1,i})} \tag{4.16b}$$

$$\alpha_R^{(n_{1,i})}(t) \approx \alpha_R^{(n_{1,i})} \tag{4.16c}$$

$$\beta_R^{(n_{1,i})}(t) \approx \beta_R^{(n_{1,i})}. \tag{4.16d}$$

c) In the case of the single-bounced components $SB_{l,3}$ for the lth tap resulting from the elliptic-cylinder, time-varying AAoA ($\alpha_R^{(n_{l,3})}(t)$) and EAoA ($\beta_R^{(n_{l,3})}(t)$) can be expressed as

$$\alpha_R^{(n_{l,3})}(t) = \pi - \arccos \frac{v_R t - \xi_R^{(n_{l,3})} \cos \alpha_R^{(n_{l,3})}}{\sqrt{{\xi_R^{(n_{l,3})}}^2 + (v_R t)^2 - 2\xi_R^{(n_{l,3})} v_R t \cos \alpha_R^{(n_{l,3})}}} \tag{4.17a}$$

$$\beta_R^{(n_{l,3})}(t) = \arctan \frac{\xi_R^{(n_{l,3})} \tan \beta_R^{(n_{l,3})}}{\sqrt{{\xi_R^{(n_{l,3})}}^2 + (v_R t)^2 - 2\xi_R^{(n_{l,3})} v_R t \cos \alpha_R^{(n_{l,3})}}}. \tag{4.17b}$$

Note that the time-varying AAoD ($\alpha_T^{(n_{l,3})}(t)$) and EAoD ($\beta_T^{(n_{l,3})}(t)$), are correlated with time-varying AAoA ($\alpha_R^{(n_{l,3})}(t)$) and EAoA ($\beta_R^{(n_{l,3})}(t)$) for single-bounced rays resulting from the elliptic-cylinder model. Hence, the relationship between the AoD and AoA for multiple confocal elliptic-cylinder models can be given by

$$\alpha_T^{(n_{l,3})}(t) = \arcsin \frac{b(t)^2 \sin \alpha_R^{(n_{l,3})}(t)}{a(t)^2 + f(t)^2 + 2a(t)f(t)\cos \alpha_R^{(n_{l,3})}(t)} \tag{4.18a}$$

$$\beta_T^{(n_{l,3})}(t) = \arccos \frac{a(t)^2 + f(t)^2 + 2a(t)f(t)\cos \alpha_R^{(n_{l,3})}(t)}{\left(a(t) + f(t)\cos \alpha_R^{(n_{l,3})}(t)\right) \xi_T^{(n_{l,3})}(t)}. \tag{4.18b}$$

d) In terms of the double-bounced component $DB_{1,1}$ for the first tap resulting from the Tx and Rx spheres, time-varying AAoD ($\alpha_T^{(n_{1,1})}(t)$), EAoD ($\beta_T^{(n_{1,1})}(t)$), AAoA ($\alpha_R^{(n_{1,2})}(t)$), and EAoA ($\beta_R^{(n_{1,2})}(t)$) can be expressed as

$$\alpha_T^{(n_{1,1})}(t) \approx \alpha_T^{(n_{1,1})} \tag{4.19a}$$

$$\beta_T^{(n_{1,1})}(t) \approx \beta_T^{(n_{1,1})} \tag{4.19b}$$

$$\alpha_R^{(n_{1,2})}(t) \approx \beta_R^{(n_{1,2})} \tag{4.19c}$$

$$\beta_R^{(n_{1,2})}(t) \approx \beta_R^{(n_{1,2})}. \tag{4.19d}$$

e) In terms of the double-bounced component $DB_{l,1}$ for other taps resulting from the Tx sphere and elliptic-cylinder, time-varying AAoD ($\alpha_T^{(n_{l,1})}(t)$), EAoD ($\beta_T^{(n_{l,1})}(t)$), AAoA ($\alpha_R^{(n_{l,3})}(t)$), and EAoA ($\beta_R^{(n_{l,3})}(t)$) can be expressed as

$$\alpha_T^{(n_{l,1})}(t) = \alpha_T^{(n_{1,1})}(t) = \alpha_T^{(n_{1,1})} \tag{4.20a}$$

$$\beta_T^{(n_{l,1})}(t) = \beta_T^{(n_{1,1})}(t) = \beta_T^{(n_{1,1})} \tag{4.20b}$$

$$\alpha_R^{(n_{l,3})}(t) = \pi - \arccos \frac{v_R t - \xi_R^{(n_{l,3})} \cos \alpha_R^{(n_{l,3})}}{\sqrt{{\xi_R^{(n_{l,3})}}^2 + (v_R t)^2 - 2\xi_R^{(n_{l,3})} v_R t \cos \alpha_R^{(n_{l,3})}}} \tag{4.20c}$$

$$\beta_R^{(n_{l,3})}(t) = \arctan \frac{\xi_R^{(n_{l,3})} \tan \beta_R^{(n_{l,3})}}{\sqrt{{\xi_R^{(n_{l,3})}}^2 + (v_R t)^2 - 2\xi_R^{(n_{l,3})} v_R t \cos \alpha_R^{(n_{l,3})}}}. \tag{4.20d}$$

f) In terms of the double-bounced component $DB_{l,2}$ for other taps resulting from the elliptic-cylinder and Rx sphere, time-varying AAoD ($\alpha_T^{(n_{l,3})}(t)$), EAoD ($\beta_T^{(n_{l,3})}(t)$), AAoA ($\alpha_R^{(n_{l,2})}(t)$), and EAoA ($\beta_R^{(n_{l,2})}(t)$) can be expressed as

$$\alpha_T^{(n_{l,3})}(t) = \arcsin \frac{b(t)^2 \sin \alpha_R^{(n_{l,3})}(t)}{a(t)^2 + f(t)^2 + 2a(t)f(t) \cos \alpha_R^{(n_{l,3})}(t)} \tag{4.21a}$$

$$\beta_T^{(n_{l,3})}(t) = \arccos \frac{a(t)^2 + f(t)^2 + 2a(t)f(t) \cos \alpha_R^{(n_{l,3})}(t)}{\left(a(t) + f(t) \cos \alpha_R^{(n_{l,3})}(t)\right) \xi_T^{(n_{l,3})}(t)} \tag{4.21b}$$

$$\alpha_R^{(n_{l,2})}(t) = \alpha_R^{(n_{1,2})}(t) = \alpha_R^{(n_{1,2})} \tag{4.21c}$$

$$\beta_R^{(n_{l,2})}(t) = \beta_R^{(n_{1,2})}(t) = \beta_R^{(n_{1,2})}. \tag{4.21d}$$

Again, the two-sphere model describes the moving scatterers around the Tx and Rx, and the elliptic-cylinder model depicts the static roadside scatterers. Therefore, the AoDs and AoAs of LoS component and the two-sphere model including both single- and double-bounced rays are actually time-invariant due to the feature of relative rest. The reason behind is that we assume moving vehicles/scatterers around the Tx and Rx having the same velocity (i.e., both in speed and direction) of the Tx and

Rx, respectively. Therefore, the original fixed parameters can be replaced by these time-varying parameters so that the proposed model is able to capture the channel non-stationarity.

4.3 Local Statistical Properties of the Proposed 3D Wideband non-WSS MIMO V2V Channel Model

4.3.1 Local space-time correlation function

The local correlation properties of two arbitrary CIRs $h_{pq}(t,\tau')$ and $h_{p'q'}(t,\tau')$ of a MIMO V2V channel are completely determined by the correlation properties of $h_{l,pq}(t)$ and $h_{l,p'q'}(t)$ in each tap, so that no correlations exist between the underlying processes in different taps. Therefore, we can restrict our investigations to the following local ST CF:

$$\rho_{h_{l,pq}h_{l,p'q'}}(t,\tau) = \mathbf{E}\left[h_{l,pq}(t)\, h^{*}_{l,p'q'}(t-\tau)\right] \tag{4.22}$$

where $(\cdot)^*$ denotes the complex conjugate operation and $\mathbf{E}[\cdot]$ designates the statistical expectation operator. Since the LoS, single-, and double-bounced components are independent to each other, based on (4.2) we have the following local ST CF for the first tap

$$\rho_{h_{1,pq}h_{1,p'q'}}(t,\tau) = \rho_{h^{LoS}_{1,pq}h^{LoS}_{1,p'q'}}(t,\tau) + \sum_{i=1}^{I} \rho_{h^{SB_i}_{1,pq}h^{SB_i}_{1,p'q'}}(t,\tau) + \rho_{h^{DB}_{1,pq}h^{DB}_{1,p'q'}}(t,\tau)\,. \tag{4.23}$$

Whereas for other taps, according to (4.4) we have the ST CF as

$$\rho_{h_{l,pq}h_{l,p'q'}}(t,\tau) = \rho_{h^{SB_3}_{l,pq}h^{SB_3}_{l,p'q'}}(t,\tau) + \rho_{h^{DB_1}_{l,pq}h^{DB_1}_{l,p'q'}}(t,\tau) + \rho_{h^{DB_2}_{l,pq}h^{DB_2}_{l,p'q'}}(t,\tau)\,. \tag{4.24}$$

Applying the corresponding VMF distribution, trigonometric transformations, and following the similar reasoning in [81], we can obtain the local ST CF of the LoS, single-, and double-bounced components as follows.

(a) In the case of the LoS component,

$$\rho_{h_{1,pq}^{LoS} h_{1,p'q'}^{LoS}}(t,\tau) = K e^{\frac{j2\pi}{\lambda} A^{LoS}} \times e^{j2\pi\tau(f_{T_{max}} \cos\gamma_T - f_{R_{max}} \cos\gamma_R)}. \tag{4.25}$$

where $A^{LoS} = 2D \cos\varphi_R \cos\theta_R$.

(b) In terms of the single-bounced components $SB_{1,i}$ $(i = 1, 2)$ for the first tap resulting from the Tx sphere and Rx sphere, respectively,

$$\rho_{h_{1,pq}^{SB_{1,i}} h_{1,p'q'}^{SB_{1,i}}}(t,\tau) = \eta_{SB_{1,i}} \int_{-\pi}^{\pi}\int_{-\pi}^{\pi} \Big[e^{\frac{j2\pi}{\lambda} A^{(1,i)}} \times e^{j2\pi\tau\left(f_{T_{max}} B^{(1,i)} + f_{R_{max}} C^{(1,i)}\right)} \times f(\alpha_{T/R}^{(1,i)}, \beta_{T/R}^{(1,i)}) \Big] d(\alpha_{T/R}^{(1,i)}, \beta_{T/R}^{(1,i)}) \tag{4.26}$$

with $A^{(1,1)} = \delta_T \big[\sin\beta_T^{(1,1)} \sin\varphi_T + \cos\beta_T^{(1,1)} \cos\varphi_T \cos\left(\theta_T - \alpha_T^{(1,1)}\right) \big] + \frac{\delta_R}{\xi_{n_{1,1}}} \big[R_T \sin\beta_T^{(1,1)} \times \sin\varphi_R - Q_{n_{1,1}} \cos\varphi_R \cos\left(\theta_R - \alpha_R^{(1,1)}\right) \big]$, $B^{(1,i)} = \cos\left(\alpha_T^{(1,i)} - \gamma_T\right) \cos\left(\beta_T^{(1,i)}\right)$, $C^{(1,i)} = \cos\left(\alpha_R^{(1,i)} - \gamma_R\right) \times \cos\left(\beta_R^{(1,i)}\right)$, $A^{(1,2)} = \delta_R \big[\sin\beta_R^{(1,2)} \sin\varphi_R + \cos\beta_R^{(1,2)} \cos\varphi_R \cos\left(\theta_R - \alpha_R^{(1,2)}\right) \big] + \frac{\delta_T}{\xi_{n_{1,2}}} \big[R_R \sin\beta_R^{(1,2)} \times \sin\varphi_T + Q_{n_{1,2}} \cos\varphi_T \cos\left(\theta_T - \alpha_T^{(1,2)}\right) \big]$, where the expressions of $\alpha_R^{(1,i)}$, $\beta_R^{(1,i)}$, $Q_{n_{1,i}}$, $\xi_{n_{1,i}}$, and $\xi_{T(R)}^{n_{1,3}}$ are given in Section II. Note that the subscripts T and R are applied to $i = 1$ and $i = 2$, respectively.

(c) In the case of the single-bounced component $SB_{l,3}$ for the lth tap resulting from the elliptic-cylinder,

$$\rho_{h_{l,pq}^{SB_{l,3}} h_{l,p'q'}^{SB_{l,3}}}(t,\tau) = \eta_{SB_{l,3}} \int_{-\pi}^{\pi}\int_{-\pi}^{\pi} \Big[e^{-\frac{j2\pi}{\lambda} A^{(l,3)}} \cdot e^{j2\pi\tau\left(f_{T_{max}} B^{(l,3)} + f_{R_{max}} C^{(l,3)}\right)} \times f(\alpha_R^{(l,3)}, \beta_R^{(l,3)}) \Big] d(\alpha_R^{(l,3)}, \beta_R^{(l,3)}) \tag{4.27}$$

with $A^{(l,3)} = \frac{\delta_T}{\xi_T^{(n_{l,3})}} \big[\xi_R^{(n_{l,3})} \sin\beta_R^{(l,3)} \sin\varphi_T + Q_{n_{l,3}} \cos\varphi_T \cos\left(\theta_T - \alpha_T^{(l,3)}\right) \big] + \delta_R \big[\sin\beta_R^{(l,3)} \times \sin\varphi_R + \cos\beta_R^{(l,3)} \cos\varphi_R \cos\left(\theta_R - \alpha_R^{(l,3)}\right) \big]$, $B^{(l,3)} = \cos\left(\alpha_T^{(l,3)} - \gamma_T\right) \cos\left(\beta_T^{(l,3)}\right)$, $C^{(l,3)} = \cos\left(\alpha_R^{(l,3)} - \gamma_R\right) \times \cos\left(\beta_R^{(l,3)}\right)$, where the expressions of $\alpha_T^{(l,3)}$, $\beta_T^{(l,3)}$, $Q_{n_{l,3}}$, and $\xi_{T(R)}^{(n_{l,3})}$ are given in Section 4.2.

(d) In terms of the double-bounced component for the first tap resulting from the Tx and Rx spheres,

$$\rho_{h_{1,pq}^{DB}h_{1,p'q'}^{DB}}(t,\tau) = \eta_{DB_{1,1}}\int_{-\pi}^{\pi}\int_{-\pi}^{\pi}\int_{-\pi}^{\pi}\int_{-\pi}^{\pi}\Big[e^{\frac{j2\pi}{\lambda}A^{DB}}\cdot e^{j2\pi\tau\left(f_{T_{max}}B^{DB}+f_{R_{max}}C^{DB}\right)} \times f(\alpha_T^{(1,1)},\beta_T^{(1,1)})\cdot f(\alpha_R^{(1,2)},\beta_R^{(1,2)})\Big]\, d(\alpha_T^{(1,1)},\beta_T^{(1,1)})d(\alpha_R^{(1,2)},\beta_R^{(1,2)}) \quad (4.28)$$

where $A^{DB} = \delta_T\big[\sin\beta_T^{(1,1)}\sin\varphi_T + \cos\beta_T^{(1,1)}\cos\varphi_T\cos\left(\theta_T-\alpha_T^{(1,1)}\right)\big] + \delta_R\big[\sin\beta_R^{(1,2)}\times \sin\varphi_R + \cos\beta_R^{(1,2)}\cos\varphi_R\cos\left(\theta_R-\alpha_R^{(1,2)}\right)\big]$, $B^{DB} = \cos\left(\alpha_T^{(1,1)}-\gamma_T\right)\cos\beta_T^{(1,1)}$, and $C^{DB} = \cos\left(\alpha_R^{(1,2)}-\gamma_R\right)\times\cos\beta_R^{(1,2)}$.

(e) In terms of the double-bounced component $DB_{l,1}$ for other taps resulting from the Tx sphere and elliptic-cylinder,

$$\rho_{h_{l,pq}^{DB_1}h_{l,p'q'}^{DB_1}}(t,\tau) = \eta_{DB_{l,1}}\int_{-\pi}^{\pi}\int_{-\pi}^{\pi}\int_{-\pi}^{\pi}\int_{-\pi}^{\pi}\Big[e^{\frac{j2\pi}{\lambda}A^{DB_{l,1}}}\cdot e^{j2\pi\tau\left(f_{T_{max}}B^{DB_{l,1}}+f_{R_{max}}C^{DB_{l,1}}\right)} \times f(\alpha_T^{(1,1)},\beta_T^{(1,1)})\cdot f(\alpha_R^{(l,3)},\beta_R^{(l,3)})\Big]\, d(\alpha_T^{(1,1)},\beta_T^{(1,1)})d(\alpha_R^{(l,3)},\beta_R^{(l,3)}) \quad (4.29)$$

where $A^{DB_{l,1}} = \delta_T\big[\sin\beta_T^{(1,1)}\sin\varphi_T + \cos\beta_T^{(1,1)}\cos\varphi_T\cos\left(\theta_T-\alpha_T^{(1,1)}\right)\big] + \delta_R\big[\sin\beta_R^{(l,3)}\times \sin\varphi_R + \cos\beta_R^{(l,3)}\cos\varphi_R\cos\left(\theta_R-\alpha_R^{(l,3)}\right)\big]$, $B^{DB_{l,1}} = \cos\left(\alpha_T^{(1,1)}-\gamma_T\right)\cos\beta_T^{(1,1)}$, and $C^{DB_{l,1}} = \cos\left(\alpha_R^{(l,3)}-\gamma_R\right)\times\cos\beta_R^{(l,3)}$.

(f) In terms of the double-bounced component $DB_{l,2}$ for other taps resulting from the elliptic-cylinder and Rx sphere,

$$\rho_{h_{l,pq}^{DB_2}h_{l,p'q'}^{DB_2}}(t,\tau) = \eta_{DB_{l,2}}\int_{-\pi}^{\pi}\int_{-\pi}^{\pi}\int_{-\pi}^{\pi}\int_{-\pi}^{\pi}\Big[e^{\frac{j2\pi}{\lambda}A^{DB_{l,2}}}\cdot e^{j2\pi\tau\left(f_{T_{max}}B^{DB_{l,2}}+f_{R_{max}}C^{DB_{l,2}}\right)} \times f(\alpha_T^{(l,3)},\beta_T^{(l,3)})\cdot f(\alpha_R^{(1,2)},\beta_R^{(1,2)})\Big]\, d(\alpha_T^{(l,3)},\beta_T^{(l,3)})d(\alpha_R^{(1,2)},\beta_R^{(1,2)}) \quad (4.30)$$

where $A^{DB_{l,2}} = \delta_T\big[\sin\beta_T^{(l,3)}\sin\varphi_T + \cos\beta_T^{(l,3)}\cos\varphi_T\cos\left(\theta_T-\alpha_T^{(l,3)}\right)\big] + \delta_R\big[\sin\beta_R^{(1,2)}\times \sin\varphi_R + \cos\beta_R^{(1,2)}\cos\varphi_R\cos\left(\theta_R-\alpha_R^{(1,2)}\right)\big]$, $B^{DB_{l,3}} = \cos\left(\alpha_T^{(l,3)}-\gamma_T\right)\cos\beta_T^{(l,3)}$, and $C^{DB_{l,2}} = \cos\left(\alpha_R^{(1,2)}-\gamma_R\right)\times\cos\beta_R^{(1,2)}$.

Finally, the local ST CF of the CIRs $h_{pq}(t,\tau')$ and $h_{p'q'}(t,\tau')$ can be expressed as:

$$\rho_{h_{pq}h_{p'q'}}(t,\tau) = \sum_{l=1}^{L(t)} c_l^2 \rho_{h_{l,pq}h_{l,p'q'}}(t,\tau). \tag{4.31}$$

4.3.2 Local FCF and PDP

The local FCF $\rho_{H_{pq}H_{p'q'}}(t,\Delta f')$ of the proposed wideband V2V channel model is defined as

$$\rho_{H_{pq}H_{p'q'}}(t,\Delta f') = \mathbf{E}\left[H_{pq}(t,f')\,H_{pq}^{*}(t,f'-\Delta f')\right] \tag{4.32}$$

where, $H_{pq}(t,f')$ denotes the time-variant transfer function, which is the Fourier transform of the CIR $h_{pq}(t,\tau')$ and can be expressed as $H_{pq}(t,f') = \sum_{l=1}^{L(t)} c_l h_{l,pq}(t)\, e^{-j2\pi f'\tau'}$. Therefore, the local FCF can be derived as

$$\rho_{H_{pq}H_{p'q'}}(t,\Delta f') = \sum_{l=1}^{L(t)} c_l^2(t) e^{-j2\pi f'\tau_l'}. \tag{4.33}$$

Applying the inverse Fourier transform to the local FCF $\rho_{H_{pq}H_{p'q'}}(\Delta f')$ in (4.33), we can obtain the corresponding local PDP as

$$S_{H_{pq}H_{p'q'}}(t,\tau') = \sum_{l=1}^{L(t)} c_l^2(t)\delta(\tau'-\tau_l'). \tag{4.34}$$

It is obvious that the local FCF and the local PDP are completely determined by the number of propagation paths $L(t)$ (i.e., clusters or taps), the path gains c_l, and the propagation delays τ_l'. Appropriate values for these parameters can be found in many measurement campaigns for wideband V2V channels, e.g., those in [8], [58], [82]. This allows us to fit the local FCF $\rho_{H_{pq}H_{p'q'}}(t,\Delta f')$ and the corresponding local PDP $S_{H_{pq}H_{p'q'}}(t,\tau')$ of the proposed model to any specified or measured FCF and PDP characterised by the sets $\{c_l\}_{l=1}^{L(t)}$ and $\{\tau_l'\}_{l=1}^{L(t)}$.

4.4 3D Non-WSS Wideband SoS Simulation Model for MIMO V2V Channels

Based on the proposed 3D theoretical RS-GBSM described in Section II, the corresponding SoS simulation model can be further developed by using finite numbers of scatterers or sinusoids $N_{l,1}$, $N_{l,2}$, and $N_{l,3}$. According to (4.1), the SoS simulation model for the link $T_p \to T_q$ can be expressed as

$$\hat{h}_{pq}\left(t,\tau'\right) = \sum_{l=1}^{L(t)} c_l \hat{h}_{l,pq}(t)\delta\left(\tau' - \tau_l'\right) \tag{4.35}$$

where for the first tap and other taps it can be expressed respectively

$$\hat{h}_{1,pq}\left(t\right) = \hat{h}_{1,pq}^{LoS}\left(t\right) + \sum_{i=1}^{I} \hat{h}_{1,pq}^{SB_i}\left(t\right) + \hat{h}_{1,pq}^{DB}\left(t\right) \tag{4.36}$$

$$\hat{h}_{l,pq}\left(t\right) = \hat{h}_{l,pq}^{SB_3}\left(t\right) + \hat{h}_{l,pq}^{DB_1}\left(t\right) + \hat{h}_{l,pq}^{DB_2}\left(t\right). \tag{4.37}$$

Actually, the unknown simulation model parameters to be determined are only the discrete AoDs and AoAs, while the remaining parameters are identical to those of the theoretical model. Therefore, a proper parameter computation method has to apply to obtain these discrete AoDs and AoAs.

4.4.1 MEV for parameterization of the proposed SoS simulation model

VMF distribution is adopted in order to jointly consider the impact of the azimuth and elevation angles on channel statistics. Furthermore, the CDF of α and β, i.e., the double integral of the 3D VMF PDF, denotes the value of volume. The idea of MEV is designed to select the set of $\left\{\alpha^{(n_{1,i})}, \beta^{(n_{1,i})}\right\}_{n_{1,i}=1}^{N_{1,i}}$ in such a manner that the volume of the VMF PDF $f(\alpha,\beta)$ in different ranges of $\left\{\alpha^{(n_{1,i}-1)}, \beta^{(n_{1,i}-1)}\right\} \leqslant \{\alpha,\beta\} <$

TABLE 4.2: Key parameters of different VTD scenarios (wideband).

	K	$k^{(l,1)}$	$k^{(l,2)}$	$k^{(l,3)}$	$\eta_{SB_{1,1}}$	$\eta_{SB_{1,2}}$	$\eta_{SB_{1,3}}$	$\eta_{DB_{1,1}}$	$\eta_{SB_{l,3}}$	$\eta_{DB_{l,1}}$	$\eta_{DB_{l,2}}$
Low VTD	3.786	9.6	3.6	11.5	0.335	0.203	0.411	0.051	0.758	0.121	0.121
High VTD	1.351	0.6	1.3	11.5	0.126	0.126	0.063	0.685	0.088	0.466	0.456

$\left\{\alpha^{(n_{1,i})}, \beta^{(n_{1,i})}\right\}$ are equal to each other with the initial condition, i.e.,

$$\int_{-\pi}^{\alpha^{(1,1)}} \int_{-\pi}^{\beta^{(1,1)}} f(\alpha,\beta) d\alpha d\beta = \frac{1-1/4}{N_{1,i}}. \tag{4.38}$$

The detailed procedure of MEV can be found in [81]. In this chapter, the MEV is also applied to the novel proposed 3D non-WSS wideband V2V simulation model.

4.4.2 Local statistical properties of the proposed SoS simulation model

Based on our 3D MIMO V2V theoretical RS-GBSM and MEV, it is achievable to derive the corresponding statistical properties for the SoS simulation model by applying the discrete angular parameters to (4.2), and (4.4). As the detailed derivations have been explained in Chapter 4.3 for the theoretical model, those of the corresponding simulation model with similar derivations are neglected here.

4.5 Numerical Results and Analysis

4.5.1 Model validation using local stationary time

Stationary Interval (SI) is an important concept for non-WSS channel models. It is the maximum time length within which the correlation of channel coefficients exceeds a pre-defined threshold. In [58], it is defined as Stationarity Region Length (SRL). Please note that our non-WSS model only supports the scenarios 2 and 3 in [58] as the proposed model can only capture the non-stationarity when the Tx and Rx are driving in same direction. Moreover, it is worth mentioning that the measured

scenarios 2 and 3 in [58], i.e., highway and urban, are corresponding to the low VTD and high VTD in our case. To validate the proposed non-WSS models in terms of the derived local statistical properties, the following parameters can be used to match the measurements in [58]. Unless otherwise specified, basic parameters in this section are obtained using $f_c = 5.2$ GHz, $f_{T_{max}} = f_{R_{max}} = 433$ Hz for high VTD, $f_{T_{max}} = f_{R_{max}} = 144$ Hz for low VTD, $D = 300$ m, $a_1 = 160$ m, $a_2 = 180$ m, $R_T = R_R = 10$ m, $\gamma_T = \gamma_R = 0°$, $\varphi_T = \varphi_R = 45°$, $\theta_T = \theta_R = 45°$, $\alpha_{T0}^{(1)} = 21.7°$, $\beta_{T0}^{(1)} = 6.7°$, $\alpha_{R0}^{(2)} = 147.8°$, $\beta_{R0}^{(2)} = 17.2°$, $\alpha_{R0}^{(3)} = 171.6°$, and $\beta_{R0}^{(3)} = 31.6°$. Considering the constraints of the Ricean factor and power-related parameters to fit the measurements in [58], we have $k^{(1,1)} = 9.6$, $k^{(1,2)} = 3.6$, $k^{(1,3)} = 11.5$, $K = 3.786$, $\eta_{SB_{1,1}} = 0.335$, $\eta_{SB_{1,2}} = 0.203$, $\eta_{SB_{1,3}} = 0.411$, and $\eta_{DB_{1,1}} = 0.051$ for tap one low VTD. For tap one high VTD, we have $k^{(1,1)} = 0.6$, $k^{(1,2)} = 1.3$, $k^{(1,3)} = 11.5$, $K = 1.351$, $\eta_{SB_{1,1}} = 0.126$, $\eta_{SB_{1,2}} = 0.126$, $\eta_{SB_{1,3}} = 0.063$, and $\eta_{DB_{1,1}} = 0.685$. For tap two low VTD, we have $k^{(2,1)} = 9.6$, $k^{(2,2)} = 3.6$, $k^{(2,3)} = 11.5$, $\eta_{SB_{2,3}} = 0.758$, and $\eta_{DB_{2,1}} = \eta_{DB_{2,2}} = 0.121$. For tap two high VTD, we have $k^{(2,1)} = 0.6$, $k^{(2,2)} = 1.3$, $k^{(2,3)} = 11.5$, $\eta_{SB_{2,3}} = 0.088$, and $\eta_{DB_{2,1}} = \eta_{DB_{2,2}} = 0.456$. Table 4.2 summarises key parameters adopted by low and high VTD scenarios. The environment-related parameters $k^{(l,1)}$, $k^{(l,2)}$, and $k^{(l,3)}$ are related to the distribution of scatterers (normally, the smaller values of $k^{(l,1)}$ and $k^{(l,2)}$ the denser moving vehicles/scatterers, i.e., the higher VTD). In both high and low VTDs, $k^{(l,3)}$ is large as the scatterers reflected from static roadsides are normally concentrated. Also, Ricean factor K is small in higher VTD, as the LoS component does not have dominant power. The reason is that dense vehicles (i.e., more vehicles/obstacles between the Tx and Rx) on the road result in less likelihood of strong LoS components.

For the SoS simulation model, we must first choose adequate values for the numbers of discrete scatterers $N_{1,1}$, $N_{1,2}$, and $N_{l,3}$. Based on our own simulation experiences and suggested by [47], a reasonable values can be 40, which can be considered as a good trade-off between realisation complexity and accuracy. To simulate rigorous channels, e.g., very high VTD, the number of effective scatterers can be increased to improve the performance of the channel simulator. In addition, when $\beta_T^{(n1)} = \beta_R^{(n2)} = \beta_R^{(n3)} = 0°$, the proposed 3D model will be reduced to a 2D two-ring and multiple ellipses model.

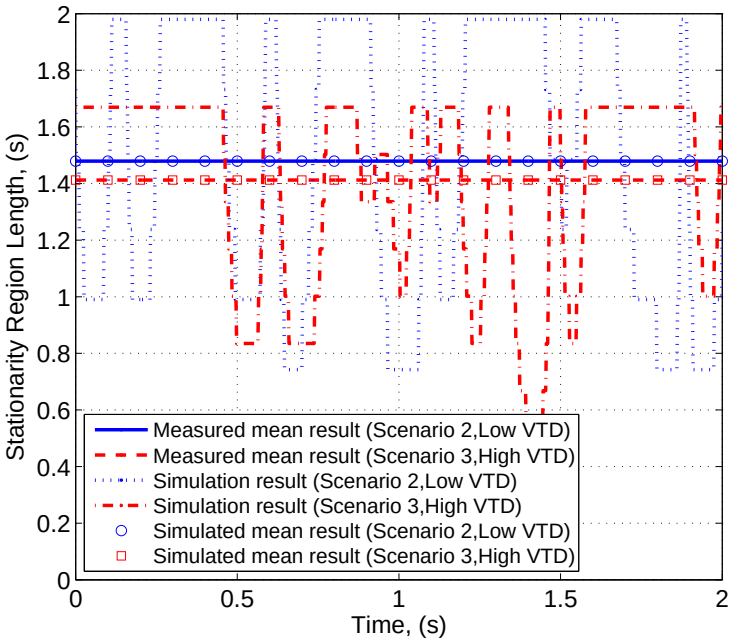

FIGURE 4.5: The SRL of measured results and the simulation results (corresponding to scenarios 2 and 3 in [58].)

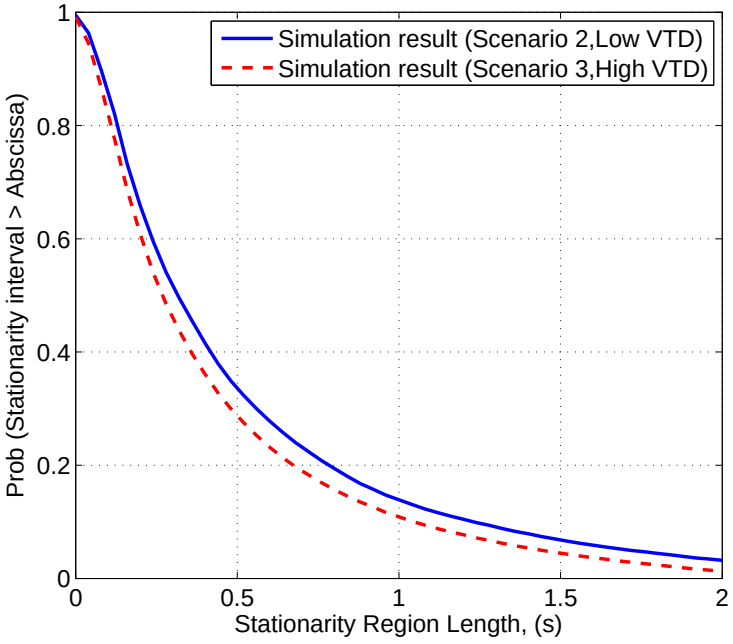

FIGURE 4.6: Simulated CCDF of the stationary interval for different VTDs.

The impact of elevation angle has been evaluated in [81] by comparing between the 3D and 2D models in terms of narrowband statistical properties.

Fig. 4.5 shows the simulation results compared with the measurement results in [58]. As the local SI is time-variant value, by using the proper channel model parameters, the simulation mean result can fit the measured results, i.e., the 1479 ms and 1412 ms

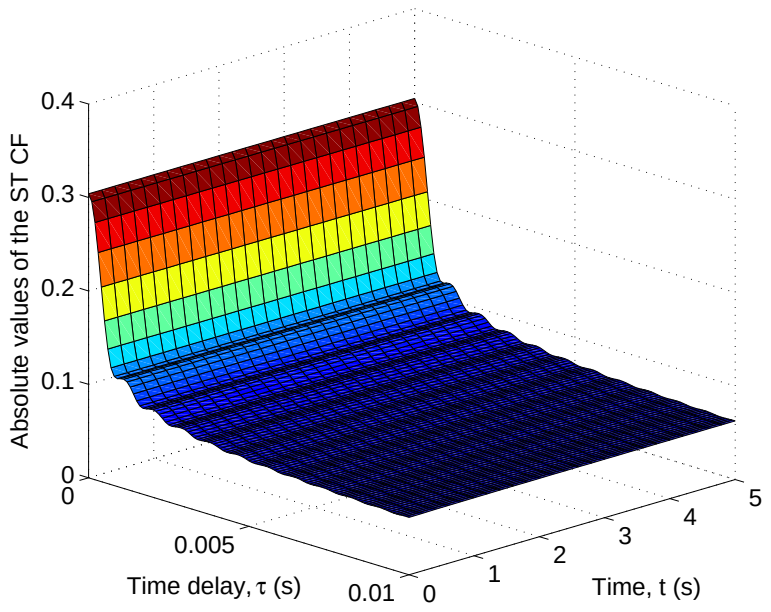

FIGURE 4.7: The absolute value of the local ST CF for the 3D reference model at tap 1 in high VTD scenario ($\delta_T = \delta_R = 3\lambda$, $\beta_{T0}^{(1)} = 6.7°$, $\beta_{R0}^{(2)} = 17.2°$, $\beta_{R0}^{(3)} = 31.6°$).

for scenarios 2 and 3, respectively. Furthermore, the Complementary CDF (CCDF) of the SRL are compared in Fig. 4.6. Observing form Fig. 4.5, the mean value of simulated results can match the measured results very well. Both the measured and simulation results in Fig. 4.5 and Fig. 4.6 demonstrate that low VTD channels have longer SI when the Tx and Rx moving in the same direction. So that the proposed 3D wideband non-WSS V2V channel model has the ability to capture the channel non-stationarity when the Tx and Rx are driving in the same direction.

4.5.2 Local space-time correlation function

Fig. 4.7 depicts the absolute value of 3D local ST CFs when $\delta_T = \delta_R = 3\lambda$ for tap 1 at high VTD. Fig. 4.8 shows the absolute value of the local ST CF for the 3D reference model, simulation model, and simulated result in different VTD scenarios. Observing from Fig. 4.8, the 3D reference model, simulation model, and simulated result of tap 1 at low VTD t =0 s closely match to each other, which indicates the correctness of our derivations. Therefore, we only show the simulation results of the rest curves for clarity purpose. It is obvious that the VTD greatly affects the ST CF at different taps. In low VTD scenario, the local ST CF is always higher than that in

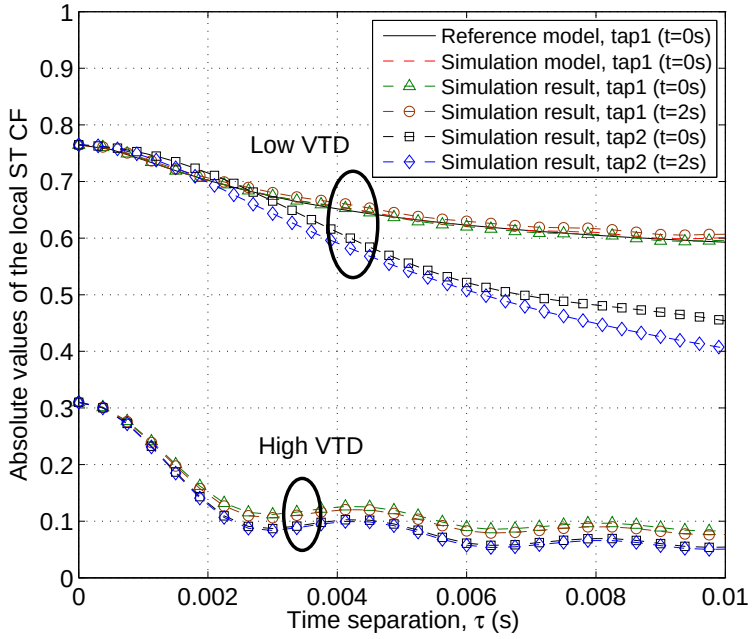

FIGURE 4.8: The absolute value of the local ST CF for the 3D reference model, simulation model, and simulated result in different VTD scenarios ($\delta_T = \delta_R = 3\lambda$, $\beta_{T0}^{(1)} = 6.7°$, $\beta_{R0}^{(2)} = 17.2°$, $\beta_{R0}^{(3)} = 31.6°$).

high VTD scenario. In others words, the local ST CF in high VTD is fading faster than that in low VTD scenario. For further comparison along different time slots, i.e., t =0 s and 2 s, the variations of local ST CFs for low and high VTDs at first tap and second tap are indiscernible due to the assumption of same moving velocities of the Tx and Rx. By considering the theory of relative motion, the state between the Tx and Rx is actually relative stationary. In fact, only the single-bounced component resulting from the elliptic-cylinder model shows the channel non-stationarity on the local ST CF. Because, the elliptic-cylinder model characterises the roadside stationary scatterers. Nevertheless, it is necessary to extend our 3D non-WSS model to support the V2V channel of opposite motion in future work. The challenge in this future work is that three different locations between the Tx and Rx have to be distinguished, i.e., vehicles are approaching, passing, and leaving.

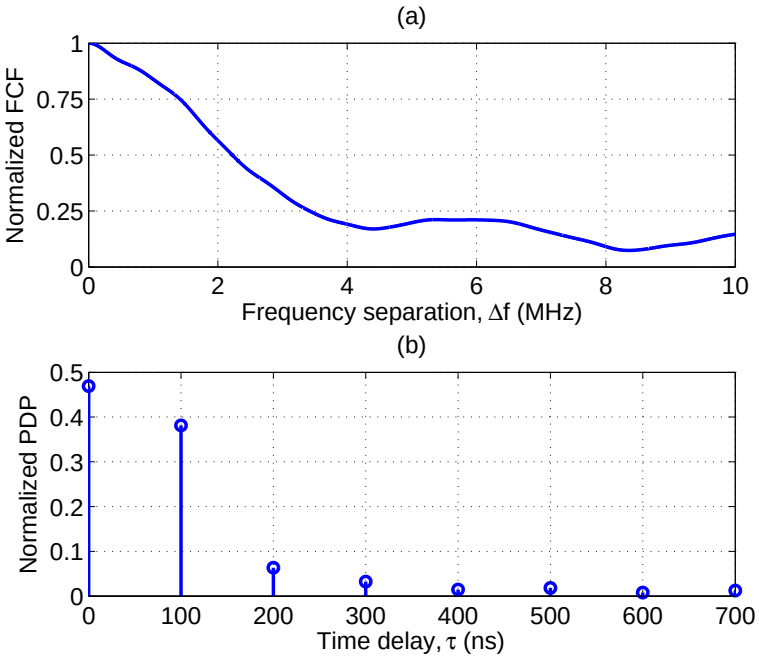

FIGURE 4.9: The absolute value of the FCF (a) and PDP (b) for the 3D V2V channel models.

4.5.3 Local FCF and PDP

Fig. 4.9 (a) and Fig. 4.9 (b) show the local FCF and corresponding PDP of the proposed models, respectively. The results are obtained by using the following parameters reported in [8], i.e., the propagation delays $\{\tau'\}_{l=1}^{8} = \{0, 100, 200, 300, 400, 500, 600, 700\}$ns and the tap powers $\{c_l^2\}_{l=1}^{8} = \{$-10.3, -11.2, -19, -21.9, -25.3, -24.4, -28.0, -26.1$\}$dB when the Tx and Rx are moving in the same direction. Again, it is obvious that the local FCF and the PDP are completely determined by the number of propagation paths L (i.e., taps), the path gains c_l, and the propagation delays τ_l'. Once we have the measured local FCF and PDP at different time slots, we can easily fit the proposed model to measurement data.

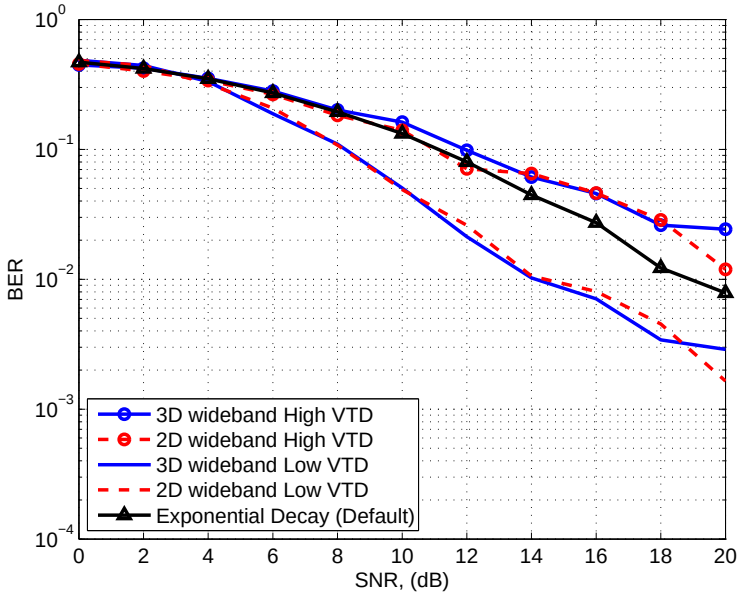

FIGURE 4.10: The BER performance of the IEEE 802.11p system using different channel models

4.6 Test of the Proposed Wideband Models in IEEE 802.11p Systems

To test the proposed V2V channel models, we apply our models to the IEEE 802.11p system [91]. This system simulator is provided by Wireless Communications and Signal Processing Research Centre at Peking University, China. Fig. 4.10 shows the BER performance of the IEEE 802.11p system by considering the different channel models. The same parameters in Table 4.2 are used to distinguish the different VTDs. Again, when the elevation angles are set to be zero, the 3D models are degraded to 2D models. The exponential decay with 7 taps is the default channel model used in the IEEE 802.11p system. In Fig. 4.10, we can observe that from the system's point of view, if the rest parameters are fixed, the BER performance is only determined by VTDs. The BER performance with the low VTD V2V channel models is always better than that with high VTD channel models as illustrated in Fig. 4.10. In the same VTD condition, the difference between the 2D and 3D models is barely discernible in terms of the system BER performance. Due to the system robustness, if the basic configuration of a V2V communication system is fixed, such as total number of transmitted bits, modulation method, Signal-to-Noise Ratio (SNR), etc., the BER

performance is mainly determined by amplitude PDF, i.e, σ_0^2 and Ricean factor K. The results agree with the conclusions in Chapter 3, i.e., the elevation angle has minor impact on the envelope LCR and AFD.

4.7 Summary

In this chapter, we have proposed a non-WSS 3D theoretical RS-GBSM and corresponding SoS simulation model for non-isotropic scattering wideband MIMO V2V Ricean fading channels. The novel parameter computation method, named as MEV, has been used to jointly calculate the azimuth and elevation angles for the simulation model. Based on proposed channel models, important local statistical properties have been derived and thoroughly investigated, i.e., local ST CF, local FCF, and PDP. The proposed 3D reference and simulation models are verified by simulated results indicating the correctness of our derivations and simulations.

In addition, the non-stationarity of the proposed channel models is verified by measurements in terms of local SI. By comparing these results, we can conclude that the VTD has major impact on local statistical properties. The numerical and simulation results have clearly shown that the low VTD condition always results in better channel performance than the high VTD case. Finally, the BER performance of the proposed models is tested by using IEEE 802.11p system. Consequently, the proposed models have the ability to investigate the impact of the VTD on channel statistics and capture the non-stationarity of the V2V channel when the Tx and Rx are moving in the same direction.

Chapter 5

Statistical Properties and Complexity Analysis of IMT-A and LTE-A MIMO Channel Models

5.1 Introduction

MIMO technologies, employing multiple antennas at both the Tx and Rx, can greatly improve the link reliability and increase the overall system capacity [92], [93]. MIMO has widely been used in various advanced wireless communication systems such as the 4G and 5G systems. Realistic MIMO channel models are indispensable [71], [94], [95] for the performance evaluation of candidate technologies for LTE-A and IMT-A systems. This requires a proper balance between the model accuracy and complexity, i.e., it must accurately reflect important statistical properties of real MIMO propagation channels with reasonable computational complexity. Inaccurate or over-simplified channel models may lead to either too optimistic or too pessimistic performance evaluation results of chosen transmission schemes, which may cause wrong decisions on product development or standardisation. On the other hand, too complex channel models may significantly increase the simulation time and reduce the model usability.

Standardised F2M MIMO channel models can roughly be classified into CBSMs, or KBSMs, and GBSMs. A KBSM assumes that channel coefficients are complex Gaussian distributed [48]. It also assumes the separability of the correlations between the Tx and Rx so that the spatial correlation matrix of the MIMO channel can be expressed as the Kronecker product of the Tx and Rx correlation matrices. This assumption implies the independence between AoDs and AoAs, which is unrealistic in certain scenarios such as in pico- and micro-cells. The IEEE 802.11 TGn channel model [15], LTE channel model [16]–[18], and LTE-A channel model [22] all belong to KBSMs. A GBSM characterises the propagation environment using a geometric description. Standardised GBSMs are often characterized by using selected random parameters such as AoD, AoA, and propagation delay. They all adopt the SoS based double directional channel modelling approach. The 3GPP SCM [25], [26], SCME [27], WIM1 [28], WIM2 [29], WIM+ [30], and IMT-A channel model [31], [32] belong to GBSMs.

In the literature, there are only few references comparing GBSMs and KBSMs [20], [21], [96], [97], while [9] is the only paper analysing the ST CFs of the SCM [25] and a typical KBSM [48] in a great detail. However, in [9] some important statistical properties, e.g., the envelope LCR, AFD, PDP, and FCF, were not analysed and compared. Also, the computational complexities of both types of MIMO channel models were not investigated in [9]. The LTE-A [22] and IMT-A [32] channel models represent the latest developments of the standardised KBSM and GBSM, respectively. To the best of our knowledge, no one has studied and compared the accuracy, in terms of channel statistical properties, and computational complexities of both models. The first part of this chapter aims to fill this research gap.

The comparison of the accuracy and computational complexities of the LTE-A and IMT-A MIMO channel models shows that the LTE-A model is highly inaccurate in terms of some important statistical properties despite its simplicity. For example, it only describes the average spatial-temporal statistical properties of MIMO channels and can only support system bandwidths up to 50 MHz, not the claimed 100 MHz. The IMT-A channel model is complex but has much better accuracy. It allows us to

simulate the variations of different MIMO channel realisations and can indeed support system bandwidths up to 100 MHz [10]. Therefore, the second part of this chapter concentrates on studying various complexity reduction methods to simplify the IMT-A channel model, e.g., removing the randomness of some parameters, reducing the number of clusters, removing the correlation of LSPs, and the combination of the above methods. These methods are further developments of the approximation methods for GBSMs suggested in [50], [65], [98]. The resulting models are named as the simplified IMT-A channel models. We will use the number of ROs [97] and channel coefficient computing time as the complexity metrics to compare the simplified models with the original one. For the accuracy metrics, we will use important channel statistical properties and system throughput of a system-level LTE simulator. It can be shown that the proposed complexity reduction methods do not degrade much the accuracy of the standardised IMT-A MIMO channel model, while can significantly reduce the complexity in terms of the number of ROs and the channel coefficient computing time.

The major contributions and novelties of this chapter are summarised as follows:

1. We derive and compare theoretical expressions of the statistical properties of the IMT-A and LTE-A channel models, such as the spatial CCF, temporal ACF, amplitude PDF, envelope LCR/AFD, PDP, and FCF.

2. The theoretical derivation results are verified by corresponding simulation results. The inaccuracy problems of the LTE-A model were discussed.

3. The computational complexities of both channel models, in terms of the required numbers of ROs to generate channel coefficients, are thoroughly investigated.

4. To simplify the IMT-A channel model, several complexity reduction methods are proposed, which are shown to be effective in achieving a better trade-off between the model accuracy and complexity.

The rest of this chapter is organised as follows. In Section 5.2, the statistical properties of the IMT-A and LTE-A channel models are fully investigated and compared.

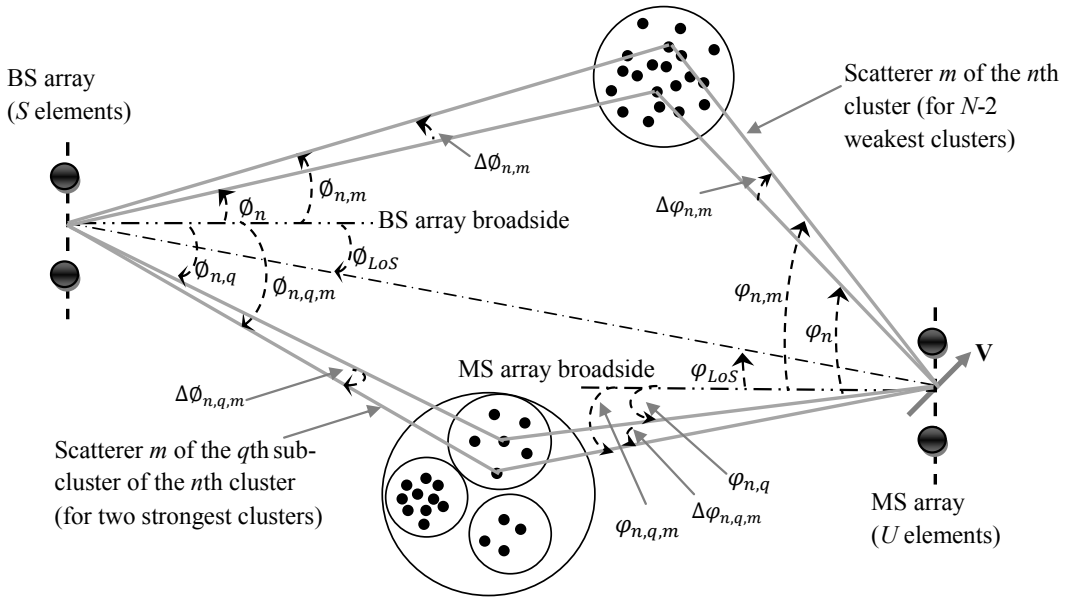

FIGURE 5.1: The BS and MS angular parameters in the IMT-A channel model.

The complexity comparison of the IMT-A and LTE-A channel models is made in Section 5.3. Various complexity reduction methods are studied for the IMT-A channel model in Section 5.4. Finally, conclusions are drawn in Section 5.5.

5.2 Statistical Properties of the IMT-A and LTE-A Channel Models

In this chapter, the BS and MS are used to refer to the eNode B (eNB) and UE in [22], respectively. Considering a downlink transmission system with an S element linear BS array and a U element linear MS array, we will derive and compare some important statistical properties of the IMT-A [32] and LTE-A [22] MIMO channel models, including spatial CCF, temporal ACF, envelope LCR, AFD, PDP, and FCF.

5.2.1 Statistical properties of the IMT-A MIMO channel model

Fig. 5.1 illustrates the spatial angles, defined in a similar way to those as defined in the 3GPP SCM [9]. However, in the IMT-A channel model, the clusters with the total cluster number N are further classified into two strongest clusters ($n = 1, 2$) and $N - 2$ weakest clusters ($n = 3, 4, \ldots, N$). A strongest cluster still contains $M = 20$ sub-paths but is subdivided into 3 sub-clusters, each of which contains M_q ($q = 1, 2, 3$) sub-paths. For clarity purposes, in the following we will focus on describing the angle definitions and deriving statistical properties for weakest clusters ($n = 3, 4, \ldots, N$). These can be easily applied to strongest clusters ($n = 1, 2$) by replacing the number of clusters M by M_q ($M_1 = 10, M_2 = 6, M_3 = 4$) (see Table A1-6 on Page 39 in [32]) and/or the subscript (n) by (n, q).

For the nth ($n = 3, 4, \ldots, N$) weakest cluster, the AoA is expressed by [32]

$$\varphi_{n,m} = \varphi_n + \Delta\varphi_{n,m} = [\varphi_{LoS} + (X_n \varphi_n{}' + Y_n)] + c_{AoA}\alpha_m \tag{5.1}$$

where $\varphi_n = \varphi_{LoS} + X_n\varphi_n{}' + Y_n$ and $\Delta\varphi_{n,m} = c_{AoA}\alpha_m$ denote the mean AoA and AoA offset, respectively. In (1), φ_{LoS} is the LoS AoA direction with respect to the broadside of the MS array, X_n is a RV with uniform distribution to the discrete set of {1, -1}, $Y_n \sim N(0, \sigma_\varphi/7)$ is a Gaussian distributed RV with σ_φ denoting the standard deviation of the AoA spread as defined in Table A1-7 on in [32], c_{AoA} is the cluster-wise Root Mean Square (RMS) azimuth spread of arrival angles (cluster ASA) given in Table A1-7 in [32], α_m is the ray offset angles of the m ($m = 1, 2, ..., M$) subpaths given in Table A1-5 in [32], and

$$\varphi_n{}' = \frac{2\sigma_{AoA}\sqrt{-\ln\left(\frac{P_n}{\max\{P_n\}}\right)}}{C} \tag{5.2}$$

$$\varphi_n{}' = \frac{\sigma_{\varphi_n} - \ln\left(\frac{P_n}{\max\{P_n\}}\right)}{C} \tag{5.3}$$

for the wrapped Gaussian PAS and Laplacian PAS, respectively [32]. Here, P_n is the power of the nth cluster/path that consists of M sub-paths (irresolvable rays) with the same delay τ_n, C is a tabulated scaling factor, and $\sigma_{AoA} = \sigma_{\varphi_n}/\sqrt{2}$ is the

standard deviation of the AoA. The angle definitions related to the AoD are similar to the above definitions for the AoA, e.g., $\phi_{n,m} = \phi_n + \Delta\phi_{n,m}$, where ϕ_n and $\Delta\phi_{n,m}$ denote the mean AoD and AoD offset, respectively.

Note that the AoA $\varphi_{n,m}$ and AoD $\phi_{n,m}$ are determined by several parameters, each of which can be either a constant or a RV. Different from [9], we redefine and distinguish between two simulation levels, namely, link level and system level. At the link level, the cell layout, BS and MS locations, and cluster positions are fixed, while only the scatterer positions within a cluster are random. This means that the mean AoA φ_n and mean AoD ϕ_n are kept constant, while the AoA offsets $\Delta\varphi_{n,m}$ and AoD offsets $\Delta\phi_{n,m}$ are RVs. At the system level, the BS/MS locations and cluster/scatterer positions are all considered as random, indicating that φ_n, $\Delta\varphi_{n,m}$, ϕ_n, and $\Delta\phi_{n,m}$ are all RVs.

Without considering the antenna polarisation, the channel coefficients from the Tx antenna element s ($s = 1, 2, \ldots, S$) to Rx antenna element u ($u = 1, 2, \ldots, U$) for the cluster n can be expressed as [32]

$$h_{u,s,n}(t) = \sqrt{\frac{P_n}{M}} \sum_{m=1}^{M} e^{jd_s k \sin(\phi_{n,m})} e^{jd_u k \sin(\varphi_{n,m})} e^{j2\pi v_{n,m} t} e^{j\Phi_{n,m}}. \tag{5.4}$$

Here, $h_{u,s,n}(t)$ denotes a narrowband process, $k = 2\pi/\lambda$ is the wave number with λ denoting the carrier wavelength, and the Doppler frequency is $v_{n,m} = \lambda^{-1} \|\mathbf{v}\| \cos(\varphi_{n,m} - \theta_v)$, where θ_v is the MS direction of travel and $\|\mathbf{v}\|$ is the magnitude of the MS velocity. The random phases $\Phi_{n,m}$ are uniformly distributed within $[-\pi, \pi)$.

5.2.1.1 Space-time correlation function

The normalised ST CF $\rho^{s_1 u_1}_{s_2 u_2}(\Delta d_s, \Delta d_u, \tau')$ between two arbitrary channel coefficients connecting two different sets of antenna elements ($s_1 \to u_1$ and $s_2 \to u_2$) is defined as [9]

$$\rho^{s_1 u_1}_{s_2 u_2}(\Delta d_s, \Delta d_u, \tau') = \mathrm{E}\left\{ \frac{h_{u_1,s_1,n}(t) h^*_{u_2,s_2,n}(t - \tau')}{\sigma_{h_{u_1,s_1,n}} \sigma_{h_{u_2,s_2,n}}} \right\} \tag{5.5}$$

where $\Delta d_s = d_{s_1} - d_{s_2}$ is the distance between antenna elements s_1 and s_2 at the BS, $\Delta d_u = d_{u_1} - d_{u_2}$ is the distance between antenna elements u_1 and u_2 at the MS, τ' is the time difference, $\mathrm{E}\{\cdot\}$ denotes the assemble average, $h^*_{u_2,s_2,n}(t)$ is the complex conjugate of $h_{u_2,s_2,n}(t)$, and $\sigma_{h_{u_i,s_i,n}} = \sqrt{P_n}$ is the standard deviation of $h_{u_i,s_i,n}(t)$ $(i = 1, 2)$. Substituting (5.4) into (5.5) results in

$$\rho^{s_1u_1}_{s_2u_2}(\Delta d_s, \Delta d_u, \tau') = \frac{1}{M}\sum_{m=1}^{M} \mathrm{E}\{e^{jk\|\mathbf{v}\|\cos(\varphi_{n,m}-\theta_v)\tau'} e^{jk[\Delta d_s \sin(\phi_{n,m})+\Delta d_u \sin(\varphi_{n,m})]}\}. \quad (5.6)$$

By imposing $\tau' = 0$ in (5.6), we can get the spatial CCF $\rho^{s_1u_1}_{s_2u_2}(\Delta d_s, \Delta d_u)$ between two arbitrary channel coefficients at the same time instant

$$\rho^{s_1u_1}_{s_2u_2}(\Delta d_s, \Delta d_u) = \frac{1}{M}\sum_{m=1}^{M} \mathrm{E}\{e^{jk[\Delta d_s \sin(\phi_{n,m})+\Delta d_u \sin(\varphi_{n,m})]}\}. \quad (5.7)$$

By imposing $\Delta d_s = 0$, we can obtain the spatial CCF observed at the MS

$$\rho^{MS}_{u_1u_2}(\Delta d_u) = \frac{1}{M}\sum_{m=1}^{M} \mathrm{E}\{e^{jk\Delta d_u \sin(\varphi_{n,m})}\}. \quad (5.8)$$

Similarly, substituting $\Delta d_u = 0$ into (5.7) results in the spatial CCF observed at the BS

$$\rho^{BS}_{s_1s_2}(\Delta d_s) = \frac{1}{M}\sum_{m=1}^{M} \mathrm{E}\{e^{jk\Delta d_s \sin(\phi_{n,m})}\}. \quad (5.9)$$

It is clear that for the IMT-A channel model the spatial separability $\rho^{s_1u_1}_{s_2u_2} = \rho^{BS}_{s_1s_2}\rho^{MS}_{u_1u_2}$ does not always hold that is different from the LTE-A channel model as shown later.

In case the number of sub-paths in IMT-A channel model tends to infinity, i.e., $M \to \infty$, the spatial CCF in (5.6) can be expressed as

$$\lim_{M\to\infty} \rho^{s_1u_1}_{s_2u_2}(\Delta d_s, \Delta d_u) = \int_0^{2\pi}\int_0^{2\pi} p_{us}(\phi_{n,m}, \varphi_{n,m}) e^{jk\Delta d_s \sin(\phi_{n,m})} e^{jk\Delta d_u \sin(\varphi_{n,m})} d\phi_{n,m} d\varphi_{n,m}, \quad (5.10)$$

where $p_{us}(\phi_{n,m}, \varphi_{n,m})$ represents the joint PDF of the AoD and AoA.

By substituting $\Delta d_s = 0$ in (5.10), we have

$$\lim_{M\to\infty} \rho^{MS}_{u_1 u_2}(\Delta d_u) = \int_0^{2\pi} e^{jk\Delta d_u \sin(\varphi_{n,m})} p_u(\varphi_{n,m}) d\varphi_{n,m}, \tag{5.11}$$

where $p_u(\varphi_{n,m})$ denotes the PDF of AoA.

Imposing $\Delta d_u = 0$ in (5.10) results in

$$\lim_{M\to\infty} \rho^{BS}_{s_1 s_2}(\Delta d_s) = \int_0^{2\pi} e^{jk\Delta d_s \sin(\phi_{n,m})} p_s(\phi_{n,m}) d\phi_{n,m}, \tag{5.12}$$

where $p_s(\phi_{n,m})$ stands for the PDF of the AoD.

By substituting $\Delta d_s = 0$ and $\Delta d_u = 0$ into (5.6), we can obtain the temporal ACF as

$$r(\tau') = \frac{1}{M} \sum_{m=1}^{M} \mathrm{E}\{e^{jk\|\mathbf{v}\| \cos(\varphi_{n,m} - \theta_v)\tau'}\}. \tag{5.13}$$

Again, for the IMT-A channel model, the spatial-temporal separability, i.e., $\rho^{s_1 u_1}_{s_2 u_2}(\Delta d_s, \Delta d_u, \tau') = \rho^{s_1 u_1}_{s_2 u_2}(\Delta d_s, \Delta d_u) r(\tau')$, is not necessarily fulfilled.

5.2.1.2 Envelope LCR and AFD

The amplitude process $R(t)$ is obtained by taking the absolute value of the complex process $h_{u,s,n}(t)$, i.e., $R(t) = |h_{u,s,n}(t)|$. It can be shown that the envelope LCR can be expressed by [10], [99]

$$N_R(r_E) = 4\pi p_R(r_E) \int_0^{\infty} \int_0^{\infty} [\prod_{m=1}^{M} J_0(4\pi^2 |c_m f_m| x)] J_0(2\pi xy) xy^2 dx dy \tag{5.14}$$

where r_E denotes the envelope level, $c_m = \sqrt{\frac{P_n}{m}}$, $f_m = v_{n,m}$, and $J_0(\cdot)$ is the zeroth order Bessel function of the first kind. Following the similar derivation procedure to

that in [78], [99], [100], the amplitude PDF $p_R(z)$ can be expressed as

$$p_R(z) = 4\pi^2 z \int_0^\infty [\prod_{m=1}^{M} J_0(2\pi c_m y)] J_0(2\pi z y) y dy, z \geq 0. \tag{5.15}$$

If M is sufficiently large, e.g., $M \geq 10$, the LCR in (5.14) can be approximated by [10], [99]

$$N_R(r_E) \approx \sqrt{\pi \sum_{m=1}^{M} (c_m f_m)^2} \cdot p_R(r_E). \tag{5.16}$$

The AFD is defined as $T_R(r_E) = \frac{P_R(r_E)}{N_R(r_E)}$, where $P_R(r_E)$ is the CDF of the amplitude process $R(t)$, i.e., $P_R(r_E) = \int_0^{r_E} p_R(z)dz$, where $p_R(z)$ defined in (5.15). The resulted CDF $P_R(r_E)$ can be expressed by $P_R(r_E) = 4\pi^2 r_E \int_0^\infty [\prod_{m=1}^{M} J_0(2\pi c_m y)] J_1(2\pi r_E y) y dy$ [99], where $J_1(\cdot)$ is the first-order Bessel function of the first kind.

5.2.2 Statistical properties of the LTE-A MIMO channel model

5.2.2.1 Space-time correlation function

The complex spatial CCF at the MS is given by the inverse Fourier transform of the PAS $p_u(\widehat{\varphi}_{AoA})$ of the absolute AoA $\widehat{\varphi}_{AoA}$ [9], i.e.,

$$\widehat{\rho}^{MS}_{u_1 u_2}(\Delta d_u) = \int_0^{2\pi} e^{jk\Delta d_u \sin(\widehat{\varphi}_{AoA})} p_u(\widehat{\varphi}_{AoA}) d\widehat{\varphi}_{AoA}. \tag{5.17}$$

Similarly, the complex spatial CCF at the BS is given by [9]

$$\widehat{\rho}^{BS}_{s_1 s_2}(\Delta d_s) = \int_0^{2\pi} e^{jk\Delta d_s \sin(\widehat{\phi}_{AoD})} p_s(\widehat{\phi}_{AoD}) d\widehat{\phi}_{AoD} \tag{5.18}$$

where $\widehat{\phi}_{AoD}$ is the AoD and $p_s(\widehat{\phi}_{AoD})$ denotes the PAS of the absolute AoD. The spatial CCF $\widehat{\rho}^{s_1 u_1}_{s_2 u_2}(\Delta d_s, \Delta d_u)$ between two arbitrary transmission coefficients is the product of the spatial CCF $\widehat{\rho}^{BS}_{s_1 s_2}(\Delta d_s)$ at the BS and the spatial CCF at the MS $\widehat{\rho}^{MS}_{u_1 u_2}(\Delta d_u)$ [9], i.e., $\widehat{\rho}^{s_1 u_1}_{s_2 u_2}(\Delta d_s, \Delta d_u) = \widehat{\rho}^{BS}_{s_1 s_2}(\Delta d_s)\widehat{\rho}^{MS}_{u_1 u_2}(\Delta d_u)$, which implies the spatial separability of the LTE-A channel model.

The temporal ACF is given by

$$\widehat{r}(\tau') = J_0(2\pi \left\|\mathbf{v}\right\| \tau'/\lambda). \tag{5.19}$$

Because of the spatial-temporal separability feature, the ST CF of the LTE-A channel model can be expressed as the product of the spatial CCF and the temporal ACF, i.e., $\widehat{\rho}^{s_1u_1}_{s_2u_2}(\Delta d_s, \Delta d_u, \tau') = \widehat{\rho}^{s_1u_1}_{s_2u_2}(\Delta d_s, \Delta d_u)\widehat{r}(\tau')$.

5.2.2.2 Envelope LCR and AFD

The theoretical LCR for the LTE-A channel model follows the LCR for a Rayleigh model given by [2]

$$\widehat{N}_R(r) = \sqrt{2\pi} f_{max} r e^{-r^2} \tag{5.20}$$

where $r = r_E/\sqrt{2\sigma^2}$ is the normalised envelope level with $2\sigma^2 = P_n$ denoting the total power [2] and $f_{max} = \left\|\mathbf{v}\right\|/\lambda$ is the maximum Doppler shift. The AFD is given by [2]

$$\widehat{T}_R(r) = \frac{e^{r^2} - 1}{\sqrt{2\pi} f_{max} r}. \tag{5.21}$$

5.2.2.3 PDP and FCF

For TDL models, let us denote L, τ_l, and c_l^2 as the number of taps, tap delay, and numerical power of the lth ($l = 1, \ldots, L$) path, respectively. The normalised PDP can be expressed as $\widehat{R}_\tau(\tau) = \frac{1}{X_p}\sum_{l=0}^{L-1} c_l^2 \delta(\tau - \tau_l)$, where $X_p = \sum_{l=0}^{L-1} c_l^2$ is the total power of all taps, τ denotes the delay, and $\delta(\cdot)$ denotes a Delta function. The normalised FCF $\widehat{\Psi}_T(\Delta f)$ can be easily obtained by applying the Fourier transformation on the normalised PDP $\widehat{R}_\tau(\tau)$. The resulted normalized FCF can be expressed as

$$\widehat{\Psi}_T(\Delta f) = \frac{1}{X_p}\sum_{l=0}^{L-1} c_l^2 \cdot e^{-j2\pi\Delta f \tau_l} \tag{5.22}$$

where Δf denotes the frequency spacing. It is clear that $\widehat{\Psi}_T(\Delta f)$ is periodic with the period $\Upsilon = \frac{1}{\gcd\{\tau_0, \tau_1, \cdots, \tau_{L-1}\}}$, where $\gcd\{\cdot\}$ denotes the greatest common divisor.

Therefore, we can write $\widehat{\Psi}_T(\Delta f) = \widehat{\Psi}_T(\Delta f + \widehat{k} \cdot \Upsilon)$, where $\widehat{k}$ is an integer. Note that $\Upsilon \to \infty$ as $\gcd\{\tau_0, \tau_1, \cdots, \tau_{L-1}\} \to 0$. Based on the fact that the FCF exhibits the Hermitian symmetry property, i.e., $\widehat{\Psi}_T(\Delta f) = \widehat{\Psi}_T^*(-\Delta f)$, it can be concluded that $\widehat{\Psi}_T(\Delta f) = \widehat{\Psi}_T^*(\widehat{k} \cdot \Upsilon - \Delta f)$ and $\widehat{\Psi}_T((2\widehat{k}+1)/2 \cdot \Upsilon - \Delta f) = \widehat{\Psi}_T^*((2\widehat{m}+1)/2 \cdot \Upsilon + \Delta f)$, where $\widehat{m}$ is also an integer. Therefore, the real and imaginary parts of the FCF are even and odd functions, respectively, and the FCF is Hermitian symmetric with respect to a half of the period $\Delta f = \Upsilon/2$. Consequently, the complete information on the FCF is contained in a half of the period of the FCF. Finally, since $\widehat{R}_\tau(\tau) = 0$ for $\tau < 0$, the real and imaginary parts of $\widehat{\Psi}_T(\Delta f)$ are related to each other by the Hilbert transform $\mathrm{Re}\{\widehat{\Psi}_T(\Delta f)\} = \mathbf{H}\{\mathrm{Im}\{\widehat{\Psi}_T(\Delta f)\}\}$, where $\mathrm{Re}\{\cdot\}$, $\mathrm{Im}\{\cdot\}$, and $\mathbf{H}\{\cdot\}$ denote the real part, imaginary part, and Hilbert transform, respectively.

5.2.3 Comparison and verification results

5.2.3.1 Spatial CCFs

The spatial CCFs of the IMT-A and LTE-A channel models are investigated at two levels, namely, link level and system level. In Fig. 5.2, using the NLoS UMi scenario with cluster ASA c_{AoA}= 22° and cluster-wise RMS azimuth spread of departure angles (cluster ASD) c_{AoD} = 10°, we show the absolute values of the link-level and system-level spatial CCFs at the MS and between two arbitrary channel coefficients versus the normalised MS antenna spacing $\Delta d_u/\lambda$ for both IMT-A and LTE-A channel models. For calculating link-level spatial CCFs, the mean AoA φ_n and mean AoD ϕ_n are kept constant and they were set as 60° for both channel models. For calculating system-level spatial CCFs, both channel models used the same mean AoA/AoD, following wrapped Gaussian distributions. Fig. 5.2 clearly shows that at the system level both channel models have very closely matched spatial CCFs, i.e., $\rho_{u_1u_2}^{MS}(\Delta d_u) = \widehat{\rho}_{u_1u_2}^{MS}(\Delta d_u)$ and $\rho_{s_2u_2}^{s_1u_1}(\Delta d_s, \Delta d_u) = \widehat{\rho}_{s_2u_2}^{s_1u_1}(\Delta d_s, \Delta d_u)$, demonstrating that IMT-A channel model tends to be spatially separable at the system level. However, at the link level, the IMT-A channel model experiences different behavior from the LTE-A model using the same parameters since the spatial separability is not fulfilled for the IMT-A model.

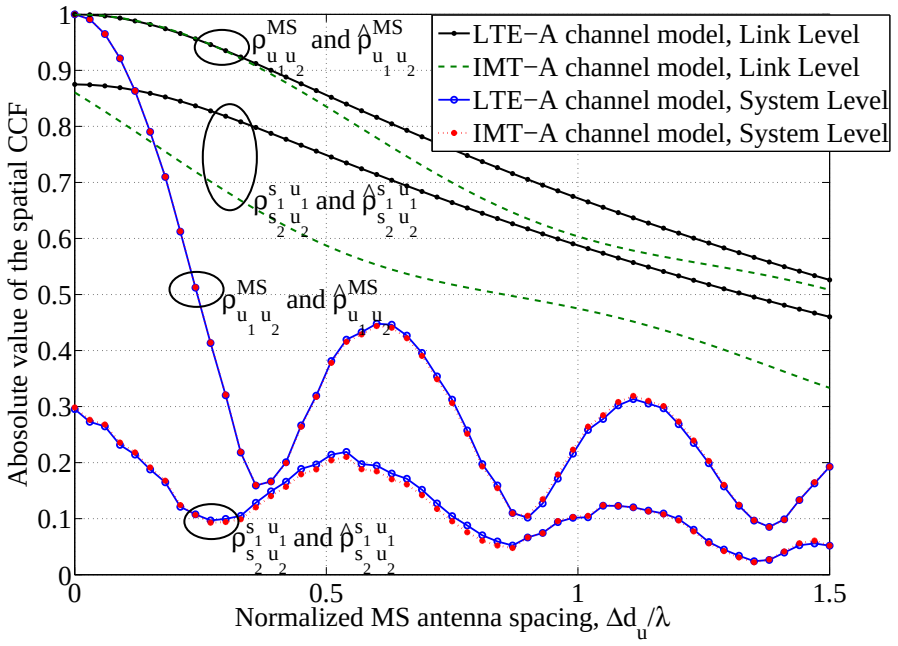

FIGURE 5.2: The absolute values of the spatial CCFs of the IMT-A and LTE-A channel models at the link and system levels.
(NLoS UMi scenario, Cluster ASD = 10°, Cluster ASA = 22°, $\Delta d_s/\lambda = 1$)

5.2.3.2 Temporal ACFs

Fig. 5.3 shows the absolute values of the temporal ACFs of the LTE-A and IMT-A channel models at both link and system levels. We still use the NLoS UMi scenario, while the MS speed was chosen as 1 m/s and MS direction $\theta_v = 60°$. The ACF for the LTE-A channel model keeps the same at both levels. Both models tend to have identical ACFs at the system level using the same parameters while the IMT-A channel model exhibits different behavior at the link level. Similar to the conclusions in [9], the LTE-A channel model actually only models the average behavior of MIMO channels, while the IMT-A channel model provides us with more details regarding the variations across different realisations of MIMO channels.

Note that we have obtained simulation results for all the theoretical results shown in Fig. 5.2 and Fig. 5.3, and they match very well, indicating the correctness of both theoretical derivations and simulations. For presentation clarity purposes, simulation results are not shown in Fig. 5.2 and Fig. 5.3.

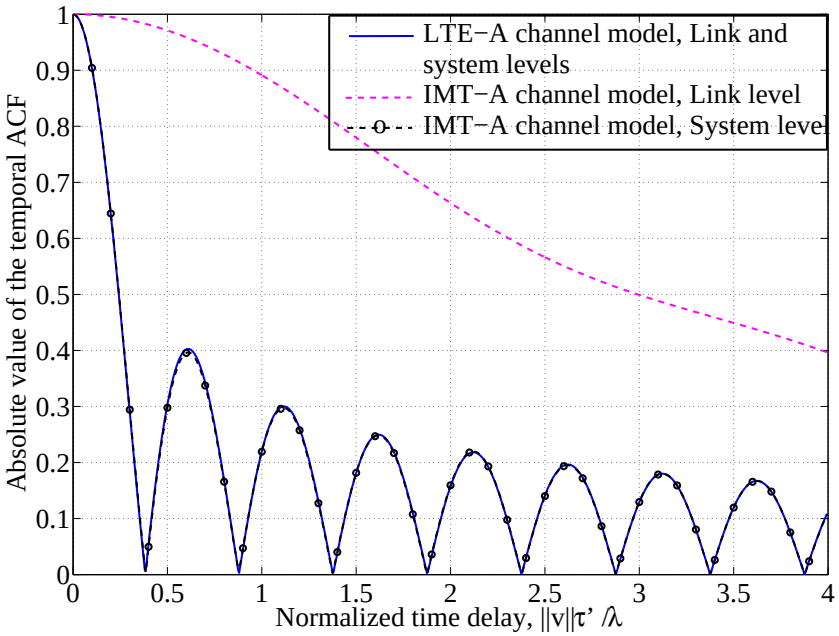

FIGURE 5.3: The absolute values of the temporal ACFs of the LTE-A and IMT-A channel models at the link and system levels ($P_n = 2\sigma^2 = 1, \theta_v = 60°$)

5.2.3.3 Envelope LCRs

As indicated by (5.14) and (5.20), the expressions of envelope LCRs have no difference between the link level and system level simulations. In other words, it presents the deterministic feature on this property. Fig. 5.4 shows the theoretical normalised envelope LCRs for the LTE-A and IMT-A channel models against the corresponding simulation results. The simulation results closely match the corresponding theoretical results. This verifies the correctness of both theoretical derivations and simulations.

5.2.3.4 PDPs and FCFs

Fig. 5.5 illustrates the normalised FCFs of the LTE-A channel model for the EPA scenario [22] and the IMT-A channel model for the NLoS UMi scenario. It is clear that the FCF of the IMT-A channel model has the period of 200 MHz and is symmetrical with respect to 100 MHz. This means that the IMT-A channel model can indeed support system bandwidths up to 100 MHz. For the LTE-A channel model, the FCF has the period of 100 MHz and is symmetrical with respect to 50 MHz, implying that the complete information of the FCF is contained within 50 MHz. This shows that

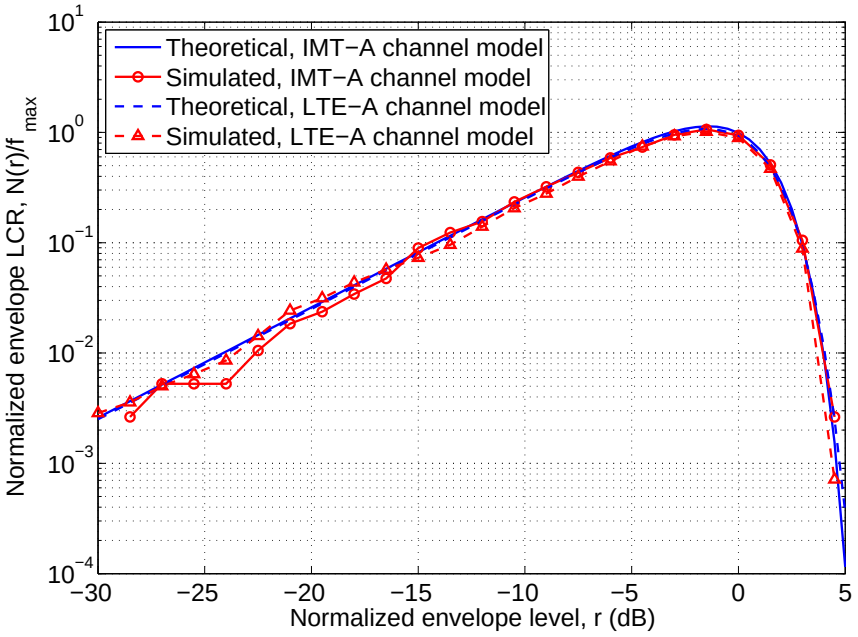

FIGURE 5.4: The normalized envelope LCRs for the LTE-A and IMT-A channel models ($P_n = 2\sigma^2 = 1, M = 20$).

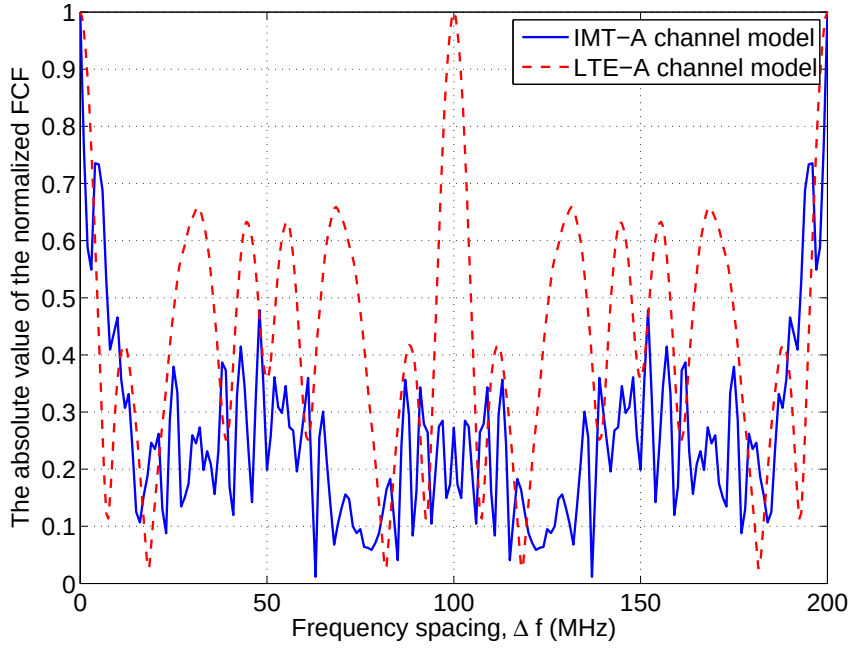

FIGURE 5.5: The normalized FCFs of the LTE-A channel model (NLoS EPA scenario) and the IMT-A channel model (NLoS UMi scenario).

the LTE-A channel model can only support system bandwidths up to 50 MHz, rather than the claimed 100 MHz.

TABLE 5.1: Required number of ROs for several mathematical operations.

Operation	Required ROs
Exponential (e^x)	15
Uniform distributed RV	5
Gaussian distributed RV	72
Complex multiplication	6
Complex division	11
Complex addition	2
Complex norm	5
Sin(x)	7
Look up table	1
Log(x)	1

5.3 Computational Complexities of the IMT-A and LTE-A Channel Models

Computational complexity of channel models has become an important issue due to the increasing requirements of wireless communication systems, e.g., numbers of antennas/users and advanced network topologies. In this section, a thorough investigation about the IMT-A and LTE-A channel models will be performed considering the number of ROs as the complexity metric. The number of ROs of any mathematical operations is based on four basic operations, i.e., real multiplication, real division, real addition, and look up table, each requiring one RO. All the complex operations and other functions are transformed to or approximated by these four basic operations. Table 5.1 shows the required numbers of ROs for some mathematical operations similar to those proposed in [97], where the computational complexity of WIM2 and KBSM were compared.

5.3.1 Computational complexity of the IMT-A channel model

We will formulate mathematically the number of ROs of generating a time sample of channel coefficients in the IMT-A channel model, following the generation procedure in [32]. The total required number of ROs for the IMT-A channel model should

be obtained by multiplying the above RO number (for a sample) by the number of generated time samples.

5.3.1.1 Generation of correlated LSPs

The five LSPs, namely, DS, AS of Arrival (ASA), AS of Departure (ASD), Shadow Fading (SF), and Ricean K-factor are log-normal distributed in the IMT-A channel model. Generation of the Z=5 correlated LSPs follows the procedure described in [29]. First, the cross-correlation between the LSPs is generated independently by linear transformation, i.e., $\tilde{S}_{Z\times 1} = \sqrt{C_{Z\times Z}}\xi_{Z\times 1}$ where $C_{Z\times Z}$ is the correlation matrix, $\xi_{Z\times 1}$ is a vector of Z independent zero-mean Gaussian RVs, while $\tilde{S}_{Z\times 1} = [\tilde{S}_{DS}, \tilde{S}_{ASA}, \tilde{S}_{ASD}, \tilde{S}_{SF}, \tilde{S}_K]^T$. The elements of $C_{Z\times Z}$ are defined in Table A1-7 in [32].

From Table 5.1, generating a Gaussian RV requires 72 ROs. Therefore, generating the vector $\xi_{Z\times 1}$ requires 72×5=360 ROs. Generating all the elements of $C_{Z\times Z}$ using the look up table technique requires 10 ROs. Performing the square root operation requires 1 RO. The multiplication of $\sqrt{C_{Z\times Z}}$ by $\xi_{Z\times 1}$ requires 25 real multiplications and 20 real additions. Therefore, the number of the ROs required to calculate $\tilde{S}_{Z\times 1}$ is $C_{LS-corr}$ = 360+10+1+25+20 = 416 ROs.

Then, the 5 Gaussian distributed elements of $\tilde{S}_{Z\times 1}$ are transformed into log-normal distributed RVs. The log-normal distributed RV of the DS is given by $S_{DS} = 10^{(\sigma_{DS}\tilde{S}_{DS}+\mu_{DS})}$, where μ_{DS} and σ_{DS} are the logarithmic mean and standard deviation of the distribution of DS, respectively. By analogy, the log-normal distributed RVs of the ASA S_{ASA} and ASD S_{ASD} can be calculated with their own logarithmic means and standard deviations. The log-normal distributed RV of the SF is given by $S_{SF} = 10^{(\frac{\sigma_{SF}\tilde{S}_{SF}}{10})}$, where σ_{SF} is the corresponding logarithmic standard deviation. The log-normal distributed RV of the K-factor is given by $S_K = 10^{(\frac{\sigma_K\tilde{S}_K+\mu_K}{10})}$, where μ_K and σ_K are the relevant logarithmic mean and standard deviation, respectively.

Note that calculating $10^x = e^{xln10}$ needs 17 ROs. Therefore, for each LSP except SF, finding the logarithmic mean and standard deviation of the distributions using Table A1-7 in [32] needs 2 ROs. Additional 2 ROs are needed to calculate x for S_{DS},

S_{ASA}, and S_{ASD}, while additional 3 ROs are needed for S_K. For S_{SF}, calculating x requires 3 ROs (look up table, division, and multiplication). Thus, transforming to the 5 log-normal distributed RVs requires C_{trans}=5×17+3×4+5+3=105 ROs. For each channel coefficient sample, the total number of ROs required to generate the correlated LSPs is

$$C_{LS} = C_{LS-corr} + C_{trans} = 521 ROs. \tag{5.23}$$

It is important to mention that [97] has underestimated the complexity of generating the correlated LSPs by neglecting the generation of the linear transformation matrix $\tilde{S}_{Z\times 1}$ and ignoring the logarithmic mean and standard deviation of the distribution of the LSPs.

5.3.1.2 Generation of small scale parameters

The five Small Scale Parameters (SSPs) in the IMT-A channel model are delays, cluster powers, AoAs, AoDs, and random coupling of rays within clusters. In the following, a thorough analysis will be performed for each of them.

The delays with an exponential distribution can be calculated by $\tau_n{}' = -r_\tau \sigma_\tau \ln X_n$ [32], where r_τ is the delay distribution factor, σ_τ is the DS, and X_n is uniform RV. Calculating $\tau_n{}'$ will cost 2 real multiplications and 1 logarithm, in addition to 5 ROs to generate the uniform RV X_n. The delays $\tau_n{}'$ will be subtracted by the smallest one and then sorted in a descending order so that normalised delays τ_n are obtained. The normalisation process costs 1 RO for each delay, while the descending order costs $(N-1)^2$ ROs, where N represents the number of clusters. Thus, the number of ROs required to generate the delays τ_n is $C_\tau = (2+1+1+5)N + (N-1)^2 = N^2+7N+1$.

The cluster powers are calculated by $P_n{}' = e^{\left(\tau_n \frac{1-r_\tau}{r_\tau \sigma_\tau}\right) 10^{-\frac{Z_n}{10}}}$ [32], where Z_n is a Gaussian RV representing the per cluster shadowing term (dB). The powers are then normalised so that the sum of all the normalised cluster powers P_n equals one. This normalisation process costs $N-1$ real additions and N real divisions. Calculating the expression $10^{-\frac{Z_n}{10}}$ costs 1 real division, 17 ROs for 10^x, and 72 ROs to generate the Gaussian RV Z_n. Calculating the left exponential costs 2 ROs and 15 ROs for the value inside

the exponential function. Therefore, the number of ROs to generate powers P_n is $C_P = (16 + 1 + 72) + (2 + 15) + N + (N - 1) = 2N + 106$.

The AoAs $\varphi_{n,m}$ are calculated according to (5.1). Calculating $\varphi_n{}'$ based on (5.2) or (5.3) requires 2 real multiplications, 2 real divisions, 1 square root, and 1 logarithm, totaling 6 ROs per cluster. For the $N - 2$ weakest clusters, calculating $\varphi_{n,m} = \varphi_n + c_{AoA}\alpha_m$ requires 2 ROs per ray (M) per cluster and calculating $\varphi_n = X_n\varphi'_n + Y_n + \varphi_{LoS}$ requires 3 ROs per cluster. For the 2 strongest clusters, each cluster consists of 3 sub-clusters which has M_q ($q = 1, 2, 3$) rays. Note that $M_1 + M_2 + M_3 = M$ holds. Thus, calculating $\varphi_{n,q,m}$ requires 2 ROs per ray per sub-cluster and calculating $\varphi_{n,q}$ needs 3 ROs per sub-cluster. From Table 5.1, X_n needs 5 ROs, Y_n needs 72 ROs, while c_{AoA} and α_m need 1 RO each. Calculating AoDs follows the same procedure as above and requires the same number of ROs as for calculating AoAs. Therefore, the total number of ROs required to generate the AoAs and AoDs is

$$\begin{aligned} C_{az} &= 2[(72+5+6+1)N+3(N-2)+2(N-2)M+3\times2\times3+2\times2(M_1+M_2+M_3)] \\ &= 174N + 4MN + 24. \end{aligned} \tag{5.24}$$

The increased complexity of the IMT-A channel model in comparison with WIM2 in [29] is due to the strongest clusters concept introduced by the IMT-A channel model [32].

The random coupling of AoDs $\phi_{n,m}$ to AoAs $\varphi_{n,m}$ can be easily obtained by assigning a RV with a uniform distribution to the M rays within a cluster n, or within a sub-cluster in case of the two strongest clusters. Thus, we have $C_{coup} = 5MN$.

Finally, the total number of ROs required to generate the SSPs is

$$C_{SS} = C_\tau + C_P + C_{az} + C_{coup} = N^2 + 183N + 9MN + 131. \tag{5.25}$$

5.3.1.3 Channel coefficients generation in the IMT-A channel model

Without considering polarisation, the required number of ROs for generating channel coefficients in the IMT-A channel model can be calculated as $C_{cc} = C_\Phi + C_H$, where C_Φ and C_H represent the required numbers of ROs for generating random initial phases $\Phi_{m,n}$ and channel coefficient matrix $\mathbf{H}$, respectively. The initial phases have a uniform distribution within $[-\pi, \pi)$, which costs 5 ROs. Thus, we can write $C_\Phi = 5MN$. For the weakest clusters and uniform linear arrays, the channel coefficients or elements of $\mathbf{H}$ are given by (5.4). The expression $e^{jk[d_s \sin(\phi_{n,m}) + d_u \sin(\varphi_{n,m})]}$ contains 2 sines, 3 real multiplications, 1 real addition, and 1 exponential, which requires 2×7+3+1+15=33 ROs in total. The expression $e^{j2\pi\nu_{n,m}t}$ with $v_{n,m} = \lambda^{-1} \|\mathbf{v}\| \cos(\varphi_{n,m} - \theta_v)$ has 1 cosine, 1 subtraction, 1 multiplication, 1 division, and 1 exponential, which needs 15+8+3=26 ROs per ray per cluster. Calculating $e^{j\Phi_{n,m}}$ requires 15 ROs. Note that the product of the above 3 exponentials requires 2 complex multiplications, costing 2×6=12 ROs. Therefore, the required number of ROs to generate the channel coefficient matrix $\mathbf{H}$ is

$$C_H = [(33 + 26 + 15 + 12)M + 3]USN = (86M + 3)USN. \tag{5.26}$$

Then, C_{cc} can be calculate as

$$C_{cc} = C_\Phi + C_H = (86M + 3)USN + 5MN. \tag{5.27}$$

The sum of (5.23), (5.25), and (5.27) gives the total required number C_{IMT-A} of ROs to compute a time sample of the IMT-A channel model, i.e.,

$$C_{IMT-A} = C_{LS} + C_{SS} + C_{cc} = (86M + 3)USN + N^2 + 183N + 14MN + 652. \tag{5.28}$$

Using the 2×2 MIMO configuration and NLoS UMi scenario as an example, we have $U = S = 2$, M=20, and N=19. Substituting these values to (5.28), we have C_{IMT-A}=140758 ROs.

5.3.2 Computational complexity of the LTE-A channel model

Based on the procedure of generating the channel coefficients per tap in [48], the required number of ROs for the LTE-A channel model can be expressed by

$$C_{LTE-A} = L(C_{Kron} + C_{Dopp} + C_{Matrix}) \tag{5.29}$$

where C_{Kron} is the number of ROs required to perform the Kronecker product of Rx and Tx correlation matrices, C_{Dopp} is the number of ROs of performing Doppler shaping filtering with a Kth order IIR filter, C_{Matrix} is the number of ROs in matrix multiplications, and L is the number of taps.

The spatial correlation matrix $\mathbf{R}_{MIMO}$ of the MIMO channel is the Kronecker product of the correlation matrix $\mathbf{R}_{MS}$ at the MS and the correlation matrix $\mathbf{R}_{BS}$ at the BS, i.e., $\mathbf{R}_{MIMO} = \mathbf{R}_{MS} \bigotimes \mathbf{R}_{BS}$, where $\bigotimes$ is the Kronecker product. Thus, the computation of $U \times S$ MIMO configuration costs US real multiplications and $(US-1)US$ complex multiplications. So, we have $C_{Kron} = 6(US-1)US + US = 6U^2S^2 - 5US$.

The complexity of applying the Doppler shaping filtering is given by $C_{Dopp} = C_{i.i.d} + C_{filter}$. First, we need to generate complex i.i.d. RVs with zero mean. The total number of ROs in generating the real and imaginary components of these complex Gaussian RVs is $C_{i.i.d} = 2 \times 72US = 144US$. These RVs are then Doppler shaped using a Kth order IIR filter, which takes $2(K-1)$ complex multiplications, $2K$ complex additions, and 1 complex division per MIMO antenna pair. Assuming an $8th$ order IIR filter, we have $C_{filter} = (2(8-1) \times 6 + (2 \times 8) \times 2 + 1 \times 11)US = 127US$. Therefore, $C_{Dopp} = C_{i.i.d} + C_{filter} = 144US + 127US = 271US$ holds.

The output of the Doppler shaping filter is a $US \times 1$ vector, which is multiplied by the $US \times US$ matrix $\mathbf{R}_{MIMO}$ to obtain the LTE-A channel coefficients. This takes $(US)^2$ complex multiplications and $(US)^2$ complex additions. Thus, the number of ROs required to perform the matrix multiplication is $C_{Matrix} = 6(US)^2 + 2(US)^2 = 8(US)^2$.

According to (5.29), we can get the total number of ROs in generating channel coefficients as

$$C_{LTE-A} = L(C_{Kron} + C_{Dopp} + C_{Matrix}) = L(14U^2S^2 + 266US) \tag{5.30}$$

which is in general much less than the required number of ROs C_{IMT-A} in (5.25) for the IMT-A channel model. Using $U = S = 2$ and $L = 20$ as an example, we have $C_{LTE-A} = 25760$ ROs.

5.4 Complexity Reduction Methods for the IMT-A Channel Model

From Section 5.2 and Section 5.3, it is clear that the LTE-A channel model has poor model accuracy in terms of some important channel statistical properties. Despite its simplicity, it cannot be recommended to be used, in particular for system-level simulations. The IMT-A channel model has good accuracy but is too complex. This section will therefore focuses on investigating simplification methods for the IMT-A channel model, i.e., fixing the PDP, reducing the number of clusters, removing the correlation of LSPs, and the combination of the above. We aim to reduce the computational complexity of the IMT-A channel model as much as possible without sacrificing too much the model accuracy. Some statistical properties such as the FCF are used as the accuracy metrics. In addition, the impact of the simplified IMT-A channel models on the LTE system throughput is investigated. For complexity metrics, we use the number of ROs and the channel coefficient computing time.

5.4.1 Fixed PDP

Here, we fix the PDP when generating channel coefficients. According to the calculations described in Section 5.3.1, this will only affect the number of ROs for the generation of delays and powers, while the required numbers of ROs to generate other

parameters remain unchanged. Simply using a look up table to generate delays τ_n and cluster powers P_n, C_τ and C_P can be rewritten as $C_\tau = N$ and $C_P = N$, respectively. Consequently, the total number of ROs required to generate the SSPs in (5.25) should be rewritten as $C_{SS} = C_\tau + C_P + C_{az} + C_{coup} = N + N + (174N + 4MN + 24) + 5MN = 176N + 9MN + 24$. It follows that the number of ROs of the IMT-A channel model in (5.28) can be re-expressed as

$$\begin{aligned} C_{IMT-A} &= C_{LS} + C_{SS} + C_{cc} \\ &= 521 + (176N + 9MN + 24) + (86M + 3)USN + 5MN \\ &= (86M + 3)USN + 14MN + 176N + 545. \end{aligned} \tag{5.31}$$

Compared with (5.28), C_{IMT-A} in (5.31) for the simplified IMT-A channel model has been reduced by $N^2 + 7N + 107$. When considering the NLoS UMi scenario with U=S=2, M=20, and N=19, we have 140758 ROs and 140157 ROs according to (5.28) and (5.31), respectively. This represents (140758-140157)/140758=0.43% of complexity reduction. On the other hand, this will not degrade the accuracy in terms of statistical properties.

5.4.2 Reducing the number of clusters

Further to fixing the PDP, we try to simplify the PDP by reducing the number of clusters. This is conducted by merging some adjacent clusters/delays with low powers in the PDP according to the following criteria: 1) The greatest common divisor of the revised delays will remain unchanged, indicating that the modified FCFs keep the same period Υ according to (5.22); 2) The resulting average delay and RMS DS should be as close as possible to the original ones of the IMT-A channel model; 3) The resulting FCF should approximate well the original FCF with a very small RMS error. Using the NLoS UMi scenario as an example, in Table 5.2 we show the original PDP with 19 clusters and the modified PDPs of the simplified IMT-A channel model with 15, 12, and 10 clusters. Clearly, the modified delays in all the cases keep the same greatest common divisor, i.e., 5 ns. In Table 5.3, we compare the resulting average

TABLE 5.2: The PDPs of the IMT-A channel model (UMi scenario) and its simplified models.

19 clusters			15 clusters			12 clusters			10 clusters		
Clu. No.	Delay [ns]	Power [dB]	Clu. No.	Delay [ns]	Power [dB]	Clu. No.	Delay [ns]	Power [dB]	Clu. No.	Delay [ns]	Power [dB]
1	0	-6.7	1	0	-6.7	1	0	-6.7	1	0	-6.7
2	10	-4.9	2	10	-4.9	2	10	-4.9	2	10	-4.9
	15	-7.1		15	-7.1		15	-7.1		15	-7.1
	20	-8.9		20	-8.9		20	-8.9		20	-8.9
3	20	-1.9	3	20	-1.9	3	20	-1.9	3	20	-1.9
4	35	-6.3	4	35	-6.3	4	35	-6.3	4	35	-6.3
5	40	-3	5	40	-3	5	40	-3	5	40	-3
	45	-5.2		45	-5.2		45	-5.2		45	-5.2
	50	-7		50	-7		50	-7		50	-7
6	55	-7.5	6	55	-7.5	6	55	-3.9	6	55	-3.9
7	55	-6.4	7	55	-6.4						
8	200	-10.8	8	200	-10.8	7	205	-4.1	7	220	-1.5
9	205	-5.2	9	205	-5.2						
10	250	-4.9	10	250	-4.9	8	290	-3.5			
11	330	-9.2	11	330	-9.2				8	400	-7.7
12	440	-15.5	12	440	-13.0	9	440	-13.0			
13	440	-16.7									
14	515	-12.4	13	525	-11.1	10	525	-11.1	9	540	-8.8
15	530	-16.9									
16	580	-12.7	14	585	-12.4	11	585	-12.4			
17	590	-23.5							10	650	-18.2
18	625	-22.1	15	680	-19.8	12	680	-19.8			
19	730	-23.6									

delays and RMS DSs, which are at maximum 6.26% and 1.92% difference from the original ones, respectively. Fig. 5.6 compares the FCFs of the original IMT-A channel model with 19 clusters and simplified IMT-A channel models with 15, 12, and 10 clusters. They all look close to each other. To further investigate their differences, we define the following RMS error ε of the FCF:

$$\varepsilon = \sqrt{\frac{\sum \left(\Psi_T(\triangle f) - \Psi_T^{sim}(\triangle f)\right)^2}{Q}} \tag{5.32}$$

where $\Psi_T(\triangle f)$ and $\Psi_T^{sim}(\triangle f)$ denote the FCFs of the IMT-A channel model and simplified IMT-A channel model, respectively, and Q is the total number of samples of the FCF. After simple calculations, we find that the RMS errors ε of the resulting

TABLE 5.3: Evaluation of several complexity reduction methods.

Simplification methods		**Average delay (ns)**	**RMS DS (ns)**	**FCF RMS error**	**Throughput (Mbps)**	**Complexity reduction**	**Computing time (s)**
Fixed PDP (19 clusters)		101.8956	132.8613	0%	827.12 (0.51%)	0.43%	1.416879
Fixed PDP (15 clusters)		95.5181 (6.26%)	130.3076 (1.92%)	4.39%	874.20 (6.23%)	21.31%	1.362895
Fixed PDP (12 clusters)		97.5656 (4.25%)	132.6077 (0.19%)	10.75%	836.76 (1.68%)	36.97%	1.347849
Fixed PDP (10 clusters)		95.9122 (5.87%)	130.9396 (1.45%)	13.97%	824.41 (0.18%)	47.41%	1.325738
Removing the correlation of LSPs		101.8956	132.8613	0%	829.32 (0.78%)	1.35%	1.419689
Combined method	19 clus.	101.8956	132.8613	0%	828.22 (0.65%)	1.78%	1.394587
	15 clus.	95.5181 (6.26%)	130.3076 (1.92%)	4.39%	820.76 (0.26%)	22.38%	1.345518
	12 clus.	97.5656 (4.25%)	132.6077 (0.19%)	10.75%	837.81 (1.81%)	37.83%	1.301662
	10 clus.	95.9122 (5.87%)	130.9396 (1.45%)	13.97%	800.86 (2.68%)	48.13%	1.286018

FCFs with 15, 12, and 10 clusters are 4.39%, 10.75%, and 13.97%, respectively.

With respect to the complexity reduction, we calculate the number of ROs based on (5.31). With $U = S = 2$, M=20, and N=15, 12, and 10, we have C_{IMT-A}=110765, 88721, and 74025 ROs, respectively. Compared with 140758 ROs for the IMT-A channel model using (5.28), the corresponding computational complexities have been reduced by (140758-110765)/140758=21.31%, (140758-88721)/140758=36.97%, and (140758-74025)/140758=47.41%. In the meanwhile, we recorded the MATLAB channel coefficient computing time for generating channel coefficients with 10000 sets of 2×2 channel matrices. The PC we used to run the simulations has Intel Core i5, 2×3.47 GHz CPU, and 4 G RAM. Table 5.3 presents the computing time in different cases. Clearly, with the decrease of the number of clusters, the computing time can be reduced to a good extent. This complexity reduction method will accelerate the simulation speed dramatically in real simulations, where millions of channel coefficients samples are required to be generated.

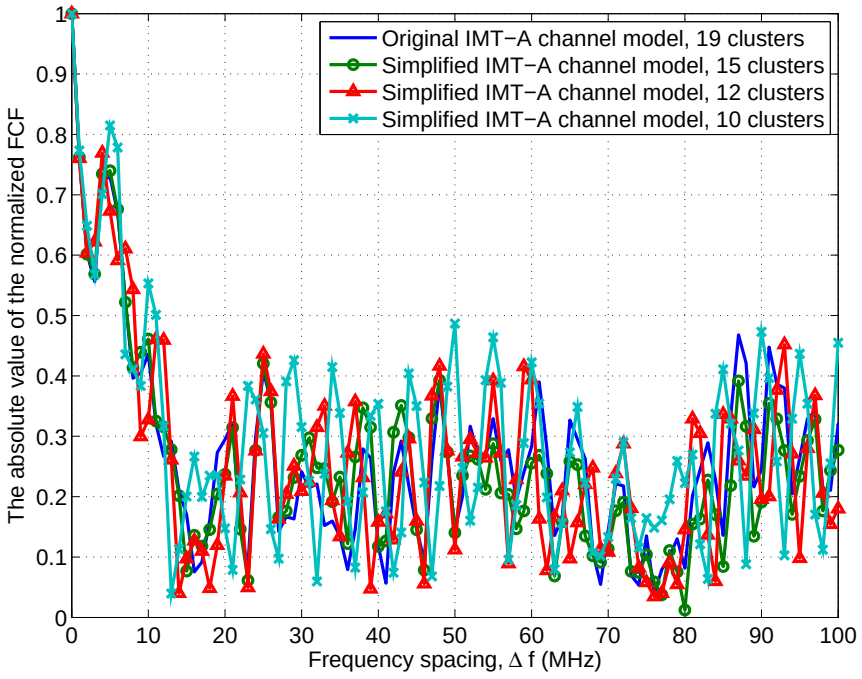

FIGURE 5.6: The normalized FCFs of the IMT-A and simplified IMT-A channel models (NLoS UMi scenario).

In summary, reducing the number of clusters can significantly reduce the complexity of the IMT-A channel model in terms of the number of ROs and the computing time, while the accuracy degradation is acceptable based on the average delay, RMS delay, and FCF.

5.4.3 Removing the correlation of LSPs

Another method of reducing the complexity of the IMT-A channel model is to remove the correlation of LSPs. In this case, the correlation matrix $\mathbf{C}_{Z\times Z}$ will become a $Z \times Z$ identity matrix, which can save 10 ROs without using the look up table. Then, C_{LS} in (5.23) can be rewritten as C_{LS}=521-10=511 ROs. Also, there is no mutual coupling between AoAs and AoDs, which results in a further reduction of $C_{coup} = 5MN$ ROs when generating SSPs. Therefore, C_{SS} in (5.25) is reduced to $C_{SS} = N^2 + 183N + 4MN + 131$. Note that C_{cc} in (5.27) is not affected. The total

number of ROs in (5.28) is therefore reduced to

$$C_{IMT-A} = C_{LS} + C_{SS} + C_{cc} = (86M + 3)USN + N^2 + 183N + 9MN + 642. \quad (5.33)$$

Substituting $U = S = 2$, $M = 20$, and $N = 19$ into (5.33), we have 138848 ROs, which represents (140758-138848)/140758 = 1.36% of complexity reduction. After some investigations, we find that this method has little effect on the model accuracy in terms of statistical properties, such as the spatial CCF and FCF, which are not shown here for space limitations.

5.4.4 Combination of the above methods

It is worth investigating the impact of the combination of all the above methods on the model accuracy and complexity. Specifically, we first remove the correlation of LSPs. Then, we fix the PDP, followed by reducing the number of clusters. As removing the correlation of LSPs can save $5MN + 10$ ROs and fixing the PDP can save $N^2 + 7N + 107$ ROs, in total $N^2 + 7N + 5MN + 117$ ROs can be saved with the combined method. Therefore, we can re-express the required number of ROs in (5.28) as

$$C_{IMT-A} = C_{LS} + C_{SS} + C_{cc} = (86M + 3)USN + 9MN + 176N + 535. \quad (5.34)$$

Again, using U=S=2, M=20, N=19, 15, 12, and 10, we have 138247, 109255, 87511, 73015 ROs, respectively. In comparison with 140758 ROs of the original IMT-A channel model, the relevant complexities have been reduced by 1.78%, 22.38%, 37.83%, and 48.13%.

5.4.5 System throughput of a system-level LTE simulator

For the interest of system engineers, we further investigate the impact of the simplified IMT-A channel models on the system throughput of a system-level LTE simulator [101]–[103]. Throughput is a very important accuracy metric to evaluate the

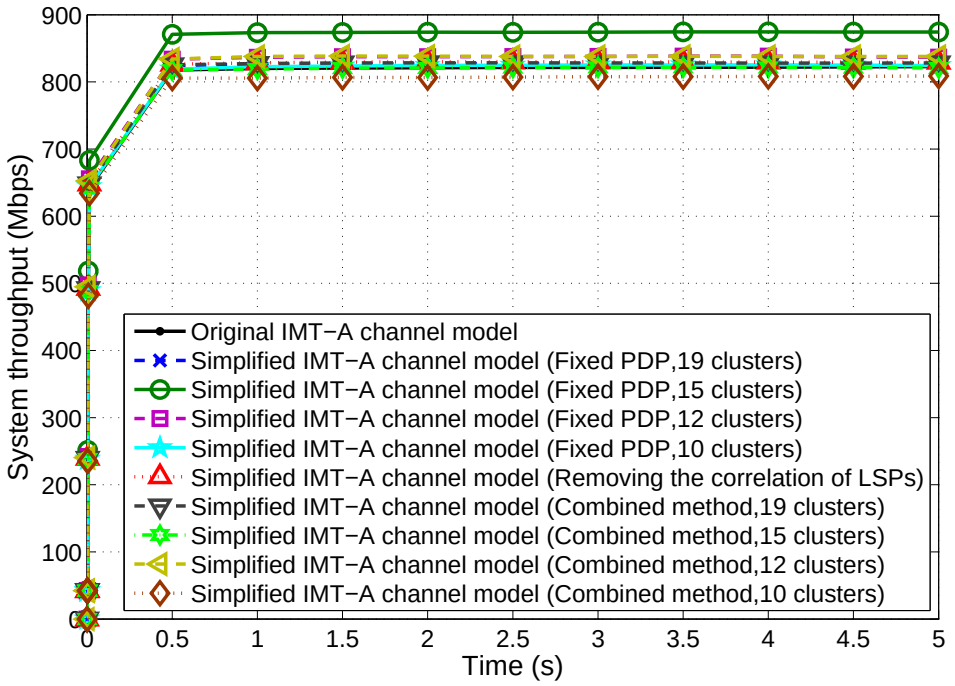

FIGURE 5.7: System throughput obtained using a system-level LTE simulator with IMT-A and simplified IMT-A channel models (5000 TTIs).

system performance and is defined as the average rate (in Mbps) of successful message delivery over a communication channel. For the system-level LTE simulator, we used the following parameters. The carrier frequency is 2.14 GHz, the bandwidth is 20 MHz, the distance of BSs is 500 m with a map resolution of 20 m, the speed of MSs is 5 km/h (i.e., 1.38 m/s), and there are 7 BSs, each having 3 sectors with 10 MSs per sector. We replaced the underlying WIM2 in the LTE simulator by the IMT-A channel model and the above developed simplified IMT-A channel models. Fig. 5.7 compares the system throughputs, calculated as the sum of throughputs of all the MSs in the system, of the system-level LTE system using the original IMT-A channel model and simplified IMT-A channel models with 5000 Transmission Time Intervals (TTIs). Note that 1 TTI represents 10^{-3} s. For clarity purposes, in Table 5.3 we also compare the throughputs in Fig. 5.7 at $t = 5$ s, i.e., the 5000th TTIs. Compared with the throughput of 822.91 Mbps using the original IMT-A channel model, the resulting throughputs using the simplified IMT-A channel models only change slightly (in maximum 6.23% difference). This means that the proposed complexity reduction methods do not affect the model accuracy significantly in terms of the system throughput.

5.5 Summary

We have thoroughly investigated the statistical properties and computational complexities, in terms of the number of ROs, of the LTE-A and IMT-A channel models. Theoretical expressions have been derived for the spatial CCFs, temporal ACFs, envelope LCRs, AFDs, PDPs, and FCFs, verified by the corresponding simulation results. In general, the LTE-A channel model is simpler and requires much less number of ROs than the IMT-A channel model. However, the LTE-A channel model has significant flaws in terms of the model accuracy. From its FCF, it is clear that the LTE-A channel model can only support system bandwidths up to 50 MHz, not the claimed 100 MHz. Also, the LTE-A channel model describes only the average spatial-temporal properties of MIMO channels. The IMT-A channel model allows us to simulate the variations of different MIMO channel realisations and can indeed support system bandwidths up to 100 MHz.

To simplify the IMT-A channel model, we have proposed several complexity reduction methods. Besides the statistical properties, we have employed the system throughput of a LTE system as an additional accuracy metric. The number of ROs and the channel coefficient computing time are used as the complexity metrics. It has been demonstrated that the proposed complexity reduction methods are effective for the IMT-A channel model in the sense that the channel coefficient computing time and number of ROs can be reduced significantly (in maximum nearly 50%), while the accuracy is not degraded much (in most cases $< 10\%$).

Chapter 6

Non-WSS IMT-A MIMO Channel Models with Time-Varying AoDs and AoAs

6.1 Introduction

In Chapter 5, we introduced that many standardised channel models in the literature are based on the assumption of Wide Sense Stationary Uncorrelated Scattering (WSSUS), e.g., IEEE 802.11 TGn channel model [15], LTE-A channel model [22]–[24], 3GPP SCM [25], [26], SCME [27], WIM1 [28], WIM2 [29], WIM+ [30], and IMT-A channel model [31], [32]. All these standardised models have neglected the non-stationarity of the fading channels.

Although the statistical characterisation of WSSUS MIMO channels has been investigated extensively in the literature, such as [9] and [54]–[56]. Many practical measurement campaigns [57], [82]–[85], [104]–[106] have proved that the assumption of WSSUS channels is violating by considering the time variation of wireless channels caused by the significant movements of MCs and MSs. The IMT-A channel model is recognised as the latest development of channel modelling. However, the non-stationarity of IMT-A MIMO channel model has not been investigated yet. The research of non-stationary channel modelling has gradually become a hot topic.

In the literature, only few papers [89], [107], [108] have studied the statistical properties of non-stationary channels in terms of the LSF and channel correlation function. Based on the measurement campaign for V2V communications, the non-stationary behaviour of both large-scale and small-scale fading statistics has investigated by the proposed narrowband statistical channel models [82]–[85]. Moreover, the impact of the channel non-stationarity on the channel capacity has been introduced for non-WSSUS wideband V2V channels in [88].

Different modelling approaches have been adopted in the literature to model non-stationary channels. A non-stationary GBDM have been proposed by [104] and [109] to model V2V and HST channels, respectively. Both models used ray-tracing technique that incorporates the non-stationarity of the communication channel but it requires a detailed and time-consuming geometric description of the propagation environment. [82], [110]–[113] proposed Random Cluster Models (RCMs) for non-stationary channels. RCMs are convenient to characterise the death/birth properties of the MCs using the process of Markov chains. However, the local statistical properties of the non-stationary RCMs have not been investigated yet.

Time-variant GBSMs with time-varying parameters were proposed in [86], [87], [114], [115], where some interesting local statistical properties were derived by taking time-varying parameters into account. However, these existing time-variant GBSMs are only modeled for some specific scenarios, such as specific moving directions for MCs and MSs [114], fixed Tx and Rx indoor scenario [115], and the specific roadside conditions [86], [87].

In conventional cellular wireless network, the BS is fixed while a MS is moving towards a certain direction with a constant speed. In non-stationary IMT-A channel models, we assume that the movements of MCs and MSs result in the time-variant properties. Following the trajectory of the MCs and a MS, we can obtain SSPs, such as the number of clusters, the number of rays per cluster, the mean power and delay of each cluster (PDP), AoDs, and AoAs. The lack of implementation for non-stationarity IMT-A MIMO channel models and the aforementioned research gaps inspire us to propose a

non-stationary channel model with time-varying AoDs and AoAs. The proposed time-varying functions of these parameters can be applied to various scenarios in terms of the moving features of MCs and MSs. Based on our previous work in Chapter 5, we summarise the major contributions and novelties of this chapter as follows:

1. We establish a non-stationary IMT-A channel model that includes only time-varying AoDs and AoAs.
2. These time-varying or time-dependent parameters are derived as functions of time t, with some parameters which are not time-varying and can be adjusted.
3. Based on the proposed non-stationary IMT-A channel model and time-varying functions, important statistical properties, i.e., the local spatial CCF and local temporal ACF are derived and analysed.
4. The impacts of time-varying parameters on these statistical properties are compared and investigated thoroughly by MATLAB simulations.

The rest of this chapter is structured as follows. In Section 6.2, the baseline IMT-A MIMO channel model is briefly introduced. Section 6.3 presents the proposed novel non-stationary IMT-A channel models with time-varying AoDs and AoAs. The local statistical properties of the non-stationary IMT-A channel model with time-varying parameters are derived and analysed in Section 6.4 and Section 6.5. Finally, the conclusions are drawn in Section 6.6.

6.2 The Baseline WSSUS IMT-A MIMO Channel Model

For the evaluation of IMT-A systems the ITU has defined a channel model [32] consisting of a primary module and an extension module. The primary module consists of path loss models, scenario-specific parameter sets for the InH, UMi, UMa, RMa, and SMa scenarios, and a so-called generic model. The generic model specifies the

mathematical model and the algorithms used for channel modeling that apply to all scenarios. It is based on the WIM2 channel model [29]. The optional extension module allows alternate parameter sets for different scenarios to be generated. In this chapter, we will focus on the primary module with its default parameter sets because this was actually used for the IMT-A evaluations on channel modelling.

Fig. 6.1 illustrates the IMT-A channel model between each BS antenna s and each MS antenna u for a link between a BS and a MS with multi-bounced scattering. The generic model employs a GBSM approach to represent the multi-path propagation channel between a BS and MSs. WSSUS channel assumes that the channel fading statistics remain invariant over a short period of time and that the scatterers with different path delays are uncorrelated. Please note that the WSSUS assumption is only valid to describe the short-term variations of the radio channel. Based on the WSSUS assumption and the TDL concept, the original IMT-A MIMO channel model has the complex CIR between the BS antenna element s and MS antenna element u as [32]:

$$h_{u,s}\left(t,\tau\right)=\sum_{n=1}^{N}h_{u,s,n}(t)\delta\left(\tau-\tau_{n}\right) \tag{6.1}$$

where

$$h_{u,s,n}\left(t\right)=\sqrt{\frac{P_{n}}{M}}\sum_{m=1}^{M}e^{jd_{s}k\sin(\phi_{n,m})}e^{jd_{u}k\sin(\varphi_{n,m})}e^{j2\pi\upsilon_{n,m}t}e^{j\Phi_{n,m}}. \tag{6.2}$$

Here, $h_{u,s,n}(t)$ denotes a narrowband process where all the M sub-paths within each of the N clusters are irresolvable rays and have the same delay τ_n, P_n is the power of the nth cluster associated with the delay τ_n, d_s and d_u are the antenna element spacings at the BS and MS, respectively, $k=\frac{2\pi}{\lambda}$ is the wave number where λ is the carrier wavelength, $\phi_{n,m}$ and $\varphi_{n,m}$ denote the AoD and AoA, respectively, and the random phases $\Phi_{n,m}$ are uniformly distributed within $[-\pi,\pi)$. The Doppler frequency component is represented by $\upsilon_{n,m}=\frac{||\vec{v}_{MS}||\cos(\varphi_{n,m}-\theta_{MS})}{\lambda}$, where $||\vec{v}_{MS}||$ and θ_{MS} denote the magnitude of the MS velocity and MS direction of travel, respectively. In fact, all of

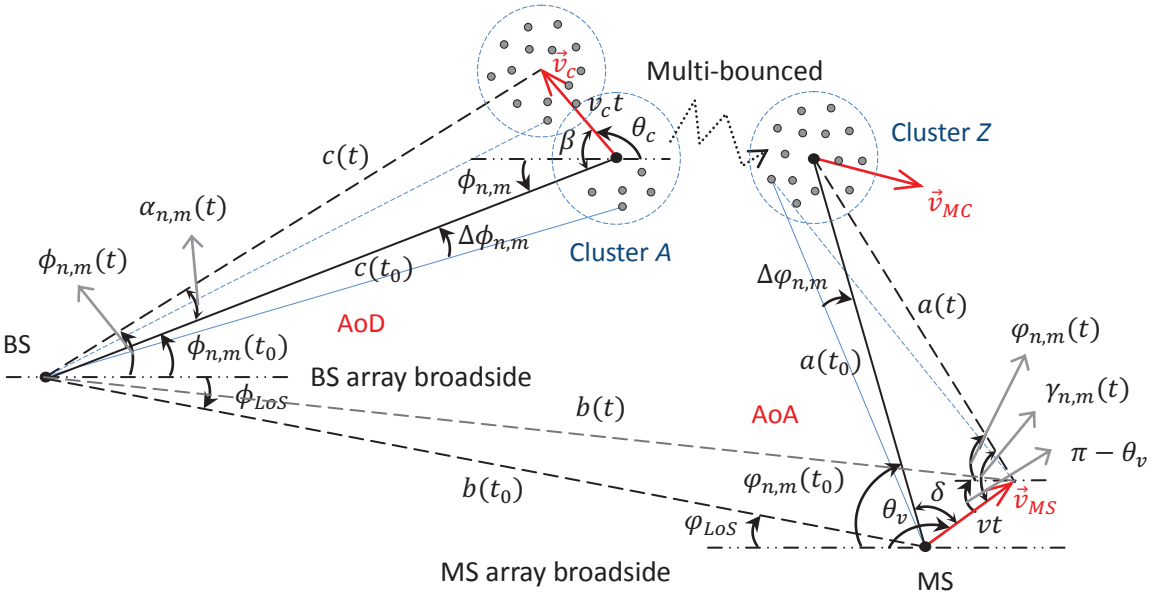

FIGURE 6.1: The angular parameters in non-WSS IMT-A channel model.

the aforementioned parameters are time-invariant because of the WSSUS assumption in the original IMT-A channel model.

6.3 Derivations of Novel Non-WSS IMT-A Channel Models with Time-Varying Parameters

In reality, because of the observable movement of MCs and/or MSs, the WSSUS assumption may be violated and the channel model parameters will change over the time. In this case, the complex impulse response of the new non-stationary IMT-A channel model with time-varying parameters can be expressed as

$$h_{u,s}(t,\tau) = \sum_{n=1}^{N(t)} h_{u,s,n}(t)\,\delta(\tau - \tau_n(t)) \tag{6.3}$$

where

$$h_{u,s,n}(t) = \sqrt{\frac{P_n(t)}{M}} \sum_{m=1}^{M} e^{jd_s k \sin(\phi_{n,m}(t))}\; e^{jd_u k \sin(\varphi_{n,m}(t))} e^{jk||\vec{v}_{MS}||\cos(\varphi_{n,m}(t)-\theta_{MS})t} e^{j\Phi_{n,m}}. \tag{6.4}$$

Here, the channel model parameters $N(t)$, $\tau_n(t)$, $P_n(t)$, $\phi_{n,m}(t)$, and $\varphi_{n,m}(t)$ need to be represented using proper time-varying functions. In the following, we will explain all parameters in Fig. 6.1 and derive corresponding time-varying functions for these parameters.

Fig. 6.1 illustrates the angular parameters of the proposed non-stationary IMT-A channel model, which is derived from the original IMT-A channel model [32]. Note that $\phi_{n,m}(t_0)$, $\varphi_{n,m}(t_0)$, $\Delta\phi_{n,m}$ and $\Delta\varphi_{n,m}$ denote the initial mean AoD, initial mean AoA, the AoD offset and AoA offset, respectively. The subscripts n, m indicate one of the N paths and one of the M rays/sub-paths in the wideband channel. The geometric description covers that AoD relates to the first bounce (Cluster A) interacted from the BS side and AoA is from the last bounce (Cluster Z) at the MS side. There are multi-bounced clusters happened between the BS and MS. Furthermore, angles of ϕ_{LoS} and φ_{LoS} are the line-of-sight (LoS) components for BS and MS, respectively.

In Fig. 6.1, we assume that the first cluster, cluster A, $\vec{v}_c$, is in motion with the direction θ_c and speed v_c. As we consider multi-bounced scattering occurred for each path, cluster Z refers to the last bounce MC ($\vec{v}_{MC}$), with the moving direction θ_{MC} and speed v_{MC}. For the MS ($\vec{v}_{MS}$), θ_{MS} is the moving direction with the speed v_{MS}. Further to assume that $c(t_0)$ and $a(t_0)$ are known, which present the initial distances between the BS and first cluster (i.e., Cluster A), and the initial distance between the MS and last cluster (i.e., Cluster Z), respectively. $b(t_0)$ is the initial distance of the LoS components between BS and MS. To derive the time-varying function of AoD and AoA, we set four assistant angles, which are $\alpha_{n,m}(t)$, β, $\gamma_{n,m}(t)$, and δ in Fig. 6.1. Note that $\alpha_{n,m}(t)$ and $\gamma_{n,m}(t)$ have the time variabilities.

Based on the geometric relations in Fig. 6.1, we derive the time-varying functions of AoDs and AoAs. The detailed derivations are lengthy and therefore presented in the appendices. In addition, the theoretical ranges of all angular parameters, i.e, θ_c, θ_{MC}, θ_{MS}, $\phi_{n,m}(t_0)$, $\phi_{n,m}(t)$, $\varphi_{n,m}(t_0)$, and $\varphi_{n,m}(t)$, are within the range of $[-\pi, \pi)$. The distance parameters, i.e., $c(t_0)$, $a(t_0)$, and $b(t_0)$ are in $[0, +\infty)$ m. The speed parameters, i.e., v_c, v_{MC}, and v_{MS}, are in $[0, +167)$ m/s.

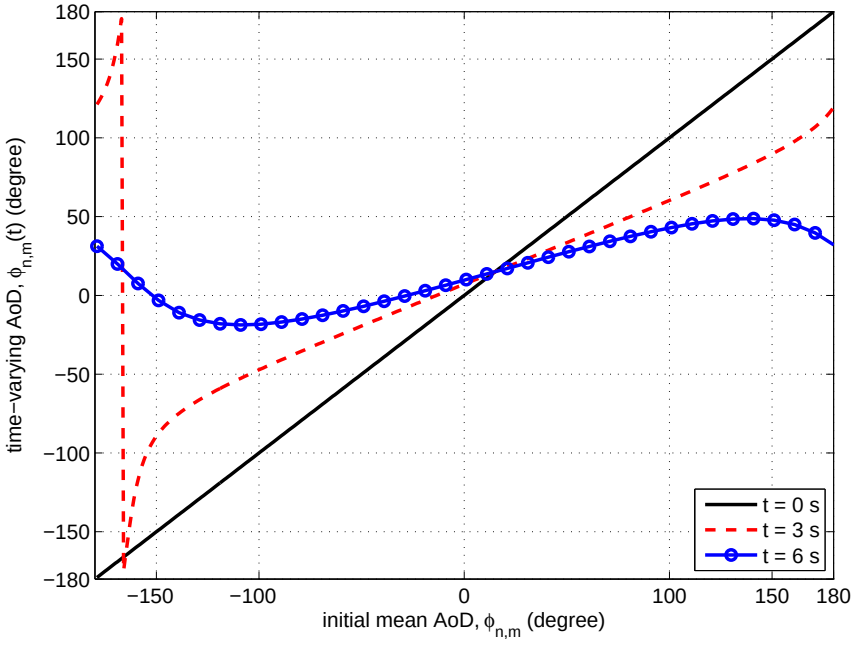

FIGURE 6.2: The range of time-varying AoD.
($\phi_{n,m}(t_0) \in [-\pi, \pi)$, $c(t_0) = 100$ m, $\theta_c = 15°$, $v_c = 30$ m/s)

6.3.1 Time-varying AoD

In terms of the interaction of relevant parameters, referring to the derivation in the Appendix A, the time-varying function of AoD $\phi_{n,m}(t)$ can be expressed as follows:

1) if $-\pi \leq \phi_{n,m}(t_0) < 0$,

$$\phi_{n,m}(t) = \phi_{n,m}(t_0) - \alpha_{n,m}(t), \quad if \ -\pi \leq \theta_c \leq \phi_{n,m}(t_0) \cup \phi_{n,m}(t_0) + \pi \leq \theta_c < \pi, \tag{6.5}$$

$$\phi_{n,m}(t) = \phi_{n,m}(t_0) + \alpha_{n,m}(t), \quad if \ \phi_{n,m}(t_0) < \theta_c < \phi_{n,m}(t_0) + \pi. \tag{6.6}$$

2) if $0 \leq \phi_{n,m}(t_0) < \pi$,

$$\phi_{n,m}(t) = \phi_{n,m}(t_0) + \alpha_{n,m}(t), \quad if - \pi \leq \theta_c \leq \phi_{n,m}(t_0) - \pi \cup \phi_{n,m}(t_0) \leq \theta_c < \pi, \tag{6.7}$$

$$\phi_{n,m}(t) = \phi_{n,m}(t_0) - \alpha_{n,m}(t), \quad if \ \phi_{n,m}(t_0) - \pi < \theta_c < \phi_{n,m}(t_0), \tag{6.8}$$

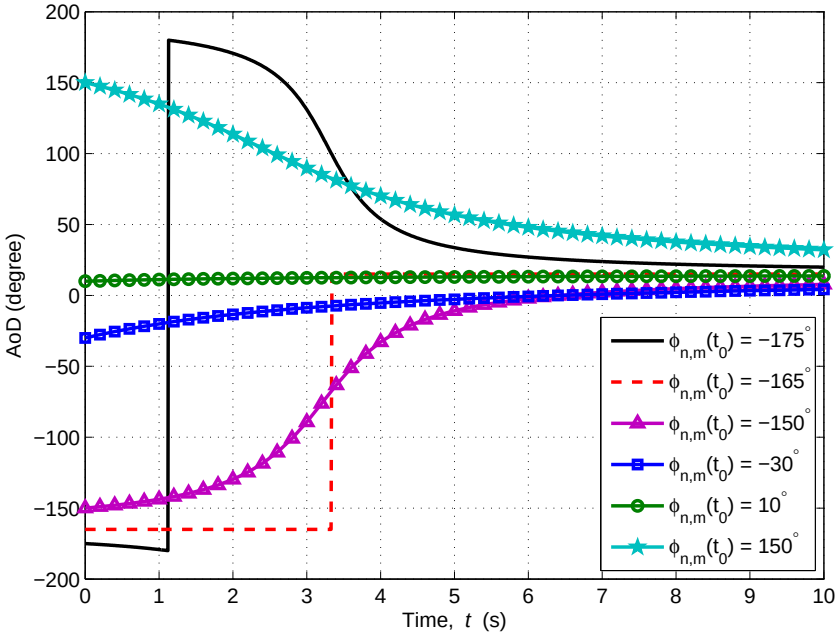

FIGURE 6.3: AoD vs. time t with different $\phi_{n,m}(t_0)$.
($\phi_{n,m}(t_0)$ varies, $c(t_0) = 100$ m, $\theta_c = 15°$, $v_c = 30$ m/s)

where

$$\alpha_{n,m}(t) = \arccos \frac{c(t_0) + v_c t \cos(\phi_{n,m}(t_0) - \theta_c)}{\sqrt{c^2(t_0) + (v_c t)^2 + 2c(t_0) v_c t \cos(\phi_{n,m}(t_0) - \theta_c)}}. \tag{6.9}$$

Note that $\phi_{n,m}(t_0)$, $c(t_0)$, θ_c and v_c are assumed to be obtained from a measurement campaign. Now we are aiming to verify the theoretical results of the time-varying AoD. For example, if $t = 0$ s, the AoD $\phi_{n,m}(t)$ can be expressed as being proportional to the initial AoD $\phi_{n,m}(t_0)$ with the proportionality constant equal to 1. The numerical result as the solid line in Fig. 6.2 is consistent with this conclusion, which exemplifies the validation of the theoretical range for the AoD $\phi_{n,m}(t)$. In other words, both the initial AoD $\phi_{n,m}(t_0)$ and time-varying AoD $\phi_{n,m}(t)$ fall in the range of $[-\pi, \pi)$ at $t = 0$ s, while at other instantaneous time, i.e. $t = 3$ or 6 s, the time-varying AoD $\phi_{n,m}(t)$ may not be the same, but still within the range of $[-\pi, \pi)$. Furthermore, when time tends to infinity, we have $\lim_{t\to\infty} \phi_{n,m}(t) = \theta_c$.

To investigate the impact of important parameters on the time-varying function of AoD, relevant parameters should be carefully selected in terms of the real environment. For example, the angular direction of AoD can go anywhere and the speed of the

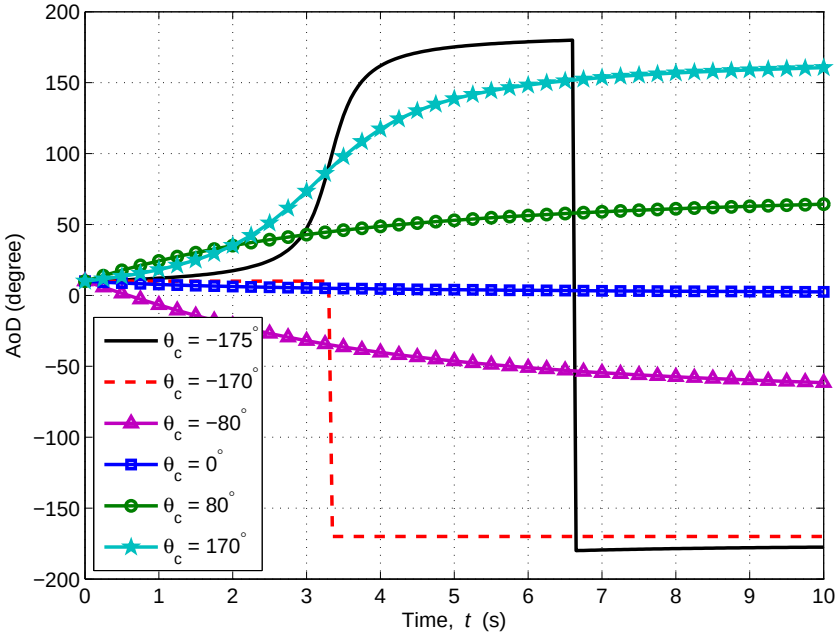

FIGURE 6.4: AoD vs. time t with different θ_c.
($\phi_{n,m}(t_0) = 10°$, $c(t_0) = 100$ m, θ_c varies, $v_c = 30$ m/s)

MCs might be from 0 to 100 m/s. The distance parameter $c(t_0)$ can be chosen from 0 to 2 km depending on the scenario. The impacts of parameters $c(t_0)$ and v_c are much more obvious compared with $\phi_{n,m}(t_0)$ and θ_c. Therefore, we plot Fig. 6.3 and Fig. 6.4 for time-varying AoD, $\phi_{n,m}(t)$, with different parameters, i.e., $\phi_{n,m}(t_0)$ and θ_c respectively.

The variations of $\phi_{n,m}(t_0)$ are investigated by choosing the representative values in Fig. 6.3. The reason to select these values is to cover the four cases, i.e., (6.5) – (6.8), in the time-varying function of AoD as well as two special cases. One is $\phi_{n,m}(t_0) = 10°$ selected from the first strongest cluster of NLoS Umi scenario in the standard IMT-A CDL channel model [32]. The other one is $\phi_{n,m}(t_0) = -165°$, which follows the inverse direction of the MC A, i.e., $\theta_c = 15°$. To sum up, Fig. 6.3 shows that different $\phi_{n,m}(t_0)$ will only affect the initial AoDs. With time going, the time-varying $\phi_{n,m}(t)$ will gradually approach the extreme value θ_c.

Fig. 6.4 compares the $\phi_{n,m}(t)$ with different θ_c. Observing from Fig. 6.4, we can see that starting from the same $\phi_{n,m}(t_0)$, the different θ_c will be approached separately. It is also worth mentioning that the choices of the different θ_c aim to cover the four

cases in the time-varying function of AoD as well as two special cases, i.e., $\theta_c = -170°$ and $\theta_c = 0°$.

In summary, with the motion of the cluster A, Fig. 6.3 and Fig. 6.4 show that whatever the parameters we change, all AoDs will approach the moving direction θ_c of the MC A when time tends to infinity. Fig. 6.3 shows that different $\phi_{n,m}(t_0)$ will only affect the initial AoDs. In Fig. 6.4, the simulation results show that starting from the same $\phi_{n,m}(t_0)$, the different θ_c will be approached with time going. The impacts of parameters $c(t_0)$ and v_c are obvious. Because, the larger $c(t_0)$, the more time will be needed to reach the θ_c, since the long distance slacks the impact of the motion on the time varying $\phi_{n,m}(t)$. It is clearer that if the speed of MC A (i.e., v_c) increases, the $\phi_{n,m}(t)$ will approach the θ_c faster.

6.3.2 Time-varying AoA

Here, we consider both motion effects from MC Z and MS. However, by considering the relative velocity, the time-varying AoA function can be simplified to that the MS is only in motion with a velocity relative to MC Z. As the velocity is a vector, which is equivalent to a specification of its speed and direction of motion, we define the velocity of MC Z as $\vec{v}_{MC} = v_{MC} \cdot e^{j\theta_{MC}}$ and that of MS as $\vec{v}_{MS} = v_{MS} \cdot e^{j\theta_{MS}}$, where v_{MC} and v_{MS} are the speeds of the MC and MS, respectively. θ_{MC} and θ_{MS} are the moving directions of the MC and MS, respectively.

In terms of the Newton's classical mechanics, we assume that the MC is fixed as a reference point, the velocity of MS relative to the MC can be expressed as

$$\begin{aligned}
\vec{v}_{MS/MC} &= \vec{v}_{MS} - \vec{v}_{MC} \\
&= v_{MS} \cdot e^{j\theta_{MS}} - v_{MC} \cdot e^{j\theta_{MC}} \\
&= v_{MS} \cdot \cos\theta_{MS} + j \cdot v_{MS} \cdot \sin\theta_{MS} - v_{MC} \cdot \cos\theta_{MC} - j \cdot v_{MC} \cdot \sin\theta_{MC} \\
&= (v_{MS} \cdot \cos\theta_{MS} - v_{MC} \cdot \cos\theta_{MC}) + j\,(v_{MS} \cdot \sin\theta_{MS} - v_{MC} \cdot \sin\theta_{MC})\,.
\end{aligned} \tag{6.10}$$

Therefore, $v_{MS/MC}$ and $\theta_{MS/MC}$ can be calculated by taking the magnitude and argument of $\vec{v}_{MS/MC}$, i.e., $v_{MS/MC} = ||\vec{v}_{MS/MC}||$ and $\theta_{MS/MC} = \mathbf{arg}(\vec{v}_{MS/MC})$, respectively.

Similarly, based on the interaction of relevant parameters, referring to the derivation in the Appendix B, the time-varying function of AoA $\varphi_{n,m}(t)$ can be expressed as follows:

1) If $-\pi \leq \varphi_{n,m}(t_0) < 0$,

$$\varphi_{n,m}(t) = \theta_v - \gamma_{n,m}(t) \pm \pi, \quad if\ -\pi \leq \theta_v < \varphi_{n,m}(t_0) \cup \pi + \varphi_{n,m}(t_0) < \theta_v < \pi, \tag{6.11}$$

$$\varphi_{n,m}(t) = \theta_v + \gamma_{n,m}(t) \pm \pi, \quad if\ \varphi_{n,m}(t_0) \leq \theta_v \leq \pi + \varphi_{n,m}(t_0), \tag{6.12}$$

2) if $0 \leq \varphi_{n,m}(t_0) < \pi$,

$$\varphi_{n,m}(t) = \theta_v + \gamma_{n,m}(t) \pm \pi, \quad if - \pi \leq \theta_v < \varphi_{n,m}(t_0) - \pi \cup \varphi_{n,m}(t_0) < \theta_v < \pi, \tag{6.13}$$

$$\varphi_{n,m}(t) = \theta_v - \gamma_{n,m}(t) \pm \pi, \quad if\ \varphi_{n,m}(t_0) - \pi \leq \theta_v \leq \varphi_{n,m}(t_0), \tag{6.14}$$

where

$$v = v_{MS/MC} = ||\vec{v}_{MS/MC}||, \tag{6.15}$$

$$\theta_v = \theta_{MS/MC} = \mathbf{arg}(\vec{v}_{MS/MC}), \tag{6.16}$$

$$\gamma_{n,m}(t) = \arccos \frac{vt - a(t_0)\cos(\theta_v - \varphi_{n,m})}{\sqrt{a^2(t_0) + (vt)^2 - 2a(t_0)\, vt \cos(\theta_v - \varphi_{n,m})}}. \tag{6.17}$$

Again, $\varphi_{n,m}(t_0)$, $a(t_0)$, θ_{MC}, v_{MC}, θ_{MS}, and v_{MS} are assumed to be obtained from measurement campaign. It is worth mentioning that "$\pm\pi$" in (6.11) – (6.14) is the corrector to ensure $\varphi_{n,m}(t)$ within the range of $[-\pi, \pi)$. To verify the range of time-varying AoA, the same procedure has been conducted as the time-varying AoD does. Due to the similar results for AoA, we will not show the corresponding figures here. Nevertheless, the results demonstrate that when $\varphi_{n,m}(t_0)$ within $[\pi, \pi)$, the time-varying $\varphi_{n,m}(t)$ is still in the range of $[\pi, \pi)$ at $t = 0$ s. However, at other instantaneous time, i.e. $t = 3$ or 6 s, the time-varying $\varphi_{n,m}(t)$ varies with the variation of $\varphi_{n,m}(t_0)$.

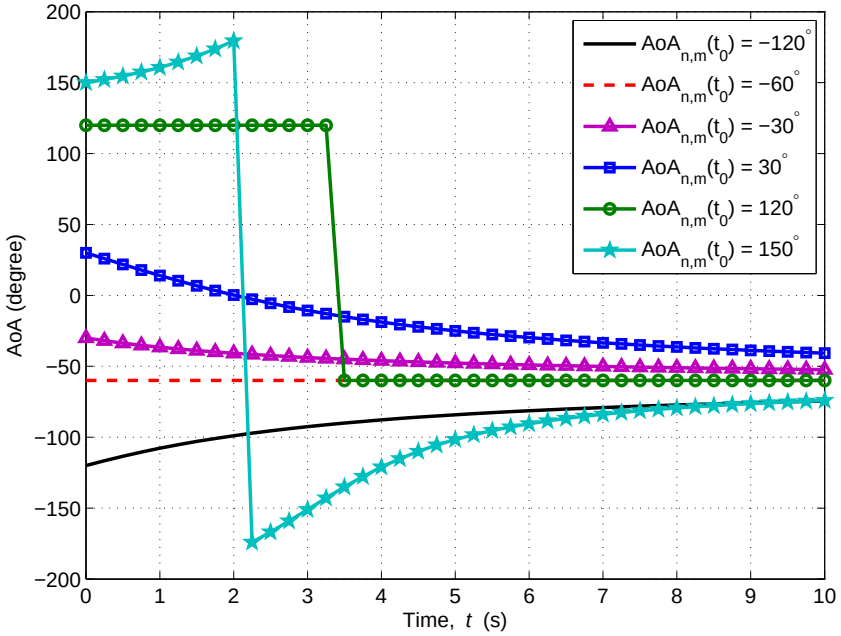

FIGURE 6.5: AoA vs. time t with different $\varphi_{n,m}(t_0)$. (Note: $AoA_{n,m}(t_0)$ indicates $\varphi_{n,m}(t_0)$ in the figure.) ($\varphi_{n,m}(t_0)$ varies, $a(t_0) = 70$ m, $\theta_{MC} = -60°$, $v_{MC} = 5$ m/s, $\theta_{MS} = 120°$, $v_{MS} = 15$ m/s.)

Furthermore, when time tends to infinity, $\varphi_{n,m}(t)$ is approaching the inverse direction of $\theta_{MS/MC}$, i.e., a supplementary angle of $\theta_{MS/MC}$.

To investigate the impact of important parameters on the time-varying functions of AoA, we should select the parameters in terms of the real environment. For example, the direction of AoAs can be from anywhere and the speed of the MC Z and MS can be from 0 to 100 m/s. The distance parameter (i.e., $a(t_0)$) can be chosen from 0 to 1 km depending on the scenario.

By considering the four cases, i.e., (6.11) – (6.14), of the AoAs time-varying function, we investigate the impact of parameters $\varphi_{n,m}(t_0)$, θ_{MC}, and θ_{MS}, which are more interested than $a(t_0)$, v_{MC}, and v_{MS}. As the impacts of parameters $a(t_0)$, v_{MC} and, v_{MS} are obvious. Therefore, we plot Fig. 6.5 and Fig. 6.5 for different $\varphi_{n,m}(t_0)$, θ_{MC}, and θ_{MS}, respectively. In general, time-varying AoAs will gradually approach the inverse direction of the MS when time tends to infinity.

The comparison of the $\varphi_{n,m}(t)$ with the different $\varphi_{n,m}(t_0)$ has been analysed in Fig. 6.5. It presents that different $\varphi_{n,m}(t_0)$ only affect the initial AoAs. Again, six curves cover four cases in the time-varying function of AoAs also with two special cases, which is

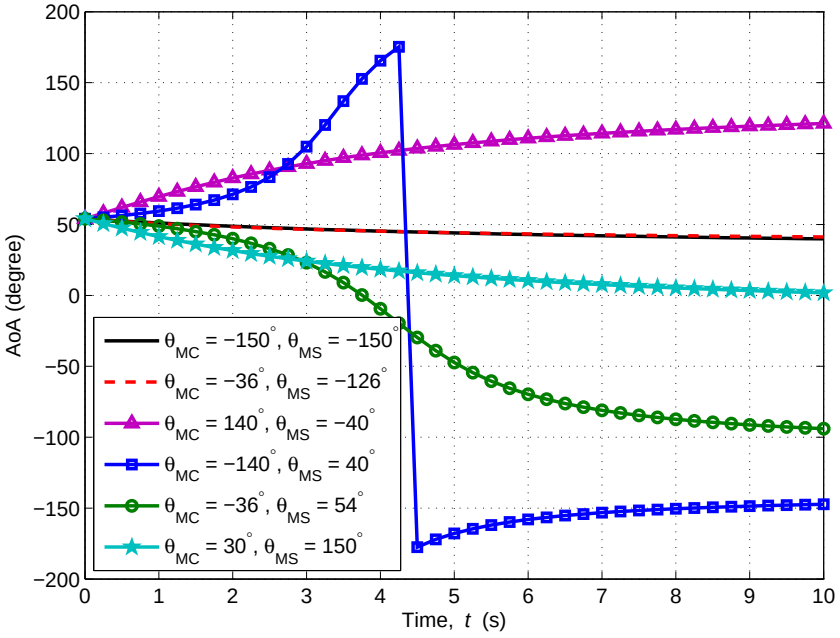

FIGURE 6.6: AoA vs. time t with different θ_v.
($\varphi_{n,m}(t_0) = 54°$, $a(t_0) = 70$ m, θ_{MC} & θ_{MS} vary, $v_{MC} = 5$ m/s, $v_{MS} = 15$ m/s.)

$\varphi_{n,m}(t_0) = 120°$ and $\varphi_{n,m}(t_0) = -60°$. One is the same direction as θ_v. The other one is the inverse direction of θ_v.

The impact of the θ_{MC} and θ_{MS} on the $\varphi_{n,m}(t)$ has been studied in Fig. 6.6. With the variation of the θ_{MC} and θ_{MS}, different extreme AoAs will be achieved, although the initial $\varphi_{n,m}(t_0)$ are identical. Similarly, the angles we chose by taking into account all cases in the time-varying function of AoAs, such as θ_{MC} and θ_{MS} are in the same direction, opposition, and arbitrary direction. It is worth mentioning that the example of $\varphi_{n,m}(t_0) = 54°$ is taken from the first strongest of the NLoS Umi scenario in the IMT-A standard CDL channel model [32].

In summary, regarding the motions of MC Z and MS, Fig. 6.5 and Fig. 6.6 show that all AoAs will gradually approach the inverse direction of $\theta_{MS/MC}$ when the time tends to infinite. Fig. 6.5 illustrates that different $\varphi_{n,m}(t_0)$ only affects the initial AoAs. Fig. 6.6 is observed that the different θ_{MC} and θ_{MS} result in different extreme AoA. Similarly, $a(t_0)$ have more obvious effect, i.e., the shorter $a(t_0)$, the less time is needed to reach the inverse direction of $\theta_{MS/MC}$. Again, the faster $v_{MS/MC}$ experiences a shorter time to approach the inverse direction of $\theta_{MS/MC}$.

6.4 Statistical Properties of Non-WSS IMT-A MIMO Channel Models

6.4.1 Derivations of local spatial CCF

For WSSUS systems, the spatial CCF depends only on the relative BS and MS antenna element spacings, $\Delta d_s = |d_{s_1} - d_{s_2}|$ and $\Delta d_u = |d_{u_1} - d_{u_2}|$, respectively. However, for non-stationary systems, the spatial CCF does not only depend on the relative antenna spacings, but also on time t. Due to this dependency, spatial CCF of non-stationary channel model is called local spatial CCF and can be expressed as [86]

$$\begin{aligned} \rho_{s_2u_2}^{s_1u_1}(t, \triangle d_s, \triangle d_u) = & \ \mathbf{E}\left\{h_{u_1,s_1,n}(t)\, h_{u_2,s_2,n}^{*}(t)\right\} \\ = & \frac{1}{M}\sum_{m=1}^{M}\mathbf{E}\left\{P_n(t) e^{jk\triangle d_s \sin(\phi_{n,m}(t))}\ e^{jk\ \triangle d_u \sin(\varphi_{n,m}(t))}\right\} \end{aligned} \tag{6.18}$$

where $(\cdot)^*$ denotes the complex conjugation operation and $\mathbf{E}\{\cdot\}$ designates the statistical expectation operator.

Under the WSSUS assumption, the AoAs and AoDs are considered as time-invariant. In this case, the spatial CCF will be reduced to [10]

$$\begin{aligned} \rho_{s_2u_2}^{s_1u_1}(\triangle d_s, \triangle d_u) = & \ \mathbf{E}\left\{h_{u_1,s_1,n}(t)\, h_{u_2,s_2,n}^{*}(t)\right\} \\ = & \frac{P_n}{M}\sum_{m=1}^{M}\mathbf{E}\left\{e^{jk\triangle d_s \sin(\phi_{n,m})} e^{jk\ \triangle d_u \sin(\varphi_{n,m})}\right\}. \end{aligned} \tag{6.19}$$

6.4.2 Derivations of local temporal ACF

Based on the proposed non-stationary IMT-A channel model, the local temporal ACF can be expressed as

$$\begin{aligned} r(t, \tau') = & \ \mathbf{E}\left\{h_{u,s,n}(t)\, h_{u,s,n}^{*}(t-\tau')\right\} \\ = & \frac{1}{M}\sum_{m=1}^{M}\mathbf{E}\left\{P_n(t) A_{\varphi_{n,m}}(t,\tau') B_{\phi_{n,m}}(t,\tau') C_{\varphi_{n,m}}(t,\tau')\right\} \end{aligned} \tag{6.20}$$

where

$$A_{\varphi_{n,m}}(t,\tau') = e^{jkd_u[\sin(\varphi_{n,m}(t))-\sin(\varphi_{n,m}(t+\tau'))]}, \tag{6.21a}$$

$$B_{\phi_{n,m}}(t,\tau') = e^{jkd_s[\sin(\phi_{n,m}(t))-\sin(\phi_{n,m}(t+\tau'))]}, \tag{6.21b}$$

$$C_{\varphi_{n,m}}(t,\tau') = e^{-jk||\mathrm{v}||[\cos(\varphi_{n,m}(t)-\theta_v)(t)-\cos(\varphi_{n,m}(t+\tau')-\theta_v)(t+\tau')]}. \tag{6.21c}$$

By applying the WSSUS assumption on (6.21), we get

$$A_{\varphi_{n,m}}(t,\tau') = 0, \tag{6.22a}$$

$$B_{\phi_{n,m}}(t,\tau') = 0, \tag{6.22b}$$

$$C_{\varphi_{n,m}}(t,\tau') = e^{jk||\mathrm{v}||\cos(\varphi_{n,m}-\theta_v)\tau'}. \tag{6.22c}$$

Therefore, (6.20) can be written as [10]

$$r(\tau') = \frac{P_n}{M}\sum_{m=1}^{M}\mathbf{E}\left\{e^{jk||\mathrm{v}||\cos(\varphi_{n,m}-\theta_v)\tau'}\right\}. \tag{6.23}$$

6.5 Simulation Results and Analysis

6.5.1 Local spatial CCF

By using the NLoS UMa scenario and main simulation parameters as follows: $\phi_{n,m}(t_0) =$ random, $c(t_0) = 100$ m, $\theta_c = 15°$, $v_c = 30$ m/s, $\varphi_{n,m}(t_0) =$ random, $a(t_0) = 150$ m, $\theta_v = 120°$, and $v = 20$ m/s, Fig. 6.7 shows the absolute values of three-dimensional (3D) local spatial CCF of the non-stationary IMT-A channel model at the system level. It is obvious that the absolute value of the local spatial CCF changes with time t due to the non-stationarity of the channel.

To highlight these changes, Fig. 6.8 shows two-dimensional (2D) theoretical and simulated system-level local spatial CCF at three time instants, i.e., $t = 0, 5, 10$ s. It is worth noting that $t = 0$ represents the WSSUS case. It is clear that simulated

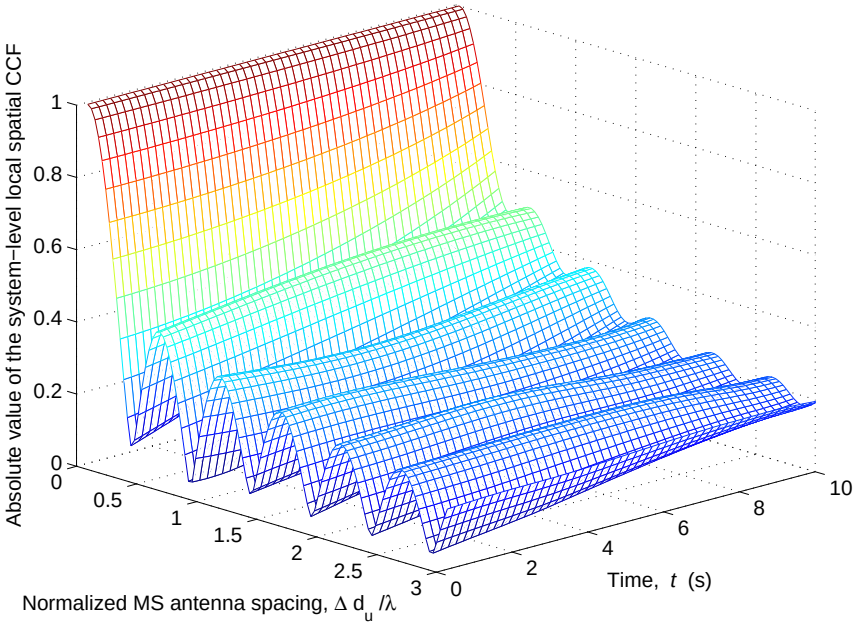

FIGURE 6.7: The absolute value of the system-level local spatial CCF of the non-stationary IMT-A channel model (UMa NLoS scenario).

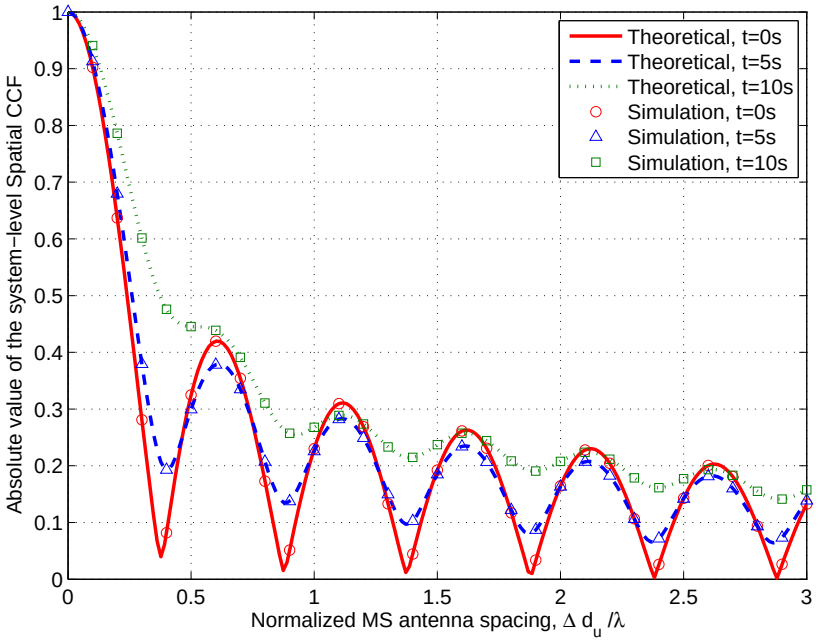

FIGURE 6.8: The theoretical and simulated system-level local spatial CCF of the non-stationary IMT-A at different time instants (UMa NLoS scenario).

results match theoretical ones very well, verifying the correctness of our theoretical derivations as well as simulations.

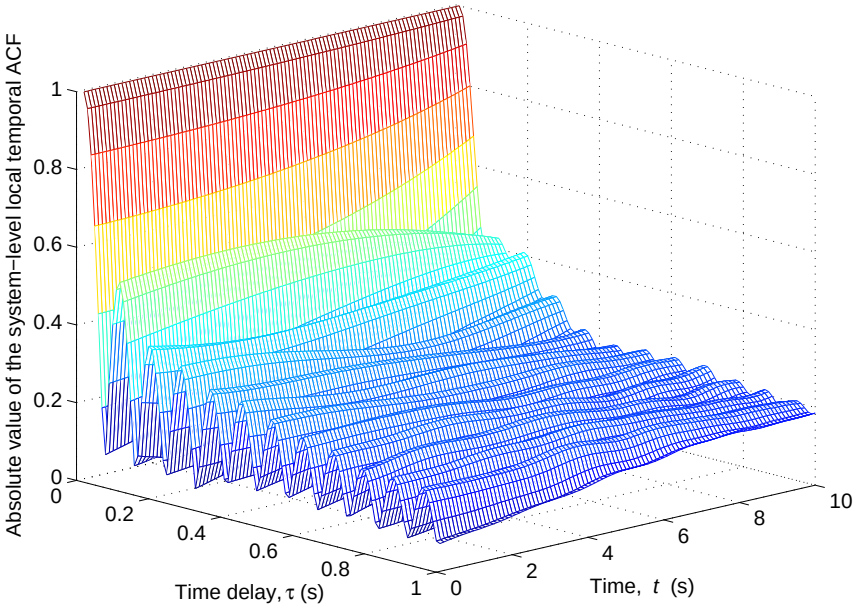

FIGURE 6.9: The absolute value of the system-level local temporal ACF of the non-stationary IMT-A channel model (UMa NLoS scenario).

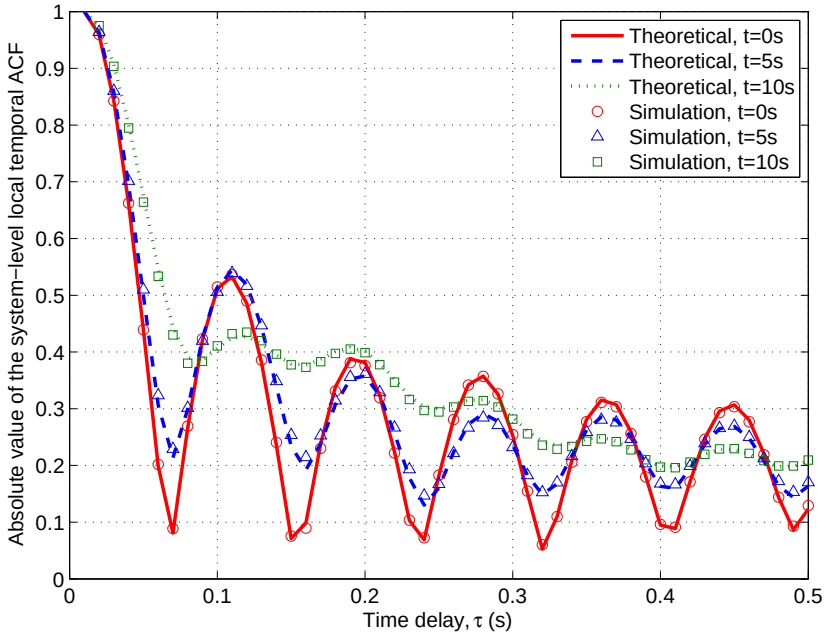

FIGURE 6.10: The theoretical and simulated system-level local temporal ACF of the non-stationary IMT-A at different time instants (UMa NLoS scenario).

6.5.2 Local temporal ACF

Still using the NLoS UMa scenario, the following parameters are used for simulating the local temporal ACF: $\phi_{n,m}(t_0)$ = random, $c(t_0)$ = 100 m, $\theta_c = 15°$, v_c = 30 m/s,

$\varphi_{n,m}(t_0)$ = random, $a(t_0) = 70$ m, $\theta_{MC} = -140°$, $v_{MC} = 5$ m/s, $\theta_{MS} = 120°$, and $v_{MS} = 20$ m/s,.

Fig. 6.9 shows the absolute value of the 3D local temporal ACF of the non-stationary IMT-A channel model at the system level for the NLoS UMa scenario. Similar to the local spatial CCF, the absolute value of the local temporal ACF varies with time t because of the time-varying AoDs and AoAs. Fig. 6.10 illustrates this differences by plotting the 2D theoretical and simulated system-level local temporal ACF at three different time instants, i.e., $t = 0$ s (WSSUS), $t = 5$ s, and $t = 10$ s. Again, the simulated results match theoretical results very well, verifying the correctness of our theoretical derivations as well as simulations.

6.6 Summary

Based on the original WSSUS IMT-A channel model, this chapter has developed a non-stationary IMT-A MIMO channel model to investigate the time variation of the wireless channels in different moving scenarios by considering only time-varying AoDs and AoAs. The impacts of these parameters on the time-varying functions have been investigated thoroughly. According to the proposed non-stationary IMT-A channel model, the statistical properties in terms of the local spatial CCF and local temporal ACF have been derived. Furthermore, the corresponding simulation results have been obtained by MATLAB simulations. Satisfied agreement between the theoretical results and simulated results is achieved to prove the correctness of our derivations. Finally, numerical results have demonstrated that the local statistical properties would vary with time due to the time-variant angular parameters of the proposed channel model.

Chapter 7

Conclusions and Future Work

For the successful design and development of wireless communication systems, propagation channel modelling and simulations are crucial and indispensable. This thesis presents a wealth of comprehensive research on geometry-based wireless channel modelling and simulation for advanced MIMO V2V communication systems (i.e., Chapter 3 and Chapter 4) and F2M cellular systems (i.e., Chapter 5 and Chapter 6). The importance of our research has been proved and introduced in detail. In this concluding chapter, the key findings of my PhD research are summarised and several potential future research directions are proposed as well.

7.1 Summary of Results

- **V2V Channel Models**

In Chapter 3, a novel 3D theoretical RS-GBSM and corresponding SoS simulation model have been proposed for non-isotropic scattering MIMO V2V fading channels. The proposed models have the ability to investigate the impact of the VTD and elevation angle on channel statistics. In addition, we have developed a novel parameter computation method, named as MEV, to jointly calculate the azimuth and elevation angles. Based on proposed models, comprehensive statistical properties have been

derived and thoroughly investigated. The simulation results have validated the utility of the proposed model. The difference between the proposed 3D and existing 2D models has been investigated and analysed in terms of the impact of the elevation angle on channel statistical properties. By comparing these results, we can see that the VTD has a great impact on all channel statistical properties, whereas the elevation angle has significant impact only on ST CF and Doppler PSD. Our simulations and analysis have demonstrated that the low VTD condition always shows better channel performance than the high VTD case. Compared with the existing less complex 2D RS-GBSMs and 3D RS-GBSMs, the proposed 3D MIMO V2V RS-GBSMs are more practical to mimic a real V2V communication environment.

In Chapter 4, a non-WSS 3D theoretical RS-GBSM and corresponding SoS simulation model have been proposed for non-isotropic scattering wideband MIMO V2V fading channels. The impact of the VTD and non-stationarity on channel statistics can be captured by the proposed models. Again, the MEV proposed in Chapter 3 is used to jointly calculate the azimuth and elevation angles. Based on proposed channel models, important local statistical properties have been derived and thoroughly investigated, i.e., local ST CF, local FCF and PDP. The proposed 3D reference and simulation models are verified by simulated results indicating the correctness of our derivations. It has shown that the VTD has major impact on these local statistical properties. To demonstrate the utility of proposed wideband non-WSS model, the channel simulator has been validated by measurements in terms of local SI.

- **F2M Cellular Channel Models**

In Chapter 5, the statistical properties and computational complexities of the LTE-A and IMT-A channel models have been thoroughly investigated in terms of the number of ROs. Theoretical expressions have been derived for the spatial CCF, temporal ACF, envelope LCR, AFD, PDP, and FCF, verified by the corresponding simulation results. Overall, the LTE-A channel model is simpler and requires much less number of ROs than the IMT-A channel model. However, the IMT-A channel model has better accuracy to simulate the various MIMO scenarios but with higher complexities. To

simplify the IMT-A channel model, several complexity reduction methods have been proposed. Besides the statistical properties, we have employed the system throughput of the 4G LTE-A system as an additional accuracy metric. The number of ROs and the channel coefficient computing time are used as the complexity metrics. The simulation results have shown that the proposed simplification methods can significantly reduce the complexity of the IMT-A channel model whereas the accuracy is not degraded much. Therefore, it has been demonstrated that the proposed complexity reduction methods are effective to apply to the original IMT-A channel model.

In Chapter 6, a framework of non-stationary IMT-A MIMO channel model has been developed according to the baseline WSS IMT-A channel model. The non-WSS IMT-A model is expected to investigate the time variation of the wireless channels in different moving scenarios by considering time-varying AoDs and AoAs. The impacts of these parameters on the time-varying functions have been investigated thoroughly. Moreover, important local statistical properties have been derived, such as the local spatial CCF and local temporal ACF. After that, the corresponding simulation results have been obtained by MATLAB simulations, which indicate a satisfactory agreement between the theoretical results and simulated proving the correctness of our derivations. It is concluded that the local statistical properties vary with time due to the time-variant parameters of the proposed channel model.

7.2 Future Research Directions

There are several potential directions of this thesis that can be further expanded.

- **V2V Channel Measurements**

Although our contributions have been limited to proposing theoretical RS-GBSMs and simulation models of MIMO V2V wireless channels, it can be considered as a theoretical guidance for establishing more purposeful V2V measurement campaigns in the future. A few publications on V2V channel measurements can be found in the

literature, there are research gaps to verify these proposed RS-GBSMs compared with more purposeful measurement data, such as the measurements for high VTD scenarios and the channel non-stationarity. Therefore, future research efforts may be devoted to conducting measurement campaigns cooperating with other universities or industries. Combining with actual measurements, it is interesting to compare the performance of different V2V models, such as pure-GBSM and semi-GBSM. It may be useful for the development of a new type of V2V channel model that provides better compromise between the model accuracy and complexity.

- **Realistic non-WSSUS Channel Models**

In the future advanced wireless communication systems, high speed moving scenarios will be ubiquitous, such high speed train and motorway vehicular communications [116]. The high mobility results in the existence of many moving scatterers around the Tx/Rx so that the time variation in such channels can be more rapid than that in conventional channels. This essentially means that non-stationarity has to be considered in realistic non-WSS channel models, since the WSSUS conditions pertain to a much shorter time period.

The framework of the non-WSS V2V and F2M channels models have been introduced in Chapter 4 and Chapter 6, respectively. However, the trade-off between the model accuracy and complexity in capturing the non-stationarity still needs more comprehensive investigations. This requires that the realistic channel models have to associate with the measurement data. Therefore, it is desirable to further extend the proposed channel models to be more realistic for capturing the non-stationarity of dynamic channels. Moreover, the correlated scattering (i.e., non-US) should be considered in non-WSSUS channel models. For the channel simulation, the optimal number of N should be performed as well. It is worth investigating if the experienced value (i.e., N=40) is still sufficient in non-WSSUS channel models.

Due to the fact that the non-WSSUS GBSMs make the models extremely complicated, it is also interesting to investigate whether it is worth sacrificing the complexity to

capture the non-stationarity by using GBSMs. Again, how to properly incorporate the non-stationarity into channel models is still an open question. Based on the conducted measurement campaigns in the future, it is extremely important to investigate the features of different types of modelling approach (e.g., NGSM and GBSM) in capturing the non-stationarity of channels in order to find a feasible approach to fill this research gap. On the other hand, the proposed channel models should be tested by integrated communication systems to evaluate the model performance.

- **Massive MIMO Channel Models**

Massive MIMO, also known as large MIMO, is an emerging technology in advanced wireless communications, such as 5G systems. It has been shown both in theory and in practical propagation environments that massive MIMO has very promising features, including large gains in spectral efficiency and several orders of magnitude lower transmitted power [117], compared with conventional MIMO systems with a small number of antennas.

In massive MIMO systems, either the Tx or Rx or both can be equipped with a large number of antennas (e.g., tens to hundreds). Modelling the effective scatterers in massive MIMO, it is observed that some scatterers may be invisible over the whole antenna array, and for scatterers being visible over the whole antenna array, their power contribution may vary considerably. Thus, the fading variation caused by the large antenna array can be critical to performance evaluation for massive MIMO systems. However, current theoretical studies of massive MIMO channel models are mostly done with i.i.d. complex Gaussian coefficients. To efficiently evaluate such a new technique in real scenarios, new channel models are needed that capture important properties of massive MIMO propagation channels.

Appendix A

Derivation of time-varying AoD for IMT-A

To derive the time-varying function of AoD, we assume that $\phi_{n,m}(t_0)$, $c(t_0)$, θ_c, and v_c are known, and can be obtained from a measurement campaign.

A.1 Case A.1

$(-\pi \leq \phi_{n,m}(t_0) < 0)$

A.1.1 Sub-case A.1.1

$(-\pi \leq \theta_c \leq \phi_{n,m}(t_0) \ \cup \ \phi_{n,m}(t_0) + \pi \leq \theta_c < \pi)$

In Fig. A.1, the sub-case A.1.1 $\phi_{n,m}(t)$ is expressed as

$$\phi_{n,m}(t) = \phi_{n,m}(t_0) - \alpha_{n,m}(t) \tag{A.1}$$

In trigonometry, based on the law of cosines, $\alpha_{n,m}(t)$ and $c(t_0)$ can be expressed as

$$\alpha_{n,m}(t) = \arccos \frac{c^2(t_0) + c^2(t) - (v_c t)^2}{2 \cdot c(t_0) \cdot c(t)}, \quad \alpha_{n,m}(t) \in [0, \pi] \tag{A.2}$$

$$c\left(t\right)=\sqrt{c^{2}\left(t_{0}\right)+\left(v_{c}t\right)^{2}-2\cdot c\left(t_{0}\right)\cdot v_{c}t\cdot\cos\beta} \tag{A.3}$$

Moreover, β can be expressed as:

$$\beta=\left(\pi+\phi_{n,m}(t_{0})-\theta_{c}\right),\quad \beta\in[0,\pi] \tag{A.4}$$

By substituting (A.3) and (A.4) into (A.2), we get

$$\begin{aligned}\alpha_{n,m}\left(t\right)&=\arccos\frac{c^{2}\left(t_{0}\right)+c^{2}\left(t\right)-\left(v_{c}t\right)^{2}}{2\cdot c\left(t_{0}\right)\cdot c(t)}\\&=\arccos\frac{c^{2}\left(t_{0}\right)+c^{2}\left(t_{0}\right)+\left(v_{c}t\right)^{2}-2\cdot c\left(t_{0}\right)\cdot v_{c}t\cdot\cos\left(\pi+\phi_{n,m}(t_{0})-\theta_{c}\right)\ -\left(v_{c}t\right)^{2}}{2\cdot c\left(t_{0}\right)\sqrt{c^{2}\left(t_{0}\right)+\left(v_{c}t\right)^{2}-2\cdot c\left(t_{0}\right)\cdot v_{c}t\cdot\cos\left(\pi+\phi_{n,m}(t_{0})-\theta_{c}\right)}}\\&=\arccos\frac{c\left(t_{0}\right)-v_{c}t\cdot\cos\left(\pi+\phi_{n,m}(t_{0})-\theta_{c}\right)}{\sqrt{c^{2}\left(t_{0}\right)+\left(v_{c}t\right)^{2}-2\cdot c\left(t_{0}\right)\cdot v_{c}t\cdot\cos\left(\pi+\phi_{n,m}(t_{0})-\theta_{c}\right)}}\\&=\arccos\frac{c\left(t_{0}\right)+v_{c}t\cdot\cos\left(\phi_{n,m}(t_{0})-\theta_{c}\right)}{\sqrt{c^{2}\left(t_{0}\right)+\left(v_{c}t\right)^{2}+2\cdot c\left(t_{0}\right)\cdot v_{c}t\cdot\cos\left(\phi_{n,m}(t_{0})-\theta_{c}\right)}}\end{aligned} \tag{A.5}$$

And then, put (A.5) into (A.1), we finally obtain the $\phi_{n,m}\left(t\right)$ as

$$\begin{aligned}\phi_{n,m}\left(t\right)&=\phi_{n,m}(t_{0})-\alpha_{n,m}\left(t\right)\\&=\phi_{n,m}(t_{0})-\arccos\frac{c\left(t_{0}\right)+v_{c}t\cdot\cos\left(\phi_{n,m}\left(t_{0}\right)-\theta_{c}\right)}{\sqrt{c^{2}\left(t_{0}\right)+\left(v_{c}t\right)^{2}+2\cdot c\left(t_{0}\right)\cdot v_{c}t\cdot\cos\left(\phi_{n,m}\left(t_{0}\right)-\theta_{c}\right)}}\end{aligned} \tag{A.6}$$

To expressly show the result, we re-write $\phi_{n,m}\left(t\right)$ as follows in this thesis.

$$\phi_{n,m}\left(t\right)=\phi_{n,m}\left(t_{0}\right)-\alpha_{n,m}\left(t\right) \tag{A.7}$$

where

$$\alpha_{n,m}\left(t\right)=\arccos\frac{c\left(t_{0}\right)+v_{c}t\cdot\cos\left(\phi_{n,m}\left(t_{0}\right)-\theta_{c}\right)}{\sqrt{c^{2}\left(t_{0}\right)+\left(v_{c}t\right)^{2}+2\cdot c\left(t_{0}\right)\cdot v_{c}t\cdot\cos\left(\phi_{n,m}\left(t_{0}\right)-\theta_{c}\right)}}. \tag{A.8}$$

A.1.2 Sub-case A.1.2

$(\phi_{n,m}(t_0) < \theta_c < \phi_{n,m}(t_0) + \pi)$

In Fig. A.1, the sub-case A.1.2 $\phi_{n,m}(t)$ is expressed as

$$\phi_{n,m}(t) = \phi_{n,m}(t_0) + \alpha_{n,m}(t). \tag{A.9}$$

Following the same procedure as in (A.2), (A.3), (A.4) and (A.5) we can express the $\phi_{n,m}(t)$ as

$$\begin{aligned}\phi_{n,m}(t) &= \phi_{n,m}(t_0) + \alpha_{n,m}(t) \\ &= \phi_{n,m}(t_0) + \arccos \frac{c(t_0) + v_c t \cdot \cos(\phi_{n,m}(t_0) - \theta_c)}{\sqrt{c^2(t_0) + (v_c t)^2 + 2 \cdot c(t_0) \cdot v_c t \cdot \cos(\phi_{n,m}(t_0) - \theta_c)}}.\end{aligned} \tag{A.10}$$

Again, to expressly show the result, we re-write $\phi_{n,m}(t)$ as follows in this thesis.

$$\phi_{n,m}(t) = \phi_{n,m}(t_0) + \alpha_{n,m}(t), \tag{A.11}$$

where

$$\alpha_{n,m}(t) = \arccos \frac{c(t_0) + v_c t \cdot \cos(\phi_{n,m}(t_0) - \theta_c)}{\sqrt{c^2(t_0) + (v_c t)^2 + 2 \cdot c(t_0) \cdot v_c t \cdot \cos(\phi_{n,m}(t_0) - \theta_c)}}. \tag{A.12}$$

A.2 Case A.2

$(0 \leq \phi_{n,m}(t_0) < \pi)$

A.2.1 Sub-case A.2.1

$(-\pi \leq \theta_c \leq \phi_{n,m}(t_0) - \pi \ \cup \ \phi_{n,m}(t_0) \leq \theta_c < \pi)$

In Fig. A.1, the sub-case A.2.1 $\phi_{n,m}(t)$ is expressed as:

$$\phi_{n,m}(t) = \phi_{n,m}(t_0) + \alpha_{n,m}(t). \tag{A.13}$$

Similar to (A.2), (A.3), (A.4) and (A.5), we can write the $\phi_{n,m}(t)$ as:

$$\begin{aligned}\phi_{n,m}(t) &= \phi_{n,m}(t_0) + \alpha_{n,m}(t) \\ &= \phi_{n,m}(t_0) + \arccos \frac{c(t_0) + v_c t \cdot \cos\left(\phi_{n,m}(t_0) - \theta_c\right)}{\sqrt{c^2(t_0) + (v_c t)^2 + 2 \cdot c(t_0) \cdot v_c t \cdot \cos\left(\phi_{n,m}(t_0) - \theta_c\right)}}.\end{aligned} \tag{A.14}$$

A.2.2 Sub-case A.2.2

$(\phi_{n,m}(t_0) - \pi < \theta_c < \phi_{n,m}(t_0))$

In Fig. A.1, the sub-case A.2.2 $\phi_{n,m}(t)$ is expressed as:

$$\phi_{n,m}(t) = \phi_{n,m}(t_0) - \alpha_{n,m}(t). \tag{A.15}$$

Following the same procedure as before, $\phi_{n,m}(t)$ can be expressed as:

$$\begin{aligned}\phi_{n,m}(t) &= \phi_{n,m}(t_0) - \alpha_{n,m}(t) \\ &= \phi_{n,m}(t_0) - \arccos \frac{c(t_0) + v_c t \cdot \cos\left(\phi_{n,m}(t_0) - \theta_c\right)}{\sqrt{c^2(t_0) + (v_c t)^2 + 2 \cdot c(t_0) \cdot v_c t \cdot \cos\left(\phi_{n,m}(t_0) - \theta_c\right)}}.\end{aligned} \tag{A.16}$$

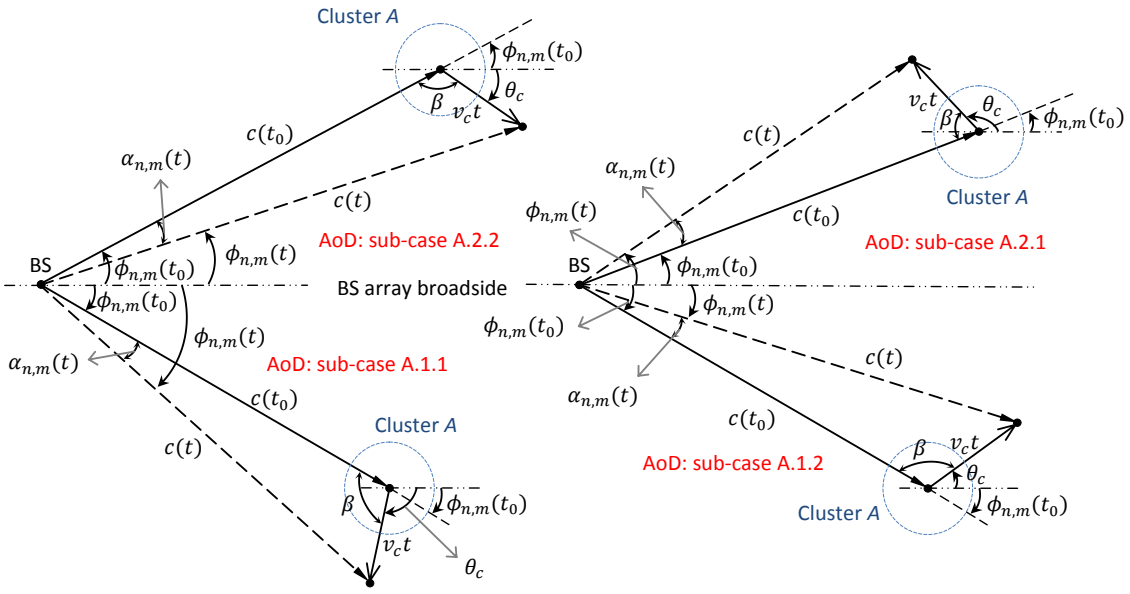

FIGURE A.1: Sub-case A.1.1 ($-\pi \leq \theta_c \leq \phi_{n,m}(t_0) \ \cup \ \phi_{n,m}(t_0) + \pi \leq \theta_c < \pi$)
Sub-case A.1.2 ($\phi_{n,m}(t_0) < \theta_c < \phi_{n,m}(t_0) + \pi$)
Sub-case A.2.1 ($-\pi \leq \theta_c \leq \phi_{n,m}(t_0) - \pi \ \cup \ \phi_{n,m}(t_0) \leq \theta_c < \pi$)
Sub-case A.2.2 ($\phi_{n,m}(t_0) - \pi < \theta_c < \phi_{n,m}(t_0)$).

Appendix B

Derivation of time-varying AoA for IMT-A

To derive the time-varying function of AoA with both cluster and MS are in motion, we assume that $\varphi_{n,m}(t_0)$, $a(t_0)$, $\theta_v = \theta_{MS/MC}$ and $v = v_{MS/MC}$ are known.

B.1 Case B.1

$(-\pi \leq \varphi_{n,m}(t_0) < 0)$

B.1.1 Sub-case B.1.1

$(-\pi \leq \theta_v < \varphi_{n,m}(t_0) \ \cup \ \pi + \varphi_{n,m}(t_0) < \theta_v < \pi)$

In Fig. B.1, the sub-case B.1.1 $\varphi_{n,m}(t)$ is expressed as:

$$\varphi_{n,m}(t) = \theta_v - \gamma_{n,m}(t) \pm \pi, \quad \varphi_{n,m}(t) \in [-\pi, \pi) \tag{B.1}$$

In trigonometry, based on the law of cosines, $\gamma_{n,m}(t)$ and $a(t)$ can be derived as:

$$\gamma_{n,m}(t) = \arccos \frac{a^2(t) + (vt)^2 - a^2(t_0)}{2 \cdot a(t) \cdot vt}, \quad \gamma_{n,m}(t) \in [0, \pi] \tag{B.2}$$

$$a\left(t\right)=\sqrt{a^{2}\left(t_{0}\right)+\left(vt\right)^{2}-2\cdot a\left(t_{0}\right)\cdot vt\cdot\cos\delta}\ . \tag{B.3}$$

Moreover, δ can be expressed as:

$$\delta=\left(\varphi_{n,m}(t_{0})-\theta_{v}\right),\qquad\delta\in[0,\pi] \tag{B.4}$$

So, we put (6.14) and (6.17) into (6.13), we have

$$\begin{aligned}\gamma_{n,m}\left(t\right)&=\arccos\frac{a^{2}\left(t\right)+\left(vt\right)^{2}-a^{2}\left(t_{0}\right)}{2\cdot a\left(t\right)\cdot vt}\\&=\arccos\frac{a^{2}\left(t_{0}\right)+\left(vt\right)^{2}-2\cdot a\left(t_{0}\right)\cdot vt\cdot\cos\left(\varphi_{n,m}(t_{0})-\theta_{v}\right)\ +\left(vt\right)^{2}-a^{2}\left(t_{0}\right)}{2\cdot vt\sqrt{a^{2}\left(t_{0}\right)+\left(vt\right)^{2}-2\cdot a\left(t_{0}\right)\cdot vt\cdot\cos\left(\varphi_{n,m}(t_{0})-\theta_{v}\right)}}\\&=\arccos\frac{vt-a\left(t_{0}\right)\cdot\cos\left(\varphi_{n,m}(t_{0})-\theta_{v}\right)}{\sqrt{a^{2}\left(t_{0}\right)+\left(vt\right)^{2}-2\cdot a\left(t_{0}\right)\cdot vt\cdot\cos\left(\varphi_{n,m}(t_{0})-\theta_{v}\right)}}\end{aligned} \tag{B.5}$$

Therefore, putting (6.17) into (6.12), we finally obtain the $\varphi_{n,m}\left(t\right)$ as:

$$\begin{aligned}\varphi_{n,m}\left(t\right)&=\theta_{v}-\gamma_{n,m}\left(t\right)\pm\pi\\&=\theta_{v}-\arccos\frac{vt-a\left(t_{0}\right)\cdot\cos\left(\varphi_{n,m}(t_{0})-\theta_{v}\right)}{\sqrt{a^{2}\left(t_{0}\right)+\left(vt\right)^{2}-2\cdot a\left(t_{0}\right)\cdot vt\cdot\cos\left(\varphi_{n,m}(t_{0})-\theta_{v}\right)}}\ \pm\pi\end{aligned} \tag{B.6}$$

To expressly show the result, we re-write $\varphi_{n,m}\left(t\right)$ as follows in this thesis.

$$\varphi_{n,m}\left(t\right)=\theta_{v}-\gamma_{n,m}\left(t\right)\pm\pi, \tag{B.7}$$

where

$$\gamma_{n,m}\left(t\right)=\arccos\frac{vt-a\left(t_{0}\right)\cdot\cos\left(\varphi_{n,m}(t_{0})-\theta_{v}\right)}{\sqrt{a^{2}\left(t_{0}\right)+\left(vt\right)^{2}-2\cdot a\left(t_{0}\right)\cdot vt\cdot\cos\left(\varphi_{n,m}(t_{0})-\theta_{v}\right)}}. \tag{B.8}$$

B.1.2 Sub-case B.1.2

$(\varphi_{n,m}(t_0) \leq \theta_v \leq \pi + \varphi_{n,m}(t_0))$

In Fig. B.1, the sub-case B.1.2 $\varphi_{n,m}(t)$ is expressed as:

$$\varphi_{n,m}(t) = \theta_v + \gamma_{n,m}(t) \pm \pi, \quad \varphi_{n,m}(t) \in [-\pi, \pi) \tag{B.9}$$

and

$$\delta = \left(\theta_v - \varphi_{n,m}(t_0)\right), \qquad \delta \in [0, \pi]. \tag{B.10}$$

By repeating the similar calculation for sub-case B1.1, we derive the $\varphi_{n,m}(t)$ as:

$$\begin{aligned} \varphi_{n,m}(t) &= \theta_v + \gamma_{n,m}(t) \pm \pi \\ &= \theta_v + \arccos \frac{vt - a(t_0) \cdot \cos\left(\varphi_{n,m}(t_0) - \theta_v\right)}{\sqrt{a^2(t_0) + (vt)^2 - 2 \cdot a(t_0) \cdot vt \cdot \cos\left(\varphi_{n,m}(t_0) - \theta_v\right)}} \pm \pi. \end{aligned} \tag{B.11}$$

B.2 Case B.2

$(0 \leq \varphi_{n,m}(t_0) < \pi)$

B.2.1 Sub-case B.2.1

$(-\pi \leq \theta_v < \varphi_{n,m}(t_0) - \pi \ \cup \ \varphi_{n,m}(t_0) < \theta_v < \pi)$

In Fig. B.1, the sub-case B.2.1 $\varphi_{n,m}(t)$ is expressed as:

$$\varphi_{n,m}(t) = \theta_v + \gamma_{n,m}(t) \pm \pi, \quad \varphi_{n,m}(t) \in [-\pi, \pi) \tag{B.12}$$

and

$$\delta = \left(\theta_v - \varphi_{n,m}(t_0)\right), \quad \delta \in [0, \pi]. \tag{B.13}$$

Again, by repeating the similar calculation for sub-case B1.1, we derive the $\varphi_{n,m}(t)$ as:

$$\begin{aligned}\varphi_{n,m}(t) &= \theta_v + \gamma_{n,m}(t) \pm \pi \\ &= \theta_v + \arccos \frac{vt - a(t_0) \cdot \cos\left(\varphi_{n,m}(t_0) - \theta_v\right)}{\sqrt{a^2(t_0) + (vt)^2 - 2 \cdot a(t_0) \cdot vt \cdot \cos\left(\varphi_{n,m}(t_0) - \theta_v\right)}} \pm \pi.\end{aligned} \tag{B.14}$$

B.2.2 Sub-case B.2.2

$(\varphi_{n,m}(t_0) - \pi \leq \theta_v \leq \varphi_{n,m}(t_0))$

In Fig. B.1, the sub-case B.2.2 $\varphi_{n,m}(t)$ is expressed as:

$$\varphi_{n,m}(t) = \theta_v - \gamma_{n,m}(t) \pm \pi, \quad \varphi_{n,m}(t) \in [-\pi, \pi) \tag{B.15}$$

and

$$\delta = \left(\theta_v - \varphi_{n,m}(t_0)\right), \quad \delta \in [0, \pi]. \tag{B.16}$$

Again, by repeating the similar calculation for sub-case B1.1, we derive the $\varphi_{n,m}(t)$ as:

$$\begin{aligned}\varphi_{n,m}(t) &= \theta_v - \gamma_{n,m}(t) \pm \pi \\ &= \theta_v - \arccos \frac{vt - a(t_0) \cdot \cos\left(\varphi_{n,m}(t_0) - \theta_v\right)}{\sqrt{a^2(t_0) + (vt)^2 - 2 \cdot a(t_0) \cdot vt \cdot \cos\left(\varphi_{n,m}(t_0) - \theta_v\right)}} \pm \pi.\end{aligned} \tag{B.17}$$

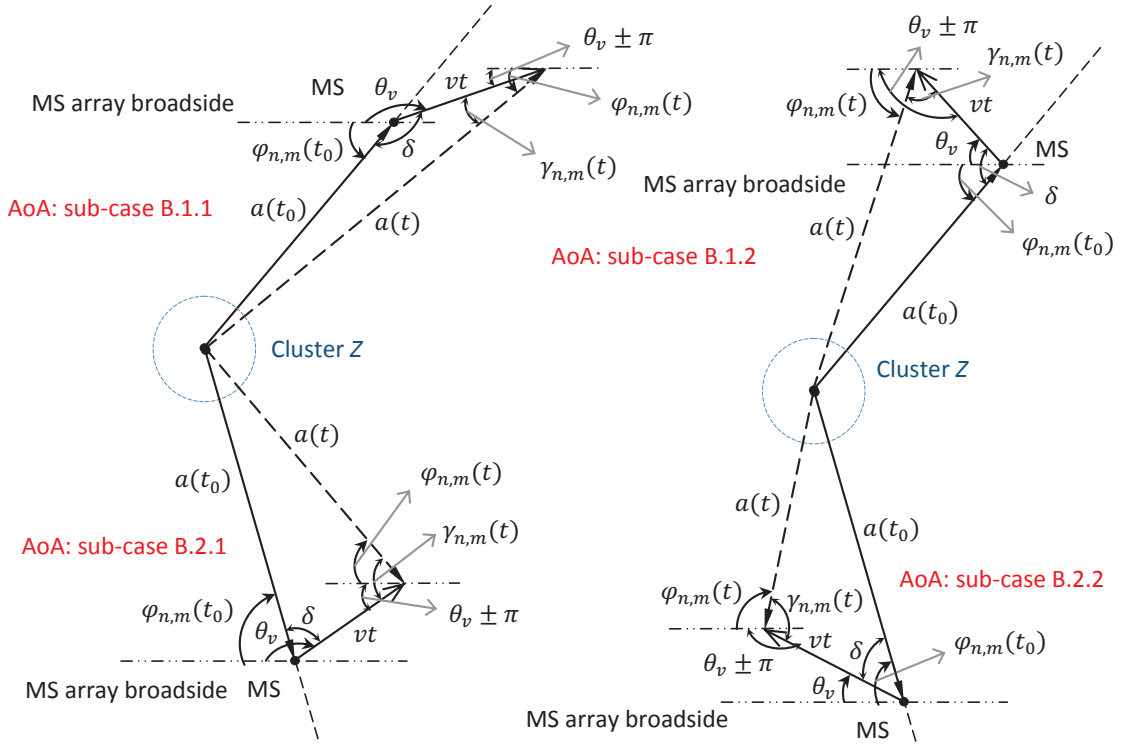

FIGURE B.1: Sub-case B.1.1 $(-\pi \leq \theta_v < \varphi_{n,m}(t_0) \ \cup \ \pi + \varphi_{n,m}(t_0) < \theta_v < \pi)$
Sub-case B.1.2 $(\varphi_{n,m}(t_0) \leq \theta_v \leq \pi + \varphi_{n,m}(t_0))$
Sub-case B.2.1 $(-\pi \leq \theta_v < \varphi_{n,m}(t_0) - \pi \ \cup \ \varphi_{n,m}(t_0) < \theta_v < \pi)$
Sub-case B.2.2 $(\varphi_{n,m}(t_0) - \pi \leq \theta_v \leq \varphi_{n,m}(t_0))$.

References

[1] R. Steele, *Mobile Radio Communications*, London, UK: Pentech Press, 1992.

[2] G. L. Stüber, *Principles of Mobile Communication*. 3rd Edition, New York: Springer, 2011.

[3] W. Chen and S. Cai, "Ad hoc peer-to-peer network architecture for vehicle safety communications," *IEEE Commun. Mag.*, vol. 43, no. 4, pp. 100–107, Apr. 2005.

[4] H. Hartenstein and K. P. Laberteaux, "A tutorial survey on vehicular ad hoc networks," *IEEE Commun. Mag.*, vol. 46, no. 6, pp. 164–171, Jun. 2008.

[5] M. Conti and S. Giordano, "Mobile ad hoc networking: milestones, challenges, and new research directions," *IEEE Commun. Mag.*, vol. 52, no. 1, pp. 85–96, Jan. 2014, doi: 10.1109/MCOM.2014.6710069.

[6] C.-X. Wang, X. Hong, X. Ge, X. Cheng, G. Zhang, and J. S. Thompson, "Cooperative MIMO channel models: a survey," *IEEE Commun. Mag.*, vol. 48, no. 2, pp. 80–87, Feb. 2010.

[7] B. Talha, and M. Pätzold, "Channel models for mobile-to-mobile cooperative communication systems: a state of the art review," *IEEE Veh. Technol. Mag.*, vol. 6, no. 2, pp. 33–43, Jun. 2011.

[8] G. Acosta and M. A. Ingram, "Six time- and frequency-selective empirical channel models for vehicular wireless LANs," *IEEE Veh. Technol. Mag.*, vol. 2, no. 4, pp. 4–11, Dec. 2007.

[9] C.-X. Wang, X. Hong, H. Wu, and W. Xu, "Spatial temporal correlation properties of the 3GPP spatial channel model and the Kronecker MIMO channel model," *EURASIP J. Wireless Commun. and Networking*, vol. 2007, Article ID 39871, 9 pages, Feb. 2007. doi:10.1155/2007/39871.

[10] Q. Yao, Y. Yuan, A. Ghazal, C.-X. Wang, L. Luan, and X. Lu, "Comparison of the statistical properties of the LTE-A and IMT-A channel models," in *Proc. IEEE WCNC'12*, Paris, France, Apr. 2012, pp. 393–398.

[11] L. Correia, *Wireless Flexible Personalised Communications (COST 259 Final Report)*, Chichester (UK): Wiley, 2001.

[12] A. F. Molisch, H. Asplund, R. Heddergott, M. Steinbauer, and T. Zwickg, "The COST 259 directional channel model-Part I overview and methodology," *IEEE Trans. Wireless Commun.*, vol. 5, no. 12, pp. 3421–3433, Dec. 2006.

[13] H. Asplund, A. A. Glazunov, A. F. Molisch, K. I. Pedersen, and M. Steinbauer, "The COST 259 directional channel model-Part II macrocells," *IEEE Trans. Wireless Commun.*, vol. 5, no. 12, pp. 3434–3450, Dec. 2006.

[14] A. F. Molisch, H. Hofstetter, et al., "The COST 273 channel model," *COST 273 Final Report*, Springer, New York, USA, 2006.

[15] V. Erceg, et al., IEEE 802.11 document 03/940r4, "TGn Channel Models", May 2004.

[16] 3GPP, TS36.101, V8.13.1, "3rd Generation Partnership Project; Technical Specification Group Radio Access Network; Evolved Universal Terrestrial Radio Access (E-UTRA); User Equipment (UE) radio transmission and reception (Release 8)," Apr. 2011.

[17] Motorola, etc., 3GPP, R4-071444, "Text proposal to 36.803 for MIMO correlation matrices," Aug. 2007.

[18] Agilent etc., 3GPP, R-071825, "Proposal for MIMO correlation matrices," Nov. 2007.

[19] Agilent Technologies, 3GPP, R4-070572, "Proposal for LTE channel models", May 2007.

[20] Agilent Technologies, 3GPP, R4-070879, "LTE MIMO correlation matrices," Jun. 2007.

[21] Agilent Technologies, 3GPP, R4-071318, "LTE MIMO correlation matrices," Aug. 2007.

[22] 3GPP, TS36.101, V10.2.1, "3rd Generation Partnership Project; Technical Specification Group Radio Access Network; Evolved Universal Terrestrial Radio Access (E-UTRA); User Equipment (UE) radio transmission and reception (Release 10)," Apr. 2011.

[23] S. Parkvall, E. Dahlman, A. Furuskar, Y. Jading, M. Olsson, S. Wanstedt and K. Zangi, "LTE-Advanced - evolving LTE towards IMT-Advanced," in *Proc. IEEE VTC'08-Fall*, Calgary, BC, Sep. 2008, pp. 1–5.

[24] J. Lee, J-K. Han and J. Zhang, "MIMO technologies in 3GPP LTE and LTE-Advanced," *EURASIP J. Wireless Commun. and Networking*, Article ID 302092, Jul. 2009. doi:10.1155/2009/302092.

[25] 3GPP TR 25.996 v10.0.0, "Spatial channel model for multiple input multiple output (MIMO) simulations," Release 10, Mar. 2011.

[26] 3GPP TR 25.996 v11.0.0, "Spatial channel model for multiple input multiple output (MIMO) simulations", Release 11, Sep. 2012.

[27] D. S. Baum, J. Hansen, and J. Salo, "An interim channel model for beyond-3G systems: extending the 3GPP spatial channel model (SCM)," in *Proc. IEEE VTC'05-Spring*, Stockholm, Sweden, May-Jun. 2005, pp. 3132–3136.

[28] D. S. Baum, H.El-Sallabi, et al., "Final report on link level and system level channel models," IST-2003-507581, WINNER D5.4 v1.4, Nov. 2005. http://www.ist-winner.org.

[29] P. Kyösti, et al., "WINNER II channel models," IST-4-027756, WINNER II D1.1.2, v1.2, Apr. 2008.

[30] J. Meinila, P. Kyosti, L. Hentila, T. Jamsa, E. Suikkanen, E. Kunnari, and M. Narandzia, "D5.3: WINNER+ final channel models," CELTIC/CP5-026, Jun. 2010. http://projects.celtic-initiative.org/winner+/index.html.

[31] ITU-R M.2135, "Guidelines for evaluation of radio interface technologies for IMT-Advanced," Geneva, Switzerland, Rep. ITU-R M.2135, 2008.

[32] ITU-R M.2135-1, "Guidelines for evaluation of radio interface technologies for IMT-Advanced," Geneva, Switzerland, Rep. ITU-R M.2135-1, Dec. 2009.

[33] IEEE P802.11p/D2.01, "Standard for wireless local area networks providing wireless communications while in vehicular environment," *IEEE Std. 802.11p*, Mar. 2007.

[34] L. Cheng, B. E. Henty, D. D. Stancil, F. Bai, and P. Mudalige, "Mobile vehicle-to-vehicle narrowband channel measurement and characterization of the 5.9 GHz dedicated short range communication (DSRC) frequency band," *IEEE J. Sel. Areas Commun.*, vol. 25, no. 8, pp. 1501–1516, Oct. 2007.

[35] A. S. Akki and F. Haber, "A statistical model for mobile-to-mobile land communication channel," *IEEE Trans. Veh. Technol.*, vol. 35, no. 1, pp. 2–10, Feb. 1986.

[36] A. S. Akki, "Statistical properties of mobile-to-mobile land communication channels," *IEEE Trans. Veh. Technol.*, vol. 43, no. 4, pp. 826–831, Nov. 1994.

[37] M. Pätzold, B. O. Hogstad, and N. Youssef, "Modeling, analysis, and simulation of MIMO mobile-to-mobile fading channels," *IEEE Trans. Wireless Commun.*, vol. 7, no. 2, pp. 510–520, Feb. 2008.

[38] A. G. Zajić and G. L. Stüber, "Space-time correlated mobile-to-mobile channels: modelling and simulation," *IEEE Trans. Veh. Technol.*, vol. 57, no. 2, pp. 715–726, Mar. 2008.

[39] X. Cheng, C.-X. Wang, D. I. Laurenson, S. Salous, and A. V. Vasilakos, "An adaptive geometry-based stochastic model for non-isotropic MIMO mobile-to-mobile channels," *IEEE Trans. Wireless Commun.*, vol. 8, no. 9, pp. 4824–4835, Sep. 2009.

[40] A. G. Zajić and G. L. Stüber, "Three-dimensional modeling, simulation, and capacity analysis of space-time correlated mobile-to-mobile channels," *IEEE Trans. Veh. Technol.*, vol. 57, no. 4, pp. 2042–2054, Jul. 2008.

[41] A. G. Zajić and G. L. Stüber, "Three-dimensional modeling and simulation of wideband MIMO mobile-to-mobile channels," *IEEE Trans. Wireless Commun.*, vol. 8, no. 3, pp. 1260–1275, Mar. 2009.

[42] H. Boeglen, B. Hilt, P. Lorenz, J. Ledy, A.-M. Poussard, and R. Vauzelle, "A survey of V2V channel modeling for VANET simulations," in *Proc. IEEE WONS'11*, Bardonecchia, Italy, Jan. 2011, pp. 117–123.

[43] G. Bakhshi, K. Shahtalebi, and H. S. Rad, "A novel full-three-dimensional MIMO mobile-to-mobile channel reference model," in *Proc. IEEE ICSPCS'09*, Omaha, NE, Sep. 2009, pp. 1–6.

[44] T.-M. Wu and T.-H. Tsai, "Novel 3-D mobile-to-mobile wideband channel model," in *Proc. IEEE APSURSI'10*, Chungli, Taiwan, Jul. 2010, pp. 1–4.

[45] P. T. Samarasinghe, T. A. Lamahewa, T. D. Abhayapala, and R. A. Kennedy, "3D mobile-to-mobile wireless channel model," in *Proc. IEEE AusCTW'10*, Canberra, Australian, Feb. 2010, pp. 30–34.

[46] K. Mammasis, R. W. Stewart, and E. Pfann, "3-Dimensional channel modeling using spherical statistics for multiple input multiple output systems," in *Proc. IEEE WCNC'08*, Las Vegas, USA, Mar./Apr. 2008, pp. 769–774.

[47] M. Pätzold, *Mobile Radio Channels*. 2nd Edition, Chichester: John Wiley & Sons, 2012.

[48] J. P. Kermoal, L. Schumacher, K. I. Pedersen, P. E. Mogensen and F. Frederiksen, "A stochastic MIMO radio channel model with experimental validation," *IEEE J. Selected Areas in Commun.*, vol. 20, no. 6, pp. 1211–1226, Aug. 2002.

[49] K. I. Pedersen, J. B. Andersen, J. P. Kermoal and P. Mogensen, "A stochastic multiple-input-multiple-output radio channel model for evaluation of space-time coding algorithms," in *Proc. IEEE VTC'00-Fall*, vol. 2, Boston, MA, Sep. 2000, pp. 893–897.

[50] T. Jämsä and J. Iinatti, "Approximation of geometry based stochastic channel models," in *Proc. IEEE Wireless VITAE'09*, Aalborg, Denmark, May 2009, pp. 693–697.

[51] G. Calcev, D. Chizhik, B. Goransson, S. Howard, H. Huang, A. Kogiantis, A.F. Molisch, A.L. Moustakas, D. Reed, and H. Xu, "A wideband spatial channel model for system-wide simulations," *IEEE Trans. on Veh. Technol.*, vol. 56, no. 2, pp. 389–403, Mar. 2007.

[52] K. Mammasis, R. W. Stewart, E. Pfann, and G. Freeland, "3-Dimensional channel modeling using spherical statistics for smart antennas," *IET Electronics Letter*, vol. 44, no. 2, 2008.

[53] K. Mammasis and R. W. Stewart, "3-Dimensional channel modelling using spherical statistics for multiple input multiple output systems," *IET Journal of Communications*, Jan. 2007, doi: 10.1049/iet-com:20070518.

[54] Y. Ma and M. Pätzold, "A wideband one-ring MIMO channel model under non-isotropic scattering conditions," in *Proc. IEEE VTC'08-Spring*, Singapore, May 2008, pp. 424–429.

[55] Y. Ma and M. Pätzold, "Wideband two-ring MIMO channel models for mobile-to-mobile communications," in *Proc. WPMC'07*, Jaipur, India, Dec. 2007, pp. 380-384.

[56] P. Almers, E. Bonek, A. Burr, N. Czink, M. Debbah, V. Degli-Esposti, H. Hofstetter, P. Kyosti, D. Laurenson, G. Matz, A. F. Molisch, C. Oestges, and

H. Ozcelik "Survey of channel and radio propagation models for wireless MIMO systems," *EURASIP J. Wireless Commun. and Networking*, vol. 2007, Article ID 19070, Feb. 2007. doi:10.1155/2007/19070.

[57] J. Karedal, F. Tufvesson, N. Czink, A. Paier, C. Dumard, T. Zemen, C. F. Mecklenbrauker, and A. F. Molisch, "A geometry-based stochastic MIMO model for vehicle-to-vehicle communications," *IEEE Trans. Wireless Commun.*, vol. 8, no. 7, pp. 3646–3657, Jul. 2009.

[58] A. Paier, T. Zemen, L. Bernado, G. Matz, J. Karedal, N. Czink, C. Dumard, F. Tufvesson, A.F. Molisch, Mecklenbrauker, and F. Christoph, "Non-WSSUS vehicular channel characterization in highway and urban scenarios at 5.2 GHz using the local scattering function," in *Proc. IEEE International ITG WSA'08*, Vienna, Austria, Feb. 2008, pp. 9–15.

[59] L. Schumacher, and B. Raghothaman, "Closed-form expressions for the correlation coefficient of directive antennas impinged by a multimodal truncated Laplacian PAS," *IEEE Trans. Wireless Commun.*, vol. 4, no. 4, pp. 1351–1359, Jul. 2005.

[60] E. Bonek, H. Ozcelik, M. Herdin, W. Weichselberger, and J. Wallace, "Deficiencies of a popular stochastic MIMO radio channel model," in *Proc. International. Symp. Wireless Personal Multimedia Commun.*, Yokosuka, Japan, Oct. 2003.

[61] T. Svantesson and J.W. Wallace, "Tests for assessing multivariate normality and the covariance structure of MIMO data," in *Proc. IEEE ICASSP'03*, vol. 4, Apr. 2003.

[62] W. Weichselberger, M. Herdin, H. Ozcelik and E. Bonek, "A stochastic MIMO channel model with joint correlation of both link ends," *IEEE Trans. on Wireless Commun.*, vol. 5, no. 1, pp. 90-100, Jan. 2006.

[63] N. Patwari, and P. Agrawal, "Effects of correlated shadowing: connectivity, localization, and RF tomography," in *Proc. IEEE IPSN'08*, St. Louis, MO, Apr. 2008, pp. 82–93.

[64] P. Agrawal and N. Patwari, "Correlated link shadow fading in multi-hop wireless networks," *IEEE Trans. on Wireless Commun.*, vol. 8, no. 8, pp. 4024–4036, Aug. 2009.

[65] T. Jämsä, P. Kyösti, and J. Meinilä, "Practical aspects of using IMT-Advanced channel models," in *Proc. IEEE ChinaCOM'09*, Xi'an, P. R. China, Aug. 2009, pp. 1–8.

[66] A. Algans, K. I. Pedersen, and P. E. Mogensen, "Experimental analysis of the joint statistical properties of azimuth spread, delay spread, and shadow fading," *IEEE J. Sel. Areas Commun.*, vol. 20, no. 3, Apr. 2002, pp. 523–531.

[67] G. Bakhshi, R. Saadat, and K. Shahtalebi, "Modeling and simulation of MIMO mobile-to-mobile wireless fading channels," *International Journal of Antennas and Propagation*, vol. 2012, Article ID 846153, 13 pages, Mar. 2012. doi: 10.1155/2012/846153.

[68] J. Maurer, T. Fugen, M. Porebska, T. Zwick, and W. Wisebeck, "A ray-optical channel model for mobile to mobile communications," *COST 2100 4th MCM'08*, TD(08) 430, Wroclaw, Poland, Feb. 2008.

[69] X. Cheng, C.-X. Wang, D. I. Laurenson, S. Salous, and A. V. Vasilakos, "New deterministic and stochastic simulation models for non-isotropic scattering mobile-to-mobile Rayleigh fading channels," *Wireless Commun. Mobile Computing*, John Wiley & Sons, vol. 11, no. 7, pp. 829–842, Jul. 2011.

[70] X. Cheng, C.-X. Wang, Y. Yuan, D. I. Laurenson, and X. Ge, "A novel three-dimensional regular-shaped geometry-based stochastic model for MIMO mobile-to-mobile Ricean fading channels," invited paper, in *Proc. IEEE VTC'10-Fall*, Ottawa, Canada, Sep. 2010, pp. 1–5.

[71] X. Cheng, C.-X. Wang, H. Wang, X. Gao, X.-H. You, D. Yuan, B. Ai, Q. Huo, L. Song, and B. Jiao, "Cooperative MIMO channel modeling and multi-link spatial correlation properties," *IEEE J. Sel. Areas Commun.*, vol. 30, no. 2, pp. 388–396, Feb. 2012.

[72] C.-X. Wang, X. Cheng, and D.I. Laurenson, "Vehicle-to-vehicle channel modeling and measurements: recent advances and future challenges," *IEEE Commun. Mag.*, vol. 47, no. 11, pp. 96–103, Nov. 2009.

[73] M. Boban, T. T. V. Vinhoza, M. Ferreira, J. Barros, and O. K. Tonguz, "Impact of vehicles as obstacles in vehicular ad hoc networks," *IEEE J. Sel. Areas Commun.*, vol. 29, no. 1, pp. 15–28, Jan. 2011.

[74] Y. Yuan, X. Cheng, C.-X. Wang, D. I. Laurenson, X. Ge, and F. Zhao, "Space-time correlation properties of a 3D two-sphere model for non-isotropic MIMO mobile-to-mobile channels," in *Proc. IEEE GLOBECOM'10*, Miami, FL, Dec. 2010, pp. 1–5.

[75] T. Abbas, F. Tufvesson, K. Sjöberg, and J. Karedal, "Measurement based shadow fading model for vehicle-to-vehicle network simulations," *IEEE Trans. Veh. Technol.*, arXiv: 1203.3370v3, Jun. 2013.

[76] K. V. Mardia and P. E. Jupp, *Directional Statistics*. Chichester: John Wiley & Sons, 2000.

[77] A. Abdi, J. A. Barger, and M. Kaveh, "A parametric model for the distribution of the angle of arrival and the associated correlation function and power spectral at the mobile station," *IEEE Trans. Veh. Technol.*, vol. 51, no. 3, pp. 425–434, May 2002.

[78] M. Pätzold and B. Talh, "On the statistical properties of sum-of-cisoids-based mobile radio channel models," in *Proc. WPMC'07*, Jaipur, India, Dec. 2007, pp. 394–400.

[79] A. G. Zajić, G. L. Stüber, T. G. Pratt, and S. Nguyen, "Envelope level crossing rate and average fade duration in mobile-to-mobile fading channels," in *Proc. IEEE ICC'08*, Atlanta, America, May 2008, pp. 4446–4450.

[80] X. Cheng, Q. Yao, C.-X. Wang, B. Ai, G. L. Stuber, D. Yuan, and B. Jiao, "An improved parameter computation method for a MIMO V2V Rayleigh fading

channel simulator under non-isotropic scattering environments," *IEEE Commun. Letters*, vol. 17, no. 2, pp. 265–268, Feb. 2013.

[81] Y. Yuan, C.-X. Wang, X. Cheng, B. Ai, and D. I. Laurenson, "Novel 3D geometry-based stochastic models for non-isotropic MIMO vehicle-to-vehicle channels," *IEEE Trans. Wireless Commun.*, vol. 14, no. 1, Jan. 2014.

[82] I. Sen and D. W. Matolak, "Vehicle-vehicle channel models for the 5-GHz band," *IEEE Trans. Intell. Transp. Syst.*, vol. 9, no. 2, pp. 235–245, Jun. 2008.

[83] O. Renaudin, V.-M. Kolmonen, P. Vainikainen, and C. Oestges, "Car-to-car channel models based on wideband MIMO measurements at 5.3 GHz," in *Proc. IEEE EuCAP'09*, Berlin, Germany, Mar. 2009, pp. 635–639.

[84] O. Renaudin, V.-M. Kolmonen, P. Vainikainen, and C. Oestges, "Non-stationary narrowband MIMO inter-vehicle channel characterization in the 5-GHz band," *IEEE Trans. on Veh. Technol.*, vol. 59, no. 4, pp. 2007–2015, May 2010.

[85] O. Renaudin, V.-M. Kolmonen, P. Vainikainen, and C. Oestges, "Wideband measurement-based modeling of inter-vehicle channels in the 5 GHz band," *IEEE Trans. on Veh. Technol.*, vol. 62, no. 8, pp. 3531–3540, Oct. 2013.

[86] A. Chelli and M. Pätzold, "A non-stationary MIMO vehicle-to-vehicle channel model based on the geometrical T-junction model," in *Proc. IEEE WCSP'09*, Nanjing, China, Nov. 2009, pp. 1–5.

[87] A. Chelli and M. Pätzold, "A non-stationary MIMO vehicle-to-vehicle channel model derived from the geometrical street model," in *Proc. IEEE VTC'11-Fall*, San Francisco, USA, Sep. 2011, pp. 1–6.

[88] U.A.K.C. Okonkwo, S.Z.M. Hashim, R. Ngah, N.F. Nanyan, and T. Abd Rahman, "Time-scale domain characterization of nonstationary wideband vehicle-to-vehicle propagation channel," in *Proc. IEEE APACE'10*, Port Dickson, Malaysia, Nov. 2010, pp.1–6.

[89] G. Matz, "On non-WSSUS wireless fading channels," *IEEE Trans. on Wireless Commun.*, vol. 4, pp. 2465–2478, Sep. 2005.

[90] T. Zwick, C. Fischer, D. Didascalou, and W. Wiesbeck, "A stochastic spatial channel model based on wave-propagation modeling," *IEEE J. Sel. Areas Commun.*, vol. 18, no. 1, pp. 6–15, Jan. 2000.

[91] Z. Zhao, X. Cheng, M. Mao, C.-X. Wang, and B. Jiao, "Channel estimation schemes for IEEE 802.11p standard," *IEEE Intelligent Transportation Systems Mag.*, vol. 5, no. 4, pp. 38–49, Oct. 2013.

[92] I. E. Talatar, "Capacity of multi-antenna Gaussian channels," *Tech. Rep.*, AT & T Bell Labs, Florham Park, NJ, USA, Jun. 1995.

[93] G. J. Foschini and M. J. Gans, "On limits of wireless communications in a fading environment when using multiple antennas," *Wireless Personal Commun.*, vol. 6, no. 3, pp. 311–335, Mar. 1998.

[94] C.-X. Wang, M. Pätzold, and D. Yuan, "Accurate and efficient simulation of multiple uncorrelated Rayleigh fading waveforms," *IEEE Trans. Wireless Commun.*, vol. 6, no. 3, pp. 833–839, Mar. 2007.

[95] C.-X. Wang, D. Yuan, H.-H. Chen, and W. Xu, "An improved deterministic SoS channel simulator for efficient simulation of multiple uncorrelated Rayleigh fading channels," *IEEE Trans. Wireless Commun.*, vol. 7, no. 9, pp. 3307–3311, Sep. 2008.

[96] P. J. Smith and M. Shafi, "The impact of complexity in MIMO channel models," in *Proc. IEEE ICC'04*, Paris, France, Jun. 2004, pp. 2924–2928.

[97] P. Kyösti, T. Jämsä, A. Byman, and M. Narandzić, "Computational complexity of drop based radio channel simulation," in *Proc. IEEE ISSSTA'08*, Bologna, Italy, Aug. 2008, pp. 287–291.

[98] Y. Zhang, J. Zhang, P. J. Smith, M. Shafi, and P. Zhang, "Reduced complexity channel models for IMT-Advanced evaluation," *EURASIP J. Wireless Commun. and Networking*, Article ID 195480, Apr. 2009. doi:10.1155/2009/195480.

[99] M. Pätzold and C. A. Gutiérrez, "Level-crossing rate and average duration of fades of the envelope of a sum-of-cisoids," in *Proc. IEEE VTC'08-Spring*, Singapore, May 2008, pp. 488–494.

[100] C.-X. Wang, N. Youssef, and M. Pätzold, "Level-crossing rate and average duration of fades of deterministic simulation models for Nakagami-Hoyt fading channels," in *Proc. IEEE WPMC'02*, Hawaii, USA, Oct. 2002, pp. 272–276.

[101] [Online]. Available: http://www.nt.tuwien.ac.at/ltesimulator.

[102] J.C. Ikuno, M. Wrulich, and M. Rupp, "System level simulation of LTE networks," in *Proc. IEEE VTC'10-Spring*, Taipei, May 2010, pp. 1–5.

[103] 3GPP, TS36.101, v11.3.0, "3rd Generation Partnership Project; Technical Specification Group Radio Access Network; Evolved Universal Terrestrial Radio Access (E-UTRA); User Equipment (UE) radio transmission and reception (Release 11)", Jan. 2013.

[104] J. Karedal, F. Tufvesson, N. Czink, A. Paier, C. Dumard, T. Zemen, C. F. Mecklenbrauker, and A. F. Molisch, "Measurement-based modeling of vehicle-to-vehicle MIMO channels," in *Proc. IEEE ICC'09*, Dresden, Jun. 2009, pp. 1–6.

[105] J. W. Wallace, and M. A. Jensen, "Measurement and characterization of the time variation of indoor and outdoor MIMO channels at 2.4 and 5.2 GHz," in *Proc. IEEE VTC'05-Fall*, vol. 2, Sep. 2005, pp. 1289–1293.

[106] J. W. Wallace, and M. A. Jensen, "Time-varying MIMO channels: measurement, analysis, and modeling," *IEEE Trans. on Antennas and Propagation*, vol. 54, no. 11, pp. 3265–3273, Nov. 2006.

[107] G. Matz, "Characterization of non-WSSUS fading dispersive channels," in *Proc. IEEE ICC'03*, vol. 4, May 2003, pp. 2480–2484.

[108] G. Matz, "Doubly underspread non-WSSUS channels: analysis and estimation of channel statistics," in *Proc. IEEE SPAWC'03.*, Jun. 2003, pp. 190–194.

[109] S. Knorzer, M. A. Baldauf, T. Fugen, and W. Wiesbeck, "Channel analysis for an OFDM-MISO train communications system using different antennas, in *Proc. IEEE VTC'07-Fall*, Baltimore, USA, Oct. 2007, pp. 809–813.

[110] D. Shutin, and G. Kubin, "Cluster analysis of wireless channel impulse responses with hidden Markov models," in *Proc. IEEE ICASSP'04*, vol. 4, no. 1, May 2004, pp.949–952.

[111] N. Czink, R. Tian, S. Wyne, G. Eriksson, T. Zemen, J. Ylitalo, F. Tufvesson, and A. F. Molisch, "Cluster parameters for time-variant MIMO channel models," in *Proc. IET EuCAP'07*, Edinburgh, UK, Nov. 2007, pp. 1–8.

[112] N. Czink, T. Zemen, J.-P. Nuutinen, J. Ylitalo, and E. Bonek, "A time-variant MIMO channel model directly parametrised from measurements," *EURASIP J. Wireless Commun. and Networking*, vol. 2009, Article ID 687238, Apr. 2009. doi:10.1155/2009/687238.

[113] J. A. Gubner, B. N. Bhaskar, and K. Hao, "Multipath-cluster channel models," *2012 IEEE ICUWB'12*, 17-20 Sep. 2012, pp.292–296.

[114] H. Xiao, A.G. Burr, and L. Song, "A time-variant wideband spatial channel model based on the 3GPP model," in *Proc. IEEE VTC'06-Fall*, Montreal, Canada, Sep. 2006, pp. 1–5.

[115] S. Thoen, L. Van Der Perre, and M.Engels, "Modeling the channel time-variance for fixed wireless communications," *IEEE Commun. Letters*, vol. 6, no. 8, pp. 331–333, Aug. 2002.

[116] C.-X. Wang, F. Haider, X. Gao, X.-H. You, Y. Yang, D. Yuan, H. M. Aggoune, H. Haas, S. Fletcher, and E. Hepsaydir, "Cellular architecture and key technologies for 5G wireless communication networks," *IEEE Commun. Mag.*, vol. 52, no. 2, pp. 122–130, Feb. 2014.

[117] E. G. Larsson, O. Edfors, F. Tufvesson, and T. L. Marzetta, "Massive MIMO for next generation wireless systems," *IEEE Commun. Mag.*, vol. 52, no. 2, pp. 186–195, Feb. 2014.